SURFACE INTERACTIONS OF BIOMASS DERIVED OXYGENATES WITH HETEROGENEOUS CATALYSTS

A Dissertation
Presented to
The Academic Faculty

by

Guo Shiou Foo

In Partial Fulfillment
of the Requirements for the Degree
Doctor of Philosophy in the
School of Chemical & Biomolecular Engineering

Georgia Institute of Technology
December 2015

SURFACE INTERACTIONS OF BIOMASS DERIVED OXYGENATES WITH HETEROGENEOUS CATALYSTS

Approved by:

Dr. Carsten Sievers, Advisor
School of Chemical & Biomolecular Engineering
Georgia Institute of Technology

Dr. Pradeep K. Agrawal
School of Chemical & Biomolecular Engineering
Georgia Institute of Technology

Dr. William J. Koros
School of Chemical & Biomolecular Engineering
Georgia Institute of Technology

Dr. Michael A. Filler
School of Chemical & Biomolecular Engineering
Georgia Institute of Technology

Dr. Pamela Peralta-Yahya
School of Chemistry and Biochemistry
Georgia Institute of Technology

Date Approved: August 12, 2015

To my family and friends who have supported me over the years

ACKNOWLEDGEMENTS

This dissertation represents not only my work in the laboratory, it is a special milestone in four years of research at Georgia Tech, specifically within the Sievers group. My experience at Georgia Tech has been nothing short of amazing. I feel privileged to be accepted by the School of Chemical & Biomolecular Engineering at Georgia Tech, and was given unique opportunities to teach and work with some of the most dedicated and brilliant minds in the department. The successful completion of my Ph.D. degree has been the most difficult task in my life thus far, and it would not have been possible without the support of many wonderful people.

Firstly, I wish to express my special appreciation and thanks to my advisor, Dr. Carsten Sievers, for supporting me during these past four years. His encouragement and intellectual contributions allowed me to grow as a research scientist, making my experience in graduate school unforgettable. I would also like to thank my thesis committee members, William Koros, Pradeep Agrawal, Michael Filler and Pamela Peralta-Yahya, for their valuable feedback and guidance in my thesis work. They pushed me to think about the validity and impact of my research, its future advancement, and its application on an industrial level. This allowed me to view my work from a larger perspective.

There were other experts who also made significant contributions to my thesis. Matthew Yung gave valuable input and aided in some of the experimental work. Johannes Leisen was very patient in teaching me experiments related to NMR spectroscopy. Jeffrey Andrews and Brad Parker from the machine shop helped me to

construct the IR cell body and gave me advice on mechanical repairs for laboratory instruments.

In addition, I want to thank all the alumni and present members of the Sievers Group. I would not have made it through graduate school without their help and support over the years. First of all, I want to give special acknowledgment to Dr. John Copeland. He was a great mentor and friend, who was instrumental in helping me through candidacy and for sharing his valuable wisdom. I also want to thank the rest of the group members for their support and encouragement. They are Jessica Rogers, Sarah Schimming, Adam Van Pelt, Gautami Newalker, Jared McGrath, Abiola Shitta, Olga Simakova, Paige Pomeroy, Jungseob So, Chukwuemeka Okolie, Akil Syed, Sireesha Aluri, Alex Brittain, and Jason Lee. I must also thank Daniel Krötschel, an exchange student from the University of Leipzig in Germany, who toiled so hard during his stint at Georgia Tech. Undergraduate researchers (Allyson Rogers, Benjamin Sauk and Cayla Jolly) are also gratefully acknowledged for their hard work in the lab.

In addition to my thesis, I also had the golden opportunity to collaborate with several renowned research groups. These collaborations widened my breadth in research, giving me a lasting intellectual curiosity. Firstly, I must thank Dr. David Sholl and Daniel Wei for their crucial involvement in the second chapter of my dissertation. Secondly, I thank Dr. Christopher Jones and his group members (Sumit Bali, Stephanie Didas, and Mustafa Alkhabbaz) for several collaborations in studying the adsorption of carbon dioxide. I was exposed to the world of metal-organic frameworks by collaborations with Dr. Krista Walton, Nicholas Burtch, Dr. Sankar Nair and Jason Bentley. Lastly, I also

like to thank Dr. Bert Weckhuysen, Pieter Bruijnincx, Jan Hofmann, and Anna Jongerius from the University of Utrecht at the Netherlands for a long-distance collaboration.

Besides people whom I worked with, I must also thank several friends and classmates who helped me with their company and advice. They are Lu Xu, Zhenguan Tang, Chad He, Ming-Chien Hsieh, Shilu Fu, Ho Yee Hui, Huayu Li, Boyi Fu, Li-Wei Chou, Wei-Ming Yeh, Rui Chang, Michael Mangarella, Sudhir Sharma, Miles Sakwa-Novak, Shuai Tan, Xu Du, Chen Zhang, and Wei Mu. These people showed me that I could still have a social life in graduate school despite the long work hours and depression from failed experiments. I wish them all the best in their future endeavors as they move on to the next phase of their lives.

I wish to take this opportunity to thank my family from the bottom of my heart for their unconditional support. I thank my parents, especially my mother, Peck Sim, for being such an incredible mother. She has been my pillar of strength in life. Her continuous support and encouragement allowed me to tread through the tough times in life. I thank my sister, Ling Yann, and my brother-in-law, James, for been such good listeners and giving me sound advice. I must also thank my niece (Shi Man, ten months old) and nephew (Zheng Yu, three years old) for being the light in my life.

Finally, I would like to thank a special person in my life. The best outcome from these past four years is finding my girlfriend and soulmate. Yu-Chia Wu is the only person who can appreciate my awkwardness. Yu-Chia has been a true and great supporter and has unconditionally loved me during both good and bad times. She is extremely understanding and has placed a great deal of faith in me. I truly thank Yu-Chia for standing by my side these past years.

TABLE OF CONTENTS

LIST OF TABLES

LIST OF FIGURES

LIST OF SYMBOLS AND ABBREVIATIONS

ɣ	gamma
δ	deformation vibrational mode
ν	stretching vibrational mode
τ	twisting vibrational mode
ω	wagging vibrational mode
ρ	rocking vibrational mode
DFT	density functional theory
FTIR	fourier transform infrared
BET	Brunauer-Emmett-Teller
BJH	Barrett-Joyner-Halenda
TGA	thermalgravimetric analysis
DTA	differential thermal analysis
HV	high vacuum
MCT/A	mercury cadmium telluride antimonide
RTP	room temperature and pressure
NMR	nuclear magnetic resonance
MAS NMR	magic angle spinning nuclear magnetic resonance
PIXE	proton induced x-ray emission
RTUHV	room temperature and ultra high vacuum
TPD	temperature programmed desorption
XPS	x-ray photoelectron spectroscopy
DRIFTS	diffuse reflectance infrared fourier transform spectroscopy
XRD	x-ray diffraction

LAS	Lewis acid site
BAS	Brønsted acid site
W/F	Ratio of catalyst mass to molar flow rate of reactant

SUMMARY

The global economy is anticipated to grow four-fold by 2050 and energy demand is projected to increase by 56% between 2010 and 2040. Currently, most energy-consuming sectors (especially the transportation sector) and chemical industries rely heavily on non-renewable fossil-based fuels to meet their energy and petrolchemical feedstock requirements. Not only are fossil fuels undergoing fast depletion, but its consumption results in the emission of greenhouse gases, which can increase up to 130% by 2050 at current rates. Alternative energy sources must be developed to meet the projected energy demand in the future in a sustainable and environmentally conscious manner. Currently, biomass is the only sustainable source of organic carbon and liquid fuels. Furthermore, biofuels generate less carbon footprint compared to fossil fuels and can even achieve to be greenhouse gas neutral if efficient conversion methods are developed.

One major method of converting biomass into fuels and targeted chemicals involve heterogeneous catalysis. As such, heterogeneous catalysts are vital to many of these downstream processes. However, there is still a lack of understanding in some of these areas, especially the nature of surface interactions between these biomass-derived carbohydrates and the surface of different catalysts. Such knowledge would aid in the design of catalysts and optimization of the biorefinery processes. The purpose of this dissertation is to utilize different experimental techniques to elucidate the surface interactions and reaction mechanisms of these biomass derived oxygenates. Specifically, there are four different objectives in this thesis: to elucidate the role of Lewis and

Brønsted acid sites in the dehydration of glycerol, to elucidate the reaction mechanism in the hydrolysis of cellulose using functionalized carbon catalysts, to understand the effect of weak and strong acid sites in the hydrolysis of cellobiose, and to understand the steric effect and deactivation mechanism in the hydrodeoxygenation of various bio-oil model compounds.

The first study investigates the role of Lewis and Brønsted sites in the dehydration of glycerol on niobium oxide and Na^+-exchanged niobium oxide using FTIR spectroscopy supported by DFT calculations. Glycerol is impregnated on the catalysts at room temperature using an *ex-situ* method. Under high vacuum conditions, glycerol forms a stable multidentate alkoxy species through its primary hydroxyl groups with the Lewis sites. When coordinated this way, the primary C-O bonds are polarized, favoring dehydration in this position to form hydroxyacetone. In contrast, dehydration of the secondary alcohol group is kinetically favored over Brønsted acid sites in the absence of steric constraints. The primary product of this reaction, 1,3-propenediol, is further dehydrated to acrolein. When more than a monolayer of glycerol is impregnated on niobia, monoaromatic compounds are also formed on the surface upon heating.

The second study investigates the chemical oxidation of activated carbon by H_2O_2 and H_2SO_4, its structural and chemical modifications, and the materials are used as catalysts for the hydrolysis for cellulose. Treatment with H_2O_2 enlarges the pore size while imparting functional groups such as phenols, lactones and carboxylic acids. H_2SO_4 treatment primarily targets the edges of carbon sheets, and this effect is more pronounced with higher temperature. Adsorption isotherms demonstrate that the adsorption of oligomers on functionalized carbon is dominated by van der Waals forces. The

chemically treated materials are active for the hydrolysis of cellulose despite the relative weakness of most of their acid sites. It is proposed that a synergistic effect between defect sites and functional groups enhances the activity by inducing a conformational change in the glucan chains when adsorbed on defect sites. The exposed glycosidic bonds interact with in-plane functional groups to be hydrolyzed.

The third study investigates the functionalization of activated carbon by different treatments with sulfuric acid and hot liquid water and used as catalyst for the hydrolysis of cellobiose in a continuously operated fixed bed reactor. Characterization results reveal that the chemically treated materials are more disordered with a lower degree of graphitization, while adsorption isotherms demonstrate that van der Waals forces dominate the interaction between carbohydrates and the surface of catalysts. All catalysts are stable during the hydrolysis of cellobiose under flow conditions. Carbon catalysts with a limited fraction of sulfonic acid groups exhibit moderate cellobiose conversion but a higher and sustained glucose selectivity. The high selectivity is attributed to a higher fraction of weak acid sites, where degradation of glucose only occurs to a limited extent due to less accessibility and competitive adsorption with cellobiose. Furthermore, the strong sulfonic acid groups are more accessible for degradation reactions to occur. In contrast, the catalyst with a higher fraction of sulfonic acid groups shows increased cellobiose conversion but decreased glucose selectivity because glucose monomers can be converted to degradation products at these sites.

The fourth study investigates the hydrodeoxygenation of various bio-oil model compounds (anisole, m-cresol and guaiacol) over Pt/HBEA and the evolution of surface species. Depending on the functional group, different surface species are formed when

the compounds are adsorbed in the presence of Lewis acid sites. For anisole, the methoxy group is decomposed to form phenate species. The methyl and methoxy group remains intact on m-cresol and guaiacol to form cresolate and methoxy phenate species, respectively. The position of these functional groups have a strong influence in the degree of hydrodeoxygenation due to steric hindrance. This resulted in anisole to have the highest degree of hydrodeoxygenation, followed by m-cresol and guaiacol. Based on *operando* transmission FTIR spectroscopy, a timeline for the formation of polynuclear aromatics and catalyst deactivation is constructed. It was observed that the catalysts deactivated significantly in the first 2 h time on stream due to the formation of heavy monoaromatics and polynuclear aromatics, where the presence of methyl groups can accelerate its formation. Coke was rapidly formed in a higher quantity from guaiacol due its strong surface interaction. The presence of lower carbon content on spent Pt/HBEA catalysts compared to HBEA could be related to the high carbon diffusion barrier on Pt metal, or the suppression of hydrogen abstraction reaction in coke formation by hydrogen spilt-over species on Lewis acid sites.

CHAPTER 1

INTRODUCTION

1.1 Future of Fossil Fuels

The discovery of crude oil in the 19th century helped to industrialize the world and improved standards of living. Current energy systems are based on these fossil resources such as coal, petroleum and natural gas. In 2013, the U.S.A consumed 18.5 millions of barrels per day, followed by China at 10.3 millions of barrels per day.[1] These two countries are the leading consumer of crude oil, followed by Japan (4.5 M bbl/day), India and Russia (3.5 M bbl/day). Despite the overwhelming amount of crude oil consumed, the demand is expected to increase by a conservative amount of 35 percent from 2010 to 2040.[2] This is largely due to the increase in population size and the standards of living. However, this trend is expected to vary significantly around the world, as countries have different trajectories. For example, China and India are expected to account for half the growth in global energy demand due to increase in population. India is projected to become the most populous country with an anticipated 1.6 billion people by 2040, followed by China at 1.4 billion.

Global primary power consumption today is more than 13 terawatt (TW), most of which is fossil-based.[3] Figure 1.1 depicts U.S. energy use by source in 2003. The graph indicates that fossil fuels provide about 86% of the U.S. energy needs, with small contributions from carbon-free sources such as nuclear and renewables at 8% and 6%, respectively. U.S. Department of Energy (DOE) projected the total energy consumption in U.S. to increase at an annual average rate of 1.5% out to 2025, which is more rapid than the projected growth in domestic energy production. This would lead to increasing

dependence on imported fossil fuels. In general, the similar trend holds true for the majority of industrialized countries.

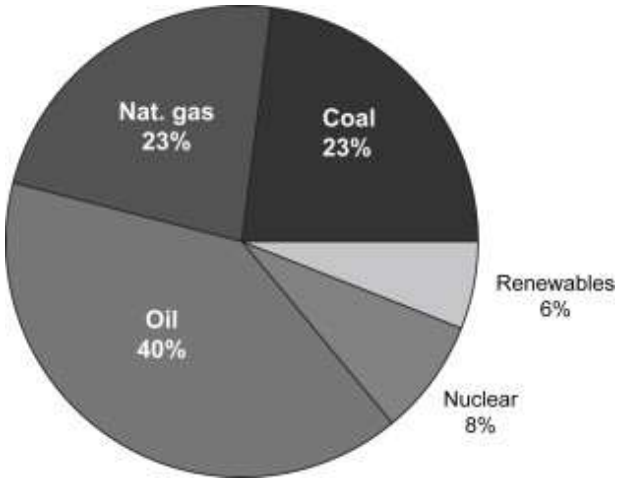

Figure 1.1 Percentage of energy sources in the United States.[1]

Many countries rely heavily on crude oil as it is a versatile natural resource. It is mainly composed of paraffins, napthenes and aromatics.[4] There is also a small amount of nitrogen (0.1 to 2%), sulfur (0.5-6%), and trace metals. Through refining, it can be converted to various petroleum products such as gasoline, diesel, jet fuel, heating oil, lubricants, asphalt and petrochemicals.[5] Figure 1.2 shows a simplified flow chart for refining crude oil, including alkylation, hydrocracking, reforming, hydrotreating, hydrodesulfurization and isomerization. The refining processes and operations can be classified into separation, conversion, formulating and blending and auxiliary refining operations. Heterogeneous catalysts are central to many of these processes, along with hydrogen gas in some cases to remove sulfur and nitrogen-containing impurities. About 74% of natural crude oil is converted to transportation fuels, and less than 5% is being converted to petrochemicals.[1] While a majority of crude oil is being converted into liquid transportation fuels, which is important for developing and sustaining modern society,

petrochemical feedstocks are equally important. These chemicals are the precursor to the production of polymers, solvents, and specialty chemicals that improve our standard of living.

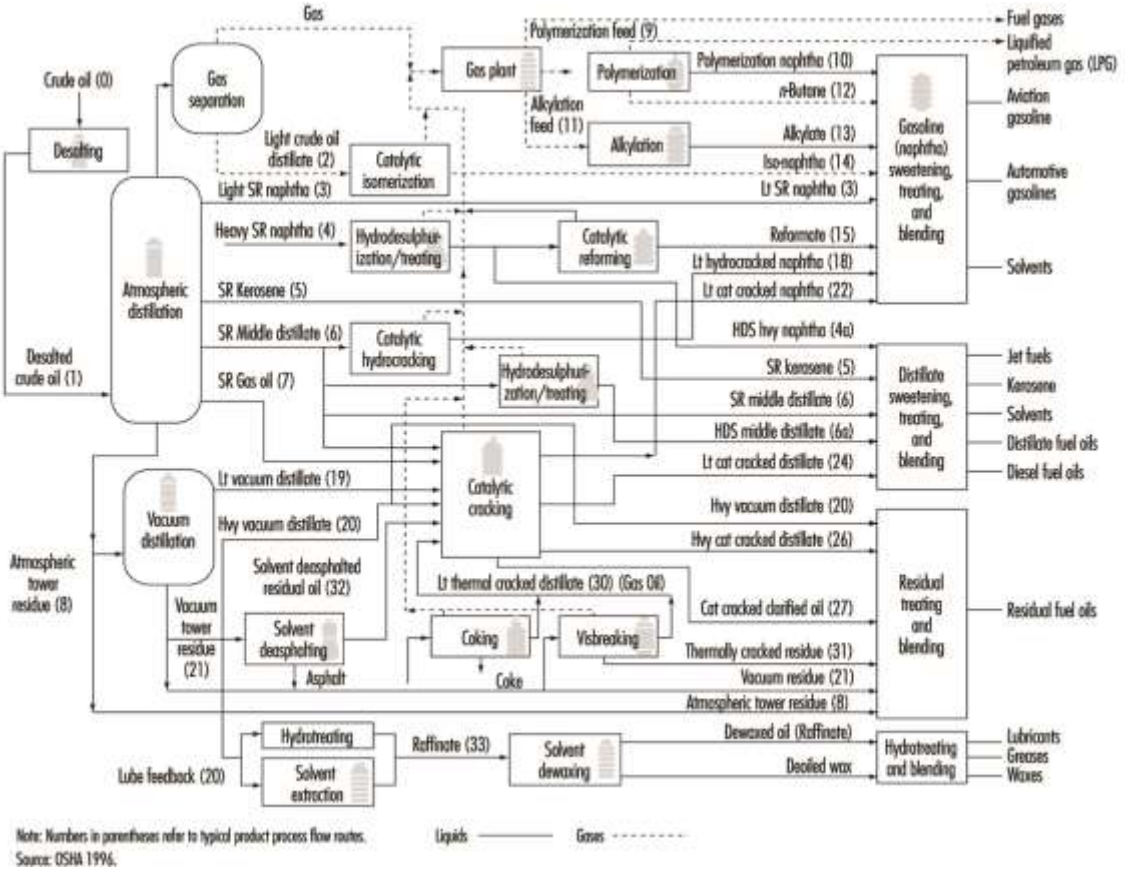

Figure 1.2 Simplified refinery process chart of crude oil.[5]

Unfortunately, crude oil is a finite resource. With its current consumption rate and increasing demand, oil is expected to be depleted in 40 years.[6] On the other hand, coal and gas reserves are predicted to last about 200 and 70 more years, respectively. Since oil and gas organizations such as Organization of the Petroleum Exporting Countries (OPEC) tried to dominate the fossil fuel market and control the prices, the huge coal reserve and its cheap price are the main factors in improving coal potential as the most

available fossil fuel in the future.[6] Even though coal is also a non-renewable natural resource, it has many important uses such as the generation of electricity and liquid fuels. Since coal comprises of mainly carbon, it can undergo gasification to form syngas, which is a primary mixture of hydrogen and carbon monoxide. Gasification is a process in which a carbonaceous material reacts with air, oxygen or steam at high temperature. Subsequently, syngas can undergo water gas shift reaction to produce hydrogen and carbon dioxide, which is used in methanol production by methanol synthesis, or produce alkanes from Fischer Tropsch reaction.[7]

Existing coal-fired power plants in the United States provide about 50% of the total power generated and represent more than 30% of carbon dioxide emissions, along with air and water pollution.[8] The utilization of crude and natural gas also results in the addition of carbon dioxide emission. The continued increase in the atmospheric concentration of carbon dioxide due to anthropogenic emissions is predicted to lead to significant changes in climate.[9] It is estimated that an increase of atmospheric carbon dioxide concentration by 250 ppm would result in a global warming of 5.5 K. Another study reported that following the cessation of emissions, removal of atmospheric carbon dioxide would decrease slowly.[10] Figure 1.3 shows that a quasi-equilibrium amount of carbon dioxide (40% of the peak concentration) is expected to be retained in the atmosphere by the end of the millennium. According to Hoffert et al., the stabilization of atmospheric carbon dioxide concentrations at 550, 450 and 350 ppm levels would require generation of 15, 25 and >30 TW, respectively, of carbon-free power by 2050.[11] It is realized that this will be an extremely difficult task requiring the development of revolutionary technologies in energy production, conversion, storage and distribution areas. Two prominent options for sustainable production of carbon-free energy that seem feasible are nuclear energy systems and renewable energy resources.

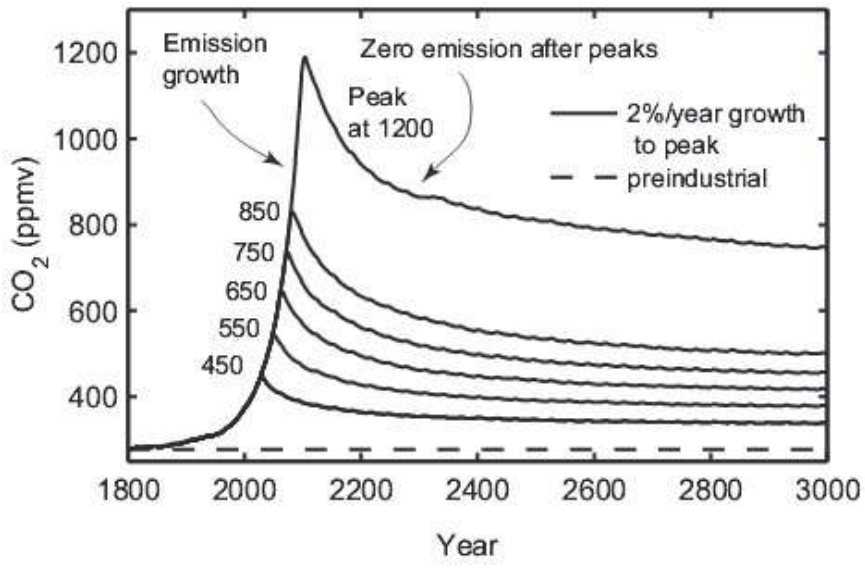

Figure 1.3 Concentration of carbon dioxide at a ramp rate of 2%/year to various values followed by zero emission.[10]

While many countries are dependent on fossil fuel for its energy and petrochemical products, it is certain that its depletion is inevitable in the future. In addition, the increase in demand by emerging economies would result in a higher cost. Coupled with political and environmental concerns, it is imperative to develop economical and energy-efficient processes for the sustainable production of fuels and chemicals.

1.2 Biomass as a Renewable Source of Energy and Chemicals

Currently, biomass is the only sustainable source of organic carbon and liquid fuels.[12] In addition, biofuels generate less carbon footprint compared to fossil fuels. Furthermore, biofuels can even achieve to be greenhouse gas neutral if efficient methods are developed.[13] Oak Ridge National Laboratory estimated that the United States could sustainably produce 1.3×10^9 metric tons of dry biomass per year using its agriculture and forest resources without disrupting food and export demands.[14] Such a huge production of biomass is equivalent to 54% of the United States' annual oil consumption. Other regions such as Europe, Africa and Latin America could also produce a significant and sustainable amount of biomass for energy.[15]

Plant biomass composed mainly of cellulose (40-80%), hemicellulose (15-30%) and lignin (10-25%) as shown in Figure 1.4.[12] Other minor components of biomass include triglycerides, alkaloids and terpenes. Cellulose is a crystalline material that consists of a linear polysaccharide with β-1,4 linkages of D-glucopyranose monomers. It is a polymer with an extended, flat and two-fold helical conformation.[16] Hydrogen bonds help to maintain and reinforce the rigid structure. Furthermore, it has a high degree of polymerization of approximately 10,000 to 15,000 glucopyranose monomers in plant biomass. Partial hydrolysis of cellulose results in the structure being broken down into various lengths of glucan chains, such as cellotriose and cellotetrose. Complete hydrolysis of cellulose results in the formation of glucose.

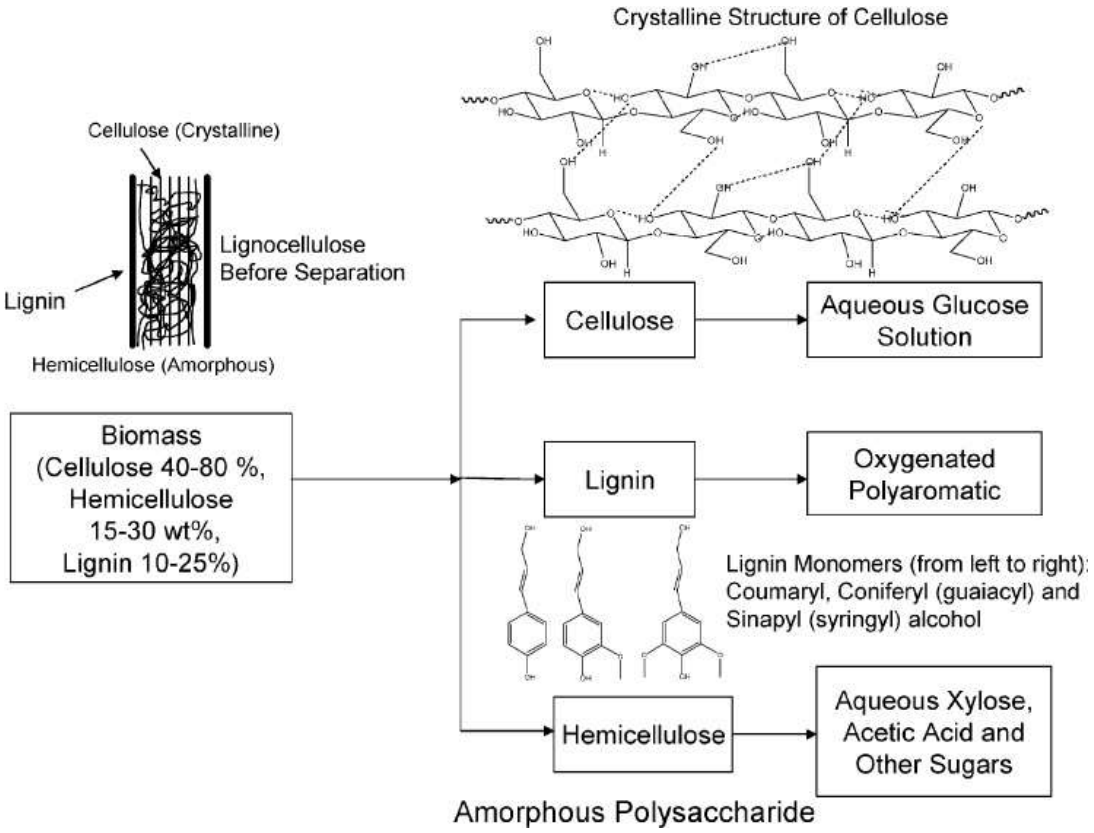

Figure 1.4 Structures of different biomass components.[12]

Hemicellulose is a polymer of five different sugars. These sugars are xylose, arabinose, galactose, glucose and mannose.[12] In addition, some fraction of these sugars are substituted with acetic acid. The most abundant building block of hemicellulose is xylose. Unlike cellulose, hemicellulose is amorphous in nature due to multiple branchings. This makes it relatively easy to hydrolyze to its monomers. Lignin is a highly branched, substituted and large aromatic polymer. It is commonly derived from wood and an integral part of secondary cell walls.

Lignocellulosic biomass has 40-45 wt% of oxygen. Removal of oxygen increases the heating value. Thus, the production of liquid fuels from lignocellulosic biomass usually involves the removal of oxygen as carbon dioxide or water. Lignocellulosic biomass can be converted into liquid fuels by three primary routes, which are syngas

production from gasification, bio-oil production by pyrolysis, and hydrolysis to produce sugar monomers.[17] Biomass gasification occurs at a lower temperature compared to coal gasification because biomass is more reactive than most types of coal.[18] As mentioned in the previous section, syngas is an intermediate in the production of ammonia, methanol, and Fischer-Tropsch hydrocarbons, which are well established industrially.

In addition to producing gases, thermochemical treatment of biomass can also produce liquids and solids. Parameters that determine the products of these thermochemical treatments are residence time, heating rate and temperature.[12] Process conditions that favor the production of bio-oil are short residence times, fast heating rates and moderate temperatures (fast pyrolysis). In contrast, slow pyrolysis produces large amounts of char, which can be used as a solid fuel. However, fast pyrolysis has emerged as an attractive and viable option as 50-90% of the biomass energy can be converted into a liquid.[19] During fast pyrolysis, a large number of reactions occur, such as hydrolysis, dehydration, isomerization, dehydrogenation, retro-condensation, and coking. This results in more than 400 organic compounds formed. Bio-oil contains acids, esters, ketones, alcohols, aldehydes, sugars, phenols and guaiacols.[20] The mixture is derived primarily from the depolymerization and fragmentation of the three components in lignocellulosic biomass: cellulose, hemicellulose and lignin. Unfortunately, bio-oil cannot directly be used as a fuel due to its poor volatility and high viscosity. In addition, it is corrosive, has low heating value and polymerizes with time. The oxygen content of bio-oils is around 35-40%.[21] Upgrading bio-oil to a conventional transport fuel requires full deoxygenation to increase its heating value. Furthermore, upgraded bio-oil can also be used as a renewable feedstock for the production of chemicals.

The two previous methods for lignocellulosic biomass conversion requires high temperature treatments for the production of gases, liquids and solids. Besides these high temperature methods, cellulosic biomass can be selectively converted into monomers under mild conditions. Subsequently, the monomer units can be further converted into

targeted fuels or chemicals. Lignocellulose is difficult to hydrolyze into monomers due to its recalcitrant nature. Thus, it must first be pretreated by separating the lignin and decreasing the crystallinity of cellulose.[13] Pretreatment methods include physical (ball milling, compression milling), chemical (hydrogen peroxide, dilute acids) and thermal. Pretreatment is one of the most expensive steps in converting biomass to sugars, thus it is desirable to use cost effective methods. Hot compressed water (200-300 °C) can be utilized to remove and hydrolyze hemicellulose.[13] As hemicellulose is broken down, acetic acid is also released, which continues to catalyze the reaction.

As mentioned earlier, cellulose is significantly more difficult to hydrolyze due to its crystalline nature and strong hydrogen bonds. Hydrolysis of cellulose can be catalyzed by acids or enzymes. Cellulase enzymes are able to catalyze the reaction with yields close to 100% at low temperature.[22] For acid hydrolysis, dilute acids or heterogeneous catalysts are used. The acid first penetrates into the cellulose structure to decrease the degree of polymerization, followed by hydrolysis into glucose monomers.[23] Lignin, which represents a large fraction of biomass (10-30 wt%), is usually used as a fuel in the pulp and paper industry, as well as in ethanol production plants.[12] Lignin can also be converted into transportation fuel and chemical by dehydroxygenation or zeolite upgrading, which are similar methods for upgrading bio-oil. The end products include phenol, benzene, naphthalene, and phenanthrene.

After hydrolysis, carbohydrate monomers that are derived from cellulose and hemicellulose are extremely important as they can be further converted to replace key petroleum-based building blocks. As shown in Figure 1.5, it is possible to produce a wide variety of potential products from glucose. In general, heterogeneous catalysts can be used to promote various types of reactions such as hydrolysis, dehydration, isomerization, aldol condensation, reforming, hydrogenation, and oxidation.[24]

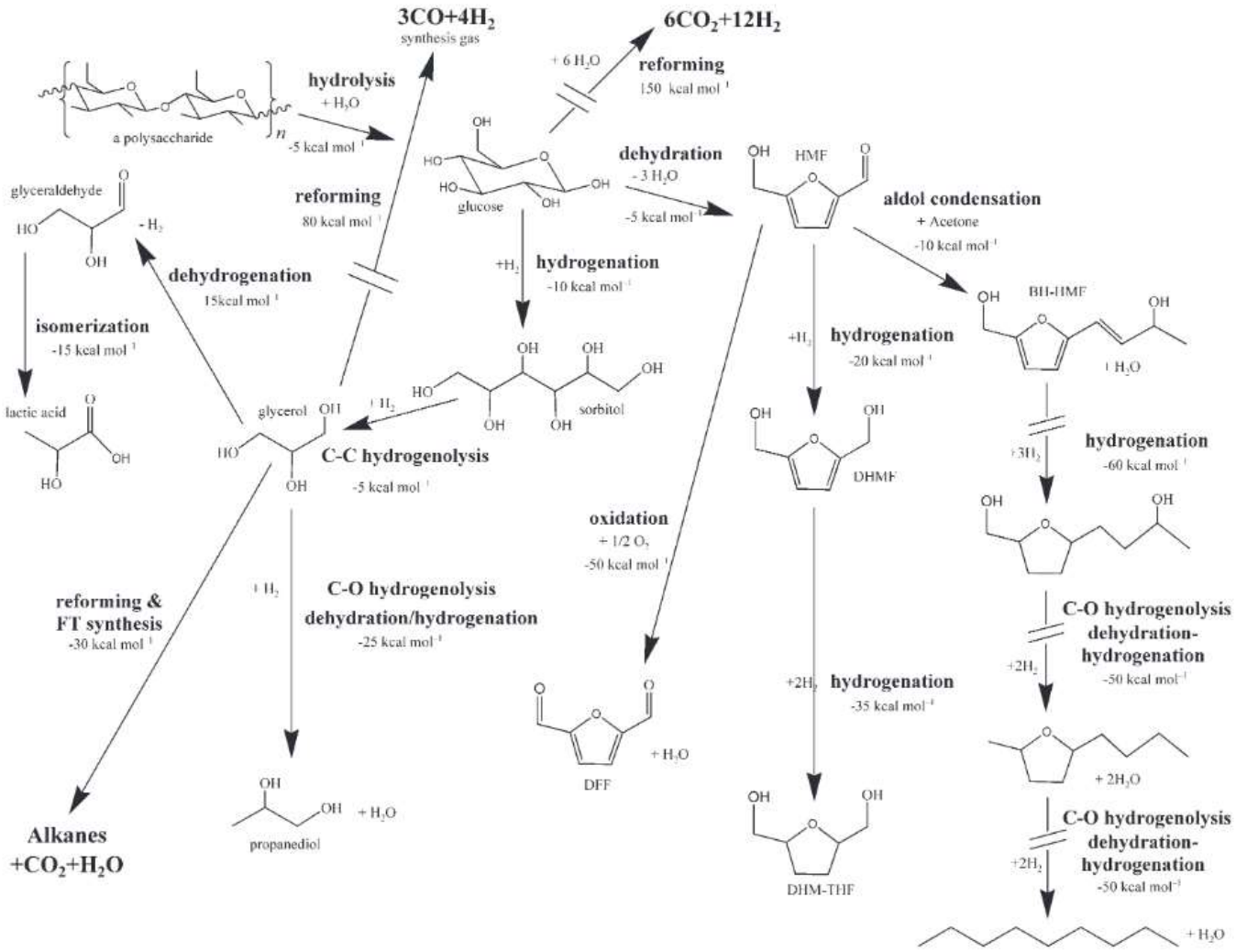

Figure 1.5 Pathways for the conversion of carbohydrates into fuels and chemicals.[24]

An alternative route for producing transportation fuel is utilizing triglycerides, which are the major component in vegetable oil and fats.[12] Triglycerides cannot be directly used as diesel due to its high viscosity and low volatility. Thus, vegetable oils must also be upgraded to be used as a fuel. Triglycerides can undergo transesterification in the presence of an acid or base catalyst to produce fatty acid-esters (biodiesel) and glycerol.[25] Methanol is usually used as the reactant due to its low cost, although other alcohols such as ethanol can produce better grades of biodiesel. Subsequently, these esters are blended with diesels from fossil fuels to meet regulations.

Since glycerol is a major by-product (10 wt%) from the transesterification process, the growth in crude glycerol is accompanied by the increase in biodiesel production. More importantly, glycerol can also be considered as an important feedstock as it has more than 1500 applications in many areas such as cosmetics, pharmaceuticals and food industries.[26] Using heterogeneous catalysts, glycerol can be valorized via partial oxidation, hydrogenolysis, etherification, dehydration, and reforming.[27] However, only a few of these processes have been industrialized, such as the production of epichlorohydrin and formation of syngas to produce methanol.

Sugars, sugar alcohols and polyols can also be converted into hydrogen or alkanes (C_1 to C_{15}) via aqueous-phase catalytic processes.[28-31] These aqueous-phase processes can be used in an integrated biorefinery to produce a range of fuels. The first step in the refining process is to convert biomass into an aqueous sugar solution. Subsequently, the products from these aqueous-phase processes would depend on the type of heterogeneous catalysts used. Production of hydrogen can be accomplished by aqueous-phase reforming.[17] Light alkanes (C_1 to C_6) can be produced via aqueous-phase dehydration and hydrogenation. These light alkanes can serve as natural gas or light naptha stream. Larger alkanes (C_7 to C_{15}) can be produced by combining dehydration/hydrogenation reactions with aldol condensation. These heavy alkanes could be used as diesel fuel.

As described above, biomass is a large source of renewable organic carbon and fuel. There are many different methods of processing biomass into fuels and targeted chemicals. However, there is still a lack of understanding in some of these areas. Since heterogeneous catalyst are vital to many of these downstream processes, it is important to study the surface interactions of these biomass-derived carbohydrates to aid in the design of catalysts and optimization of the biorefinery processes.

1.3 Objectives and Organization

One strategy for converting lignocellulosic biomass to ethanol or other liquid fuels involve the enzyme-catalyzed depolymerization of polysaccharides. However, enzymes are intrinsically expensive and high loadings are required to obtain reasonable production rates.[32] Another strategy is to utilize heterogeneous catalysts. Solid catalysts offer simplified separation and recycling, so it plays a crucial role in the conversion of renewable biomass feedstock to transportation fuels and chemicals. However, there is still a gap in the knowledge of the fundamental interactions between biomass molecules and heterogeneous catalysts. Understanding the surface interactions of important biomass molecules with the surfaces of catalysts will be essential to optimize existing processes and to enable the rational design of new catalysts with enhanced properties. The objective of this work is to understand the surface interactions of various model biomass compounds, the reaction mechanisms involved, and the properties of the catalysts that influence these steps. The knowledge gained in this work provides insight in optimizing the yield of desirable products with stable catalytic activity.

In Chapter 2, the dehydration of glycerol was studied using Fourier Transform Infrared (FTIR) spectroscopy supported by Density Functional Theory (DFT) calculations. This reaction is crucial because the catalytic dehydration of glycerol to acrolein is one of the most promising routes for valorizing glycerol. Niobium oxide was used because its acidity can be tuned by its calcination temperature, allowing the selectivity of reaction products to be correlated with the concentration of Lewis and Brønsted acid sites. In addition, Na^+-exchanged niobium oxide was also used as its Brønsted acid sites have been blocked, allowing the role of different acid sites to be elucidated. It was found that Brønsted and Lewis acid sites are involved in the formation of acrolein and hydroxyacetone, respectively. The surface interactions of glycerol, its dehydration reaction mechanism, and catalyst deactivation are discussed.

In Chapter 3, the catalytic hydrolysis of cellulose is studied. Activated carbon was used as a starting material and subjected to different types of chemical treatment to impart various functional groups and varying degree of graphitization. Subsequently, these materials were characterized and used in the hydrolysis of ball-milled cellulose in a batch reactor. Adsorption isotherms were also performed to understand the adsorption of glucose and cellobiose on carbon surfaces, which could be extrapolated to long glucan chains. The positive correlation between defect sites and acidic functional groups suggest a synergistic effect in play, and a reaction mechanism is proposed. This provides insight in optimizing the structure of carbon catalysts to improve the hydrolysis of cellulose.

Chapter 4 focuses on the effect of strong and weak acid sites of carbon catalysts by using the hydrolysis of cellobiose as a model reaction. Activated carbon was subjected to different chemical treatments to impart different fraction of sulfonic acid groups. The stability of the catalysts was determined by performing the reaction in a fixed-bed reactor and kinetic parameters were obtained. The effect of strong and weak acid sites is discussed with regards to the hydrolysis reaction, providing information to improve the yield of glucose monomers.

In Chapter 5, the hydrodeoxygenation of various bio-oil model compounds is investigated. In addition to reactivity experiments, the reactions were also performed in an *operando* transmission FTIR cell under the same reaction conditions to observe the evolution of surface species. Anisole, m-cresol and guaiacol were chosen because they have different functional groups and largely represent the composition of bio-oil. The surface interactions of these phenolic compounds, steric effect and catalyst deactivation are discussed. This study provides insight in the timeline for catalyst deactivation and the formation of polynuclear aromatic compounds and coke.

1.4 References

1. U.S. Energy Information and Administration International Energy Outlook.

2. *ExxonMobil Outlook for Energy 2015*.

3. Muradov, N. Z.; Veziroglu, T. N. "Green" path from fossil-based to hydrogen economy: An overview of carbon-neutral technologies. *Int. J. Hydrog. Energy* **2008,** *33*, 6804-6839.

4. Sauer, T. C.; Michel, J.; Hayes, M. O.; Aurand, D. V. Hydrocarbon characterization and weathering of oiled intertidal sediments along the Saudi Arabian Coast two years after the Gulf War oil spill. *Environment International* **1998,** *24*, 43-60.

5. Stellman, J. M.; Office, I. L., *Encyclopaedia of Occupational Health and Safety: Chemical, industries and occupations*. International Labour Office: 1998;

6. Shafiee, S.; Topal, E. When will fossil fuel reserves be diminished? *Energy Policy* **2009,** *37*, 181-189.

7. Khodakov, A. Y.; Chu, W.; Fongarland, P. Advances in the development of novel cobalt Fischer-Tropsch catalysts for synthesis of long-chain hydrocarbons and clean fuels. *Chem. Rev.* **2007,** *107*, 1692-1744.

8. Rochelle, G. T. Amine Scrubbing for CO2 Capture. *Science* **2009,** *325*, 1652-1654.

9. Cox, P. M.; Betts, R. A.; Jones, C. D.; Spall, S. A.; Totterdell, I. J. Acceleration of global warming due to carbon-cycle feedbacks in a coupled climate model. *Nature* **2000,** *408*, 184-187.

10. Solomon, S.; Plattner, G. K.; Knutti, R.; Friedlingstein, P. Irreversible climate change due to carbon dioxide emissions. *Proc. Natl. Acad. Sci. U. S. A.* **2009,** *106*, 1704-1709.

11. Hoffert, M. I.; Caldeira, K.; Benford, G.; Criswell, D. R.; Green, C.; Herzog, H.; Jain, A. K.; Kheshgi, H. S.; Lackner, K. S.; Lewis, J. S.; Lightfoot, H. D.; Manheimer, W.; Mankins, J. C.; Mauel, M. E.; Perkins, L. J.; Schlesinger, M. E.; Volk, T.; Wigley, T. M. L. Advanced technology paths to global climate stability: Energy for a greenhouse planet. *Science* **2002,** *298*, 981-987.

12. Huber, G. W.; Iborra, S.; Corma, A. Synthesis of transportation fuels from biomass: Chemistry, catalysts, and engineering. *Chem. Rev.* **2006,** *106*, 4044-4098.

13. Mosier, N.; Wyman, C.; Dale, B.; Elander, R.; Lee, Y. Y.; Holtzapple, M.; Ladisch, M. Features of promising technologies for pretreatment of lignocellulosic biomass. *Bioresour. Technol.* **2005,** *96*, 673-686.

14. Perlack, R. D.; Wright, L. L.; Turhollow, A.; Graham, R. L.; Stokes, B.; Erbach, D. C. *Biomass as Feedstock for a Bioenergy and Bioproducts Industry: The Technical Feasibility of a Billion-Ton Annual Supply*; DOE/GO-102995-2135; Oak Ridge National Laboratory: Oak Ridge, TN, 2005.

15. European Biomass Industry Association http://www.eubia.org.

16. Loerbroks, C.; Rinaldi, R.; Thiel, W. The Electronic Nature of the 1,4-beta-Glycosidic Bond and Its Chemical Environment: DFT Insights into Cellulose Chemistry. *Chem.-Eur. J.* **2013,** *19*, 16282-16294.

17. Huber, G. W.; Dumesic, J. A. An overview of aqueous-phase catalytic processes for production of hydrogen and alkanes in a biorefinery. *Catal. Today* **2006,** *111*, 119-132.

18. Ragauskas, A. J.; Williams, C. K.; Davison, B. H.; Britovsek, G.; Cairney, J.; Eckert, C. A.; Frederick, W. J.; Hallett, J. P.; Leak, D. J.; Liotta, C. L.; Mielenz, J. R.; Murphy, R.; Templer, R.; Tschaplinski, T. The path forward for biofuels and biomaterials. *Science* **2006,** *311*, 484-489.

19. Huber, G. W.; Corma, A. Synergies between bio- and oil refineries for the production of fuels from biomass. *Angew. Chem.-Int. Edit.* **2007,** *46*, 7184-7201.

20. Baker, E. G.; Elliott, D. C., *CATALYTIC UPGRADING OF BIOMASS PYROLYSIS OILS*. Elsevier Appl Sci Publ Ltd: Barking Essex, 1988;

21. Czernik, S.; Bridgwater, A. V. Overview of applications of biomass fast pyrolysis oil. *Energy Fuels* **2004,** *18*, 590-598.

22. Sun, Y.; Cheng, J. Y. Hydrolysis of lignocellulosic materials for ethanol production: a review. *Bioresour. Technol.* **2002,** *83*, 1-11.

23. Huang, Y.-B.; Fu, Y. Hydrolysis of cellulose to glucose by solid acid catalysts. *Green Chem.* **2013,** *15*, 1095-1111.

24. Chheda, J. N.; Huber, G. W.; Dumesic, J. A. Liquid-phase catalytic processing of biomass-derived oxygenated hydrocarbons to fuels and chemicals. *Angew. Chem.-Int. Edit.* **2007,** *46*, 7164-7183.

25. Katryniok, B.; Paul, S.; Capron, M.; Dumeignil, F. Towards the Sustainable Production of Acrolein by Glycerol Dehydration. *ChemSusChem* **2009,** *2*, 719-730.

26. Katryniok, B.; Paul, S.; Belliere-Baca, V.; Rey, P.; Dumeignil, F. Glycerol dehydration to acrolein in the context of new uses of glycerol. *Green Chem.* **2010,** *12*, 2079-2098.

27. Katryniok, B.; Paul, S.; Dumeignil, F. Recent Developments in the Field of Catalytic Dehydration of Glycerol to Acrolein. *ACS Catal.* **2013,** *3*, 1819-1834.

28. Cortright, R. D.; Davda, R. R.; Dumesic, J. A. Hydrogen from catalytic reforming of biomass-derived hydrocarbons in liquid water. *Nature* **2002,** *418*, 964-967.

29. Davda, R. R.; Shabaker, J. W.; Huber, G. W.; Cortright, R. D.; Dumesic, J. A. Aqueous-phase reforming of ethylene glycol on silica-supported metal catalysts. *Appl. Catal. B-Environ.* **2003,** *43*, 13-26.

30. Shabaker, J. W.; Davda, R. R.; Huber, G. W.; Cortright, R. D.; Dumesic, J. A. Aqueous-phase reforming of methanol and ethylene glycol over alumina-supported platinum catalysts. *J. Catal.* **2003,** *215*, 344-352.

31. Huber, G. W.; Shabaker, J. W.; Evans, S. T.; Dumesic, J. A. Aqueous-phase reforming of ethylene glycol over supported Pt and Pd bimetallic catalysts. *Appl. Catal. B-Environ.* **2006,** *62*, 226-235.

32. Banerjee, G.; Scott-Craig, J.; Walton, J. Improving Enzymes for Biomass Conversion: A Basic Research Perspective. *Bioenerg. Res.* **2010,** *3*, 82-92.

CHAPTER 2

ROLE OF LEWIS AND BRØNSTED ACID SITES IN THE DEHYDRATION OF GLYCEROL OVER NIOBIA

2.1 Background

Glycerol is a major by-product from the transesterification of vegetable oils and fats to produce biodiesel. Biodiesel production in US has increased significantly from 500,000 gallons in 1999 to 967 million gallons in 2011.[1] To ensure that this industry remains economically viable, it is crucial to convert glycerol to value-added chemicals by catalytic processes such as dehydration, reforming, oxidation, etherification, esterification, and hydrogenolysis.[2] Acrolein is an important product from the dehydration of glycerol. It is currently produced by the selective oxidation of propylene.[3] Besides being used in the synthesis of acrylic acid,[4] acrolein is also needed in the synthesis of DL-methionine, which is an essential amino acid.[5]

Many studies have been performed on the dehydration of glycerol, but controlling the selectivity of this reaction remains a challenge.[6] Early work focused on the reaction in the aqueous phase under near or at supercritical conditions using homogeneous catalysts.[7-8] However, due to the estimated high cost of reaction vessel and separation issues, the dehydration of glycerol in vapor phase over heterogeneous catalysts is preferred. Typical gas phase reactions are carried out in the temperature range of 250-350 °C using aqueous glycerol as a feedstock.[5] A number of solid acid catalysts have been reported including zeolites, heteropoly acids, niobia and alumina.[2, 9-17] The selectivity of acrolein has been correlated with low Hammett acidity.[10, 18] Low selectivity of acrolein has been reported over Lewis acids.[10] However, there is only limited insight regarding the reason for the differences in the performance of different acid sites. Therefore, it is

crucial to gain such understanding and to control the type, strength, and concentration of acid sites on solid acid catalysts for optimized performance for the production of acrolein.

Nimlos et al. investigated the dehydration of neutral and protonated glycerol using quantum mechanical calculations[19] and found that protonation will significantly lower dehydration temperatures. Laino et al. used metadynamics simulations to study the dehydration of neutral glycerol in gas phase and suggested glycerol decomposition via glycidol formation.[20] These studies, however, did not consider the influence of catalysts.

There are a few reports on surface interactions and dehydration reactions of glycerol on different solids, in which FTIR spectroscopy was used as the main technique.[21-24] Glycerol was adsorbed on H-MFI and silica-alumina by heating up the vacuum line to 353 K, but the amount of glycerol deposited could not be estimated.[21-22] Moreover, the dehydration reaction could have occurred at the deposition temperature in the presence of a catalyst as a peak due to carbonyl stretching mode (1656 cm^{-1}) was observed without further heating. To solve this problem, Copeland et al. devised an *ex-situ* method of impregnating a controlled amount of glycerol on γ-Al_2O_3.[23] This method can be performed at room temperature, thus preventing glycerol from reacting prematurely.

In this study, we report the role of Lewis and Brønsted acid sites in the dehydration of glycerol using transmission FTIR spectroscopy with the aid of density functional theory (DFT) calculations. The *ex-situ* impregnation method is used here to contact glycerol with niobium oxide, which is water-tolerant and possesses relatively strong Lewis and Brønsted acid sites.[25-29] Most importantly, the Brønsted sites can be blocked by Na^+,[29] which allows elucidating the role of different acid sites in the absence of water vapor.

2.2 Experimental

2.2.1 Materials

Glycerol (99%), acrolein (90%), hydroxyacetone (90%), NaCl (>99%), NaOH (>98%) and pyridine (>99%) were purchased from Sigma Aldrich and were used as received. Niobic acid (HY-340) was provided by CBMM (Brazil). Niobium oxide was obtained by calcining niobic acid under flowing air (200 ml/min) at a ramp rate of 10 K/min for 4 h at selected temperatures (350 °C, 400 °C, 500 °C, 600 °C, 700 °C). The samples are named as NBX, where X is the calcination temperature.

2.2.2 Synthesis of Na^+/NB500

The synthesis procedure was modified from a report in literature.[29] Na^+ exchange of NB500 was obtained by stirring 500 mg of NB500 in 200 ml of 1 M NaCl solution maintained at 60 °C and pH = 11.0-11.4. The pH was adjusted periodically by adding 0.05 M NaOH solution. After 52 h when the pH stops decreasing, the sample was collected and washed repeatedly with distilled water until Cl^- ions were no longer detected. The sample was then dried in an oven at 100 °C for 12 h.

2.2.3 Catalyst characterization

Nitrogen sorption measurements at 77 K were performed with a Micromeritics ASAP 2020 physisorption analyzer. Prior to the measurement, the samples were degassed under vacuum at 150 °C for 5 h. Surface areas were calculated using the BET method[30] and pore volumes were calculated based on the adsorption branch of the isotherm using the BJH method.[31] X-ray diffraction (XRD) measurements were performed with a Philips X'pert diffractometer equipped with an X'celerator module using Cu Kα radiation. Diffractograms were collected at incident angles from 2θ = 5 to 70° with a step size of 0.0167°. Thermal gravimetric analysis (TGA) of niobic acid was performed using a TA

Instruments SDT Q600 thermal analyzer. For each experiment, 0.20 mg of niobic acid was loaded into an aluminum pan and heated in flowing air (50 ml/min) from room temperature to 800 ℃ at a rate of 10 K/min. Raman spectra were collected on a Bruker FRA-106. 1028 scans were collected with a resolution of 2-4 cm^{-1}. A powder sample was placed in a small hemispherical sample holder. Pyridine adsorption followed by IR spectroscopy was obtained using a Nicolet 8700 FTIR spectrometer with a MCT/A detector. For each spectrum, 64 scans were recorded at a resolution of 4 cm^{-1}. Each sample was pressed into a self-supported wafer and loaded into a transmission vacuum chamber. The sample was activated at 350 ℃ for 1 h under high vacuum and cooled down to room temperature. A background spectrum was collected. Pyridine was then introduced into the chamber at 0.1 mbar for 30 min followed by evacuation for 1 h, and a spectrum was collected. For the evaluation of acid strength, the sample was heated at 150 ℃, 250 ℃ and 350 ℃ for 1 h to desorb pyridine on weak acid sites, and spectra were collected at room temperature. After each experiment, the wafer was cut using a circular stamp with a diameter of 6.35 mm and weighed to determine the density. The concentration of Lewis and Brønsted acid sites was determined from the integral of the peaks at 1445 cm^{-1} and 1540 cm^{-1}, respectively, and the density of the wafer. The molar extinction coefficients used were reported by Nakajima et al.[29]

2.2.4 FTIR spectroscopy

Niobium oxide was impregnated with glycerol via an *ex-situ* method.[23] For each niobium oxide sample, 250 mg was weighed and mixed with 10 ml of dilute aqueous glycerol solution. The concentration of the solution was chosen such that there is a deposition of desired amount on the niobium oxide to achieve the desired loading, which typically ranges from 2 to 3 wt%. After 24 h, the slurry was dried using a Schlenk line at room temperature for 8 h to obtain a dry glycerol impregnated sample. To prepare appropriate samples as subtrahends for difference spectra, each niobium oxide sample

was mixed with 10 ml of distilled water for 24 h and dried using the same method. Each impregnated sample was pressed into a self-supported wafer and loaded into a transmission vacuum chamber.

A spectrum was collected under room temperature and pressure (RTP) using an empty cell background with the same condition. The cell was subjected to high vacuum ($< 10^{-6}$ mbar), and a spectrum was collected again using an empty cell background under the same condition (RTHV). The wafer was then heated at 100 °C, 150 °C, 200 °C, 250 °C, 300 °C, and 350 °C for 1 h, and a spectrum was collected at each temperature. For experiments in the presence of water vapor, the cell was dosed with 1 mbar of water vapor for 1 h after evacuation, followed by the same heating procedure. After each experiment, the wafer was cut using a circular stamp with a diameter of 6.35 mm and weighed to determine the density.

A different procedure was used to adsorb acrolein or hydroxyacetone on NB500. The pure catalyst was pressed into a self supported wafer and loaded into a transmission vacuum chamber. The sample was activated at 350 °C for 1 h under high vacuum and was cooled down to room temperature. A background spectrum was collected. Acrolein or hydroxyacetone was introduced into the chamber as vapors at 0.1 mbar through a leak valve for 15 min. After which the cell was evacuated for 1 h and a spectrum was collected. The sample was then heated at 150, 250 and 350 °C for 1 h and a spectrum was collected at each temperature. The spectra of liquid acrolein and hydroxyacetone were collected using an ATR accessory at room temperature.

All spectra were collected using a Nicolet 8700 FTIR spectrometer with a MCT/A detector. For each spectrum, 64 scans were recorded at a resolution of 4 cm^{-1}. Thermo Fischer Scientific Inc. Grams 9.1 software was used to process the difference spectra. The spectrum of each reactant-free niobium oxide was subtracted from the respective sample.

The subtrahend spectrum was collected at room temperature after heating at 350 °C for 1 h. All spectra were normalized by its wafer density prior to subtraction.

2.2.5 DFT Calculations

Periodic density functional theory (DFT) calculations were performed with the Vienna *ab initio* simulation package (VASP).[32-35] Electron-electron exchange and correlation was described with the PW-91 GGA functional, and the electron-core interaction was described with the projector augmented wave (PAW) method.[36-39] The cutoff energy for the plane wave basis set was fixed at 400 eV. Structural relaxation was performed through a conjugate-gradient algorithm, and was considered to be converged when the forces on each unconstrained atom were < 0.03 eV/Å. Due to the size of the supercell, which contained over 300 atoms, reciprocal space was only sampled at the Γ point. The surface slab was modeled with the T phase of Nb_2O_5.[40] The crystalline structure was obtained through the Inorganic Crystal Structure Database,[41] and preliminary calculations had shown that the Nb terminated (100) surface had the lowest surface energy. Additionally, preliminary calculations had shown the inclusion of Nb atoms in the interstitial sites did not significantly impact surface property; thus, interstitial Nb atoms were excluded in the calculations. The surface slab had a thickness of 7 Å with the bottommost 4 Å immobilized. After relaxation of the surface, the entire surface slab was immobilized with the bottommost 4 Å removed from the slab. All subsequent calculations were conducted on this rigid surface. All slab calculations used a vacuum spacing of at least 15 Å normal to the surface. A single molecule was adsorbed on the surface. Various geometric configurations were examined. For dissociatively adsorbed species, it was assumed that the dissociated hydrogen atom remain chemisorbed on the surface. The vibrational frequencies of the adsorbates were evaluated within the harmonic approximation.[42] To compare to experimental results, the calculated

frequencies were scaled by a factor of 0.98. This reflected the differences between the DFT calculated and experimentally observed frequencies for gas phase CO.[23]

2.3 Results

2.3.1 Catalyst characterization

Nitrogen physisorption results showed that the surface area and pore volume of niobium oxide decreased with increasing calcination temperature (Table 1). The decrease in the latter was significant starting at a calcination temperature of 500 °C. The average pore size of the catalysts increased with increasing calcination temperature. However, the value dropped when niobium oxide was calcined at 700 °C.

Table 2.1 N_2 physisorption results for niobium oxide calcined at different temperatures.

Catalyst	BET Surface Area (m^2/g)	BJH Pore Volume (cm^3/g)	BJH Pore Size (nm)
NB350	109	0.17	6.4
NB400	78	0.16	8.1
NB500	34	0.15	20.2
NB600	13	0.08	33.6
NB700	6	0.02	16.9

The TGA and DTA curves (Fig. A.1) showed an endothermic weight loss as niobic acid loses water up to 400 °C. This was followed by a sharp exothermic peak at 582 °C, indicating that crystallization has occurred. XRD patterns of the catalysts (Fig. A.2) revealed that NB350 and NB400 were amorphous. As the calcination temperature reached 500 °C, diffraction peaks at 22.9°, 28.7°, 36.9°, 45.9°, 50.1° and 55.1° appeared. The same diffraction pattern was observed for NB600, but the peaks were more intense.

At this stage, niobium oxide had crystallized as the T phase, where Nb atoms are arranged either in distorted octahedra or pentagonal bipyramids.[25] For NB700, the diffraction peaks at 28.7° and 50.1° become doublets, which is attributed to octahedral NbO_6 blocks that share corners and edges with each other.[25] These results are in good agreement with other reports.[9, 27, 43]

Figure 1 shows the Raman spectra of the catalysts. The broad peak at 655 cm^{-1} is attributed to Nb-O-Nb vibrations in amorphous niobium oxide containing mostly distorted NbO_6 but also NbO_7 and NbO_8 polyhedra.[44] As the calcination temperature was increased, the peak blue-shifted to 694 cm^{-1} and became sharper, indicating that some of these polyhedra were rearranged. For NB350 and NB400, a broad shoulder at 860 cm^{-1} was observed. This is assigned to Nb-O-Nb vibrations in NbO_6 octahedra.[45] As the catalyst crystallized, more octahedral cages became distorted, resulting in a red-shift to 808 cm^{-1}. The presence of NbO_4 tetrahedra was indicated by a peak at 1010 cm^{-1} that corresponds to Nb=O stretching vibrations and began to appear at 500 °C.[46]

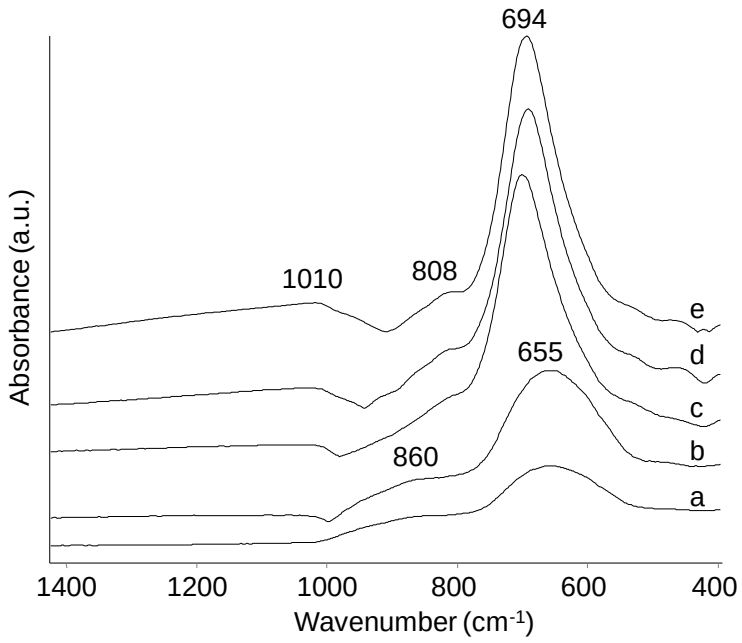

Figure 2.1 Raman spectra of (a) NB350, (b) NB400, (c) NB500, (d) NB600, (e) NB700.

Lewis and Brønsted acid sites were quantified by pyridine adsorption followed by IR spectroscopy (Table 2.2). The concentrations were obtained after heating the sample to 150 °C and 350 °C. The concentration of acid sites decreased with increasing calcination temperature. After calcination at 700 °C, no Brønsted acid sites were left on niobium oxide. For Na^+/NB500, the concentration of Lewis acid sites was the same as for NB500, indicating that Na^+ cations do not contribute to Lewis acidity. The absence of the pyridinium ion peak at 1540 cm^{-1} in the spectrum of Na^+/NB500 (Fig. A.3) shows that all Brønsted sites were successfully blocked by Na^+.[47] To understand how acidity affects acrolein formation, NB350, NB500, NB700, and Na^+/NB500 were used in this study as the catalysts have a large disparity in their acid site ratios.

Table 2.2 Concentrations of Lewis (LAS) and Brønsted acid sites (BAS) on niobium oxide calcined at different temperatures.

	150 °C		**350 °C**	
Catalyst	**LAS**	**BAS**	**LAS**	**BAS**
NB350	65	40	54	26
NB400	45	29	42	22
NB500	37	8	31	5
NB600	12	1.2	10	0.9
NB700	2.6	0	1.8	0
Na^+/NB500	38	0	29	0

Concentration in μmol/g

The strength of Lewis acid sites for both NB350 and NB500 was comparable (Fig. 2.2a). For NB700, a slightly smaller fraction of the Lewis acid sites were able to retain pyridine at 350 °C. NB500 had a slightly larger fraction of strong Brønsted acid sites than NB350 (Fig. 2.2b). This shows that NB500 possesses both strong Lewis and Brønsted acid sites even though it has a lower concentration compared to NB350.

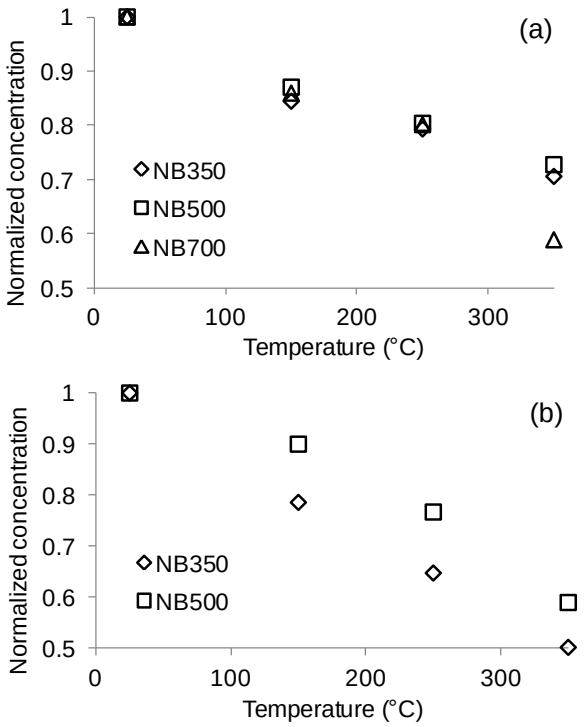

Figure 2.2 Relative strength of acid sites on niobium oxide calcined at different temperatures (a) Lewis acid sites, (b) Brønsted acid sites.

2.3.2 *In-situ* generation of Brønsted acid sites

To prove that Brønsted sites can be generated from Lewis acid sites in the presence of water, Na^+/NB500 was exposed to 1 mbar of water vapor at 350 °C in the FTIR transmission cell for 1 h after activation (350 °C), followed by pyridine adsorption. In vacuum, pyridine adsorbed on Lewis acid sites (1445 cm^{-1}) can be observed, but the absence of the characteristic peak of the pyridinium ion at 1540 cm^{-1} indicates that no Brønsted sites are present (Fig. 2.3a). In the presence of water vapor, the concentration of active Lewis acid sites (1445 cm^{-1}) on Na^+/NB500 decreased by 59% (Fig. 2.3b). At the same time, the formation of Brønsted acid sites (1.7 μmol/g) was observed, which corresponds to 34% of the Brønsted acid site concentration of NB500. This is attributed to the dissociative adsorption of water molecules on Lewis acid sites to form OH

groups.[48] Note that the number of lost Lewis acid sites exceeds the number of Brønsted acid sites formed. This indicates that adsorption of water vapor on Lewis acid sites does not always lead to the formation of a Brønsted acid site. To ensure that Brønsted acid sites were not generated due to the removal of Na^+ by steam, the sample was exposed to 1 mbar of steam followed by evacuation and dosing with pyridine. No pyridinium ions (1540 cm^{-1}) were observed (Fig. 2.3c).

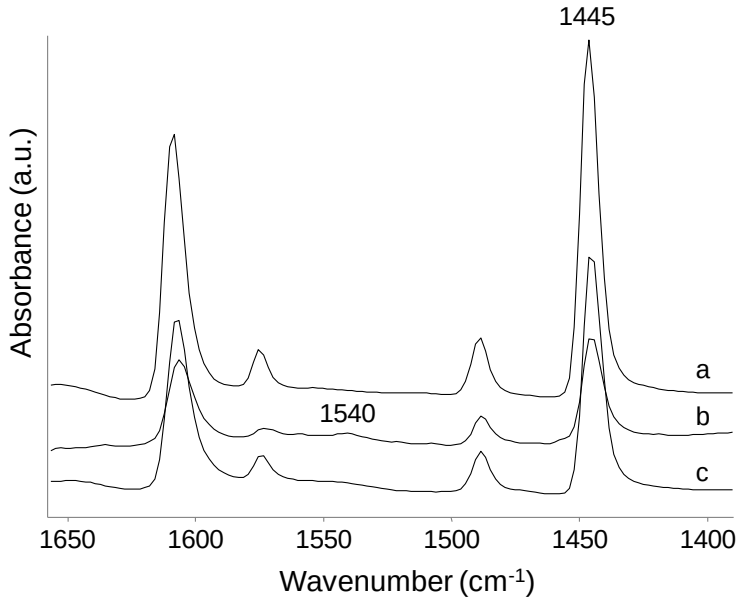

Figure 2.3 IR spectra of adsorbed pyridine on Na^+/NB500 at 350 °C (a) in vacuum, (b) in the presence of 1 mbar water vapor, (c) in vacuum after dosing 1 mbar water vapor.

2.3.3 Adsorption of acrolein and hydroxyacetone

When acrolein was adsorbed on NB500, multiple bands corresponding to νC=O vibrations were observed at 1732 cm^{-1}, 1690 cm^{-1} and 1660 cm^{-1} (Fig. 2.4a). According to the results of our DFT calculations, acrolein should only have one νC=O peak (Table 2.3), and this is for an adsorbed molecule interacting with a Lewis acid site, giving a downshifted frequency of 1694 cm^{-1} (see Appendix A). This lower frequency indicates a

weakening of the C=O bond as a result of the interaction between the carbonyl O and Nb atom. The experimental frequency at 1732 cm^{-1} corresponds to a free carbonyl group as it is also observed in the spectrum of pure acrolein (Fig. A.7a), while the red-shifted frequency at 1660 cm^{-1} could be due to conjugation with the alkene group.[49] Conjugation between the carbonyl and alkene group was also observed in the spectrum of pure acrolein (Fig. A.7a). The alkene group also interacts with the surface (Fig. 2.5a), giving a frequency of 1611 cm^{-1} (νC=C). Additional bands (1540 cm^{-1} and 1126 cm^{-1}) that are not shown by DFT calculations could arise due to cyclic structures through aldehyde auto-condensation,[50] and the interaction between an ether group of the cyclic structure and a Nb atom. At higher temperatures, the intensity of these two bands increased, suggesting that more oligomers were formed. The alkene group, together with the νC-C band at 1611 cm^{-1} and 1180 cm^{-1}, respectively, were not observed above 250 °C due to its weak intensities. The rest of the bands in the spectra (1440 cm^{-1}, 1368 cm^{-1}, 1274 cm^{-1} and 1180 cm^{-1}) are close to the frequencies from DFT calculations (Table 2.3).

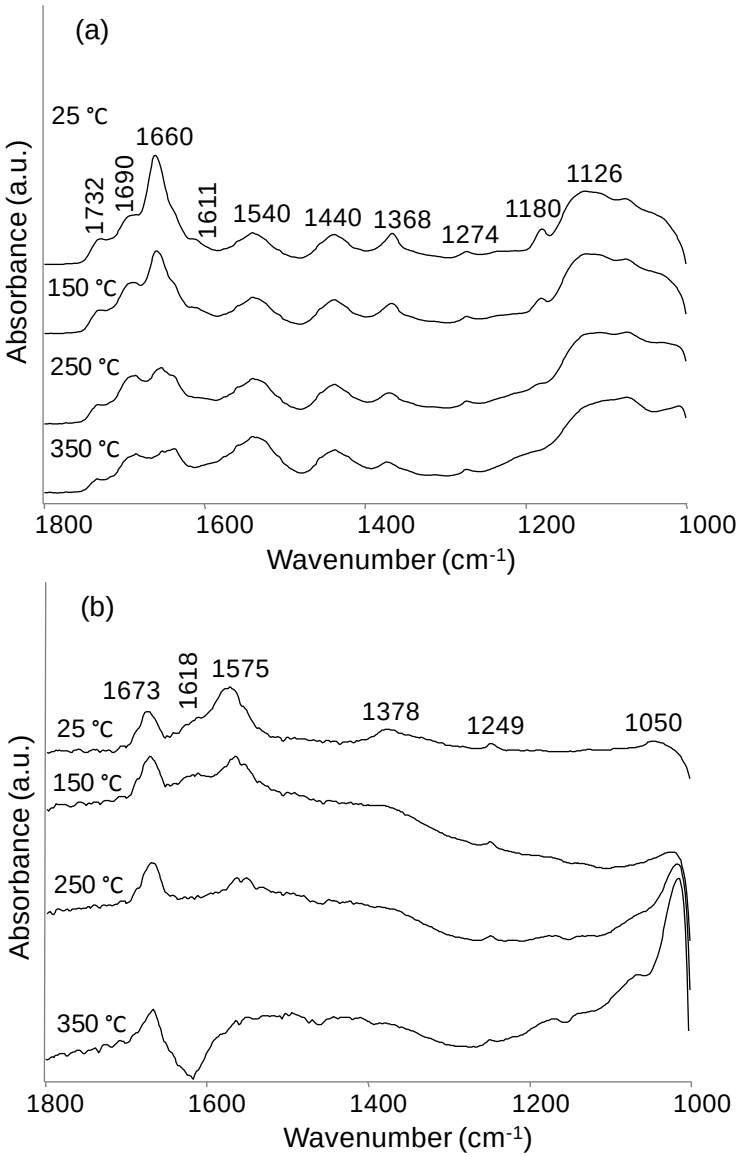

Figure 2.4 FTIR spectra of adsorbed oxygenates on NB500 at different temperatures: (a) acrolein, (b) hydroxyacetone.

Table 2.3 Calculated and experimental frequencies of acrolein and 2-propene-1,2-diol adsorbed on NB500.

Acrolein			2-propene-1,2-diol		
Calculated/ cm^{-1}	**Experimental/ cm^{-1}**	**Assignment**	**Calculated/ cm^{-1}**	**Experimental/ cm^{-1}**	**Assignment**
	1732				
1694	1690	νC=O	1578	1575	νC=C
	1660				
1611	1611	νC=C	1378	1378	δCH_2
1413	1440	ρCH in COH	1360		δCH_2
1337	1368	δCH_2	1318		δC-C
1277	1274	τCH	1303		τC-C
1153	1180	νC-C	1274	1249	ωCH_2
			1140		νC-C
			1061	1050	νCO

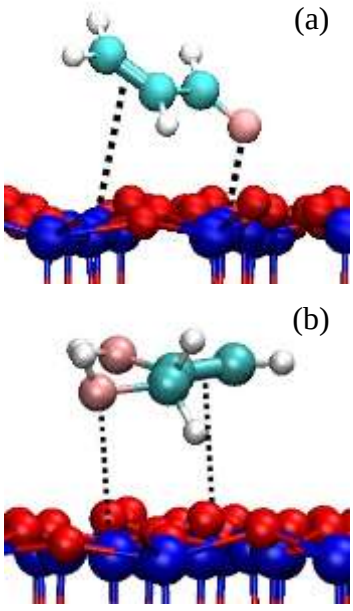

Figure 2.5 Structure of glycerol dehydration products adsorbed on T phase of Nb_2O_5 (a) acrolein, (b) 2-propene-1,2-diol. Blue, red pink, teal and white spheres correspond to Nb, surface O, adsorbate O, C and H atoms, respectively.

Hydroxyacetone is able to undergo tautomerization to form 1-propene-1,2-diol or 2-propene-1,2-diol. Under acidic conditions, the formation of 2-propene-1,2-diol is preferred.[51] The spectrum of hydroxyacetone on NB500 contains a peak at 1575 cm^{-1} and a shoulder at 1618 cm^{-1} (Fig. 2.4b). DFT calculations of 2-propene-1,2-diol adsorbed on NB500 indicated that the frequency at 1575 cm^{-1} corresponds to νC=C vibration and the functional group interacts with an unsaturated Nb atom (Table A.1). Thus, the shoulder at 1618 cm^{-1} could be assigned as the νC=C vibration of 1-propene-1,2-diol. The frequencies calculated for the adsorption of 2-propene-1,2-diol are compared with experimental results (Table 2.3). The band at 1673 cm^{-1} is attributed to νC=O of the ketone form interacting with the surface compared to its free νC=O mode at 1718 cm^{-1} (Fig. A.7b).[52] In contrast to pure hydroxyacetone, which has a νC-O band at 1076 cm^{-1}, the enol displayed a νC-O frequency at 1050 cm^{-1} when it is adsorbed on the surface. DFT calculations showed that the primary hydroxyl group forms a strong interaction with a coordinatively unsaturated Nb atom (Fig. 2.5b). Based on the spectroscopic data and DFT calculations it was not possible to determine whether this interaction of the primary alcohol group led to its dissociation or not (Table A.1 and Fig. A.5). The alkene group interacts with another Nb atom, giving a frequency at 1575 cm^{-1}. However, the secondary hydroxyl group does not interact with the surface when the enol is adsorbed on the surface. Moreover, a surface interaction of the secondary alcohol group should blue shift the νCO vibration to the range of 1070-1150 cm^{-1},[24] and no peak is observed in this part of the spectrum. The frequencies for adsorbed acrolein and 2-propene-1,2-diol can be used to identify the dehydration products from the *in-situ* FTIR experiments.

2.3.4 Formation of surface species on NB350

Pure glycerol has bands at 1454 cm^{-1} and 1413 cm^{-1}, due to δCH_2 and δOH vibrations, while bands at 1326 cm^{-1} and 1209 cm^{-1} are assigned to ρOH and ωCH_2 vibrations (Fig. 2.6Ai).[53-54] When 2 wt% of glycerol (equivalent to one monolayer) was

impregnated on NB350, these vibrational modes appeared at 1458 cm^{-1}, 1413 cm^{-1}, 1326 cm^{-1} and 1208 cm^{-1}, respectively (Fig. 2.6Aa). Pure glycerol has a primary and secondary ν*C-O* vibration at 1029 cm^{-1} and 1108 cm^{-1} respectively (Fig. 2.6Ai), and significant changes were observed in this region. For a monolayer or 2.0 wt% of glycerol impregnated on NB350 at RTP (Fig. 2.6A), peaks were observed at 1045 cm^{-1}, 1108 cm^{-1}, and 1140 cm^{-1}. Upon evacuation, the shoulder at 1140 cm^{-1} became more intense, the peak at 1108 cm^{-1} vanished, and a peak at 1093 cm^{-1} appeared (Fig. 2.6Ab). In addition, the band at 1045 cm^{-1} became a shoulder. In agreement with earlier studies, the peaks at 1093 cm^{-1} and 1045 cm^{-1} are attributed to stretching vibration of the primary C-O bonds of glycerol that are part of a bridging alkoxy bonds and a non-dissociative Lewis acid-base interaction with the surface, respectively (Inset of Fig. 2.6A).[23-24] The band at 1140 cm^{-1} is assigned to the ν*C-O* vibration of the secondary OH group of glycerol forming a hydrogen bond to a basic oxygen atom on the metal oxide surface.[23-24] This indicates that some water molecules were desorbed from the surface after evacuation, allowing a larger number of OH groups from glycerol molecules to interact with the Lewis acid sites and surface oxygen atoms.

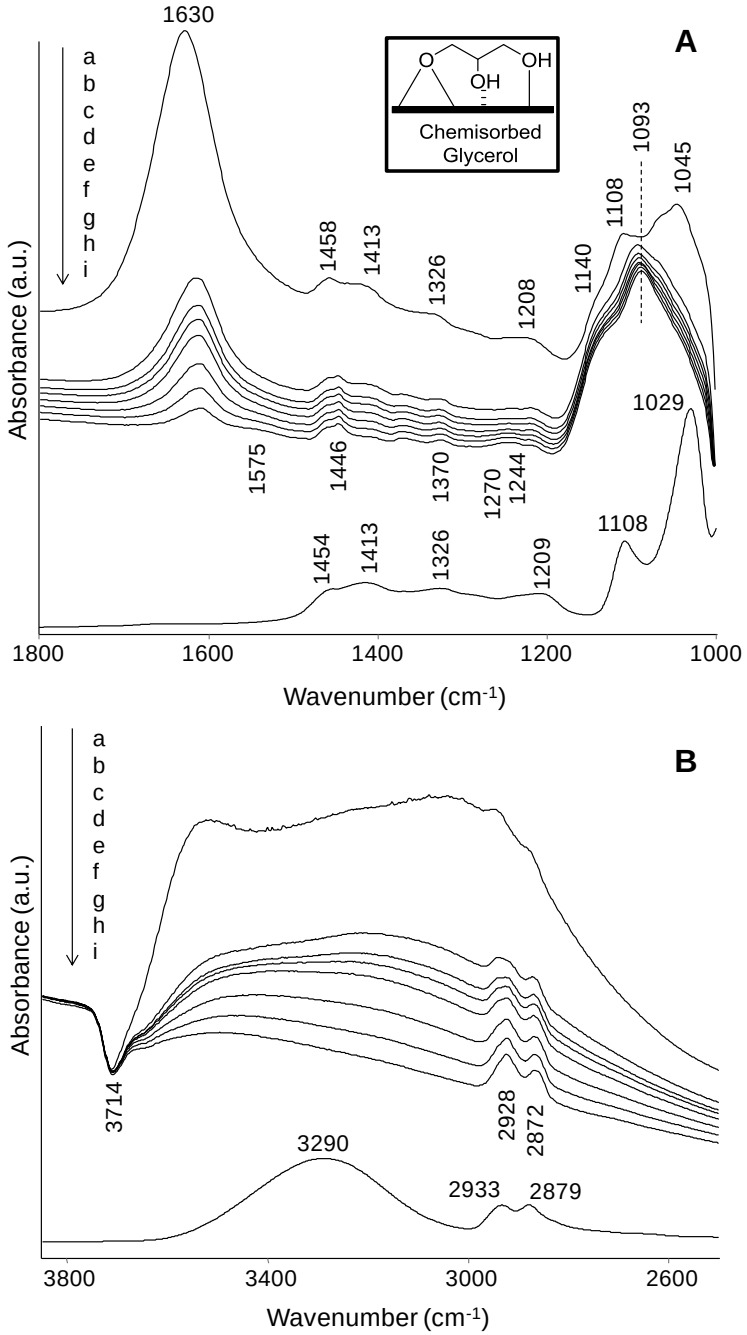

Figure 2.6 FTIR spectra of 2 wt% glycerol on NB350 at (a) RTP, (b) RTHV, (c) 100 °C HV, (d) 150 °C HV, (e) 200 °C HV, (f) 250 °C HV, (g) 300 °C HV, (h) 350 °C HV and (i) pure glycerol. (A) between 1800 cm^{-1} and 1000 cm^{-1} (B) between 3800 cm^{-1} and 2600 cm^{-1}. Inset: Scheme of chemisorbed glycerol.

In addition to the bands that are attributed to adsorbed glycerol, a number of bands were observed in every spectrum of glycerol loaded NB350. The region between 1500 and 1200 cm^{-1} contains multiple convoluted bands, but some of these may indicate the presence of acrolein (1446 cm^{-1}, 1370 cm^{-1} and 1270 cm^{-1}) and 2-propene-1,2-diol (1370 cm^{-1} and 1244 cm^{-1}), respectively (Fig. 2.6A).

A strong band at 1630 cm^{-1} is attributed to the δOH of co-adsorbed water. Upon increasing the temperature, this peak decreased in intensity and red-shifted towards 1610 cm^{-1} as water began to desorb from the surface (Fig. 2.6Ab-h). A reference experiment without adsorbed glycerol also showed a red shift to 1610 cm^{-1} as the amount of water on the surface decreases (Fig. A.8). Additionally, a small band at 1575 cm^{-1} was observed. This peak is characteristic of a νC=C vibration. Based on the position of this band and the much higher intensity of the νC=C band of adsorbed 2-propene-1,2-diol compared to acrolein, this peak is assigned to the νC=C band of 2-propene-1,2-diol. When the temperature reached 350 °C, unreacted glycerol, acrolein and 2-propene-1,2-diol were still present on the surface. Note that these surface species were also present when the experiment was performed in the presence of 1 mbar of water (Fig. A.9).

The asymmetric and symmetric νCH_2 bands of pure glycerol (2933 cm^{-1} and 2879 cm^{-1}) were slightly red-shifted, and they were observed at 2928 cm^{-1} and 2872 cm^{-1}, respectively (Fig. 2.6B). The negative peak at 3714 cm^{-1} (Fig. 2.6Ba-h) indicates that the hydroxyl groups on NB350 are perturbed, possibly interacting with the adsorbed species.[45]

When more than a monolayer of glycerol (3.0 wt%) was impregnated on NB350 and the sample was heated up, additional small bands at 2708 cm^{-1}, 1519 cm^{-1}, 1492 cm^{-1} and 1475 cm^{-1} were observed (Fig. 2.7). The weak band at 2708 cm^{-1} is assigned to the νCH vibration of the aldehyde group of acrolein.[55] This band was not observed for 2.0 wt% glycerol on NB350 as the amount of acrolein formed on the surface was not large enough for it to be visible. The bands at 1519 cm^{-1}, 1492 cm^{-1} and 1475 cm^{-1} were

observed from 100 °C and their intensity increased steadily with increasing temperature (Fig. 2.7A), suggesting that they correspond to reaction products. In some reports, these frequencies have been assigned as νC=C and δCH of coke species.[56-57] The peaks at 1519 cm^{-1} and 1492 cm^{-1} correspond to vibrations of two different types of aromatic rings.[58-59] Bands between 1500 and 1525 cm^{-1} usually arise due to aromatic rings with multiple electron donating substituents, while the peak at 1492 cm^{-1} could be due to a monosubstituted aromatic ring. The shoulder at 1475 cm^{-1} is attributed to a combination band of νCC_{ring} and δOH.[60] The presence of a methyl group attached to an aromatic ring was excluded due to the absence of a triplet band around 1475 cm^{-1}.[55] Similar bands at 1519 cm^{-1} and 1475 cm^{-1} are observed in the spectrum of hydroquinone,[61] while the band at 1492 cm^{-1} could due to the presence of benzene or phenol. For convenience, these two surface species are collectively termed as monoaromatics. Aromatic rings possess another vibrational mode due to conjugated νCC that exist around 1600 cm^{-1}. However, this weak band was not resolved as this part of the spectrum is dominated by the intense peak corresponding to the δOH vibration of water.

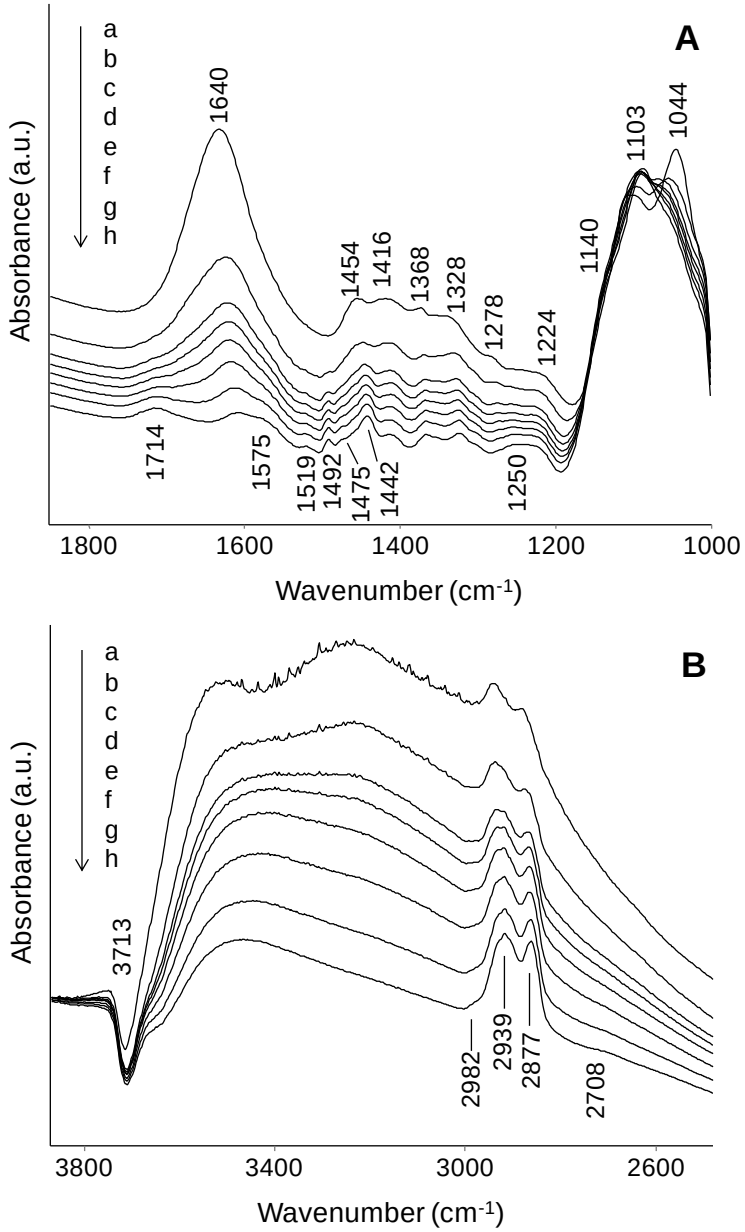

Figure 2.7 FTIR spectra of 3 wt% glycerol on NB350 at (a) RTP, (b) RTHV, (c) 100 °C HV, (d) 150 °C HV, (e) 200 °C HV, (f) 250 °C HV, (g) 300 °C HV, (h) 350 °C HV. (A) between 1800 cm^{-1} and 1000 cm^{-1} (B) between 3800 cm^{-1} and 2600 cm^{-1}.

Under RTHV, the secondary and primary νCO modes of pure glycerol (1103 cm^{-1} and 1044 cm^{-1}) were still observed as there was more than a monolayer of glycerol present (Fig. 2.7Aa). The intensity of the primary νCO mode gradually decreased as temperature increased and the alkoxy modes at 1140 cm^{-1} and 1054 cm^{-1} became visible (Fig. 2.7Ah). This indicates that a large fraction of glycerol on the surface was converted or desorbed until less than one monolayer was present. Similar to the sample with 2.0 wt% glycerol on NB350, the band corresponding to the νC=C vibration of 2-propene-1,2-diol (1575 cm^{-1}) increased in intensity at higher temperatures. The broad νC=O band of adsorbed acrolein (1714 cm^{-1}) also became noticeable as the water peak at 1640 cm^{-1} decreased in intensity, while its other vibrational modes at 1442 cm^{-1} (rCHO), 1368 cm^{-1} (δCH_2) and 1278 cm^{-1} (τCH) were still present. At higher temperatures, a small shoulder at 2988 cm^{-1} was observed while the $\nu_{asym}CH_2$ becomes broader (Fig. 2.7B). This corresponds to the rise of the asymmetric and symmetric νCH_2 of alkene groups in acrolein and 2-propene-1,2-diol, which are red-shifted relative to 3062 cm^{-1} and 2990 cm^{-1} as the alkene groups are interacting with the surface.[62] As the temperature reached 350 °C, surface species due to unreacted glycerol, acrolein, 2-propene-1,2-diol, and monoaromatics were present on the surface.

Based on previous reports,[6, 14] the possible formation of other products was considered. Specifically, 1,3-propenediol, 3-hydroxypropionaldehyde, acetaldehyde, and formaldehyde deserve attention. The vibrational spectrum of adsorbed 1,3-propenediol was modeled by DFT calculations (Table A.2). Most bands corresponding to this species were in the range of 1000 to 1400 cm^{-1}, which also contains multiple peaks from other species making a positive identification impossible. The region of C=C stretching bands is slightly better resolved. This region of spectrum can be fitted with peaks corresponding to the νC=C of 2-propene-1,2-diol (1575 cm^{-1}) and adsorbed water (1610 cm^{-1}) without requiring a contribution at the expected νC=C frequency of 1585 cm^{-1} for 1,3-propenediol. Based on these observations, it is suggested that 1,3-propenediol was not

present on the surface in a measurable concentration. 3-hydroxypropionaldehyde was not expected to exist as it is a very reactive and unstable molecule above 4 °C.[12, 63-65] It is possible that the $\nu_{asym}CH_3$ band of acetaldehyde contributes to the shoulder around 2985 cm^{-1}.[55] However, the shoulder is rather small and contains a contribution from the $\nu_{asym}CH_2$ of 2-propene-1,2-diol. Furthermore, the νC=O region of the spectrum was adequately fitted with a single peak leading to the assumption that acrolein is the only carbonyl present on the surface. No characteristic signals were observed for formaldehyde or its decomposition product CO.

2.3.5 Formation of surface species on NB500

The spectrum of 3.0 wt% glycerol on NB500 at room temperature and ambient pressure also contained peaks that cannot be attributed to glycerol or water (Fig. 2.8A). As described above, these bands indicate the presence of adsorbed acrolein (1712 cm^{-1}, 1442 cm^{-1}, 1367 cm^{-1} and 1278 cm^{-1}) and 2-propene-1,2-diol (1575 cm^{-1}, 1367 cm^{-1} and 1256 cm^{-1}). At room temperature and ambient pressure, the νC=O mode of acrolein and the νC=C mode of 2-propene-1,2-diol are only observed as shoulder at 1712 and 1575 cm^{-1}, respectively. However, the peak became more resolved upon evacuation (Fig. 2.8A). As the temperature increased, the intensity of the bands corresponding to dehydration products increased in intensity (Fig. 2.8Ab-h). Bands due to glycerol (1454 cm^{-1}, 1415 cm^{-1}, 1331 cm^{-1}, 1222 cm^{-1}, 1110 cm^{-1} and 1046 cm^{-1}) and water (1640 cm^{-1}) decreased in intensity. At temperatures of 250 °C and above, a new band was observed at 2694 cm^{-1} (Fig. 2.8B), which is assigned to the Fermi resonance of the νCH of the aldehyde group in acrolein with the ρCOH vibration at 1440 cm^{-1}.[55] Bands corresponding to monoaromatics (1520 cm^{-1}, 1492 cm^{-1} and 1472 cm^{-1}) were visible and distinct starting at 100 °C.

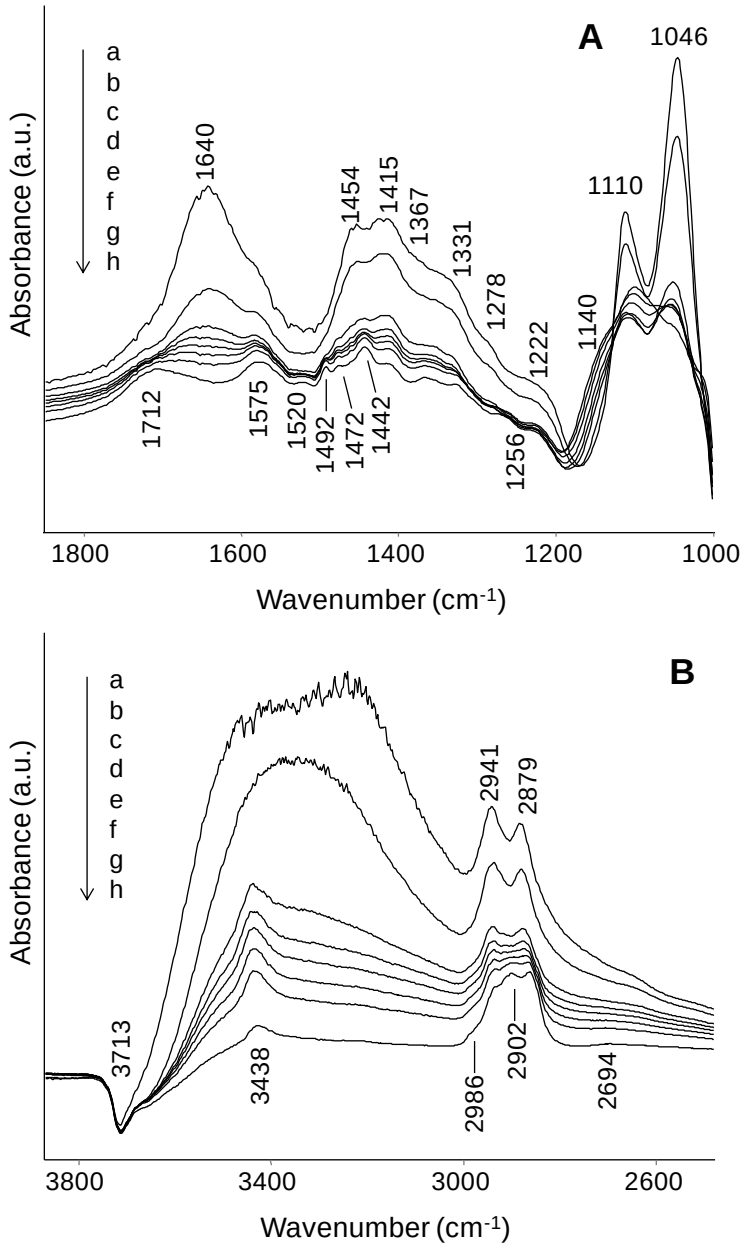

Figure 2.8 FTIR spectra of 3 wt% glycerol on NB500 at (a) RTP, (b) RTHV, (c) 100 °C HV, (d) 150 °C HV, (e) 200 °C HV, (f) 250 °C HV, (g) 300 °C HV, (h) 350 °C HV. (A) between 1800 cm^{-1} and 1000 cm^{-1} (B) between 3800 cm^{-1} and 2600 cm^{-1}.

The modes from the νC-O vibrations of bridging alkoxy group at 1100 cm^{-1} and the alcohol group engaged in the Lewis acid-base interaction at 1046 cm^{-1} became more resolved at higher temperatures as the amount of non-chemisorbed glycerol on the surface decreased. The perturbation of hydroxyl groups can be identified by the negative peak at 3713 cm^{-1} (Fig. 2.8B). The band at 3438 cm^{-1} could be due to hydroxyl groups that are engaged in hydrogen bonding interactions and they could be located in pores which are inaccessible. Note that this band was not observed for NB350. These hydroxyl groups could be formed after the oxide has crystallized. The $\nu_{asym}CH_2$ and $\nu_{sym}CH_2$ modes of glycerol at 2941 cm^{-1} and 2879 cm^{-1} remained unchanged, while the $\nu_{asym}CH_2$ and $\nu_{sym}CH_2$ vibrational modes of alkene groups began to appear from 150 °C at 2986 cm^{-1} and 2902 cm^{-1}. Similar to the sample with 3.0 wt% glycerol on NB350, the remaining surface species at 350 °C were glycerol, acrolein, hydroxyacetone enol and monoaromatics.

2.3.6 Formation of surface species on NB700

For NB700 impregnated with 3.0 wt% of glycerol, only vibrational modes corresponding to non-chemisorbed glycerol were observed under RTHV at 1458 cm^{-1}, 1418 cm^{-1}, 1333 cm^{-1}, 1217 cm^{-1}, 1110 cm^{-1} and 1042 cm^{-1} (Fig. 2.9A). Upon increasing the temperature, the intensity of these bands decreased, and they were no longer observed as the temperature reached 350 °C (Fig. 2.9Ab-g). However, the $\nu_{asym}CH_2$ and $\nu_{sym}CH_2$ vibrational modes were still present at 2924 cm^{-1} and 2868 cm^{-1} respectively (Fig. 2.9B). In addition, a shoulder at 2968 cm^{-1} appeared at higher temperatures. The perturbation of hydroxyl groups can still be observed by the negative peak at 3706 cm^{-1}. It is suggested that the remaining νCH_2 vibrations could be due to hydrocarbons that resulted from the cracking of glycerol.[11]

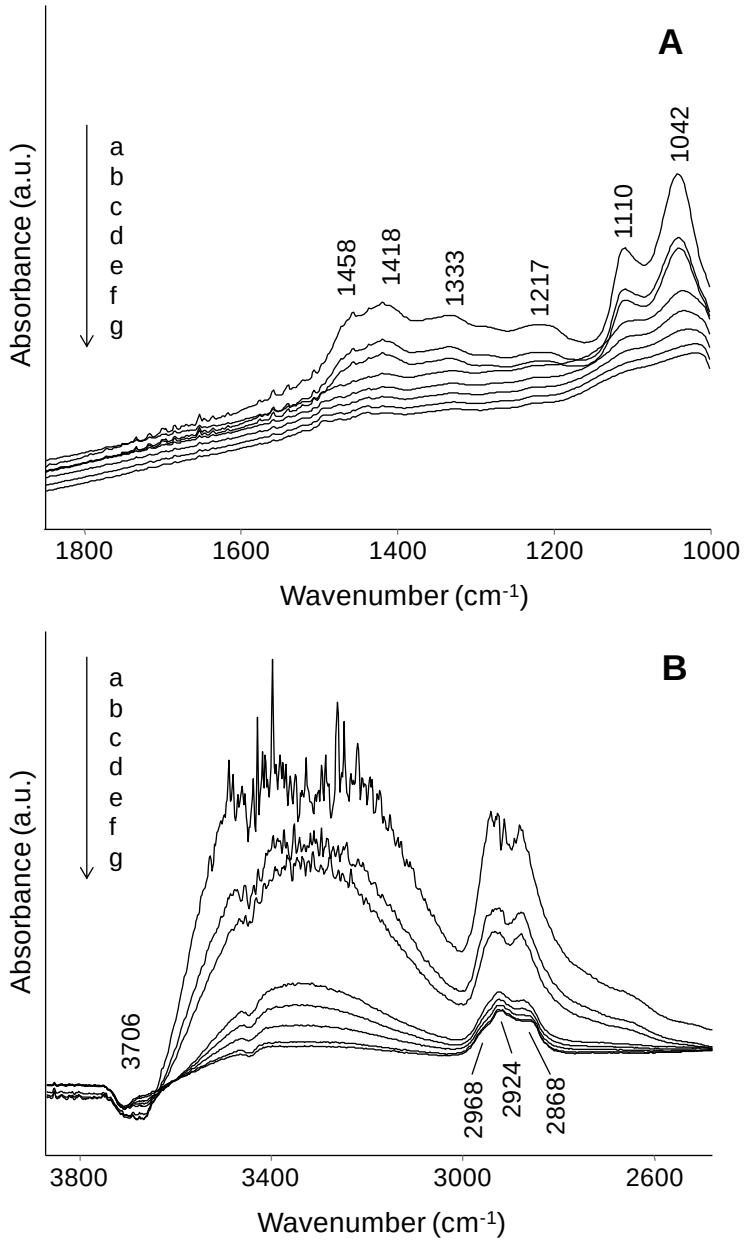

Figure 2.9 FTIR spectra of 3 wt% glycerol on NB700 at (a) RTHV, (b) 100 °C HV, (c) 150 °C HV, (d) 200 °C HV, (e) 250 °C HV, (f) 300 °C HV, (g) 350 °C HV. (A) between 1800 cm^{-1} and 1000 cm^{-1} (B) between 3800 cm^{-1} and 2600 cm^{-1}.

2.3.7 Formation of surface species on Na^+/NB500

Impregnation of Na^+/NB500 with 3.0 wt% glycerol at RTP resulted in the appearance of characteristic bands for adsorbed glycerol at 1457 cm^{-1}, 1410 cm^{-1}, 1329 cm^{-1}, 1218 cm^{-1}, 1114 cm^{-1} and 1056 cm^{-1} (Fig. 2.10A). Upon evacuation, the band at 1640 cm^{-1} (δOH of water) significantly decreased in intensity due to the absence of hydrophilic Brønsted acid sites, revealing a weak shoulder at 1575 cm^{-1} (Fig. 2.10Ab). In addition, weak bands at 1363 cm^{-1} (δCH_2) and 1260 cm^{-1} (ωCH_2) were observed, which are assigned to 2-propene-1,2-diol. It is important to note that the intensity of these characteristic peaks for adsorbed propene-diol was much lower than in the case of NB500. The characteristic bands for adsorbed acrolein were not observed. The $\nu_{asym}CH_2$ and $\nu_{sym}CH_2$ vibrational modes of glycerol were visible at 2938 cm^{-1} and 2878 cm^{-1}, respectively. As the temperature increased, the band at 2878 cm^{-1} broadened and increased in intensity (Fig. 2.10Bb-h). The perturbation of hydroxyl groups was observable by the 3735 cm^{-1} negative peak, while the band at 3434 cm^{-1} could be assigned to another set of hydroxyl groups. Bands from acrolein and monoaromatics were not observed as the temperature increased to 350 °C (Fig. 2.10Ab-h). Only glycerol and 2-propene-1,2-diol were present on the surface by 350 °C.

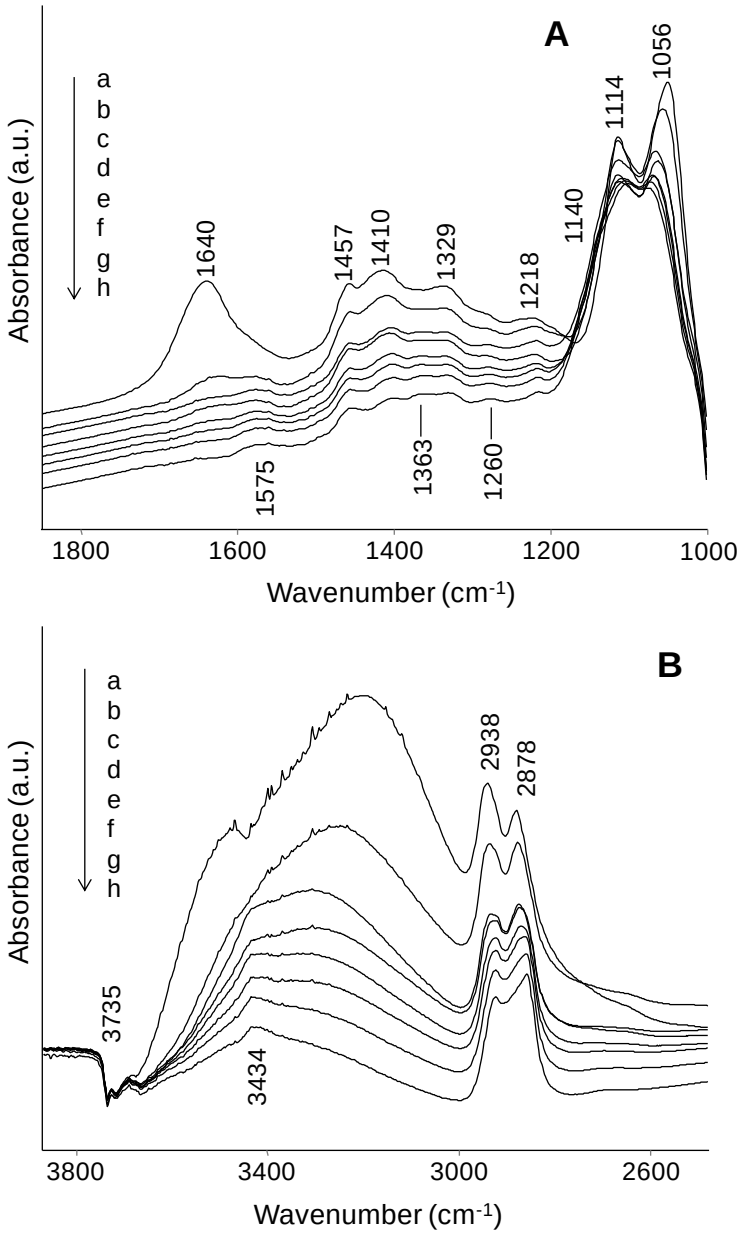

Figure 2.10 FTIR spectra of 3 wt% glycerol on Na^+/NB500 at (a) RTP, (b) RTHV, (c) 100 °C HV, (d) 150 °C HV, (e) 200 °C HV, (f) 250 °C HV, (g) 300 °C HV, (h) 350 °C HV. (A) between 1800 cm^{-1} and 1000 cm^{-1} (B) between 3800 cm^{-1} and 2600 cm^{-1}.

2.4 Discussion

2.4.1 Formation of multidentate species between glycerol and Lewis acid sites on niobium oxide.

Glycerol is able to chemisorb to the surface of various metal oxides (i.e. Al_2O_3, TiO_2, ZrO_2, CeO_2) when strong Lewis acid sites are present.[23-24] In this process, the proton of one of the primary alcohol groups dissociates to form a bridging alkoxy bond with two coordinatively unsaturated metal atoms, while the other primary OH group coordinates non-dissociatively to one of these metal atoms. The remaining secondary OH group may form a hydrogen bond to a basic surface oxygen atom, but this interaction can be inhibited by co-adsorbed water or CO_2. Over Al_2O_3, TiO_2 and ZrO2, this surface species was dominant, and there was no clear evidence for any other ones.[23-24] However, in the case of CeO_2, additional νC-O bands were observed upon evacuation due to interactions of glycerol with oxygen vacancies.[24]

The IR spectra in the present study (Fig. 2.6-2.10) show that glycerol is able to form the same multidentate surface species on all of the niobium oxide catalysts, except for NB700, which possesses very few Lewis acid sites. It was reported that Lewis acid sites of sufficient strength are needed for polyols to form alkoxy bonds with the metal oxide surface.[24] Chemisorbed glycerol was still observed on the rest of the catalysts at 350 °C, indicating a considerable strength of the surface reactions (Fig. 2.6-2.10).

Since glycerol dehydration can be performed in the gas phase in the presence of steam, it is necessary to verify whether the multidentate surface species is stable in the presence of water vapor. For experiments in the presence of 1 mbar water vapor, there were no changes in the FTIR spectrum compared to high vacuum condition (Fig. A.9). The same heating procedure for glycerol dehydration was also used in the presence of 1 mbar water vapor, and there were no changes compared to Fig. 2.6. These observations suggest that the alkoxy bonds on niobium oxide are stable at high temperatures in the

presence of water vapor. In related studies, it was reported that similar surface species are stable on Pt/γ-Al_2O_3 catalysts and that hydrolytic decay of the alumina support can be stopped in the presence of multidentate deposits from biomass-derived oxygenates.[66-67]

During the formation of the chemisorbed surface species, the chemical bonds in the adsorbing molecule are polarized. Specifically, the blue shift of the bands corresponding to C-O stretching vibrations indicates that electron density is transferred from the carbon atom to the oxygen atom resulting in a larger dipole moment and higher frequency. Copeland et al. found a positive linear correlation between the frequencies of the νC-O vibrations of the bridging alkoxy group (α) and the alcohol group engaged in a Lewis acid-base interaction (γ) with the electronegativity of the surface metal atoms.[24] Niobium has an electronegativity of 1.23, and the bands corresponding to the α and γ interactions appear at 1095 cm^{-1} and 1058 cm^{-1}, respectively.[68] These numbers fit the linear trend with other metal oxides such as γ-Al_2O_3, TiO_2, ZrO_2 and CeO_2.[24] It is interesting to note that the observed shifts for glycerol on niobia were smaller than the corresponding values on γ-Al_2O_3 and TiO_2 and comparable to the ZrO_2 samples, indicating a limited extent of polarization of this surface species on niobia.

2.4.2 Role of Lewis and Brønsted Sites in the dehydration of glycerol

Two pathways for dehydration of glycerol have been discussed in literature.[10, 12] The first pathway proceeds via the dehydration of a terminal OH group to form an intermediate enol (2-propene-1,2-diol), which easily tautomerizes to the thermodynamically favored hydroxyacetone.[10] The latter is a stable product. The second pathway proceeds via the formation of 3-hydroxypropionaldehyde by dehydration of the secondary OH group. The intermediate can either undergo a retroaldol reaction to form acetaldehyde and formaldehyde, or a second dehydration step to form acrolein.[12]

The conversion of glycerol to other surface species by dehydration was observed at room temperature on all of the niobium oxide catalysts except for NB700 (Fig. 2.6-

2.10). Surface species like acrolein and 2-propene-1,2-diol were formed on NB350 and NB500, while only a small amount of the latter was observed on Na^+/NB500. Pyridine adsorption followed by FTIR spectroscopy revealed that NB700 do not possess any Brønsted acid sites and only very few Lewis acid sites (Table 2.2). Furthermore, it has a low surface area (Table 2.1). Due to these reasons, glycerol is not able to bind to the surface to any measurable extent.

As shown in the previous section, Lewis acid sites readily chemisorb glycerol forming cyclic surface species, which involve strong surface interactions of both primary alcohol groups. The resulting polarization renders the primary alcohol group susceptible to dehydration (Fig. 2.11). Considering the preferential interaction of glycerol with Lewis acid sites, it is not surprising that the characteristic IR bands of 2-propene-1,2-diol were much stronger than the ones of acrolein when the loading on NB350 was limited to one monolayer (Fig. 2.6). Moreover, 2-propene-1,2-diol was the only identifiable product from glycerol dehydration on Na^+/NB500, which only contained Lewis acid sites (Fig. 2.10). It is interesting to point out that glycerol adsorbed on the Lewis acid sites of niobia was dehydrated, whereas this reaction was not observed at room temperature for the comparable surface species on Al_2O_3 and ZrO_2, which are polarized to the same extent or more strongly (vide supra).[24] The key differences between these materials is the presence of Brønsted acid sites in Nb_2O_5 (Table 2.2), which were absent in Al_2O_3 and ZrO_2.[24] Thus, it is concluded that dehydration of glycerol adsorbed on the Lewis acid sites of niobia involves the participation of nearby Brønsted acid sites. Further evidence for the involvement of Brønsted acid sites in the formation of 2-propene-1,2-diol is obtained from the reduced amount of 2-propene-1,2-diol on the surface of Na^+/NB500 (Fig. 2.10) compared to NB500 (Fig. 2.8). A small amount of Brønsted acid sites could be generated on Na^+/NB500 during the impregnation procedure in the presence of an aqueous solution, which explains why dehydration products are still detected. Moreover, Nimlos et al. reported that the barrier for glycerol dehydration is significantly lowered in the presence

of Brønsted acids, making it more susceptible to decomposition at much lower temperatures.[19]

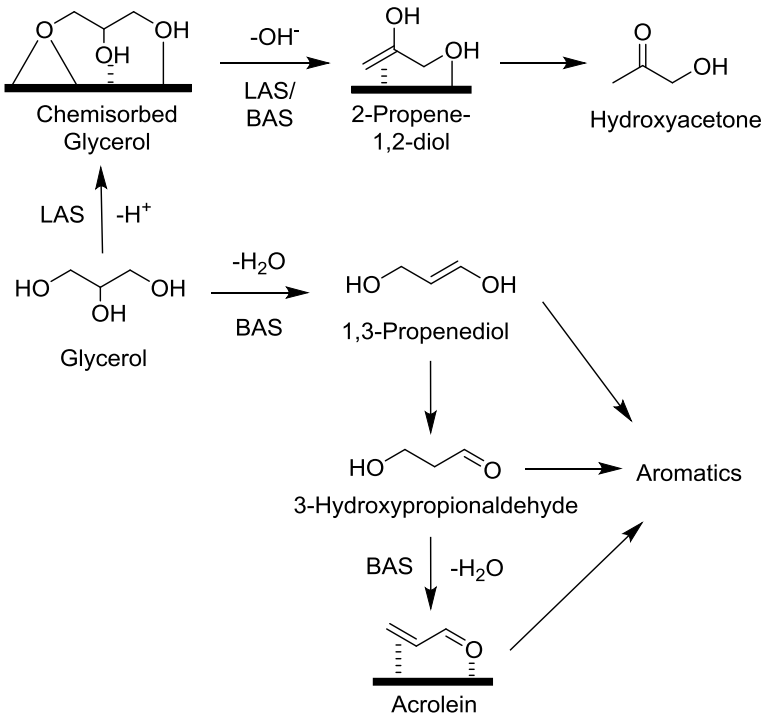

Figure 2.11 Role of Lewis (LAS) and Brønsted (BAS) acid sites in the dehydration of glycerol.

Interestingly, 2-propene-1,2-diol was observed as a product of dehydration while its ketone form (i.e. hydroxyacetone) was not present on the surface (Fig. 2.11). It is suggested that 2-propene-1,2-diol can be stabilized by formation of a bidentate surface species. DFT calculations indicated that the enol can interact with the surface through its primary alcohol group as well as the π-system of the olefinic double bond (Fig. 2.5b). The calculated vibrational frequencies for this species are in good agreement with the experimental spectra (Table 2.3). Specifically, the primary OH group of the enol interacts non-dissociatively with a Lewis acid metal atom, giving a frequency of 1050 cm^{-1}. This frequency also corresponds to the νC-O vibration of a primary alcohol group in glycerol

that is engaged in a Lewis acid-base interaction with the surface. Since this interaction is the weaker one of the two interactions of the primary alcohol groups in glycerol with the Lewis acid sites, its continued existence indicates that the eliminated alcohol group was the one forming the bridging alkoxy bond to the Lewis acid site. After the primary hydroxyl group is dehydrated, the olefinic π-system that was formed interacts with a Lewis acid site (Figure 2.5b). However, the secondary alcohol group of 2-propene-1,2-diol does not interact with the surface. In agreement with the observation of this surface species, a previous study indicated that the formation of bidentate surface species is much more favorable when there is sufficient spatial separation between the functional groups.[23] In contrast, bidentate surface species involving functional groups on vicinal carbon atoms (e.g. hydroxyacetone) are strongly strained and, thus, less stable. Subsequent to the formation of 2-propene-1,2-diol, the molecule can desorb from the surface and tautomerize to its ketone form (Figure 2.11).[18] The barrier for tautomerization is lower than dehydration and it should occur easily.[19]

It is important to note that 2-propene-1,2-diol cannot be converted to acrolein. The elimination of the secondary alcohol group would result in the formation of highly unstable adjacent C=C double bonds. Moreover, 2-propene-1,2-diol was found to interact with the niobia in a way that the secondary alcohol is pointing away from the surface, preventing its interaction with acid sites.

The formation of hydroxyacetone has been a subject of debate, but understanding the role of Lewis and Brønsted acid sites in the dehydration of glycerol can provide an explanation for the observations in the present study and previous ones. Alhanash et al. suggested that only a terminal alcohol group of glycerol is able to interact with two oxo-bridged metal atoms in heteropolyacids due to steric constraint. The alcohol group is dehydrated in a concerted manner, resulting in the conversion of the oxo-bridged metal atoms to two metal hydroxyl groups.[13] However, no direct evidence was provided for this mechanism, and the results can be explained equally well with the formation of bidentate

cyclic surface species as described above. Kinage et al. proposed a different mechanism for the formation of hydroxyacetone over CeO_2, Al_2O_3, ZrO_2 and Ga_2O_3 involving dehydrogenation, dehydration and rehydrogenation over basic sites.[69] However, all of the catalysts used in that study are Lewis acidic,[24, 70] and it was shown that the bidendate surface species described in section 2.4.1 were also abundant surface species on CeO_2, Al_2O_3, ZrO_2.[24]

As mentioned above, the formation of acrolein requires the secondary alcohol group of glycerol to be eliminated first forming 1,3-propenediol. In the absence of steric factors, this pathway is intrinsically favored over Brønsted acid sites as the secondary carbenium ion intermediate is more stable compared to the primary carbenium ion formed from during the elimination of the terminal OH group.[71] The primary dehydration product of this reaction, 1,3-propenediol, can tautomerize to 3-hydroxypropionaldehyde, which can be converted to acrolein in a thermodynamically favorable second dehydration step, which may occur with or without the involvement of a Brønsted acid site.[11, 19, 72] Suprun et al. used 3-hydroxypropionaldehyde as a reactant and they obtained 100% conversion with a high yield of acrolein.[14] Note that direct dehydration of 1,3-propenediol would result in the formation of unstable adjacent double bonds. While it is possible that the corresponding enol, 1,3-propenediol, is stabilized by interacting with the surface of niobia, the data in the present study do not provide evidence for measurable quantities of this species on the surface.

High selectivities for the formation of acrolein were reported over Brønsted acidic zeolites.[21, 73] Yoda et al. proposed that the dehydration of the secondary alcohol group of glycerol is catalyzed by a Brønsted acidic bridging hydroxyl group.[21] This reaction results in the formation of an alkoxy species, which is converted to acrolein in a sequence of desorption, re-adsorption and dehydration steps. Unfortunately, no direct evidence for the intermediates in this sequence could be obtained due to the strong absorption of the zeolite below 1300 cm^{-1}.[74] Wang et al. suggested that Lewis acid sites in ZSM-5 could

enhance the formation of acrolein in a cooperative mechanism.[73] To achieve such a cooperative effect the Lewis acid sites would have to be in direct vicinity a Brønsted acid site. Taking the spatial constraints in a zeolite cage into account it is unlikely that the multidentate species described in the present study (vide supra) can be formed in such an environment. Consequently, only Lewis acid sites outside the zeolite are expected to favor the formation of hydroxyacetone.

Using the results of the reactivity study obtained by Chai et al. who used the same synthesis procedure for niobia catalysts to dehydrate glycerol vapor at 315 °C,[9] a strong correlation between the acid site ratio and selectivity is obtained (Fig. 2.12). The selectivities to hydroxyacetone and acrolein increase linearly with the ratio of Lewis and Brønsted sites, respectively. An extrapolation of the curve for hydroxyacetone (Fig. 2.12a) leads to an intercept of 9.4% selectivity, which is likely due to non-catalytic dehydration at the reaction temperature. The curve for acrolein selectivity has an intercept at 29.6% selectivity (Fig. 2.12b). This is attributed to the transformation of Lewis to Brønsted acid sites in the presence of steam as shown in section 2.3.2.[13, 75] This correlation supports the proposed reaction network, in which Lewis acid sites activate primary C-O bonds of glycerol to form 2-propene-1,2-diol, while Brønsted acid sites are involved in the formation of acrolein (Fig. 2.11).

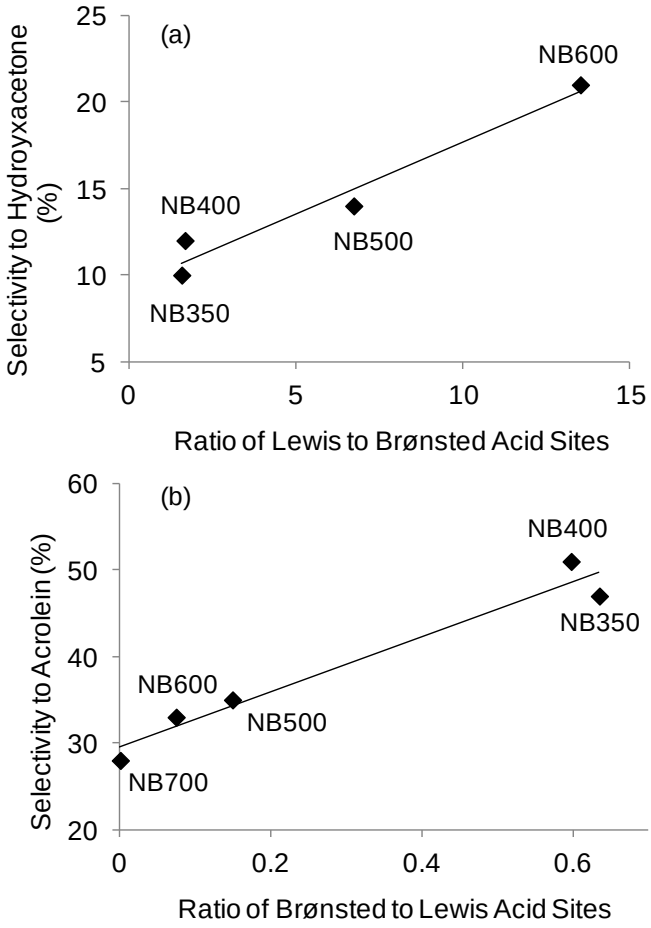

Figure 2.12 Correlation between (a) selectivity to hydroxyacetone and ratio of Lewis to Brønsted acid sites, (b) selectivity to acrolein and ratio of Brønsted to Lewis acid sites.

2.4.3 Formation of monoaromatics

One of the main challenges in glycerol dehydration is deactivation due to coke formation for all of the catalysts that have been studied.[6] A possible strategy is promoting the catalyst with Pt group metal and co-feeding of hydrogen.[13] However, this method will increase the costs of the catalyst and operations. Another possibility to avoid coke formation is to co-feed oxygen.[76-77] However, the presence of oxygen could also promote the conversion of the desired products in side reactions. In a different approach, Corma et al. used an FCC type reactor where the catalyst can be continuously separated and

regenerated.[11] Reports in literature have also shown that a large pore volume can promote condensation reactions and the formation of coke.[78-79]

Our results show that some of the acid sites remain occupied by unreacted glycerol and its dehydration products at 350 °C (Fig. 2.6-2.10). In addition, the formation of monoaromatics was observed when more than a monolayer of glycerol was impregnated and dehydrated on the surface of NB350 and NB500, suggesting that multimolecular reactions have occurred because at least two glycerol molecules are needed to form a monoaromatic compound. These multimolecular reactions are avoided when less than a monolayer of glycerol was present on the surface. The same reactions are also avoided in the absence of Brønsted acid sites on Na^+/NB500 even when there is more than a monolayer of glycerol present. This shows that either Brønsted acid sites play a critical role in the formation of aromatics and/or that products from Brønsted acid catalyzed dehydration (i.e. 3-hydroxypropionaldehyde, 1,3-propenediol, acrolein) are key intermediates for the formation of the aromatics (Scheme 1). The reaction path to aromatics could consist of dehydration, dehydrogenation and cyclization reactions of carbocation intermediates.[80]

Since hydroxyacetone by itself is unreactive in the presence of Brønsted acid sites,[13] the formation of monoaromatics must involve 1,3-propenediol, 3-hydroxypropionaldehyde and/or acrolein as intermediates (Figure 2.11). Studies done on the gas phase dehydration of glycerol at high temperature used an aqueous glycerol feed ranging from 10 to 85 wt%.[2, 9-15] The presence of monoaromatics on the surface eventually results in the formation of coke and deactivation of the catalysts.[80] It was reported that hydroquinone, which could be one of the monoaromatic compounds present in this study, enhances the rate of coke formation by undergoing condensation.[61]

In this study, it was found that the formation of monoaromatics can be hindered as long as there is less than a monolayer of glycerol on the surface of the catalyst. Thus, using a small concentration of glycerol feed can help to prevent deactivation. However,

this would shift the product distribution from acrolein to hydroxyacetone, which is usually considered the less desirable product. Alternatively, the presence of steam could aid in the desorption of the dehydration products.

2.5 Conclusions

Glycerol can chemisorb on strong Lewis acid sites on niobia forming a multidentate surface species. The proton of one of the primary alcohol groups dissociates to form a bridging alkoxy bond with two coordinatively unsaturated metal atoms, while the other primary alcohol group coordinates non-dissociatively to one of these metal atoms. The secondary alcohol group can form a hydrogen bond to a basic oxygen atom on the surface. In the absence of Brønsted acidic protons, these alkoxy bonds are stable in the presence of water vapor and at high temperature. However, the primary C-O bonds are polarized, and in the presence of an acidic proton, one of the primary hydroxyl groups is dehydrated to form 2-propene-1,2-diol, which can desorb and tautomerize to hydroxyacetone. When glycerol interacts with a Brønsted acid site without steric constraints, the dehydration of the secondary alcohol group is strongly preferred due to the higher stability of the corresponding carbenium ion that is formed as the transition state. This reaction forms 1,3-propenediol, which tautomerizes to 3-hydroxypropionaldehyde, an unstable intermediate that undergoes a second acid-catalyzed dehydration step to yield acrolein. The involvement of Lewis and Brønsted acid sites in different dehydration pathways is supported by the linear correlation between the selectivity to hydroxyacetone and acrolein, and the ratio of the concentrations of Lewis and Brønsted acid sites, respectively. However, this model may not be applicable to other catalytic systems with different porous constraints. Brønsted sites are also involved in multimolecular reactions, resulting in the formation of coke and catalyst deactivation.

2.6 References

1. Zhu, C. J.; Chiu, S.; Nakas, J. P.; Nomura, C. T. Bioplastics from waste glycerol derived from biodiesel industry. *J. Appl. Polym. Sci.* **2013,** *130,* 1-13.

2. Corma, A.; Iborra, S.; Velty, A. Chemical routes for the transformation of biomass into chemicals. *Chem. Rev.* **2007,** *107,* 2411-2502.

3. Krenzke, L. D.; Keulks, G. W.; Sklyarov, A. V.; Firsova, A. A.; Kutirev, M. Y.; Margolis, L. Y.; Krylov, O. V. Study of selective oxidation of propylene on complex oxides by means of temperature-programmed desorption. *J. Catal.* **1978,** *52,* 418-424.

4. Jekewitz, T.; Blickhan, N.; Endres, S.; Drochner, A.; Vogel, H. The influence of water on the selective oxidation of acrolein to acrylic acid on Mo/V/W-mixed oxides. *Catal. Commun.* **2012,** *20,* 25-28.

5. Katryniok, B.; Paul, S.; Belliere-Baca, V.; Rey, P.; Dumeignil, F. Glycerol dehydration to acrolein in the context of new uses of glycerol. *Green Chem.* **2010,** *12,* 2079-2098.

6. Katryniok, B.; Paul, S.; Capron, M.; Dumeignil, F. Towards the Sustainable Production of Acrolein by Glycerol Dehydration. *ChemSusChem* **2009,** *2,* 719-730.

7. Ramayya, S.; Brittain, A.; Dealmeida, C.; Mok, W.; Antal, M. J. Acid-catalyzed dehydration of alcohols in supercritical water. *Fuel* **1987,** *66,* 1364-1371.

8. Watanabe, M.; Lida, T.; Aizawa, Y.; Aida, T. M.; Inomata, H. Acrolein synthesis from glycerol in hot-compressed water. *Bioresour. Technol.* **2007,** *98,* 1285-1290.

9. Chai, S. H.; Wang, H. P.; Liang, Y.; Xu, B. Q. Sustainable production of acrolein: Gas-phase dehydration of glycerol over Nb2O5 catalyst. *J. Catal.* **2007,** *250,* 342-349.

10. Chai, S. H.; Wang, H. P.; Liang, Y.; Xu, B. Q. Sustainable production of acrolein: investigation of solid acid-base catalysts for gas-phase dehydration of glycerol. *Green Chem.* **2007,** *9,* 1130-1136.

11. Corma, A.; Huber, G. W.; Sauvanauda, L.; O'Connor, P. Biomass to chemicals: Catalytic conversion of glycerol/water mixtures into acrolein, reaction network. *J. Catal.* **2008,** *257*, 163-171.

12. Tsukuda, E.; Sato, S.; Takahashi, R.; Sodesawa, T. Production of acrolein from glycerol over silica-supported heteropoly acids. *Catal. Commun.* **2007,** *8*, 1349-1353.

13. Alhanash, A.; Kozhevnikova, E. F.; Kozhevnikov, I. V. Gas-phase dehydration of glycerol to acrolein catalysed by caesium heteropoly salt. *Appl. Catal., A* **2010,** *378*, 11-18.

14. Suprun, W.; Lutecki, M.; Haber, T.; Papp, H. Acidic catalysts for the dehydration of glycerol: Activity and deactivation. *J. Mol. Catal. A-Chem.* **2009,** *309*, 71-78.

15. Suprun, W.; Lutecki, M.; Papp, H. TPD-TG-MS Investigations of the Catalytic Conversion of Glycerol over MOx-Al2O3-PO4 Catalysts. *Chem. Eng. Technol.* **2011,** *34*, 134-139.

16. Shiju, N. R.; Brown, D. R.; Wilson, K.; Rothenberg, G. Glycerol Valorization: Dehydration to Acrolein Over Silica-Supported Niobia Catalysts. *Top. Catal.* **2010,** *53*, 1217-1223.

17. Nair, G. S.; Adrijanto, E.; Alsalme, A.; Kozhevnikov, I. V.; Cooke, D. J.; Brown, D. R.; Shiju, N. R. Glycerol utilization: solvent-free acetalisation over niobia catalysts. *Catal. Sci. Technol.* **2012,** *2*, 1173-1179.

18. Katryniok, B.; Paul, S.; Dumeignil, F. Recent Developments in the Field of Catalytic Dehydration of Glycerol to Acrolein. *ACS Catal.* **2013,** *3*, 1819-1834.

19. Nimlos, M. R.; Blanksby, S. J.; Qian, X. H.; Himmel, M. E.; Johnson, D. K. Mechanisms of glycerol dehydration. *J. Phys. Chem. A* **2006,** *110*, 6145-6156.

20. Laino, T.; Tuma, C.; Curioni, A.; Jochnowitz, E.; Stolz, S. A Revisited Picture of the Mechanism of Glycerol Dehydration. *J. Phys. Chem. A* **2011,** *115*, 3592-3595.

21. Yoda, E.; Ootawa, A. Dehydration of glycerol on H-MFI zeolite investigated by FT-IR. *Appl. Catal. A-Gen.* **2009,** *360*, 66-70.

22. Kim, Y. T.; Jung, K. D.; Park, E. D. Gas-phase dehydration of glycerol over silica-alumina catalysts. *Appl. Catal. B-Environ.* **2011,** *107*, 177-187.

23. Copeland, J. R.; Shi, X.-R.; Sholl, D. S.; Sievers, C. Surface Interactions of C2 and C3 Polyols with γ-Al2O3 and the Role of Coadsorbed Water. *Langmuir* **2012,** *29*, 581-593.

24. Copeland, J. R.; Santillan, I. A.; Schimming, S. M.; Ewbank, J. L.; Sievers, C. Surface Interactions of Glycerol with Acidic and Basic Metal Oxides. *J. Phys. Chem. C* **2013,** *117*, 21413-21425.

25. Nowak, I.; Ziolek, M. Niobium compounds: Preparation, characterization, and application in heterogeneous catalysis. *Chem. Rev.* **1999,** *99*, 3603-3624.

26. Datka, J.; Turek, A. M.; Jehng, J. M.; Wachs, I. E. Acidic properties of supported niobium oxide catalysts - An infrared-spectroscopy investigation. *J. Catal.* **1992,** *135*, 186-199.

27. Chen, Z.; Iizuka, T.; Tanabe, K. Niobic acid as an efficient catalyst for vapor-phase esterification of ethyl-alcohol with acetic-acid. *Chem. Lett.* **1984**, 1085-1088.

28. Tanabe, K.; Okazaki, S. Various reactions catalyzed by niobium compounds and materials. *Appl. Catal. A-Gen.* **1995,** *133*, 191-218.

29. Nakajima, K.; Baba, Y.; Noma, R.; Kitano, M.; Kondo, J. N.; Hayashi, S.; Hara, M. Nb(2)O(5)center dot nH(2)O as a Heterogeneous Catalyst with Water-Tolerant Lewis Acid Sites. *J. Am. Chem. Soc.* **2011,** *133*, 4224-4227.

30. Brunauer, S.; Emmett, P. H.; Teller, E. Adsorption of gases in multimolecular layers. *J. Am. Chem. Soc.* **1938,** *60*, 309-319.

31. Barrett, E. P.; Joyner, L. G.; Halenda, P. P. The determination of pore volume and area distributions in porous substances .1. Computations from nitrogen isotherms. *J. Am. Chem. Soc.* **1951,** *73*, 373-380.

32. Kresse, G.; Hafner, J. Abinitio molecular-dynamics for liquid-metals. *Physical Review B* **1993,** *47*, 558-561.

33. Kresse, G.; Hafner, J. Abinitio molecular-dynamics simulation of the liquid-metal amorpheous-semiconductor transition in germanium. *Physical Review B* **1994,** *49*, 14251-14269.

34. Kresse, G.; Furthmuller, J. Efficiency of ab-initio total energy calculations for metals and semiconductors using a plane-wave basis set. *Comput. Mater. Sci.* **1996,** *6*, 15-50.

35. Kresse, G.; Furthmuller, J. Efficient iterative schemes for ab initio total-energy calculations using a plane-wave basis set. *Physical Review B* **1996,** *54*, 11169-11186.

36. Perdew, J. P.; Chevary, J. A.; Vosko, S. H.; Jackson, K. A.; Pederson, M. R.; Singh, D. J.; Fiolhais, C. Atoms, molecules, solids, and surfaces: Applications of the generalized gradient approximation for exchange and correlation. *Physical Review B* **1992,** *46*, 6671-6687.

37. Perdew, J. P.; Chevary, J. A.; Vosko, S. H.; Jackson, K. A.; Pederson, M. R.; Singh, D. J.; Fiolhais, C. Erratum: Atoms, molecules, solids, and surfaces: Applications of the generalized gradient approximation for exchange and correlation. *Physical Review B* **1993,** *48*, 4978-4978.

38. Blochl, P. E. Projector Augmented-Wave Method. *Physical Review B* **1994,** *50*, 17953-17979.

39. Kresse, G.; Joubert, D. From ultrasoft pseudopotentials to the projector augmented-wave method. *Physical Review B* **1999,** *59*, 1758-1775.

40. Kato, K.; Tamura, S. Die Kristallstruktur von T-Nb2O5. *Acta Crystallographica Section B* **1975,** *31*, 673-677.

41. Bergerhoff, G.; Brown, I. D., Crystallographic Databases. International Union of Crystallography: 1987.

42. Sholl, D.; Steckel, J. A., *Density Functional Theory: A Practical Introduction*. John Wiley & Sons: Hoboken: 2009;

43. Iizuka, T.; Ogasawara, K.; Tanabe, K. Acidic and catalytic properties of niobium pentaoxide. *Bull. Chem. Soc. Jpn.* **1983,** *56*, 2927-2931.

44. Jehng, J. M.; Wachs, I. E. Molecular-structures of supported niobium oxide catalysts under insitu conditions. *J. Phys. Chem.* **1991,** *95,* 7373-7379.

45. Burcham, L. J.; Datka, J.; Wachs, I. E. In situ vibrational spectroscopy studies of supported niobium oxide catalysts. *J. Phys. Chem. B* **1999,** *103,* 6015-6024.

46. Pittman, R. M.; Bell, A. T. Raman studies of the structure of Nb2O5/TiO2. *J. Phys. Chem.* **1993,** *97,* 12178-12185.

47. Gott, T.; Oyama, S. T. A general method for determining the role of spectroscopically observed species in reaction mechanisms: Analysis of coverage transients (ACT). *J. Catal.* **2009,** *263,* 359-371.

48. Popova, G. Y.; Chesalov, Y. A.; Sadovskaya, E. M.; Andrushkevich, T. V. Effect of water on decomposition of formic acid over V-Ti oxide catalyst: Kinetic and in situ FTIR study. *J. Mol. Catal. A-Chem.* **2012,** *357,* 148-153.

49. Clayden, J.; Greeves, N.; Warren, S., *Organic Chemistry*. 2nd ed.; Oxford University Press, USA: 2012;

50. Delgado, M.; Desroches, M.; Ganachaud, F. Ionic oligomerization of acrolein in water. *RSC Advances* **2013,** *3,* 23057-23065.

51. Yaylayan, V. A.; Harty-Majors, S.; Ismail, A. A. Monitoring carbonyl-amine reaction and enolization of 1-hydroxy-2-propanone (Acetol) by FTIR spectroscopy. *J Agric Food Chem* **1999,** *47,* 2335-40.

52. de Jesus, J. C.; Zaera, F. Adsorption and thermal chemistry of acrolein and crotonaldehyde on Pt(111) surfaces. *Surf. Sci.* **1999,** *430,* 99-115.

53. Copeland, J. R.; Foo, G. S.; Harrison, L. A.; Sievers, C. In situ ATR-IR study on aqueous phase reforming reactions of glycerol over a Pt/γ-Al2O3 catalyst. *Catal. Today* **2013,** *205,* 49-59.

54. Raman, M. S.; Ponnuswamy, V.; Kolandaivel, P.; Perumal, K. Ultrasonic and DFT study of intermolecular association through hydrogen bonding in aqueous solutions of glycerol. *J. Mol. Liq.* **2008,** *142,* 10-16.

55. Socrates, G., *Infrared and Raman Characteristic Group Frequencies*. Third ed.; John Wiley & Sons LTD: 2001;

56. Palumbo, L.; Bonino, F.; Beato, P.; Bjorgen, M.; Zecchina, A.; Bordiga, S. Conversion of methanol to hydrocarbons: Spectroscopic characterization of Carbonaceous species formed over H-ZSM-5. *J. Phys. Chem. C* **2008,** *112*, 9710-9716.

57. Karge, H. G.; Niessen, W.; Bludau, H. In-situ FTIR measurements of diffusion in coking zeolite catalysts. *Appl. Catal., A* **1996,** *146*, 339-349.

58. Rozwadowski, M.; Lezanska, M.; Wloch, J.; Erdmann, K.; Golembiewski, R.; Kornatowski, J. Investigation of coke deposits on Al-MCM-41. *Chem. Mat.* **2001,** *13*, 1609-1616.

59. Colthup, N. B.; Daly, L. H.; Wiberley, S. E., *Introduction to Infrared and Raman Spectroscopy*. Third Edition ed.; Academic Press: 1990;

60. Popov, A.; Kondratieva, E.; Goupil, J. M.; Mariey, L.; Bazin, P.; Gilson, J. P.; Travert, A.; Mauge, F. Bio-oils Hydrodeoxygenation: Adsorption of Phenolic Molecules on Oxidic Catalyst Supports. *J. Phys. Chem. C* **2010,** *114*, 15661-15670.

61. Pinard, L.; Tayeb, K. B.; Hamieh, S.; Vezin, H.; Canaff, C.; Maury, S.; Delpoux, O.; Pouilloux, Y. On the involvement of radical "coke" in ethanol conversion to hydrocarbons over HZSM-5 zeolite. *Catal. Today* **2013,** *218–219*, 57-64.

62. Broclawik, E.; Kozyra, P.; Datka, J. IR studies and DFT quantum chemical calculations concerning interaction of some organic molecules with Cu+ sites in zeolites. *C. R. Chim.* **2005,** *8*, 491-508.

63. Hall, R. H.; Stern, E. S. ACID-CATALYSED HYDRATION OF ACRALDEHYDE - KINETICS OF THE REACTION AND ISOLATION OF BETA-HYDROXYPROPALDEHYDE. *J. Chem. Soc.* **1950**, 490-498.

64. Luthi-Peng, Q.; Scharer, S.; Puhan, Z. Production and stability of 3-hydroxypropionaldehyde in Lactobacillus reuteri. *Appl. Microbiol. Biotechnol.* **2002,** *60*, 73-80.

65. Vollenweider, S.; Grassi, G.; Konig, I.; Puhan, Z. Purification and structural characterization of 3-hydroxypropionaldehyde and its derivatives. *J Agric Food Chem* **2003,** *51*, 3287-3293.

66. Ravenelle, R. M.; Copeland, J. R.; Van Pelt, A. H.; Crittenden, J. C.; Sievers, C. Stability of Pt/gamma-Al2O3 Catalysts in Model Biomass Solutions. *Top. Catal.* **2012,** *55*, 162-174.

67. Jongerius, A. L.; Copeland, J. R.; Foo, G. S.; Hofmann, J. P.; Bruijnincx, P. C. A.; Sievers, C.; Weckhuysen, B. M. Stability of Pt/gamma-Al2O3 Catalysts in Lignin and Lignin Model Compound Solutions under Liquid Phase Reforming Reaction Conditions. *ACS Catal.* **2013,** *3*, 464-473.

68. Tamura, M.; Shimizu, K.-i.; Satsuma, A. Comprehensive IR study on acid/base properties of metal oxides. *Appl. Catal. A-Gen.* **2012,** *433*, 135-145.

69. Kinage, A. K.; Upare, P. P.; Kasinathan, P.; Hwang, Y. K.; Chang, J. S. Selective conversion of glycerol to acetol over sodium-doped metal oxide catalysts. *Catal. Commun.* **2010,** *11*, 620-623.

70. Tokmachev, A. M.; Pushkar, Y. N.; Fionov, A. V.; Lunina, E. V.; Chuvylkin, N. D. Coordination of nitroxyl radical probes to the Lewis acid sites on the surface of gallium oxide: A quantum-chemical analysis. *Russ Chem Bull* **2000,** *49*, 991-996.

71. Olah, G. A.; Baker, E. B.; Evans, J. C.; Tolgyesi, W. S.; McIntyre, J. S.; Bastien, I. J. Stable Carbonium Ions. V.1a Alkylcarbonium Hexafluoroantimonates. *J. Am. Chem. Soc.* **1964,** *86*, 1360-1373.

72. ten Dam, J.; Hanefeld, U. Renewable Chemicals: Dehydroxylation of Glycerol and Polyols. *ChemSusChem* **2011,** *4*, 1017-1034.

73. Wang, Z.; Wang, L.; Jiang, Y.; Hunger, M.; Huang, J. Cooperativity of Brønsted and Lewis Acid Sites on Zeolite for Glycerol Dehydration. *ACS Catal.* **2014,** *4*, 1144-1147.

74. Galhotra, P.; Navea, J. G.; Larsen, S. C.; Grassian, V. H. Carbon dioxide ((CO2)-O-16 and (CO2)-O-18) adsorption in zeolite Y materials: effect of cation, adsorbed water and particle size. *Energy Environ. Sci.* **2009,** *2*, 401-409.

75. Garcia-Sancho, C.; Moreno-Tost, R.; Merida-Robles, J.; Santamaria-Gonzalez, J.; Jimenez-Lopez, A.; Maireles-Torres, P. Zirconium doped mesoporous silica catalysts for dehydration of glycerol to high added-value products. *Appl. Catal. A-Gen.* **2012,** *433*, 179-187.

76. Wang, F.; Dubois, J. L.; Ueda, W. Catalytic dehydration of glycerol over vanadium phosphate oxides in the presence of molecular oxygen. *J. Catal.* **2009,** *268*, 260-267.

77. Wang, F.; Dubois, J. L.; Ueda, W. Catalytic performance of vanadium pyrophosphate oxides (VPO) in the oxidative dehydration of glycerol. *Appl. Catal. A-Gen.* **2010,** *376*, 25-32.

78. Gu, Y. L.; Cui, N. Y.; Yu, Q. J.; Li, C. Y.; Cui, Q. K. Study on the influence of channel structure properties in the dehydration of glycerol to acrolein over H-zeolite catalysts. *Appl. Catal. A-Gen.* **2012,** *429*, 9-16.

79. Possato, L. G.; Diniz, R. N.; Garetto, T.; Pulcinelli, S. H.; Santilli, C. V.; Martins, L. A comparative study of glycerol dehydration catalyzed by micro/mesoporous MFI zeolites. *J. Catal.* **2013,** *300*, 102-112.

80. Bartholomew, C. H. Mechanisms of catalyst deactivation. *Appl. Catal., A* **2001,** *212*, 17-60.

CHAPTER 3

SYNERGISTIC EFFECT BETWEEN DEFECT SITES AND FUNCTIONAL GROUPS ON THE HYDROLYSIS OF CELLULOSE OVER ACTIVATED CARBON

3.1 Background

Cellulose, a linear polysaccharide of glucose monomers linked by β-1,4-glycosidic bonds, is an abundant constituent in most types of biomass.[1] The hydrolysis of cellulose to glucose has been of great interest as the latter is a versatile intermediate for sustainable chemicals and fuels.[2] Mineral acids are inexpensive and display high catalytic activity,[3-4] but major drawbacks are related to product separation, solvent recycling and equipment corrosion. Solid acid catalysts offer simplified separation and recycling. Of all the types of solid acid catalysts, carbonaceous solid acids and amorphous carbon seem to be especially effective.[5-9] Particularly, it has been reported that carbon imparted with sulfonic groups acts as an active, stable, and reusable heterogeneous acid catalyst. Specifically, sulfonated carbon based acids with high surface area are preferred.[10]

Many studies focused on the catalytic performance of carbon catalysts, but changes in carbon structure after acid treatment, the role of different functional groups, and mechanistic information remain to be clarified. Besides using sulfonated carbon, experiments for the hydrolysis of cellulose have been performed with different solid acids like niobic acid, Nafion and Amberlyst-15.[7-8, 11] It was reported that the hydrogen bonds between the phenolic OH groups in carbon and the glycosidic bonds in β-1,4-glucan led to higher catalytic activity. However, the comparison was done between different substrates. Furthermore, the unsulfonated carbon material with carboxylic acid and phenolic groups was not tested for its catalytic activity.

Kobayashi et al. showed that unacidified carbon with oxygen functional groups also displays catalytic activity in the hydrolysis of cellulose.[12] It was further shown that the catalytic activity decreases with the specific amount of functional groups. The hydrolysis of miscanthus xylan was also proven to be effective using mesoporous carbon nanoparticles functionalized with weak acid sites.[13] It was argued that strong acid sites such as sulfonic groups could leach through ion-exchange in the presence of salts, thus weak acid sites are preferable. However, the mechanism for the hydrolysis of carbohydrates using weak acid sites has not been fully elucidated.

Katz and co-workers grafted β-glucan strands on silica and alumina and found that weakly acidic OH groups with the greatest interactions are able to hydrolyze the glycosidic bond.[14-16] They also demonstrated that glucan chains can rapidly adsorb onto the surface of mesoporous carbon nanoparticle within the confined pore space.[17] Based on these results, it was concluded that the force exerted on the constrained polymer by the pore walls and OH groups leads to hydrolysis of the glycosidic bond, which relieves some of the mechanical strain.[16] However, no study has been done to correlate the changes in carbon structure and functional groups as a result of chemical treatment to reactivity.

Here, we report the effects of chemical treatments of activated carbon (AC) with hydrogen peroxide (ACOH) and sulfuric acid at 100 °C and 200 °C (SAC100 and SAC200) as well as a treatment with hydrogen peroxide followed by sulfuric acid at 100 °C (SACOH). Different types and concentrations of acid sites are imparted by each of these treatments. The effect of the functional groups was determined by adsorption isotherms and hydrolysis of cellulose. Finally, we examine the origin of the catalytic activity, which can be linked to the synergistic effect of functional groups and the immobilization of glucan chains on edge/defect sites.

3.2 Experimental Section

3.2.1 Materials

Activated charcoal (untreated, granular, 4-8 mesh, made from peat bog), sulfuric acid (95.0-98.0%), glucose (>99.5%), cellobiose (>98%), sodium hydroxide (>98%, pellets), potassium hydrogen phthalate (>99.95%), sodium carbonate (>99%), sodium bicarbonate (>99.7%), potassium bromide (FTIR grade, >99%), acetic acid (>99.7%) and cellulose (microcrystalline powder) were purchased from Sigma Aldrich. Hydrogen peroxide (30% w/w aqueous solution) and hydrochloric acid (36.5%-38.0% w/w aqueous solution) were purchased from BDH and Alfa Aesar, respectively. Deionized water was further purified using a Barnstead NANOpure ultrapure water system to 18.2 MΩ/cm.

3.2.2 Synthesis of catalysts

Activated charcoal (2.5 g) was mixed with 30 ml of DI water in a 45 ml Teflon lined acid digestion vessel (Parr Instrument) and loaded into a rotary oven at 200 °C for 24 h. The material was filtered and washed with DI water. The resulting sample was named AC. Subsequently, 0.15 g of AC was added to 8.0 g of H_2O_2 and the suspension was continuously stirred and heated at 85 °C for 1 h in a beaker. The suspension was filtered (Fischer Scientific, Grade Q5,5-10 μm), washed with DI water, and named ACOH. To prepare other samples, AC (2.5 g) was mixed with 30 ml of 5 M H_2SO_4 in a 45 ml Teflon lined acid digestion vessel (Parr Instrument), loaded into a rotary oven, and heated at 100 °C and 200 °C for 5 h, respectively. The suspension was filtered, washed with DI water until the filtrate had a neutral pH, and the samples were named SAC100 and SAC200, respectively. A batch of ACOH was subjected to the same sulfuric acid treatment at 100 °C and the sample was named SACOH. To prevent elution of functional groups during reactions,[18] all chemically treated samples were treated with hot liquid

water at 150 °C and autogenic pressure for 24 h, filtered and washed with DI water until the filtrate had a neutral pH.

3.2.3 Characterization

Raman spectra were collected on a Confocal Raman Microscope Alpa-Witek with laser wavelength of 514 nm. Each sample was spread across a glass slide. Ten scans were accumulated and three spectra were obtained for each sample at different locations. Peak fitting was carried out with the GRAMS/AI software. X-ray diffraction (XRD) measurements were performed with a Philips X'pert diffractometer equipped with an X'celerator module using Cu Kα radiation. Diffractograms were collected at incident angles from 2θ = 5 to 70° with a step size of 0.0167°. ^{13}C direct polarization (DP) magic angle spinning (MAS) NMR spectroscopic measurements were performed on a Bruker DSX 300 spectrometer. The samples were packed into a 4 mm zirconia rotor and spun at 10 kHz. Adamantane was used as an external reference material, and the low field peak was set as the reference (δ=38.45 ppm). The resonance frequencies of ^{1}H and ^{13}C were 300.2 and 75.5 MHz, respectively. For ^{13}C detection, high power ^{1}H decoupling was used during the sampling of the ^{13}C magnetization. A short π/2 pulse (5 μs) was applied, and the recycle delay was 4 s. About 20,000 scans were accumulated for each spectrum. Nitrogen and carbon dioxide physisorption measurements were performed with a Micromeritics ASAP 2020 physisorption analyzer at 77 K and 273 K, respectively. Prior to analysis, ca. 150 mg of each sample was degassed in vacuum for 4 h at 150 °C. For nitrogen physisorption, the surface area was calculated using the BET method,[19] and the pore volumes were calculated using the BJH method.[20] For carbon dioxide physisorption, the pore volume was calculated using the DFT method.[21] FTIR spectra were collected on a Nicolet 8700 FTIR spectrometer with a MCT/A detector. For each spectrum, 64 scans were recorded at a resolution of 4 cm^{-1}. Each carbon sample was mixed with KBr at 1 wt%, pressed into a self-supported wafer and loaded into a vacuum transmission FTIR

chamber. The spectra were taken under vacuum (<10^{-6} mbar). All carbon samples and cellulose were sent to Atlantic Microlab for elemental analysis to determine their sulfur and carbon contents. Boehm titration was performed following the procedures as reported in literature to quantify the amount of functional groups present.[18, 22-23] Briefly, 1.5 g of each carbon sample was added to 50 ml of aqueous solutions of NaOH, $NaHCO_3$ and Na_2CO_3, respectively. Each base solution had a concentration of 0.05 M. The slurries were shaken for 24 h, filtered, and 10 ml aliquots of the filtrate were collected. For the $NaHCO_3$ and NaOH solutions, 20 ml of 0.05 M HCl_{aq} was added. For the Na_2CO_3 solution, 30 ml of 0.05 M of HCl_{aq} was added. The solutions were purged with N_2 for 2 h and back titrated with 0.05 M solution of NaOH until an endpoint of pH 7.0 was reached. The pH of each carbon catalyst (300 mg) was measured in 27 ml of DI water after 1 h of stirring. During stirring, the suspension was degassed with nitrogen. The pH of acetic acid (3.8 mM) and sulfuric acid (1.8 mM) was also measured. The weight average molecular weight (M_w) and number average molecular weight (M_n) of cellulose and ball-milled cellulose samples were determined by gel permeation chromatography (GPC). This was accomplished by derivatization of the cellulose samples using pyridine and phenyl isocyanate and characterization with Waters GPC system. The weight-average and number-average degree of polymerization (DP_w, DP_n) of the cellulose were obtained by dividing M_w and M_n by 519, the molecular weight of the cellulose tricarbanilate monomer. The molecular weight of the derivatized cellulose samples was determined by using a relative calibration curve. The calibration curve was created by fitting a 3rd polynomial equation to the retention volumes obtained from a series of narrow molecular weight distribution polystyrene standards. The curve fit had an R^2 value of 0.9984.

3.2.4 Hydrolysis of cellulose

As a pretreatment, a batch of 20 g of cellulose was ball-milled in a rotary mill for 48 h at room temperature. The hydrolysis of ball-milled microcrystalline cellulose was

carried out in a 100 ml stirred reactor (Parr Instrument). The catalyst (0.300 g), cellulose (0.270 g) and DI water (27 ml) were loaded into the vessel and heated to 150 °C. The mixture was continuously stirred at 500 rpm. After reaction, the aqueous phase was analyzed by HPLC-RID (Agilent 1260 Infinity HPLC with a Grace Davison Prevail Carbohydrate ES column) to determine the yield of glucose using the same method as for the adsorption isotherms. Conversion of cellulose was determined by mass difference before and after reaction. For this purpose, the samples were dried at room temperature for 12 h, and it was assumed that the mass of the catalyst remained constant during the reaction.

3.2.5 Adsorption isotherms

Standard glucose solutions were prepared in various concentrations (0.05 M, 0.1 M, 0.15 M, 0.2 M, 0.3 M, 0.4 M, 0.5 M and 0.6 M). Standard cellobiose solutions were also prepared in various concentrations (0.01 M, 0.02 M, 0.03 M, 0.04 M, 0.06 M, 0.08 M, 0.10 M and 0.12 M). Pre-weighed amounts of carbon catalysts (ca. 40 mg) were mixed with 1.000 ml of sugar solution in 1.5 ml microcentrifuge tubes, vortexed for 30 s, and placed on a shaker table for 24 h. The slurries were then centrifuged for 10 min at 10,000 rcf. The supernatant was removed and analyzed by a high-performance liquid chromatography (HPLC) using a refractive index detector (RID) to determine the concentration of the sugar molecules. Accurate concentrations were determined based on an eight-point calibration curve. HPLC-RID analysis was performed on an Agilent 1260 Infinity HPLC using a Grace Davison Prevail Carbohydrate ES column. The mobile phase consisted of 75 vol% acetonitrile and 25 vol% water. The flow rate was 1.0 ml/min and the injection volume was 0.6 µl. The uptake was calculated using $q=(V(C_0-C_e))/m_{cat}$, where q is the specific uptake (mol/g), V is the volume of sugar solution used (L), C_0 and C_e are the initial and equilibrium concentration of the sugar solution, respectively (mol/L), and m_{cat} is the mass of carbon material used (g). Three isotherms were obtained

for each molecule on each adsorbent. For each isotherm, the Langmuir isotherm parameters were determined via linear regression (see Supporting Information).

3.3 Results

3.3.1 Characterization

The Raman spectra of all carbon catalysts contained two complex peaks at 1352 cm^{-1} and 1598 cm^{-1}, respectively (Figure 3.1). These are associated with the vibrational modes of disordered and ordered graphene sheets.[24] However, due to the presence of various contributions, the spectra needed to be deconvoluted to obtain the proper structural information (Figure 3.1). The two peaks were fitted with four Lorentzian-shaped bands (D4, D1, G and D2) at 1210 cm^{-1}, 1350 cm^{-1}, 1575 cm^{-1} and 1600 cm^{-1}, respectively, and one Gaussian-shaped band (D3) at 1530 cm^{-1}.[25-26] These five components are assigned as polyenes, graphene edges, graphitic carbon, graphene sheets, and amorphous carbon, respectively.

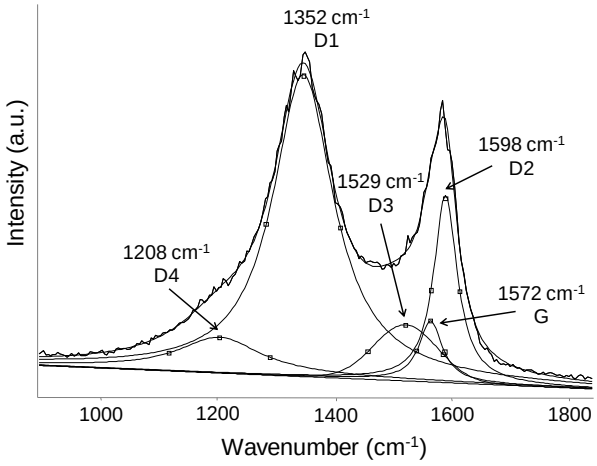

Figure 3.1 Raman spectrum and results from fitting for AC.

Table 3.1 Degree of graphitization of carbon catalysts.

Catalyst	$I_{D1}/(I_G+I_{D1}+I_{D2})$
AC	0.745
ACOH	0.746
SACOH	0.733
SAC100	0.729
SAC200	0.715

It has been suggested that the ratio $I_{D1}/(I_G+I_{D1}+I_{D2})$ is a measure of the degree of graphitization for carbonaceous materials, where I is the integral of the fitted peak.[26-27] The parameter was averaged over three spectra for each sample and is shown in Table 3.1. The highest values (i.e. most organized structures) were observed for AC and ACOH, indicating that the treatment of H_2O_2 did not affect the structural integrity of the sample. Samples treated with H_2SO_4 at 100 °C (SACOH and SAC100) had a lower degree of graphitization, while SAC200 had the least organized structure as it was subjected to a more severe treatment. The disorder of the graphene sheets is related to the abundance of edges.[25] Consequently, it is suggested that H_2SO_4 is able to break down the stacks of graphene sheets and to create step sites at the edge or cavities and that this effect is more pronounced at higher temperatures. The absence of a broad peak at 500 cm^{-1} indicates that amorphous sp^3 carbon is not present to a significant extent (Figure B.1).[28]

All XRD patterns of the carbon catalysts exhibited two broad peaks at 2θ angles of 24° and 42° (Figure B.2), which are attributed to the (002) and (100) or (101) planes of graphite crystallites, respectively.[29-30] This shows that the chemical treatments with H_2O_2 or H_2SO_4 did not change the crystallinity of the carbon structure compared to AC to measurable extent.

Figure B.3 shows the ^{13}C DP MAS NMR spectra for the carbon samples. The intense and broad peak at 119 ppm is assigned to non-protonated polyaromatic carbon in the core structure.[31] The network of activated carbon is highly complex. As such, the broad peak also contains contributions from exterior carbon species that have a chemical shift ranging between 110 ppm and 148 ppm.[32] Due to the large range of polyaromatic

carbon present, the shoulder due to carboxylic and phenolic carbon species at 180 ppm and 155 ppm can barely be observed. In addition, the low intensity of sp^3-hybridized carbon (0-40 ppm) suggests that most of the carbon is polyaromatic and sp^2-hybridized. Deconvolution was attempted, but the resolution of the spectrum was not sufficient for obtaining reliable results.

Table 3.2 shows the morphological properties of the carbon catalysts. Treatments with H_2O_2 and H_2SO_4 had a moderate effect on the surface area of the carbon catalysts. Figure 3.2 shows the pore volume distribution of the carbon catalysts obtained by both CO_2 and N_2 physisorption. AC oxidized by H_2O_2 showed a decrease in pore volume in the small pore size range (Figure 3.2A), while there was an increase in pore volume in the larger pore size range (Figure 3.2B). Treatment with H_2SO_4 after H_2O_2 (SACOH) showed an increase in pore volume as compared to ACOH. In addition, there was an increase in pore volume for pore sizes around 5 nm. Acidification by H_2SO_4 at 100 °C (SAC100) did not change the pore volume distribution, while acidification at 200 °C (SAC200) decreased the contribution of pores in the larger size range. The pore surface area of the samples showed similar trends (Table B.1).

Table 3.2 Surface area, concentration of stable acid sites, and catalytic activity of carbon catalysts.

Catalyst	S_{BET} (m^2/g)	Phenolic[a] (μmol/g)	Lactonic[a] (μmol/g)	Carboxylic acid + Sulfonic acid[a] (μmol/g)	Sulfonic acid[b] (μmol/g)	Conversion[c] (%)	Glucose Yield[c] (%)
Distilled water	-	-	-	-	-	24.1	0
AC	613	39	58	34	0	26.7	0
ACOH	634	281	252	244	0	26.3	2.1
SACOH	695	233	285	341	31	37.8	10.0
SAC100	595	152	115	147	144	32.2	8.4
SAC200	653	160	139	163	153	34.1	10.0
3.8 mM acetic acid	-	-	-	-	-	23.3	9.6
1.8 mM H_2SO_4	-	-	-	-	-	34.1	17.8

a: Determined by Boehm titration
b: Determined by elemental analysis (S content)
c: Reaction time of 24 h at 150 °C and autogenic pressure

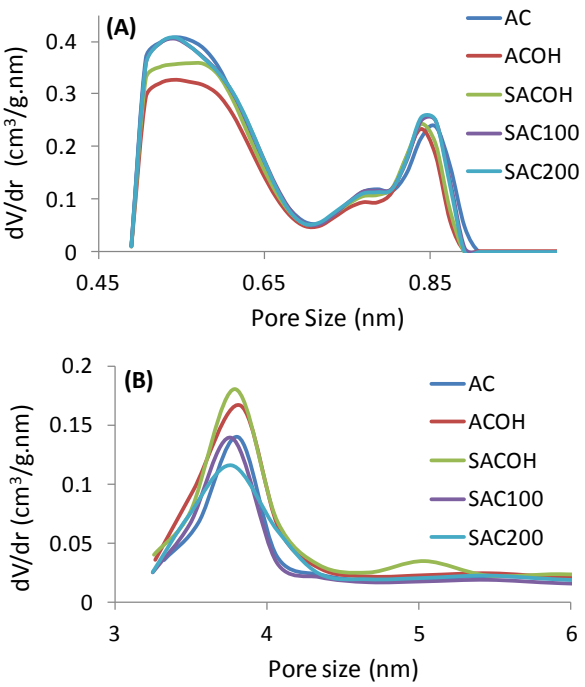

Figure 3.2 Pore size distribution of carbon catalysts (A) 0.45 nm to 1.00 nm determined by CO_2 physisorption, (B) 3 to 6 nm determined by N_2 physisorption.

FTIR spectra were obtained to identify the types of functional groups present on the carbon samples (Figure 3.3). All samples displayed a band at 1580 cm^{-1} that is assigned to the in-plane vibration of sp^2-hybridized carbon (i.e. C=C).[33] The broad features at 1260 cm^{-1} and 1020 cm^{-1} correspond to aromatic δCH.[34] For samples treated with H_2O_2 (Fig. 3.3b and 3.3e), a peak at 1720 cm^{-1} indicated the presence of carbonyls (νC=O). For SAC100 and SAC200 (Figure 3.3c and 3.3d), a broad shoulder was observed at 1109 cm^{-1}, which is assigned as the $\nu_{sym}SO_3$ for ionic sulfates, while the $\nu_{asym}SO_3$ vibration overlapped with the aromatic δCH vibration at ~1230 cm^{-1}.[35] Although this peak was observed for SACOH (Figure 3.3e), it had a low intensity. These results show that different functional groups were successfully imparted to the carbon structure by different chemical treatment.

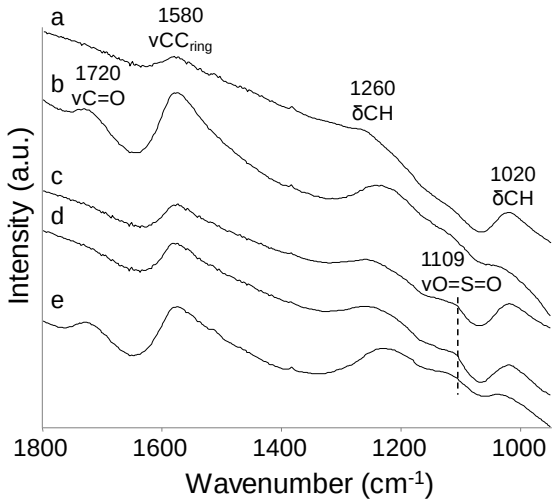

Figure 3.3 FTIR spectra of (a) AC, (b) ACOH, (c) SAC100, (d) SAC200, (e) SACOH.

For quantitative analysis, only functional groups that were stable for 24 h in liquid water at 150 °C were considered. For ACOH, chemical oxidation by H_2O_2 imparted phenolic, lactonic and carboxylic acid groups (Table 3.2). Sequential treatment with H_2O_2 and H_2SO_4 (SACOH) only imparted a small concentration of sulfonic acid groups (31 μmol/g). However, there was an increase in the concentration of lactonic and carboxylic acid groups, and a decrease in phenolic groups. Acidification by H_2SO_4 at 100 °C functionalized the carbon surface mainly with phenolic, lactonic and sulfonic acid groups. At a higher temperature treatment (SAC200), more of these functional groups are present on the surface. For reference, the concentration of sulfonic acid groups before hot liquid water treatment was also quantified (Table B.2).

Table 3.3 shows the pH of the carbon catalysts (300 mg) suspended in 27 ml of DI water as well as 3.8 mM acetic acid and 1.8 mM sulfuric acid. AC displayed the highest pH of 8.4 due to the presence of base sites.[18] Suspension of chemically treated carbon displayed a pH between 4.4 and 5.0, while acetic acid and sulfuric acid had a pH of 3.7 and 2.8, respectively.

Table 3.3 pH of slurries of 300 mg of each catalyst in 27 ml of water and homogeneous acid solutions used as references.

Catalyst	pH
AC	8.0
ACOH	5.0
SACOH	4.3
SAC100	4.5
SAC200	4.4
3.8 mM acetic acid	3.7
1.8 mM sulfuric acid	2.8

3.3.2 Hydrolysis of cellulose

Hydrolysis experiments were performed with cellulose that was ball-milled for 48 h to reduce its crystallinity (Figure B.4). The resulting material had a slightly lower degree of polymerization (Table B.3), and part of it was soluble in water.[36] The AC catalyst gave 27% conversion and 0% glucose yield after 24 h of reaction (Table 3.2). ACOH provided a similar conversion but had a higher glucose yield of 2%. SACOH showed the highest conversion of 38% and a glucose yield of 10%. SAC100 gave a glucose yield of 8%, while SAC200 had higher reactivity with a glucose yield of 10%, similar to SACOH. The rest of the products were mainly oligomers, which could not be quantified with the analytical setup used here.

For comparison, 27 ml of 3.8 mM acetic acid, which has the same amount of carboxylic acids as SACOH (300 mg), was used in the hydrolysis of cellulose. The glucose yield (10%) was comparable to SACOH and SAC200. In addition, 1.8 mM of H_2SO_4 was used for comparison, because it has the same concentration of sulfate groups as SAC200. The catalyst exhibited the highest glucose yield of 18%.

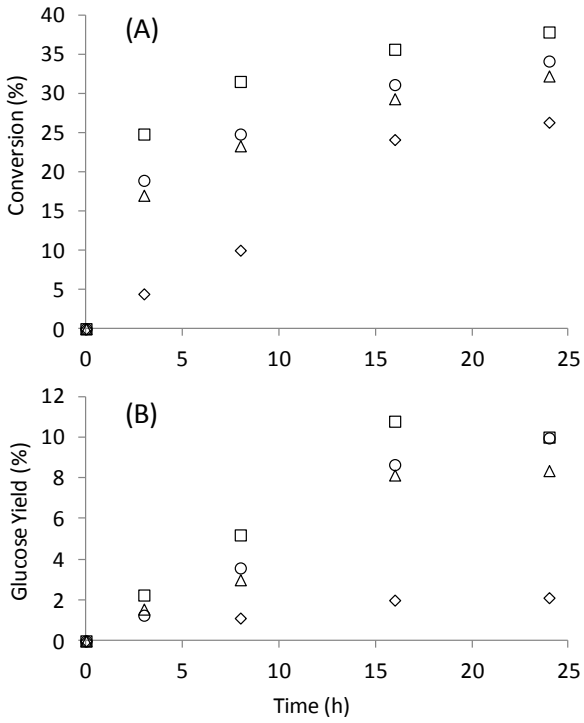

Figure 3.4 (A) Conversion and (B) glucose yield during cellulose hydrolysis at 150 °C using chemically treated carbon catalysts: (◊) ACOH, (□) SACOH, (Δ) SAC100, (○) SAC200.

The hydrolysis reactions for the carbon catalysts were also carried out over various periods of time (Figure 3.4). SACOH exhibits the highest reactivity, followed by SAC200, SAC100 and ACOH. The conversion of cellulose and the glucose yield increased significantly over the first 16 h. For the next 8 h, the glucose yield remained about the same, while the increase in conversion was not substantial. These trends are consistent with reports in literature, which indicated that a plateau is reached for the hydrolysis of cellulose using acidified carbon catalysts.[5, 7-8] This suggests that the remaining cellulose could have a recalcitrant structure that is resistant to hydrolysis by activated carbon.[5] Reactions with acetic acid and sulfuric acid also did not show a net degradation of glucose after 24 h (Figure B.5).

3.3.3 Adsorption isotherms

To understand how different functional groups on the same carbon substrate influence the adsorption of glucan molecules, adsorption isotherms of glucose and cellobiose were measured. An example of adsorption isotherms on AC is shown in Figure 3.5. The maximum uptake values in triplicate experiments were within 10% of each other for the same adsorbent and adsorbate, and all of the R^2 values were at least 0.95. Adsorption coefficients are within 12-48%. The average maximum uptake (q_m) was normalized by the Brunauer-Emmett-Teller (BET) specific surface area of each adsorbent so that comparison between adsorbents can be made. The values of the parameters are summarized in Table 3.4.

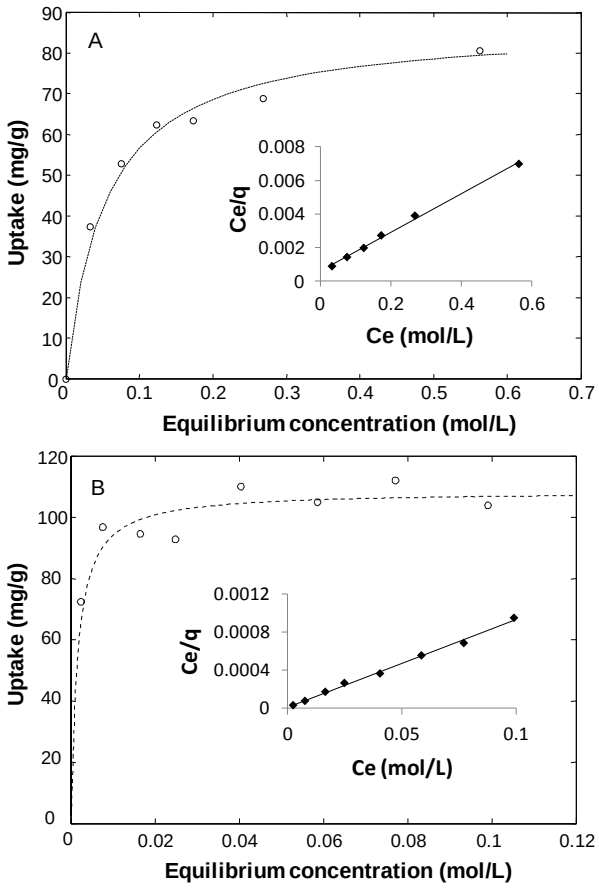

Figure 3.5 Adsorption isotherm of (A) glucose, (B) cellobiose on AC. Insets: Linear regression of Langmuir isotherm parameters.

The adsorption coefficient (K) of glucose on AC was 37 L/mol. When cellobiose was adsorbed on AC, it increased significantly to 650 L/mol. However, when the bare carbon material was functionalized, the adsorption coefficients decreased notably. For the adsorption of glucose, K decreased by about 60% for the functionalized materials compared to AC. For the adsorption of cellobiose, K also decreased, but the decrease was only about 40%. The change in standard free energy of adsorption (ΔΔG) between the adsorption of cellobiose and glucose was also calculated for each adsorbent (see Supporting Information and Table 3.4). For AC, it had a negative ΔΔG value of -1.78 kcal/mol. For the functionalized carbon materials, the value of ΔΔG decreased further to between -1.94 kcal/mol and -2.13 kcal/mol. The normalized q_m of AC for the adsorption of glucose is 0.135 mg/m^2. This increased to around 0.17 mg/m^2 for ACOH and SACOH, and 0.20 mg/m^2 for SAC100 and SAC200. However, the normalized q_m for the adsorption of cellobiose did not increase significantly relative to AC. The fractional increase was only 9-17%.

Table 3.4 Langmuir constants of glucose and cellobiose, and change in standard of free energy of adsorption between cellobiose and glucose.

	Langmuir Constants				
	Glucose		Cellobiose		
Adsorbent	Normalized q_m (mg/m^2)	K (L/mol)	Normalized q_m (mg/m^2)	K (L/mol)	ΔΔG (kcal/mol)
AC	0.135	37 ± 18	0.171	650 ± 9	-1.78 ± 0.33
ACOH	0.178	13 ± 1	0.187	379 ± 175	-1.94 ± 0.38
SACOH	0.173	14 ± 1	0.187	437 ± 53	-2.03 ± 0.13
SAC100	0.192	11 ± 2	0.200	393 ± 53	-2.11 ± 0.17
SAC200	0.201	16 ± 4	0.200	402 ± 59	-2.13 ± 0.58

q_m (mg/g): maximum uptake, K (L/mol): adsorption coefficient

3.4 Discussion

3.4.1 Effects of chemical oxidation on activated carbon

Chemical oxidation is a common approach to tailor the functionality of activated carbon catalysts.[18] Methods for modifying activated carbon include acid, base, microwave, ozone and plasma treatments.[37] These methods are usually used to enhance the adsorption of organic and inorganic pollutants. It is commonly known that oxidative modifications lead to decreases in surface area and pore volume.[37-39] Most studies in literature are only focused on quantifying the number of functional groups on carbon catalysts and correlating it to reactivity.[7-9, 40-41] In contrast, the effect of chemical treatment on the structure of carbon has not been extensively studied.

In the present study, FTIR and Boehm titration results demonstrated that oxidation by H_2O_2 functionalized the surface with phenolic, lactonic and carboxylic acid groups for ACOH, while treatment with H_2SO_4 imparts phenolic, lactonic and sulfonic acid groups (SAC100). Acidification at a higher temperature of 200 °C resulted in the presence of more functional groups. In the case of SACOH, only a small concentration of hydrothermally stable sulfonic groups (31 μmol/g) were retained on the surface after treatment in liquid water at 150 °C. Prior to the elution step, 150 μmol/g of sulfonic acid group was present on the sample (Table B.2). In agreement with previous studies, we propose that the treatment with H_2O_2 results in oxidation of sites with unsaturated and dangling bonds terminating with CH or CH_2 groups.[30, 42] It is suggested that this is followed by chemical reactions at the hexatomic-hexatomic boundaries, generating new defects after the initial points of attack are functionalized. This suggests that the second chemical treatment with H_2SO_4 results in sulfonic groups occupying newly generated sites, which are easier to elude. It is speculated that the functional groups present from the first treatment could create reactive environment on the carbon surface that are

converted to porous domains during the acidification with H_2SO_4, resulting in a slightly higher surface area for SACOH.

XRD results showed no noticeable effect of treatments with H_2O_2 and H_2SO_4 on the limited crystallinity of the activated carbon. However, the pore size distribution indicated that oxidation by H_2O_2 decreased the pore volume of the carbon material (ACOH) in the small pore size range, but the pore volume in the larger pore size range increased (Figure 3.2). This suggests that oxidation by H_2O_2 enlarges at least some of the pores of the activated carbon. Generally, two routes are possible: an attack on existing defect sites, and electrophilic addition on unsaturated C=C bonds.[43] However, Raman spectroscopy results (Table 3.1) showed that the degree of graphitization for ACOH remains the same as AC. This implies that the ratio of graphene edges to graphitic carbon and graphene sheets is largely the same, suggesting that the material that is removed or redistributed could be amorphous in nature.

In the case of SACOH, acidification with H_2SO_4 after H_2O_2 treatment increased the pore volume for existing pore sizes relative to ACOH (Figure 3.2), while the degree of graphitization decreased (Table 3.1). SAC100 had a similar pore size distribution to AC, but the degree of graphitization was also lower compared to AC, indicating that acidification with H_2SO_4 at 100 °C seems to create more edges in the carbon structure. This effect is more pronounced at a higher temperature treatment as indicated by the observation of the lowest degree of graphitization for SAC200. This observation is in agreement with a previous study that showed that intercalated sulfuric acid can exfoliate the structure and attack the active sites of carbons at temperatures higher than 100 °C.[44]

Results from ^{13}C DP MAS NMR showed that a large range of polyaromatic carbon species was present in the materials, and most of the carbon in the structure is sp^2 hybridized. In addition, the absence of a peak between 400-500 cm^{-1} in the Raman spectra of all the samples (Figure B.1) also indicated that amorphous sp^3 hybridized carbon is not present in significant amounts.[28] This suggests that the functional groups

that are imparted would have to be positioned around the edges and defect sites of the carbon structure, and in the same plane as the graphene sheet.[33, 42, 45] Specifically, the functional groups are not positioned perpendicularly to the surface limiting their accessibility for glucan chains. Figure 6 shows a simple schematic representation of the structures formed in the chemical oxidation process that can occur at the edge or existing defect sites of a graphene sheet. An aromatic or unsaturated C=C bond can be attacked by a reagent to produce a hydroxyl group.[42] The latter can be oxidized to form a quinone group, or broken up to form carboxylic acid group in the presence of a strong oxidizing agent. In close proximity, a hydroxyl group and a carboxyl or carbonyl group can condense to form a lactone.[45]

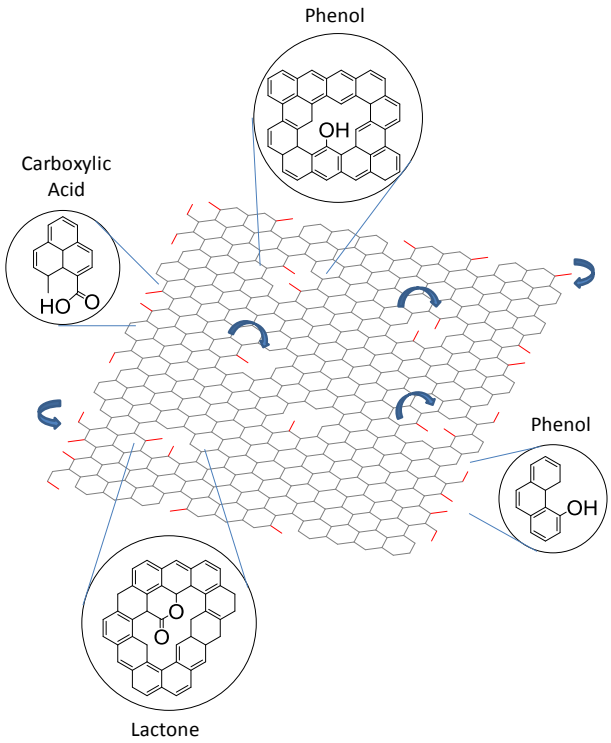

Figure 3.6 Schematic representation of the structure of functionalized carbon.

3.4.2 Adsorption properties and locality of functional groups

In studies on the hydrolysis of cellulose using functionalized amorphous carbon, it has been claimed that phenolic groups on carbon form hydrogen bonds with the oxygen atoms in glucan chains, while carboxylic and sulfonic acid groups do not function as adsorption sites.[7-8] However, this conclusion was based on the comparison between different types of catalysts, such as Nafion, niobic acid and Amberlyst-15, and these materials also differ in other properties.

In this study, adsorption isotherms revealed that all of the carbon materials are able to adsorb both glucose and cellobiose (Table 3.4). Activated carbon (AC) is commonly considered a good sorbent for biomass molecules due to its large surface area and pore volume.[46-47] The adsorption process is driven by van der Waals forces between glucans and the carbon surface.[17] Specifically, it is the interaction between CH groups and the polyaromatic rings.[48-50] The adsorption of glucose on AC had an adsorption coefficient of 37 L/mol. However, functionalization of AC reduced the adsorption coefficient of glucose by about 60% compared to AC. The large decrease is attributed to competitive adsorption with water, which becomes more pronounced as the polarity of the surface increases.

The larger number of CH groups in cellobiose resulted in an increase of the adsorption coefficient on AC to 650 L/mol. This is attributed to additional van der Waals interactions with the carbon surface. In the case of the functionalized materials, the adsorption coefficients also decreased, but the decrease was less pronounced (40%) compared to the adsorption of glucose. This suggests that the stronger van der Waals interaction allow cellobiose to compete more favorably with water for adsorption sites, even on a relatively polar surface. By extrapolation from the adsorption of glucose and cellobiose, the adsorption coefficients would also increase with the length of the glucan chain, suggesting that functionalization of the carbon surface has a limited impact on the adsorption of oligomeric species, whereas adsorption of monomeric glucose is reduced

by competition with water. This could explain the limited degradation of glucose monomers in the hydrolysis of cellulose over sulfonated activated carbon.[5]

The preference for adsorption of oligomers can be further illustrated by comparison of the change in standard free energy of adsorption between cellobiose and glucose ($\Delta\Delta G$). The value for AC was calculated to be -1.78 kcal/mol, which is close to the value of -1.4 kcal/mol obtained by Chung et al. for mesoporous carbon nanoparticles.[17] For the functionalized materials, the values of $\Delta\Delta G$ decreased further by up to 0.3 kcal/mol indicating an increase of the preference for the adsorption of cellobiose. Since this decrease in free energy of adsorption is small compared to the strength of a hydrogen bond,[51] it is suggested that interactions with functional groups are not responsible for the difference in adsorption between cellobiose and glucose. Besides solvation, $\Delta\Delta G$ also depends on the degree of contact on the molecular level.[17] We speculate that the defect sites that are formed during the chemical treatment of AC provide a spatial environment that favors the adsorption of cellobiose over glucose.

An increased uptake of glucose monomers was observed on functionalized materials compared to AC. One possible explanation is that glucose molecules are adsorbed in an orientation with a smaller footprint on defect sites. It is also interesting to note that SACOH has the same normalized adsorption capacity as ACOH even though it has more functional groups. Since the functional groups are located at the edge or defect sites of the graphene sheets (vide supra), this would suggests that they are localized in cavities of the carbon structure. Thus, in the case of SACOH, its cavities or edges would have a higher density of functional groups compared to ACOH, and there is a limit on the amount of biomass molecules that can be adsorbed in these cavities due to spatial limitation.

A recent report by Fukuoka and co-workers demonstrated that oxygenated functional groups on carbon do not affect the adsorption capacity of glucans, and there was no difference in adsorption coefficient.[48] However, the functional groups were

removed by heat treatment up to 1273 K, and this method has been shown to also increase the cross-linking of carbon sheets, which could result in a more uniform polyaromatic surface for adsorption.[6, 11] Thus, it is challenging to attribute the observed behavior to a single factor.

3.4.3 Mechanism of cellulose hydrolysis

Reports in literature have shown that weakly acidic functional groups such as hydroxyl and carboxylic acids on other types of catalysts (niobic acid and Amberlyst) are not active in the hydrolysis of cellulose.[7-8] However, when positioned on a carbon surface, these weak functional groups are able to catalyze the hydrolysis of carbohydrates if the glycosidic bonds are forced to interact with these groups.[12-16] In this study, reactivity results show that only the chemically treated carbon materials yield glucose (Table 3.2). Since no glucose is formed over AC, the weak catalytic activity of ACOH can be ascribed to the addition of the functional groups (i.e. phenolic, lactonic and carboxylic acid groups). However, the presence of these groups alone provides limited reactivity. The higher catalytic activity of SAC100 and SAC200 could be attributed to the formation of sulfonic acid groups. However, the catalytic activity of SACOH is comparable to SAC200 even though it only has a low concentration of sulfonic groups. In addition, SACOH only had 14.5% more functional groups than ACOH, but its glucose yield was about five times higher.

The improvement in catalytic activity for SACOH can be correlated with the degree of graphitization as obtained by Raman spectroscopy (Table 3.1). Only treatment with H_2SO_4 decreased the degree of graphitization, and the latter decreased more at a higher treatment temperature. The disorder of the carbon structure is attributed to abundant edges.[25] Thus, we suggest that acidification with H_2SO_4 creates more steps in the cavities or edges of the carbon structure, and these types of defects have a synergistic effect with the in-plane functional groups (vide infra).

Kobayashi et al. ball-milled carbon and cellulose together, and the reactivity was higher compared to an experiment without ball-milling them together.[12] This suggests that intimate interaction between the reactant and catalyst is a prerequisite for hydrolysis. They also showed that salicylic acid, which contains adjacent carboxylic and phenolic groups, is more effective in the hydrolysis of cellobiose than other molecular catalysts such as m- and p-hydroxybenzoic acid, in which these functional groups are further apart. This illustrates the potential synergistic effects of a coordination site in close proximity to the active site. However, ACOH and SACOH have similar concentration of weak acid sites, and there is no reason to suggest a preferential formation of paired active sites in SACOH. Furthermore, the pH values of the aqueous slurry of SACOH and SAC200 were 4.3 and 4.4 respectively, which should not be acidic enough to catalyze the hydrolysis reaction. The pH values after reaction were within 0.1 of the original values, indicating that the functional groups are stable, which is in agreement with a previous report.[18] It was proposed that a pH lower than 4 is needed for this reaction.[52] However, the environment within the vicinity of a sulfonic acid group should still be acidic enough for the reaction to occur. Moreover, the pH values of acetic acid and sulfuric acid used are 3.7 and 2.8 respectively, yet the reactivity of acetic acid did not exceed that of SACOH and SAC200 (Table 3.2). The slurries of the other carbon catalysts had a higher pH due to the existence of base sites and the delocalization of charge across the basal plane of the carbon surface.[53]

Yanovsky simulated the adsorption of organic polymer chains on different carbon surfaces (with and without defects) and demonstrated that adsorption on a carbon surface with defects is energetically more favorable and that the chains are immobilized in this environment.[54] Furthermore, Gazit et al. demonstrated that weakly acidic hydroxyl groups on silica and alumina are able to hydrolyze the β glycosidic bonds by grafting glucan strands on the surface.[16] This indicates that weakly acidic functional groups are able to carry out hydrolysis when they are interacting with a glucan chain in a constraint

position. This conclusion is in agreement with a report that conformational changes in the cellulosic chains are required for the activation of the glycosidic bond for hydrolysis.[55]

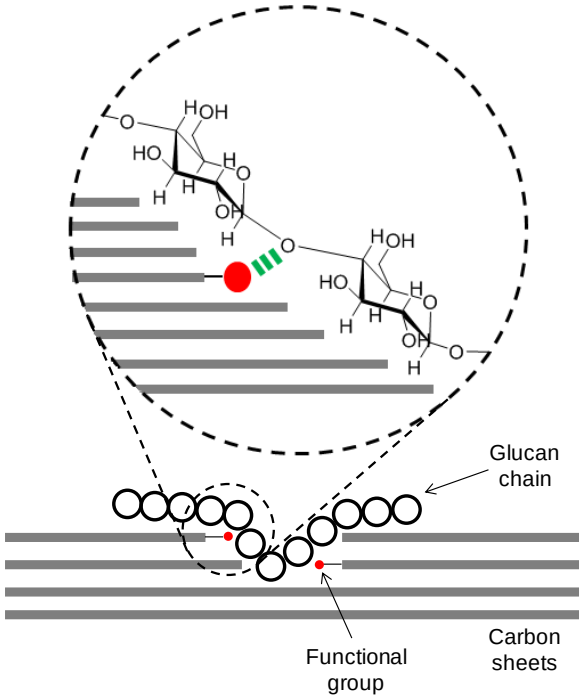

Figure 3.7 Schematic representation of the adsorption and hydrolysis mechanism.

Based on the above findings, it is proposed that the adsorption of glucan chains on defect sites or edges is critical for catalytic activity because a conformational change is induced in this environment. This enables the in-plane functional groups to attack the exposed glycosidic bonds. Figure 3.7 shows a schematic representation of the adsorption and hydrolysis process. The analysis of the adsorption isotherms indicates that interactions between the CH groups and polycyclic aromatic rings are responsible for the immobilization of long glucan chains on defect sites. As the functional groups are localized, the probability of hydrolysis increases with the density of functional groups in each defect site. Glucan chains can also adsorb on polyaromatic domains of the carbon

surface. However, we speculate that these species are much less susceptible to the hydrolysis reaction due to the lack of appropriately positioned functional groups.

In a related report, Pang et al. sulfonated carbon at elevated temperatures and reported higher catalytic activity even though the increase in acid density was not significant.[9] However, beyond a sulfonation temperature of 250 °C, the catalytic activity dropped slightly while the acid site density continued to increase. In the present study, it was found that the degree of graphitization decreases with increasing sulfonation temperature. In addition, the creation of defects and edges in the carbon structure facilitates the hydrolysis of cellulose via conformation change upon adsorption. We hypothesize that an increase of the sulfonation temperature above 250 °C leads to severe degradation of the carbon structure, which becomes less useful as the defects created could be too large for any effective conformation change of the glucan chain to occur. Chung et al. also reported that there was no proportional correlation between phenolic groups and yield for sulfonated and unsulfonated carbon material in the hydrolysis of miscanthus xylan.[13] This further supports the hypothesis that both functional group and defect site are needed for hydrolysis of glucan chains to occur effectively.

3.5 Conclusions

The effect of chemical oxidation on activated carbon was investigated. A simple chemical treatment with H_2O_2 can enlarge pore size while imparting hydrophilic functional groups such as phenols, lactones and carboxylic acids. Treatment with H_2SO_4 decreases the order of graphitization by etching the edges of the carbon structure and this effect scales with temperature. Only phenols, lactones and sulfonic groups are functionalized on the carbon material. Extrapolation of the results from adsorption isotherms shows that the functional groups only have a minor effect on the adsorption of long chain oligomers, which is dominated by van der Waals between CH groups of the

sorbate and the surface. The chemically treated materials are more active in the hydrolysis of cellulose compared to homogenous catalysts even though they possess weakly acidic functional groups. This can be explained by the synergistic effect of functional groups and defect sites and edges of the carbon surface, where the glycosidic bonds are exposed and forced to interact with the in-plane functional groups.

3.6 References

1. Huber, G. W.; Iborra, S.; Corma, A. Synthesis of transportation fuels from biomass: Chemistry, catalysts, and engineering. *Chem. Rev.* **2006,** *106*, 4044-4098.

2. Ragauskas, A. J.; Williams, C. K.; Davison, B. H.; Britovsek, G.; Cairney, J.; Eckert, C. A.; Frederick, W. J.; Hallett, J. P.; Leak, D. J.; Liotta, C. L.; Mielenz, J. R.; Murphy, R.; Templer, R.; Tschaplinski, T. The path forward for biofuels and biomaterials. *Science* **2006,** *311*, 484-489.

3. Harris, E. E.; Beglinger, E.; Hajny, G. J.; Sherrard, E. C. Hydrolysis of Wood - Treatment with Sulfuric Acid in a Stationary Digestor. *Ind. Eng. Chem.* **1945,** *37*, 12-23.

4. Harris, E. E.; Beglinger, E. Madison Wood Sugar Process. *Ind. Eng. Chem.* **1946,** *38*, 890-895.

5. Onda, A. Selective Hydrolysis of Cellulose and Polysaccharides into Sugars by Catalytic Hydrothermal Method Using Sulfonated Activated-carbon. *J. Jpn. Pet. Inst* **2012,** *55*, 73-86.

6. Nakajima, K.; Hara, M. Amorphous Carbon with SO3H Groups as a Solid Bronsted Acid Catalyst. *ACS Catal.* **2012,** *2*, 1296-1304.

7. Kitano, M.; Yamaguchi, D.; Suganuma, S.; Nakajima, K.; Kato, H.; Hayashi, S.; Hara, M. Adsorption-Enhanced Hydrolysis of β-1,4-Glucan on Graphene-Based Amorphous Carbon Bearing SO3H, COOH, and OH Groups. *Langmuir* **2009,** *25*, 5068-5075.

8. Suganuma, S.; Nakajima, K.; Kitano, M.; Yamaguchi, D.; Kato, H.; Hayashi, S.; Hara, M. Hydrolysis of cellulose by amorphous carbon bearing SO3H, COOH, and OH groups. *J. Am. Chem. Soc.* **2008,** *130*, 12787-12793.

9. Pang, J. F.; Wang, A. Q.; Zheng, M. Y.; Zhang, T. Hydrolysis of cellulose into glucose over carbons sulfonated at elevated temperatures. *Chem. Commun.* **2010,** *46*, 6935-6937.

10. Huang, Y.-B.; Fu, Y. Hydrolysis of cellulose to glucose by solid acid catalysts. *Green Chem.* **2013,** *15*, 1095-1111.

11. Fukuhara, K.; Nakajima, K.; Kitano, M.; Kato, H.; Hayashi, S.; Hara, M. Structure and Catalysis of Cellulose-Derived Amorphous Carbon Bearing SO3H Groups. *ChemSusChem* **2011,** *4*, 778-784.

12. Kobayashi, H.; Yabushita, M.; Komanoya, T.; Hara, K.; Fujita, I.; Fukuoka, A. High-Yielding One-Pot Synthesis of Glucose from Cellulose Using Simple Activated Carbons and Trace Hydrochloric Acid. *ACS Catal.* **2013,** *3*, 581-587.

13. Chung, P.-W.; Charmot, A.; Olatunji-Ojo, O. A.; Durkin, K. A.; Katz, A. Hydrolysis Catalysis of Miscanthus Xylan to Xylose Using Weak-Acid Surface Sites. *ACS Catal.* **2013,** *4*, 302-310.

14. Gazit, O. M.; Charmot, A.; Katz, A. Grafted cellulose strands on the surface of silica: effect of environment on reactivity. *Chem. Commun.* **2011,** *47*, 376-378.

15. Gazit, O. M.; Katz, A. Grafted Poly(1 -> 4-beta-glucan) Strands on Silica: A Comparative Study of Surface Reactivity as a Function of Grafting Density. *Langmuir* **2012,** *28*, 431-437.

16. Gazit, O. M.; Katz, A. Understanding the Role of Defect Sites in Glucan Hydrolysis on Surfaces. *J. Am. Chem. Soc.* **2013,** *135*, 4398-4402.

17. Chung, P.-W.; Charmot, A.; Gazit, O. M.; Katz, A. Glucan Adsorption on Mesoporous Carbon Nanoparticles: Effect of Chain Length and Internal Surface. *Langmuir* **2012,** *28*, 15222-15232.

18. Van Pelt, A. H.; Simakova, O. A.; Schimming, S. M.; Ewbank, J. L.; Foo, G. S.; Pidko, E. A.; Hensen, E. J. M.; Sievers, C. Stability of functionalized activated carbon in hot liquid water. *Carbon* **2014,** *77*, 143-154.

19. Brunauer, S.; Emmett, P. H.; Teller, E. Adsorption of gases in multimolecular layers. *J. Am. Chem. Soc.* **1938,** *60*, 309-319.

20. Barrett, E. P.; Joyner, L. G.; Halenda, P. P. The determination of pore volume and area distributions in porous substances .1. Computations from nitrogen isotherms. *J. Am. Chem. Soc.* **1951,** *73*, 373-380.

21. Lastoskie, C.; Gubbins, K. E.; Quirke, N. Pore-Size Distribution Analysis of Mircroporous Carbons - A Density-Functional Theory Approach. *J. Phys. Chem.* **1993,** *97*, 4786-4796.

22. Oickle, A. M.; Goertzen, S. L.; Hopper, K. R.; Abdalla, Y. O.; Andreas, H. A. Standardization of the Boehm titration: Part II. Method of agitation, effect of filtering and dilute titrant. *Carbon* **2010,** *48*, 3313-3322.

23. Goertzen, S. L.; Theriault, K. D.; Oickle, A. M.; Tarasuk, A. C.; Andreas, H. A. Standardization of the Boehm titration. Part I. CO2 expulsion and endpoint determination. *Carbon* **2010,** *48*, 1252-1261.

24. Ferrari, A. C.; Robertson, J. Interpretation of Raman spectra of disordered and amorphous carbon. *Phys. Rev. B* **2000,** *61*, 14095-14107.

25. Lezanska, M.; Pietrzyk, P.; Sojka, Z. Investigations into the Structure of Nitrogen-Containing CMK-3 and OCM-0.75 Carbon Replicas and the Nature of Surface Functional Groups by Spectroscopic and Sorption Techniques. *J. Phys. Chem. C* **2010,** *114*, 1208-1216.

26. Sadezky, A.; Muckenhuber, H.; Grothe, H.; Niessner, R.; Poschl, U. Raman micro spectroscopy of soot and related carbonaceous materials: Spectral analysis and structural information. *Carbon* **2005,** *43*, 1731-1742.

27. Beyssac, O.; Goffe, B.; Petitet, J. P.; Froigneux, E.; Moreau, M.; Rouzaud, J. N. On the characterization of disordered and heterogeneous carbonaceous materials by Raman spectroscopy. *Spectroc. Acta Pt. A-Molec. Biomolec. Spectr.* **2003,** *59*, 2267-2276.

28. Prawer, S.; Nugent, K. W.; Jamieson, D. N.; Orwa, J. O.; Bursill, L. A.; Peng, J. L. The Raman spectrum of nanocrystalline diamond. *Chem. Phys. Lett.* **2000,** *332*, 93-97.

29. Babu, V. S.; Seehra, M. S. Modeling of disorder and X-ray diffraction in coal-based graphitic carbons. *Carbon* **1996,** *34*, 1259-1265.

30. Manivannan, A.; Chirila, M.; Giles, N. C.; Seehra, M. S. Microstructure, dangling bonds and impurities in activated carbons. *Carbon* **1999,** *37*, 1741-1747.

31. Cheng, H. N.; Wartelle, L. H.; Klasson, K. T.; Edwards, J. C. Solid-state NMR and ESR studies of activated carbons produced from pecan shells. *Carbon* **2010,** *48*, 2455-2469.

32. Knicker, H.; Totsche, K. U.; Almendros, G.; Gonzalez-Vila, F. J. Condensation degree of burnt peat and plant residues and the reliability of solid-state VACP MAS C-13 NMR spectra obtained from pyrogenic humic material. *Org. Geochem.* **2005,** *36*, 1359-1377.

33. Su, C. L.; Acik, M.; Takai, K.; Lu, J.; Hao, S. J.; Zheng, Y.; Wu, P. P.; Bao, Q. L.; Enoki, T.; Chabal, Y. J.; Loh, K. P. Probing the catalytic activity of porous graphene oxide and the origin of this behaviour. *Nat. Commun.* **2012,** *3*.

34. Lennon, D.; Lundie, D. T.; Jackson, S. D.; Kelly, G. J.; Parker, S. F. Characterization of activated carbon using X-ray photoelectron spectroscopy and inelastic neutron scattering spectroscopy. *Langmuir* **2002,** *18*, 4667-4673.

35. Socrates, G., *Infrared and Raman Characteristic Group Frequencies*. Third ed.; John Wiley & Sons LTD: 2001;

36. Zhao, H. B.; Kwak, J. H.; Wang, Y.; Franz, J. A.; White, J. M.; Holladay, J. E. Effects of crystallinity on dilute acid hydrolysis of cellulose by cellulose ball-milling study. *Energy Fuels* **2006,** *20*, 807-811.

37. Bhatnagar, A.; Hogland, W.; Marques, M.; Sillanpaa, M. An overview of the modification methods of activated carbon for its water treatment applications. *Chem. Eng. J.* **2013,** *219*, 499-511.

38. Yu, G. X.; Jin, M.; Sun, J.; Zhou, X. L.; Chen, L. F.; Wang, J. A. Oxidative modifications of rice hull-based carbons for dibenzothiophene adsorptive removal. *Catal. Today* **2013,** *212*, 31-37.

39. Stavropoulos, G. G.; Samaras, P.; Sakellaropoulos, G. P. Effect of activated carbons modification on porosity, surface structure and phenol adsorption. *J. Hazard. Mater.* **2008,** *151*, 414-421.

40. Qi, X. H.; Guo, H. X.; Li, L. Y.; Smith, R. L. Acid-Catalyzed Dehydration of Fructose into 5-Hydroxymethylfurfural by Cellulose-Derived Amorphous Carbon. *ChemSusChem* **2012,** *5*, 2215-2220.

41. Chang, B. B.; Fu, J.; Tian, Y. L.; Dong, X. P. Multifunctionalized Ordered Mesoporous Carbon as an Efficient and Stable Solid Acid Catalyst for Biodiesel Preparation. *J. Phys. Chem. C* **2013,** *117*, 6252-6258.

42. Zhang, J.; Zou, H. L.; Qing, Q.; Yang, Y. L.; Li, Q. W.; Liu, Z. F.; Guo, X. Y.; Du, Z. L. Effect of chemical oxidation on the structure of single-walled carbon nanotubes. *J. Phys. Chem. B* **2003,** *107*, 3712-3718.

43. Li, W.; Bai, Y.; Zhang, Y. K.; Sun, M. L.; Cheng, R. M.; Xu, X. C.; Chen, Y. W.; Mo, Y. J. Effect of hydroxyl radical on the structure of multi-walled carbon nanotubes. *Synth. Met.* **2005,** *155*, 509-515.

44. Hong, Y.; Wang, Z.; Jin, X. Sulfuric Acid Intercalated Graphite Oxide for Graphene Preparation. *Sci. Rep.* **2013,** *3*.

45. Boehm, H. P. Some aspects of the surface chemistry of carbon blacks and other carbons. *Carbon* **1994,** *32*, 759-769.

46. Lee, J. W.; Kwon, T. O.; Moon, I. S. Adsorption of mono saccharides, disaccharides, and maltooligosaccharides on activated carbon for separation of maltopentaose. *Carbon* **2004,** *42*, 371-380.

47. Yoo, J. W.; Kim, T. Y.; Cho, S. Y.; Rho, S. G.; Kim, S. J. Separation characteristics of glucose and maltooligosaccharides in grannular activated carbon beds. *J. Ind. Eng. Chem.* **2004,** *10*, 257-266.

48. Yabushita, M.; Kobayashi, H.; Hasegawa, J.-y.; Hara, K.; Fukuoka, A. Entropically Favored Adsorption of Cellulosic Molecules onto Carbon Materials through Hydrophobic Functionalities. *ChemSusChem* **2014,** *7*, 1443-1450.

49. Kiehna, S. E.; Laughrey, Z. R.; Waters, M. L. Evaluation of a carbohydrate-pi interaction in a peptide model system. *Chem. Commun.* **2007**, 4026-4028.

50. Laughrey, Z. R.; Kiehna, S. E.; Riemen, A. J.; Waters, M. L. Carbohydrate−π Interactions: What Are They Worth? *J. Am. Chem. Soc.* **2008,** *130*, 14625-14633.

51. Sheu, S. Y.; Yang, D. Y.; Selzle, H. L.; Schlag, E. W. Energetics of hydrogen bonds in peptides. *Proc. Natl. Acad. Sci. U. S. A.* **2003,** *100*, 12683-12687.

52. Bobleter, O. Hydrothermal Degradation of Polymers Derived from Plants. *Progress in Polymer Science* **1994,** *19*, 797-841.

53. Leon y Leon, C. A.; Solar, J. M.; Calemma, V.; Radovic, L. R. Evidence for the protonation of basal plane sites on carbon. *Carbon* **1992,** *30*, 797-811.

54. Yanovsky, Y. G., *Nano-Modeling Structure and Micromechanical Properties of Mesoscopic Composite Systems*. Tsinghua University Press: Beijing, 2006;

55. Loerbroks, C.; Rinaldi, R.; Thiel, W. The Electronic Nature of the 1,4-beta-Glycosidic Bond and Its Chemical Environment: DFT Insights into Cellulose Chemistry. *Chem.-Eur. J.* **2013,** *19*, 16282-16294.

CHAPTER 4

HYDROLYSIS OF CELLOBIOSE OVER SELECTIVE AND STABLE SULFONATED ACTIVATED CARBON CATALYSTS

4.1 Background

Biomass is an important and renewable feedstock for the sustainable production of chemicals, fuels, and energy.[1] In particular, the depolymerization of biomass-derived polymers into monomers is crucial for its subsequent conversion into valuable chemicals.[2] The most abundant polymer in most types of biomass is cellulose. Cellulose is a recalcitrant material that is composed of glucose monomers linked by β-1,4-glycosidic bonds.[3] Hydrolysis of cellulose is an attractive method to produce glucose as a useful platform chemical that can be converted to 5-hydroxymethylfurfural (HMF) and levulinic acid using solid acid catalysts.[4] It was also reported that glucose can be converted to lactic acid and gluconic acid using supported metal catalysts in an alkaline solution.[5] Gluconic acid is used in the food and pharmaceutical industries. Additionally, the isomerization of glucose to fructose can be carried out over Lewis acidic zeolites followed by conversion to other useful products.[6] Furthermore, glucose can be fermented to obtain other important products such as succinic acid, 3-hydroxy propinoic acid, itaconic acid and glutamic acid.[7]

Enzymatic hydrolysis has received the most attention among the strategies for hydrolyzing cellulose to glucose.[8] However, the recalcitrance of feedstocks and the relatively low rates of such enzymatic reactions have limited the commercial potential of this approach. Cellulose can be hydrolyzed more rapidly using near critical or supercritical water[9-10] or strong Brønsted acid catalysts such as sulfuric acid, which are able to decompose the hydrogen bonds between the polymeric chains and the β-1,4-

glycosidic bonds between the glucose monomers.[11-14] However, such processes suffer from the formation of degradation products when the glucose remains exposed to the reaction medium and costly separation of the homogeneous reaction mixture. To a certain extent, the formation of degradation products can be reduced by limiting the residence time of the products in the reactor, but a certain part of the feedstock will be incompletely hydrolyzed to oligosaccharides if this strategy is applied.[14-15] Therefore, efforts have to be targeted towards increasing the yield of glucose so that the efficiency of these processes can be maximized.

It has been reported that sulfonated carbon is an effective and reusable catalyst for hydrolysis of cellulose and cellobiose.[16-22] However, most of these studies were performed using batch reactors. Studies using heterogeneous catalysts in flow reactors are needed to determine the feasibility of such a process on a large scale, at which flow reactors are expected to provide favorable process economics and improvements in yields.[23] Interestingly, weak acid sites on carbon such as carboxylic acid and phenol groups can also be active in the hydrolysis of carbohydrates.[15, 24] The reaction could even be induced by forced interactions between glycosidic oxygen atoms in glucan chains and weakly acidic hydroxyl groups on silica and alumina.[25-27] We recently showed that there is a substantial loss in total acid sites when sulfonated activated carbon is treated in hot liquid water between 150 °C and 225 °C, but the remaining surface functional groups after 12 h of treatment are stable.[28] In addition, it was demonstrated that these stable functional groups in synergy with defect sites created in the acidification process are effective sites for the hydrolysis of cellulose.[29] We rationalized that the adsorption of glucan chains on defect sites or the edges of the graphene sheets induces a conformational change of the glucan that allows an in-plane functional group of the catalyst to attack the exposed glycosidic bond. This enables even weak acid sites to participate in the hydrolysis reaction.[3]

However, a conundrum exists where acidification with sulfuric acid creates the needed defect sites but also imparts strongly acidic sulfonic acid groups on carbon. It is hypothesized that these strong acid sites may favor degradation reactions and, thus, have a negative impact on glucose yield in hydrolysis reactions. Figure 4.1 shows a typical degradation pathway for glucose. Cellobiose is the disaccharide of glucose and can be considered as representative model compound for glucose oligomers. By studying the hydrolysis of cellobiose in a well-defined feed stream, it is possible to gain insight into the impact of sulfonic acid groups in hydrolysis.

In this study, sulfonated activated carbon with different fractions of sulfonic acid groups were synthesized and characterized by various physicochemical techniques. The catalysts are used for the hydrolysis of cellobiose in a continuous reactor. The combination of the results from these experiments provides valuable structure-property relationships. The results of this study will help to identify the ideal strength of acid sites for the hydrolysis of carbohydrates.

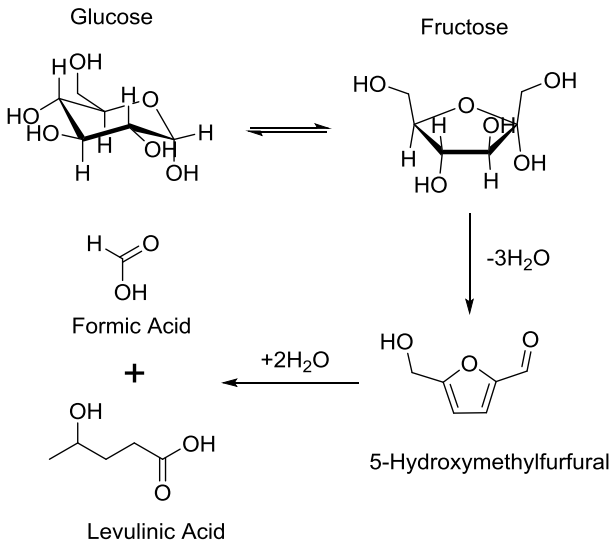

Figure 4.1 Reaction pathway for the degradation of glucose.

4.2 Experimental

4.2.1 Materials

Activated charcoal (untreated, granular, 4-8 mesh, made from peat bog), sulfuric acid (95.0-98.0%), glucose (>99.5%), cellobiose (>98%), sodium hydroxide (>98%, pellets), potassium hydrogen phthalate (>99.95%), sodium carbonate (>99%), sodium bicarbonate (>99.7%) and potassium bromide (FTIR grade, >99%) were purchased from Sigma Aldrich. Deionized water was further purified using a Barnstead NANOpure ultrapure water system to 18.2 MΩ/cm.

4.2.2 Catalyst preparation

The activated charcoal was used as received. To acidify the catalyst, 8.0 g of untreated carbon was mixed with 80 ml of sulfuric acid (10 M) at 100 °C for 30 min. The suspension was filtered and washed with DI water until the filtrate had a neutral pH. To ensure that only stable functional groups are present,[28] the sample was treated in hot liquid water at 200 °C and autogenic pressure for 24 h. The sample was filtered and washed with DI water again until the filtrate had a neutral pH. This sample was named Acidified Carbon. The catalyst that has undergone acidification and hot water treatment twice was named Reacidified Carbon. For the fourth sample, as-received carbon was initially treated in hot liquid water at 200 °C for 24 h and subsequently subjected to the same acidification and hot water treatment as the other samples. The sample is named Hot Water Treated (HWT) Acidified Carbon.

4.2.3 Raman spectroscopy

To probe the disordered carbon materials, Raman spectra were collected on a Confocal Raman Microscope Alpa-Witek with a laser wavelength of 514 nm. Each sample was placed across a glass slide. For each spectrum, ten scans were recorded and

three spectra were obtained for each sample at different locations. Peak fitting was performed with the GRAMS/AI software.

4.2.4 X-Ray diffraction (XRD)

Powder XRD patterns were measured on a Philips X'pert diffractometer equipped with an X'celerator module using Cu Kα radiation. Diffractograms were collected at incident angles from 2θ = 5 to 70° at a step size of 0.0167°.

4.2.5 NMR spectroscopy

^{13}C direct polarization (DP) magic angle spinning (MAS) NMR spectra were recorded on a Bruker DSX 300 spectrometer. The samples were loaded into a 4 mm zirconia rotor and spun at a frequency of 10 kHz. Adamantane was used as a reference material and the peak at δ=38.45 ppm was set as the reference. The resonance frequency of ^{1}H is 300.2 MHz and ^{13}C is 75.5 MHz. High power ^{1}H decoupling was used during the sampling of the ^{13}C magnetization. A π/2 pulse (5 μs) was applied, while the recycle delay was 4 s. Each spectrum was accumulated with about 20,000 scans.

4.2.6 Nitrogen and carbon dioxide physisorption

N_2 and CO_2 physisorption measurements were carried out with a Micromeritics ASAP 2020 physisorption analyzer at 77 K and 273 K, respectively. Prior to analysis, ca. 150 mg of each sample was evacuated in vacuum for 4 h at 150 °C. For nitrogen physisorption, the surface area and pore volumes were calculated using the BET method[30] and the BJH method,[31] respectively. For carbon dioxide physisorption, the pore volume was calculated by using the DFT method.[32]

4.2.7 Elemental analysis

All carbon samples were sent to Atlantic Microlab for elemental analysis to determine their sulfur contents. The samples were also sent to Elemental Analysis, Inc. for Proton Induced X-ray Emission (PIXE) analysis to determine the amount of inorganic species present.

4.2.8 Boehm titration

The type and concentration of functional groups present on the carbon materials were determined by Boehm titration. This was performed by following the procedures as reported in literature.[28-29, 33-34] In short, 1.5 g of each sample was added to 50 ml of aqueous solutions of NaOH, $NaHCO_3$ and Na_2CO_3, respectively. The concentration of each base solution was 0.05 M. The slurries were shaken for a total of 24 h, filtered, and aliquots of the filtrate (10 ml) were collected. For the aqueous $NaHCO_3$ and NaOH solutions, 20 ml of 0.05 M HCl_{aq} was added. For the aqueous Na_2CO_3 solution, 30 ml of 0.05 M of HCl_{aq} was added. The solutions were outgassed with N_2 for 2 h and back titrated with 0.05 M solution of NaOH until an endpoint (pH 7.0) was reached. The calculated standard deviations are 6 μmol/g, 10 μmol/g and 10 μmol/g for carboxylic acid group, lactonic group and phenolic group, respectively.

4.2.9 Hydrolysis of cellobiose

Hydrolysis of cellobiose (0.03 M) was performed in a fixed bed down-flow reactor (0.635 cm outer diameter Swagelok stainless steel tube). Quartz wool was used at both ends of the reactor to keep the catalyst bed in place. The reactor temperature was set at 200 °C, and the pressure was controlled at 25 bar with the use of an Equilibar EB1LF2 back pressure regulator with a PTFE/glass diaphragm. The cellobiose feed (0.03 M) was supplied from a 1 L glass bottle using an Agilent 1100 Series HPLC pump at a flow rate of 0.5 ml/min. The reaction products were collected every 20 min using a Valco selector

valve for HPLC analysis. The catalysts were tested at various residence times. The cellobiose feed was initially pumped at a flow rate of 0.5 ml/min for 3.5 h. Then, the flow rate was increased to 0.75 ml/min for another 3.5 h and 1.00 ml/min for another 3.5 h. For these tests, the reaction products were collected every 30 min. An additional experiment was performed with an aqueous glucose solution (0.03 M) as feed. The analysis of reaction products was performed using an Agilent 1260 Infinity HPLC with a Grace Davison Prevail carbohydrate column. The concentration of the sugar molecules were measured using a refractive index detector (RID). A five-point calibration curve was used to determine the concentration of cellobiose and glucose. For the conversion of cellobiose and glucose, only glucose and fructose were detected as products from HPLC analysis, respectively. Thus, the carbon balance could not be closed. The weight to feed ratio (W/F), expressed in g (mmol h^{-1})$^{-1}$, is defined as the ratio between the mass of the catalyst (g) and the molar feed rate of the reactant (mmol h^{-1}). All of the reactivity experiments were carried out under conditions free of mass transfer limitations (see Supporting Information).

4.2.10 Adsorption isotherms

Standard glucose solutions of various concentrations (0.05 M to 0.6 M) were prepared. Standard cellobiose solutions of various concentrations (0.01 M to 0.12 M) were also prepared. Pre-weighed amounts of carbon sample (ca. 80 mg) were mixed with each sugar solution (1.000 ml) in 1.5 ml microcentrifuge tubes, mixed using a vortexer for 30 s, and placed on a shaker table for 24 h. Subsequently, the slurries were centrifuged (10 min) at 10,000 rcf. The supernatant was removed and analyzed using an Agilent 1260 Infinity HPLC with a Grace Davison Prevail Carbohydrate ES column. To determine the concentration of the sugar molecules, a refractive index detector (RID) was used. The mobile phase used consisted of 75 vol% acetonitrile and 25 vol% water. The flow rate and injection volume were 1.0 ml/min and 0.6 µl, respectively. The uptake was

calculated with $q=(V(C_0-C_e))/m_{cat}$, where q and V are the specific uptake (mol/g) and volume of sugar solution used (L), respectively. C_0 and C_e are the initial and equilibrium concentration (mol/L) of the sugar solution, respectively, and m_{cat} is the mass of carbon sample used (g). For each molecule, three isotherms were obtained on each adsorbent. The Langmuir isotherm parameters were determined via linear regression for each isotherm.[29]

4.3 Results

The Raman spectra of the treated carbon materials had two sharp peaks, the D band around 1350 cm^{-1}, and the G band around 1600 cm^{-1} (Figure C.3A). These two bands are usually assigned as the A_{1g} and E_{2g} mode, respectively.[37] A broad and intense peak due to amorphous sp^3 carbon was not observed at 500 cm^{-1}, indicating that the species is not present to a large extent.[38] The two complex D and G bands can be deconvoluted into five components at 1208 cm^{-1}, 1352 cm^{-1}, 1529 cm^{-1}, 1572 cm^{-1} and 1598 cm^{-1} (Figure C.3B). These peaks are assigned as polyenes (D4), graphene edges (D1), amorphous carbon (D3), graphitic carbon (G) and graphene sheets (D2), respectively.[39] After deconvolution, the parameter $I_{D1}/(I_G+I_{D1}+I_{D2})$ can be used to gauge the degree of graphitization of the carbon materials, where I is the integral of the fitted peak.[40] As-received carbon displayed the highest degree of graphitization, indicating that it had the most organized structure (Table 4.1). After treatment with sulfuric acid, the degree of graphitization of the treated carbon samples was reduced. The $I_{D1}/(I_G+I_{D1}+I_{D2})$ values for the treated samples were within the standard deviation of 0.006. The coefficient of determination (R^2 value) for the deconvolution of individual spectra was greater than 0.99 for each spectrum.

Table 4.1 Degree of graphitization of carbon catalysts.

Catalyst	$I_{D1}/(I_{D1}+I_G+I_{D2})$
As-received	0.745
Acidified Carbon	0.716
HWT acidified Carbon	0.716
Reacidified Carbon	0.710

XRD patterns of all the carbon catalysts displayed two broad peaks at 2θ angles of 24° and 42° (Figure C.4). These are assigned as the (002) and (100) or (101) planes of graphite crystallites, respectively.[41-42] A small, sharp peak at 26.6° is also observed for all of the samples, and it is assigned to diffraction at the (002) plane of graphite-like carbon.[43-44] This demonstrates that treatment with hot liquid water and sulfuric acid did not affect the limited crystallinity of the carbon structure to a measurable extent.

^{13}C DP MAS NMR spectra of the carbon materials exhibited a broad and intense peak at 119 ppm (Figure C.5). This is assigned as the non-protonated core carbon in the polyaromatic structure.[45-46] The broad peak also contained contributions from other species such as exterior carbon in different environments, illustrating that the network of activated carbon is highly complex. The low intensity of aliphatic carbon between 0-40 ppm also suggests that most of the carbon in the structure is polyaromatic and sp^2-hybridized. The high similarity of the spectra of different samples indicates that acidification does not change the hybridization of a significant fraction of the carbon species in the sample.

The pore size distributions of the carbon catalysts obtained by CO_2 and N_2 physisorption are shown in Figure 4.2. In the microporous range, the pore size distributions of the materials were similar (Figure 4.2A). However, in the mesoporous range, HWT acidified carbon had almost the same pore size distribution compared to as-received carbon (Figure 1B). Acidified carbon and reacidified carbon had a lower

contribution of pores that were around 3.8 nm in size. The surface area of the materials remained unchanged in both the microporous and mesoporous range (Table C.2). The BET surface area of the carbon catalyst did not change significantly after treatment with sulfuric acid and hot liquid water (Table 4.2).

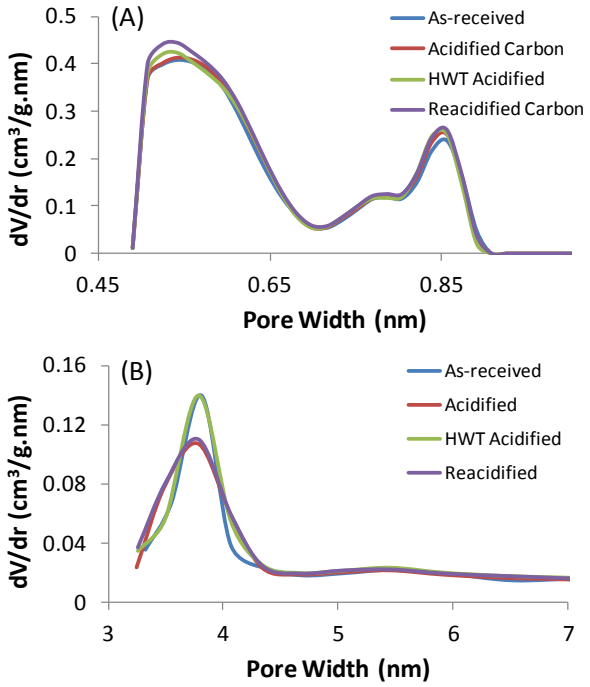

Figure 4.2 Pore size distribution of carbon catalysts (A) 0.45 nm to 1.00 nm determined by CO_2 physisorption, (B) 3 to 6 nm determined by N_2 physisorption.

Table 4.2 Surface properties and reactivity of carbon catalysts in the hydrolysis of cellobiose (200 °C, 25 bar, 100 mg catalyst, 0.5 ml/min of 0.03 M cellobiose solution).

Catalyst	Surface Area (m^2/g)[a]	Total Acid Sites (μmol/g)[b]	Sulfonic Groups (μmol/g)[c]	Fraction of Sulfonic Groups	Conversion (%)[d]	Glucose Selectivity (%)[d]
No catalyst	-	-	-	-	21	40
As-received Carbon	623	129	-	-	21	43
Acidified Carbon	620	403	169	0.42	50	42
HWT Acidified Carbon	633	510	134	0.26	41	63
Reacidified Carbon	654	544	91	0.17	40	60

a: Determined by N_2 physisorption
b: Determined by Boehm titration
c: Determined by elemental analysis
d: Determined by HPLC analysis

PIXE analysis of the carbon materials was performed to determine the amounts of different inorganic species in the catalysts that could affect hydrolysis and side reactions. As-received carbon had 0.1 to 0.5 wt% of sodium, magnesium, aluminum, silicon, sulfur, calcium and iron (Table C.3). The contents of other inorganic species were small. During acidification with sulfuric acid, the content of all inorganic elements in the chemically treated carbons were reduced significantly, except for sulfur, which is due to the formation of sulfonic acid groups.

Boehm titration revealed that as-received carbon had a low concentration of acid sites before acidification (Table 4.2). Even though PIXE analysis revealed that untreated carbon contained 0.16 wt% of sulfur, it was reported that these sulfur species are highly oxidized, and they can be attributed to metal sulfates or sulfonic esters.[28] Treatment with sulfuric acid removes these species, and the sulfur content of the treated samples can be attributed to the presence of sulfonic acid groups. Therefore, as-received carbon did not contain sulfonic acid groups (Table 4.2). The carbon materials that had been subjected to chemical treatment had increased concentrations of acid sites. Besides sulfonic acid groups, weaker acid sites such as phenol, lactone and carboxylic acid groups were also

present (Table C.4). Acidified carbon had the highest fraction of sulfonic acid group, followed by HWT acidified carbon and reacidified carbon.

The hydrolysis of cellobiose over different carbon catalysts was studied using a continuously operated fixed bed reactor (Figure C.6). Over the course of 4 h on stream, the values of conversion and glucose selectivity were always within 10% of the average value, and the fluctuation appeared to be random. This indicates that the carbon catalysts are stable during the hydrolysis reaction.[28] As-received carbon gave a conversion and glucose selectivity of 21% and 43%, respectively (Table 4.2). These values are close to the ones obtained in the absence of a catalyst. Acidified carbon displayed the highest conversion but lowest glucose selectivity compared to the rest of the catalysts (Figure C.6). Its average conversion and glucose selectivity were 50% and 42%, respectively (Table 4.2). HWT acidified carbon and reacidified carbon provided lower conversions but the highest selectivities.

Since HWT acidified carbon and reacidified carbon have similar reactivity, acidified carbon and HWT acidified carbon were further tested at various W/F ratios under the same reaction condition of 200 °C and 25 bar. Figure 4.3 shows the conversion and glucose selectivity over the carbon catalysts. As the W/F ratio decreased, the steady state conversion of both catalysts decreased. Acidified carbon had a slightly higher conversion compared to HWT acidified carbon at all W/F values. However, both catalysts had a constant glucose selectivity with increasing time on stream. Acidified carbon had an average glucose selectivity of 43% while HWT acidified carbon had an average glucose selectivity of 59%. The glucose selectivity of the reaction without catalyst is not shown because of the high error margin associated with the low glucose concentration in the product stream.

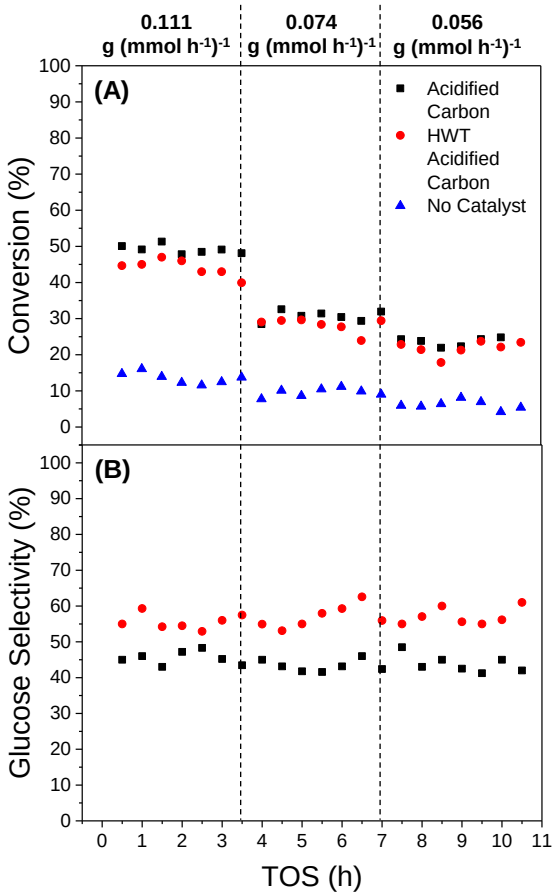

Figure 4.3 (A) Conversion and (B) glucose selectivity of cellobiose hydrolysis at various W/F ratios using acidified carbon, HWT acidified carbon and empty reactor. Reaction condition: 200 °C, 25 bar, 0.03 M cellobiose in water, 100 mg catalyst.

To further study the reason for differences in glucose selectivity over different catalysts, and aqueous glucose solution (0.03M) was fed into the fixed bed reactor setup under the same reaction conditions. Figure 4.4 shows the conversion of glucose over acidified carbon and HWT acidified carbon. For both catalysts, glucose conversion decreased with decreasing W/F ratio, and acidified carbon had a higher steady state conversion at all W/F ratios. However, conversion was low for the reaction in the absence of a catalyst. Only fructose was identified as a product using HPLC analysis and its selectivity is shown in Figure C.7.

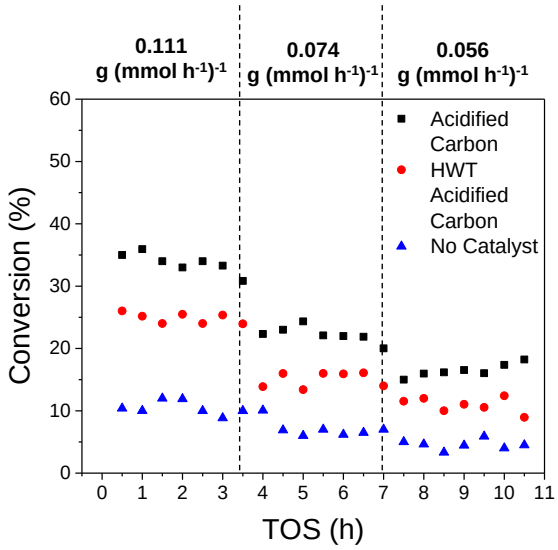

Figure 4.4 Conversion of glucose over acidified carbon, HWT acidified carbon and in an empty reactor at various W/F ratio. Reaction condition: 200 °C, 25 bar, 0.03 M glucose in water, 100 mg catalyst.

Table 4.3 shows the apparent rate constants that are calculated based on the conversion of cellobiose and glucose in Figure 4.3 and 4.4. For all reactions, the reaction rate constants for cellobiose conversion are higher than those for glucose conversion. However, the ratio of k_{CB} to k_{Glu} was higher in the presence of the catalysts, especially, HWT acidified carbon.

Table 4.3 Apparent rate constants for the conversion of cellobiose (k_{CB}) and glucose (k_{Glu}) in an empty reactor (s^{-1}) and using carbon catalysts ($L/g_{cat}.s$).

Catalyst	Rate Constants		k_{CB}/k_{Glu}
	k_{CB}	k_{Glu}	
No Catalyst	$(5.6 \pm 0.5) \times 10^{-4}$	$(4.1 \pm 0.1) \times 10^{-4}$	1.37
Acidified Carbon	$(3.7 \pm 0.2) \times 10^{-5}$	$(2.4 \pm 0.2) \times 10^{-5}$	1.55
HWT Acidified Carbon	$(3.5 \pm 0.2) \times 10^{-5}$	$(1.7 \pm 0.1) \times 10^{-5}$	2.05

Adsorption isotherms of glucose and cellobiose on the carbon materials were obtained to understand the effect of functional groups and defect sites on the adsorption of oligomers. Table 4.4 shows the Langmuir adsorption constants obtained by linear regression. An example of adsorption isotherms of glucose and cellobiose on as-received carbon is shown in Figure C.8. The maximum uptake of each adsorbent was normalized by its surface area for easier comparison. Adsorption coefficients had a standard deviation of 30%. The adsorption coefficient (K) obtained for glucose on untreated carbon was 37 L/mol, while K increased significantly when cellobiose was used as the sorbate. The adsorption coefficient for glucose and cellobiose on the acidified materials was significantly lower than the corresponding values for as-received carbon. Specifically, the decrease was ca. 60% for glucose and ca. 40% for cellobiose. K was similar in value for all of the chemically treated carbon materials. The difference in free energy (ΔΔG) between cellobiose and glucose for as-received carbon is -1.78 kcal/mol. After it was treated with sulfuric acid, the carbon materials have lower ΔΔG values. As-received carbon had a normalized maximum uptake (q_m) of 0.135 mg/m^2 and 0171 mg/m^2 for glucose and cellobiose, respectively. The treated samples had higher values of q_m for the adsorption of glucose, but the values were not significantly different for the adsorption of cellobiose compared to as-received carbon.

Table 4.4 Langmuir adsorption constants of glucose and cellobiose on carbon catalysts.

	Glucose		Cellobiose		
Adsorbent	**Normalized q_m (mg/m^2)**	**K (L/mol)**	**Normalized q_m (mg/m^2)**	**K (L/mol)**	**ΔΔG (kcal/mol)**
As-received Carbon	0.135	37	0.171	650	-1.78
Acidified Carbon	0.190	11	0.163	352	-2.06
HWT Acidified Carbon	0.196	10	0.189	415	-2.24
Reacidified Carbon	0.200	14	0.177	377	-2.01

q_m: maximum uptake (mg/g), K: adsorption coefficient

4.4 Discussion

4.4.1 Structure of carbon catalysts

Carbon based materials are increasingly used in heterogeneous catalysis with applications toward the production of fine chemicals.[21] Additionally, they are widely used as adsorbents and separation media.[47] For these applications, the performance is largely determined by its morphology and surface chemistry of the carbon material. An in-depth understanding of the structure of carbon catalysts is required so that its properties can be related to its hydrolysis activity. XRD results show that treatment with sulfuric acid and hot liquid water did not affect the low crystallinity of the graphite crystallites to a measureable extent. Furthermore, the diffraction peaks are attributed to the stacking of carbon sheets (Figure C.4).[18] The results of Raman spectroscopy and ^{13}C DP MAS NMR show that most of the carbon is sp^2-hybridized and polyaromatic in nature (Figure C.3 and C.5). As such, the functional groups present would have to be positioned around the periphery or defect sites of the carbon structure, and they would have to be in the same plane as the graphene sheets.[29, 48]

Upon chemical treatment, changes in the intensity ratio of characteristic peaks in the Raman spectra indicated increasing disorder of the carbon structures (Table 4.1), which is attributed to a lower degree of graphitization. The disorder of the carbon sheets is attributed to the formation of additional edges,[40] suggesting that there are more defects/cavities and exposed edges. The increased disorder of acidified samples is in agreement with a previous study that found that treatment with H_2SO_4 etches and exfoliates the stacks of graphene sheets, creating more edges and cavities.[29] HWT acidified carbon had the same degree of graphitization as acidified carbon, indicating that hot liquid water treatment at 200 °C does not affect the order of the carbon structures.

There were no significant changes in the pore size distribution of the catalysts in the microporous range (Figure 4.2A). In the mesoporous range, acidified and reacidified

carbon have a lower contribution of pore volume at around 3.8 nm, and this is probably due to the exfoliation of the carbon structure during acidification.[49] However, HWT acidified carbon had the same pore size distribution as as-received carbon. It was shown that treatment with hot liquid water at 200 °C is able to impart a small concentration of weak functional groups,[28] and this effect was also observed in this study (Table 4.2).

As-received carbon possessed a small concentration of weak functional groups such as phenol, lactone and carboxylic acid groups (Tables 4.2 and C.4). After acidification, the concentration of acid sites increased significantly with a fraction of 0.42 being sulfonic acid groups. The initial treatment with hot liquid water in the synthesis of HWT acidified carbon imparts a small concentration of weak acid sites.[28] This is probably due to increased self-ionization of water at higher temperatures,[50] allowing more hydronium ions to functionalize the carbon structure. It is assumed that the carbon sheets are susceptible to electrophilic attack by the hydronium ion due to pyramidalization and π misalignment that is present at the edges and curvatures of the sheet walls.[51] This reduces the number of active sites for functionalization in the subsequent acidification step, resulting in a lower fraction of sulfonic acid groups present. In the case of reacidified carbon, the second step of acidification resulted in a lower concentration of phenol groups but higher concentrations of lactone and carboxylic acid groups (Table C.4), suggesting that the sample underwent oxidation by sulfuric acid. The resulting lower concentration of sulfonic acid groups could indicate that these functional groups are not stable in the second acidification step, allowing more of the edges of the carbon to be functionalized by weak acid groups.

During the continuous reactivity studies (Figure 4.3 and 4.4), the conversion of cellobiose and glucose reached a steady state within a short time and no deactivation was observed during 11 h on stream. This indicates that the functional groups and the carbon structure are active and stable during reaction up to 200 °C. Note that these results are far less ambiguous than catalyst recycle experiments in batch reactors.

4.4.2 Adsorption of Glucose and Cellobiose

The adsorption of glucans plays a critical role in the catalytic performance of carbon catalysts. Studies have shown that adsorption occurs on the hydrophobic carbon surface and that hydrophilic functional groups have limited involvement.[29, 52-53] Specifically, interactions between the CH groups of the adsorbates and the polyaromatic rings of the carbon surface are responsible for driving the adsorption process.[54-55] In addition, these CH-π interactions are significantly stronger compared to interactions between the glucan chains.[53]

Adsorption isotherms in this study show that as-received carbon readily adsorbs both glucose and cellobiose (Table 4.4). Our results are in agreement with literature in showing that van der Waals forces are dominant in the interactions between the CH groups of the adsorbates and the polyaromatic rings of the carbon surface.[52-56] This explains the large increase of the adsorption coefficient for cellobiose, as it possesses more CH groups compared to glucose.

For the chemically treated materials, the adsorption coefficient of glucose and cellobiose decreased by about 65% and 40%, respectively, compared to as-received carbon. The decrease can be explained by competitive adsorption with water molecules as the surface becomes more hydrophilic due to the presence of functional groups. However, the adsorption process is still dominated by van der Waals forces as indicated by the relatively small changes in the energy terms that describe these interactions. Specifically, the decrease of the adsorption coefficient of cellobiose was less pronounced than that of glucose, which possesses a smaller number of CH-groups that can interact with the surface. This translates to a difference in the free energy of adsorption ($\Delta\Delta G$) between the sorbates of about 0.3 kcal/mol, which is small compared to adsorptions associated with chemisorption (<9.5 kcal/mol) or the strength of a hydrogen bond (1.6 kcal/mol – 4.8 kcal/mol).[57] Hence, functional groups are not involved in the adsorption process for the acidified materials.

It is suggested that ΔΔG is also dependent on the degree of contact at the molecular level, between the carbon surface and adsorbate.[29, 52] This refers to the extent of overlap between the polyaromatic carbon surface and the adsorbed glucans. Thus, the defect sites created in the acidification process are expected to favor the adsorption of cellobiose over glucose.

For the adsorption of glucose on the chemically treated materials, there was an increase in maximum uptake compared to as-received carbon. However, the maximum uptake did not change significantly for the adsorption of cellobiose. It is speculated that the presence of defect sites and functional groups causes rotation of adsorbed glucose to adsorb in a more tightly packed manner.

4.4.3 Effect of Strong and Weak Acid Sites in the Hydrolysis of Cellobiose

It has been demonstrated that even weak acid sites on carbon can be active for the hydrolysis of cellulose and xylan.[15, 24, 29] Chung et al. recommended the use of weak acid sites because strong acid sites could leach into the aqueous solution during hydrolysis as they are less hydrothermally stable.[24] Furthermore, these acid sites could undergo ion exchange in the presence of dissolved aqueous salts. In another study, it was reported that an increased loading of Ru on mesoporous carbon (CMK-3) resulted in a small increase of glucose yield and a large increase in the yield of by-products.[58] It was hypothesized that the Ru species formed strong acid sites that resulted in sequential side degradation reactions.

At steady state, the hydrolysis of cellobiose over as-received carbon yielded 21% conversion and 43% glucose selectivity (Table 4.2). It is not entirely surprising that this result is almost identical to the reaction in the absence of any catalyst, as the untreated carbon possessed only a small concentration of functional groups. Based on previous studies, it is expected that a certain amount of cellobiose is converted to glycosyl-fructose and glucosyl-mannose under hydrothermal conditions (>200 °C),[9-10] while a small

amount of cellobiose is hydrolyzed to glucose. Note that similar experiments in batch reactors could lead to ambiguous results because some amount of reactants and products could remain adsorbed on the catalyst when the reaction is stopped and cooled down to room temperature. By using a flow reactor, the products formed are continuously removed to prevent accumulation and the formation of undesirable products, such as insoluble humins. In this way, the results obtained from a flow reactor are reliable and indicative of the catalyst's performance under the specified reaction condition. The steady state conversion and selectivity results in the limited variability of the rate constants obtained (Table 4.2). In agreement with previous suggestions,[35-36] linear decay profiles showed that the reactions are first order in cellobiose and glucose, respectively (Figure C.9). Note that the surface chemistry and kinetics obtained in this study can be extrapolated to reactors that could be used on an industrial scale.

The glucose selectivity over acidified carbon was similar to as-received carbon, but it had a higher conversion of 50% (Table 4.2). This indicates that the enhanced catalytic activity is due to the presence of the additional functional groups, especially sulfonic acid group since these accounted for 42% of the total acid sites present. It was reported that after the hydrolysis of oligomers to monomeric glucose, the presence of an acid catalyst accelerated the isomerization of glucose to fructose, which could degrade to other products such as HMF, levulinic acid, formic acid and acetic acid under hydrothermal conditions.[4] In addition, insoluble humins could be formed by different pathways.[59] Therefore, it is speculated that the strongly acidic sulfonic acid groups in acidified carbon increased the conversion of cellobiose. However, these strong acid sites also appear to catalyze the conversion of glucose monomers to other side products, resulting in the same glucose selectivity as untreated carbon.

Cellobiose hydrolysis over HWT acidified carbon and reacidified carbon exhibited a lower conversion of about 40% but a higher glucose selectivity of 60-63% (Table 4.2). This is a result of a higher reaction rate constant of cellobiose to glucose.

Although the conversion of glucose was small in the absence of a catalyst (Figure 4.4), the limited thermal degradation suggests that the yield of glucose can be increased further by limiting the extent to which non-surface reactions occur. This could be achieved with an improved design for a fixed bed reactor setup, in which the liquid streams are heated and cooled more rapidly. In addition, a lower reaction temperature (< 200 °C) might reduce the formation of degradation products in the bulk solution. However, the rate of the desired catalytic would also decrease. Therefore, it appears as if the design of highly selective catalysts is one of the most promising routes for achieving a high glucose selectivity.

Weak acid sites on carbon, such as phenols, lactones and carboxylic acids, are located at the edges and defect sites of the carbon sheets.[29] These acid sites are active and could be selective in the hydrolysis of cellobiose to yield glucose. It was shown that these weak acid sites are less accessible than sulfonic acid groups in polar solvents.[60] Therefore, it is suggested that glucose can easily interact with strong sulfonic acid groups leading to degradation reactions. In contrast, catalysts with weaker acid sites are expected to minimize such side reactions. The high selectivity of HWT acidified carbon and reacidified carbon can be explained by the presence of the low fraction of sulfonic acid group. It was reported that maleic acid, which has a higher pKa than sulfuric acid, is equally effective in hydrolyzing cellobiose but achieves higher glucose yields.[61] This further illustrates that under certain conditions (vide infra) the hydrolysis only requires relatively weak acid sites, whereas the extent of degradation of glucose increases in the presence of stronger acid sites, such as sulfonic acid groups. Further evidence for this scenario is the lower rate of glucose conversion over HWT acidified carbon compared to acidified carbon (Figure 4.4), which seems to indicate that the strength of acid sites is crucial for glucose selectivity in the hydrolysis of cellobiose. Consequently, a higher glucose yield is achieved when there are fewer sulfonic acid groups present on the carbon

surface. In addition, a higher concentration of weak acid sites (carboxylic acid, lactone and phenol) improves the selectivity of the hydrolysis of cellobiose to glucose.

A previous study showed that the presence of defect sites can enhance the catalytic activity of activated carbon in the hydrolysis of cellulose.[29] It was hypothesized that the adsorption of oligomers on defect sites or edges of the carbon structure induces a conformational change.[3] This allows the exposed glycosidic bond to be attacked by the in-plane functional groups, allowing weak acid sites to participate in the hydrolysis reaction. In the present study, all of the chemically treated materials have a lower degree of graphitization due to acidification and exfoliation compared to as-received carbon, and the functional groups are also located around the edges and defect sites of the carbon structure (vide supra). Furthermore, the lower $\Delta\Delta G$ values from adsorption isotherms indicate that adsorption of cellobiose is preferable over materials with defect sites. Thus, it is proposed that the same adsorption and reaction mechanism can also occur on these materials, allowing weak acid sites to selectively hydrolyze cellobiose.

Adsorption isotherms show that the adsorption coefficient of glucose is small compared to cellobiose due to van der Waals interaction. Since glucose monomers compete unfavorably with water and cellobiose in its adsorption on functionalized carbon materials during the hydrolysis reaction, the surface would mostly likely be populated with cellobiose. Thus, it would be difficult for weak acid sites to further catalyze glucose into fructose and other side products. Furthermore, these weak acid sites have limited strength to catalyze these degradation reactions based on the lower rate of glucose conversion over HWT acidified carbon. This result in a higher and sustained selectivity of glucose at various W/F ratios. In addition, it is suggested that glucose can be degraded if a sulfonic acid group is within the vicinity when cellobiose is hydrolyzed, as sulfonic acid groups appear to be more accessible for glucose molecules in the presence of a polar solvent.[60] In summary, these considerations show that weak acid sites in specific environments (i.e. defect sites, edges) are sufficient to catalyze the hydrolysis of

oligosaccharides, but degradation reactions are prevented due to the limited strength of these sites.

4.5 Conclusions

This study examines the catalytic activity of activated carbon functionalized with different fractions of sulfonic acid groups and weak acid sites in the hydrolysis of cellobiose. All of the acidified materials have a lower degree of graphitization, and adsorption isotherms reveal that the adsorption of glucose and cellobiose is driven by van der Waals forces between the CH groups of the adsorbates and the polyaromatic ring surface of the carbon catalysts. Reactivity studies in a continuously operated packed bed reactor setup show that the catalysts retain their initial activity for at least 11 h on stream. A high fraction of sulfonic acid groups results in a high conversion of cellobiose and low selectivity of glucose, while the materials with a high fraction of weak acid sites exhibit high glucose selectivity but lower conversion. It is proposed that high glucose selectivity requires a synergistic effect between defects sites of the carbon structure and in-plane functional groups, which only allows weak acid sites to selectively catalyze the hydrolysis of cellobiose. This is possible because glucose competes unfavourably with cellobiose and these weak acid sites have limited strength to carry out the degradation reactions. The higher accessibility of strong sulfonic acid groups in the presence of a polar solvent can further catalyze glucose monomers into fructose and other side products. These surface interactions result in a constant glucose selectivity regardless of the residence time of the feed in the catalyst bed.

4.6 References

1. Huber, G. W.; Iborra, S.; Corma, A. Synthesis of transportation fuels from biomass: Chemistry, catalysts, and engineering. *Chem. Rev.* **2006,** *106*, 4044-4098.

2. Ragauskas, A. J.; Williams, C. K.; Davison, B. H.; Britovsek, G.; Cairney, J.; Eckert, C. A.; Frederick, W. J.; Hallett, J. P.; Leak, D. J.; Liotta, C. L.; Mielenz, J. R.; Murphy, R.; Templer, R.; Tschaplinski, T. The path forward for biofuels and biomaterials. *Science* **2006,** *311*, 484-489.

3. Loerbroks, C.; Rinaldi, R.; Thiel, W. The Electronic Nature of the 1,4-beta-Glycosidic Bond and Its Chemical Environment: DFT Insights into Cellulose Chemistry. *Chem.-Eur. J.* **2013,** *19*, 16282-16294.

4. Zakzeski, J.; Grisel, R. J. H.; Smit, A. T.; Weckhuysen, B. M. Solid Acid-Catalyzed Cellulose Hydrolysis Monitored by In Situ ATR-IR Spectroscopy. *ChemSusChem* **2012,** *5*, 430-437.

5. Onda, A.; Ochi, T.; Kajiyoshi, K.; Yanagisawa, K. A new chemical process for catalytic conversion Of D-glucose into lactic acid and gluconic acid. *Appl. Catal. A-Gen.* **2008,** *343*, 49-54.

6. Bermejo-Deval, R.; Assary, R. S.; Nikolla, E.; Moliner, M.; Román-Leshkov, Y.; Hwang, S.-J.; Palsdottir, A.; Silverman, D.; Lobo, R. F.; Curtiss, L. A.; Davis, M. E. Metalloenzyme-like catalyzed isomerizations of sugars by Lewis acid zeolites. *Proc. Natl. Acad. Sci. U. S. A.* **2012,** *109*, 9727-9732.

7. Corma, A.; Iborra, S.; Velty, A. Chemical routes for the transformation of biomass into chemicals. *Chem. Rev.* **2007,** *107*, 2411-2502.

8. Mosier, N.; Wyman, C.; Dale, B.; Elander, R.; Lee, Y. Y.; Holtzapple, M.; Ladisch, M. Features of promising technologies for pretreatment of lignocellulosic biomass. *Bioresour. Technol.* **2005,** *96*, 673-686.

9. Yu, Y.; Shafie, Z. M.; Wu, H. Cellobiose Decomposition in Hot-Compressed Water: Importance of Isomerization Reactions. *Ind. Eng. Chem. Res.* **2013,** *52*, 17006-17014.

10. Mohd Shafie, Z.; Yu, Y.; Wu, H. Insights into the Primary Decomposition Mechanism of Cellobiose under Hydrothermal Conditions. *Ind. Eng. Chem. Res.* **2014,** *53*, 14607-14616.

11. Harris, E. E.; Beglinger, E.; Hajny, G. J.; Sherrard, E. C. Hydrolysis of Wood - Treatment with Sulfuric Acid in a Stationary Digestor. *Ind. Eng. Chem.* **1945,** *37*, 12-23.

12. Sherrard, E. C.; Kressman, F. W. Review of Processes in the United States prior to World War II. *Ind. Eng. Chem.* **1945,** *37*, 4-8.

13. Harris, E. E.; Beglinger, E. Madison Wood Sugar Process. *Ind. Eng. Chem.* **1946,** *38*, 890-895.

14. Marzialetti, T.; Olarte, M. B. V.; Sievers, C.; Hoskins, T. J. C.; Agrawal, P. K.; Jones, C. W. Dilute acid hydrolysis of Loblolly pine: A comprehensive approach. *Ind. Eng. Chem. Res.* **2008,** *47*, 7131-7140.

15. Kobayashi, H.; Yabushita, M.; Komanoya, T.; Hara, K.; Fujita, I.; Fukuoka, A. High-Yielding One-Pot Synthesis of Glucose from Cellulose Using Simple Activated Carbons and Trace Hydrochloric Acid. *ACS Catal.* **2013,** *3*, 581-587.

16. Suganuma, S.; Nakajima, K.; Kitano, M.; Yamaguchi, D.; Kato, H.; Hayashi, S.; Hara, M. Hydrolysis of cellulose by amorphous carbon bearing SO3H, COOH, and OH groups. *J. Am. Chem. Soc.* **2008,** *130*, 12787-12793.

17. Kitano, M.; Yamaguchi, D.; Suganuma, S.; Nakajima, K.; Kato, H.; Hayashi, S.; Hara, M. Adsorption-Enhanced Hydrolysis of β-1,4-Glucan on Graphene-Based Amorphous Carbon Bearing SO3H, COOH, and OH Groups. *Langmuir* **2009,** *25*, 5068-5075.

18. Fukuhara, K.; Nakajima, K.; Kitano, M.; Kato, H.; Hayashi, S.; Hara, M. Structure and Catalysis of Cellulose-Derived Amorphous Carbon Bearing SO3H Groups. *ChemSusChem* **2011,** *4*, 778-784.

19. Nakajima, K.; Hara, M. Amorphous Carbon with SO3H Groups as a Solid Bronsted Acid Catalyst. *ACS Catal.* **2012,** *2*, 1296-1304.

20. Onda, A. Selective Hydrolysis of Cellulose and Polysaccharides into Sugars by Catalytic Hydrothermal Method Using Sulfonated Activated-carbon. *J. Jpn. Pet. Inst* **2012,** *55*, 73-86.

21. Huang, Y.-B.; Fu, Y. Hydrolysis of cellulose to glucose by solid acid catalysts. *Green Chem.* **2013,** *15*, 1095-1111.

22. Pang, J. F.; Wang, A. Q.; Zheng, M. Y.; Zhang, T. Hydrolysis of cellulose into glucose over carbons sulfonated at elevated temperatures. *Chem. Commun.* **2010,** *46*, 6935-6937.

23. Torget, R. W.; Kim, J. S.; Lee, Y. Y. Fundamental Aspects of Dilute Acid Hydrolysis/Fractionation Kinetics of Hardwood Carbohydrates. 1. Cellulose Hydrolysis. *Ind. Eng. Chem. Res.* **2000,** *39*, 2817-2825.

24. Chung, P.-W.; Charmot, A.; Olatunji-Ojo, O. A.; Durkin, K. A.; Katz, A. Hydrolysis Catalysis of Miscanthus Xylan to Xylose Using Weak-Acid Surface Sites. *ACS Catal.* **2013,** *4*, 302-310.

25. Gazit, O. M.; Charmot, A.; Katz, A. Grafted cellulose strands on the surface of silica: effect of environment on reactivity. *Chem. Commun.* **2011,** *47*, 376-378.

26. Gazit, O. M.; Katz, A. Grafted Poly(1 -> 4-beta-glucan) Strands on Silica: A Comparative Study of Surface Reactivity as a Function of Grafting Density. *Langmuir* **2012,** *28*, 431-437.

27. Gazit, O. M.; Katz, A. Understanding the Role of Defect Sites in Glucan Hydrolysis on Surfaces. *J. Am. Chem. Soc.* **2013,** *135*, 4398-4402.

28. Van Pelt, A. H.; Simakova, O. A.; Schimming, S. M.; Ewbank, J. L.; Foo, G. S.; Pidko, E. A.; Hensen, E. J. M.; Sievers, C. Stability of functionalized activated carbon in hot liquid water. *Carbon* **2014,** *77*, 143-154.

29. Foo, G. S.; Sievers, C. Synergistic Effect between Defect Sites and Functional Groups on the Hydrolysis of Cellulose over Activated Carbon. *ChemSusChem* **2015,** *8*, 534-543.

30. Brunauer, S.; Emmett, P. H.; Teller, E. Adsorption of gases in multimolecular layers. *J. Am. Chem. Soc.* **1938,** *60*, 309-319.

31. Barrett, E. P.; Joyner, L. G.; Halenda, P. P. The determination of pore volume and area distributions in porous substances .1. Computations from nitrogen isotherms. *J. Am. Chem. Soc.* **1951,** *73*, 373-380.

32. Lastoskie, C.; Gubbins, K. E.; Quirke, N. Pore-Size Distribution Analysis of Mircroporous Carbons - A Density-Functional Theory Approach. *J. Phys. Chem.* **1993,** *97*, 4786-4796.

33. Oickle, A. M.; Goertzen, S. L.; Hopper, K. R.; Abdalla, Y. O.; Andreas, H. A. Standardization of the Boehm titration: Part II. Method of agitation, effect of filtering and dilute titrant. *Carbon* **2010,** *48*, 3313-3322.

34. Goertzen, S. L.; Theriault, K. D.; Oickle, A. M.; Tarasuk, A. C.; Andreas, H. A. Standardization of the Boehm titration. Part I. CO2 expulsion and endpoint determination. *Carbon* **2010,** *48*, 1252-1261.

35. Xiang, Q.; Lee, Y. Y.; Pettersson, P. O.; Torget, R. Heterogeneous aspects of acid hydrolysis of alpha-cellulose. *Appl. Biochem. Biotechnol.* **2003,** *105*, 505-514.

36. Suib, S. L., *New and Future Developments in Catalysis: Catalytic Biomass Conversion*. Elsevier Science: 2013;

37. Ferrari, A. C.; Robertson, J. Interpretation of Raman spectra of disordered and amorphous carbon. *Phys. Rev. B* **2000,** *61*, 14095-14107.

38. Prawer, S.; Nugent, K. W.; Jamieson, D. N.; Orwa, J. O.; Bursill, L. A.; Peng, J. L. The Raman spectrum of nanocrystalline diamond. *Chem. Phys. Lett.* **2000,** *332*, 93-97.

39. Sadezky, A.; Muckenhuber, H.; Grothe, H.; Niessner, R.; Poschl, U. Raman micro spectroscopy of soot and related carbonaceous materials: Spectral analysis and structural information. *Carbon* **2005,** *43*, 1731-1742.

40. Lezanska, M.; Pietrzyk, P.; Sojka, Z. Investigations into the Structure of Nitrogen-Containing CMK-3 and OCM-0.75 Carbon Replicas and the Nature of Surface Functional Groups by Spectroscopic and Sorption Techniques. *J. Phys. Chem. C* **2010,** *114*, 1208-1216.

41. Babu, V. S.; Seehra, M. S. Modeling of disorder and X-ray diffraction in coal-based graphitic carbons. *Carbon* **1996,** *34*, 1259-1265.

42. Manivannan, A.; Chirila, M.; Giles, N. C.; Seehra, M. S. Microstructure, dangling bonds and impurities in activated carbons. *Carbon* **1999,** *37*, 1741-1747.

43. Manoj, B.; Kunjomana, A. G. Study of Stacking Structure of Amorphous Carbon by X-Ray Diffraction Technique. *Int. J. Electrochem. Sci.* **2012,** *7*, 3127-3134.

44. Li, Z. Q.; Lu, C. J.; Xia, Z. P.; Zhou, Y.; Luo, Z. X-ray diffraction patterns of graphite and turbostratic carbon. *Carbon* **2007,** *45*, 1686-1695.

45. Cheng, H. N.; Wartelle, L. H.; Klasson, K. T.; Edwards, J. C. Solid-state NMR and ESR studies of activated carbons produced from pecan shells. *Carbon* **2010,** *48*, 2455-2469.

46. Knicker, H.; Totsche, K. U.; Almendros, G.; Gonzalez-Vila, F. J. Condensation degree of burnt peat and plant residues and the reliability of solid-state VACP MAS C-13 NMR spectra obtained from pyrogenic humic material. *Org. Geochem.* **2005,** *36*, 1359-1377.

47. Lennon, D.; Lundie, D. T.; Jackson, S. D.; Kelly, G. J.; Parker, S. F. Characterization of activated carbon using X-ray photoelectron spectroscopy and inelastic neutron scattering spectroscopy. *Langmuir* **2002,** *18*, 4667-4673.

48. Boehm, H. P. Some aspects of the surface chemistry of carbon blacks and other carbons. *Carbon* **1994,** *32*, 759-769.

49. Hong, Y.; Wang, Z.; Jin, X. Sulfuric Acid Intercalated Graphite Oxide for Graphene Preparation. *Sci. Rep.* **2013,** *3*.

50. Pitzer, K. S. Self-Ionization of Water at High-Temperature and the Thermodynamic Properties of Properties of the Ions. *J. Phys. Chem.* **1982,** *86*, 4704-4708.

51. Quinlan, R. A. The Functionalization of Carbon Nanosheets. Ph.D. Dissertation, College of William and Mary, Williamsburg, VA, 2009.

52. Chung, P.-W.; Charmot, A.; Gazit, O. M.; Katz, A. Glucan Adsorption on Mesoporous Carbon Nanoparticles: Effect of Chain Length and Internal Surface. *Langmuir* **2012,** *28*, 15222-15232.

53. Yabushita, M.; Kobayashi, H.; Hasegawa, J.-y.; Hara, K.; Fukuoka, A. Entropically Favored Adsorption of Cellulosic Molecules onto Carbon Materials through Hydrophobic Functionalities. *ChemSusChem* **2014,** *7*, 1443-1450.

54. Kiehna, S. E.; Laughrey, Z. R.; Waters, M. L. Evaluation of a carbohydrate-pi interaction in a peptide model system. *Chem. Commun.* **2007**, 4026-4028.

55. Laughrey, Z. R.; Kiehna, S. E.; Riemen, A. J.; Waters, M. L. Carbohydrate−π Interactions: What Are They Worth? *J. Am. Chem. Soc.* **2008,** *130*, 14625-14633.

56. Chinn, D.; King, C. J. Adsorption of glycols, sugars, and related multiple -OH compounds onto activated carbons. 1. Adsorption mechanisms. *Ind. Eng. Chem. Res.* **1999,** *38*, 3738-3745.

57. Sheu, S. Y.; Yang, D. Y.; Selzle, H. L.; Schlag, E. W. Energetics of hydrogen bonds in peptides. *Proc. Natl. Acad. Sci. U. S. A.* **2003,** *100*, 12683-12687.

58. Kobayashi, H.; Ohta, H.; Fukuoka, A. Conversion of lignocellulose into renewable chemicals by heterogeneous catalysis. *Catal. Sci. Technol.* **2012,** *2*, 869-883.

59. Sievers, C.; Musin, I.; Marzialetti, T.; Olarte, M. B. V.; Agrawal, P. K.; Jones, C. W. Acid-Catalyzed Conversion of Sugars and Furfurals in an Ionic-Liquid Phase. *ChemSusChem* **2009,** *2*, 665-671.

60. Fraile, J. M.; García-Bordejé, E.; Pires, E.; Roldán, L. New insights into the strength and accessibility of acid sites of sulfonated hydrothermal carbon. *Carbon* **2014,** *77*, 1157-1167.

61. Mosier, N. S.; Sarikaya, A.; Ladisch, C. M.; Ladisch, M. R. Characterization of dicarboxylic acids for cellulose hydrolysis. *Biotechnol. Prog.* **2001,** *17*, 474-480.

Chapter 5

Steric Effect and Evolution of Surface Species in the Hydrodeoxygenation of Bio-oil Model Compounds over Pt/HBEA

5.1 Background

Biomass is a promising renewable energy source and an alternative to depleting fossil fuels. Furthermore, its utilization can reduce the overall carbon footprint.[1-2] An attractive approach for biomass utilization involves the fast pyrolysis of biomass to obtain bio-oils. Bio-oils are a complex mixture of several types of oxygenated compounds, such as carboxylic acids, aldehydes, ketones, phenolics, esters and furans.[3] Unfortunately, bio-oil cannot directly be used as a fuel because of its high oxygen content.[4] The latter leads to low stability, high viscosity, and a low heating value, which is unsuitable for current energy systems. One way of upgrading bio-oils is through catalytic hydrodeoxygenation (HDO), where the oxygen-based functional group is removed as water in the presence of hydrogen gas.[5]

Early work focused on supported CoMo and NiMo sulfide catalysts.[6-7] These commercial catalysts are commonly used for hydrodesulphurization (HDS) and hydrodenitrogenation (HDN) in oil refineries. However, they display low activity in HDO reactions.[8] In addition, hydrogen sulfide must be added into the feedstock to maintain their catalytic activity. To overcome these problems, several noble and transition metal catalysts were studied extensively in HDO reactions.[9-23] Many supported metals (Ru, Re, Rh, Pd, Pt, Ni, Fe) display activity in HDO reaction. However, most of these catalysts require a high hydrogen pressure, and they convert aromatics to products with saturated rings. Bimetallic catalysts are also utilized, such as Pt-Sn,[24] Ni-Cu,[25] Rh-Pt,[26] Pd-Fe,[27] and Fe-Mo.[28] Some of these catalysts are active and selective in the

apparent direct cleavage of C-O bond in phenolics, but a high hydrogen pressure is also required. Zhu et al. studied the hydrodeoxygenation of anisole and m-cresol over a bifunctional catalyst (Pt/HBEA) in vapor-phase under atmospheric pressure and produced deoxygenated aromatics such benzene, toluene and xylene.[18, 23] Reducible metal oxides such as MoO_3 and ceria-zirconia were also investigated.[29-31] Even in the absence of a metal, these catalysts display activity in the direct C-O bond cleavage of phenolic compounds. It is postulated that HDO is carried out via a reverse Mars-van Krevelen reaction with the aid of oxygen vacancies. Recently, it was reported that metallic Mo_2C is a selective HDO catalyst under atmospheric hydrogen pressure, producing a high yield of deoxygenated aromatics.[32]

While most of the research has focused on catalytic reactivity of HDO catalysts, there is limited literature on catalyst deactivation, which is commonly observed. Coke deposition on Ni/ZSM-5 has been studied and it was reported that the content of hard coke increased with reaction temperature.[33] However, most catalysts are only selective toward HDO at high temperatures (> 300 °C). Popov et al. studied the adsorption of various phenolic compounds on different catalyst supports.[34-36] The studies indicated that the formation of phenate species on Lewis acid sites could be the source of catalyst poisoning. However, there is still a lack of insight for metal supported catalysts, which are extensively used in HDO reactions. More importantly, the evolution of these surface species during HDO reaction has yet to be elucidated. In this regard, understanding the deactivation mechanism is critical to the development of suitable catalysts and optimizing reaction and catalyst regeneration processes.

In this work, we have focused on Pt supported on HBEA, as it was reported that this catalyst displays high HDO activity under atmospheric hydrogen pressure, making its catalytic function well understood.[18, 22] Most importantly, it was shown that Pt metal has tolerance towards coking during HDO of anisole and m-cresol.[18, 23] By understanding this phenomenon, this study offers insight to develop catalyst with improved resistance

against deactivation. HBEA was also used for comparison. Anisole, m-cresol and guaiacol are used as bio-oil model compounds as they represent a large fraction of phenolic bio-oil. Furthermore, the effect of different types and positions of functional groups on the degree of deoxygenation will be highlighted. By using *operando* transmission FTIR spectroscopy we are able to monitor the performance of the catalyst and the evolution of surface species simultaneously. A timeline was also established to determine the period for optimum activity and rapid regeneration of the catalysts.

5.2 Experimental

5.2.1 Materials

Zeolite beta (CP814E, SiO_2/Al_2O_3 = 25) was purchased from Zeolyst. Silicon carbide (200-450 mesh particle size), anisole (>99.7%), guaiacol (>98%), and tetraamineplatinum(II) chloride hydrate (99.99%) were purchased from Sigma Aldrich. Hydrogen and helium (UHP Grade 5) were purchased from Airgas. Chloroform (99.8%) and m-cresol (99%) were purchased from VWR. A Barnstead NANOpure ultrapure water system was used to further purify deionized water to 18.2 MΩ/cm.

5.2.2 Catalyst Synthesis

Zeolite Beta (HBEA) was calcined at 550 °C for 4 h. Pt/HBEA was prepared via wetness impregnation method of HBEA using a dilute aqueous solution of $Pt(NH_3)_4Cl_2$. The slurry was stirred for 12 h, followed by drying at 110 °C for 12 h. Subsequently, the catalyst was calcined at 420 °C for 4 h.

5.2.3 Characterization

Nitrogen physisorption and hydrogen chemisorption measurements were taken using a Micromeritics ASAP 2020 physisorption/chemisorption analyzer. For N_2

physisorption, the catalysts were degassed at 200 °C for 4 h prior to measurement. Surface areas and pore volumes were calculated based on the BET method[37] and the BJH method,[38] respectively. For H_2 chemisorption, the sample was degassed at 100 °C for 1 h and 400 °C for 15 min. Next, the sample was reduced under hydrogen flow at 400 °C for 30 min and evacuated for another 30 min. The temperature was decreased to 35 °C and H_2 chemisorption analysis was performed. A H_2/Pt stoichiometry of 2 was used to calculate metal dispersion. To determine the amount of Pt metal deposited, Pt/HBEA was sent to Galbraith Laboratories for inductively coupled plasma-atomic emission spectroscopy (ICP-AES) analysis. X-ray diffraction (XRD) patterns were obtained using a Philips X'pert diffractometer equipped with an X'celerator module using Cu Kα radiation. Diffractograms were collected at incident angles from $2\theta = 5$ to 70° with a step size of 0.0167°. ^{27}Al MAS NMR spectroscopy was performed with a Bruker DSX 400 spectrometer. The samples were inserted into a 4 mm zirconia rotor and spun at 12 kHz. At this spectrometer, ^{27}Al has a resonance frequency of 104.2 MHz. A $\pi/12$ pulse was used for excitation, and a recycling delay of 250 ms was used. Pyridine adsorption followed by FTIR spectroscopy was performed using a Nicolet 8700 FTIR Spectrometer with an MCT/A detector. Each spectrum was recorded with 64 scans with a resolution of 4 cm^{-1}. Each sample was pressed into a self-supported wafer and loaded into a vacuum FTIR transmission cell. The sample was activated at 400 °C for 1 h under high vacuum and cooled down to 100 °C. A background spectrum was taken. The chamber was dosed with 0.10 mbar of pyridine for 30 min. Subsequently, the cell was evacuated for 12 h to remove physisorbed pyridine and a spectrum was taken. To determine the strength of acid sites, the sample was heated to 200 °C, 300 °C and 400 °C for 1 h, and a spectrum was taken at 100 °C. After each experiment, the density of the wafer was determined by using a circular stamp of 6.35 mm to cut a disc of specific size from the wafer. The concentration of Lewis and Brønsted acid sites were determined by the integral of the

peaks at 1445 cm^{-1} and 1540 cm^{-1}, respectively. Extinction coefficients used were reported by Selli et al.[39]

5.2.4 Catalytic Performance

Reactivity experiments for the hydrodeoxygenation of anisole, m-cresol and guaiacol were performed in a trickle-bed reactor setup. A stainless steel tube (0.25 inch outer diameter with a wall thickness of 0.035 inch) was used as the reactor. The reactor was mounted in an insulated furnace. A thermocouple was placed at the middle of the reactor and it was connected to a Eurotherm 2416 Temperature Controller. The catalyst (HBEA or 1.3 wt% Pt/HBEA) was mixed with silicon carbide. The catalyst bed with a volume of 1 ml was used in all experiments. Quartz wool was placed at both ends of the catalyst bed to keep the catalyst in place. The organic model compound was fed into the reactor using an Agilent 1100 Series HPLC pump. Each experiment was performed at 400 °C and atmospheric pressure. HBEA and Pt/HBEA was reduced in the reactor for 1 h at 400 °C with 80 ml/min of hydrogen flow before the model compound was fed. All of the lines were heated to 300 °C to prevent condensation. A total hydrogen gas flow rate of 80 ml/min was used during reaction. The H_2/reactant molar ratio was kept above 50. The weight to feed ratio (W/F) is defined as the ratio between the mass of the catalyst (g_{cat}) and the molar flow rate of the reactant ($mmol_{feed}\ h^{-1}$). The products were directly analyzed and quantified online using an Agilent 7890A Gas Chromatograph equipped with a HP-5 column and a flame ionized detector. The Weisz-Prater criterion was applied to ensure that all experiments were performed under conditions free of mass transfer limitation (see Supporting Information). The following definitions are used:

$$Conversion\ (\%) = \frac{moles\ of\ carbon\ in\ reactant\ consumed}{moles\ of\ carbon\ in\ reactant\ fed} \times 100\% \quad (1)$$

$$Yield\ (\%) = \frac{moles\ of\ carbon\ in\ product}{moles\ of\ carbon\ in\ reactant\ fed} \times 100\% \quad (2)$$

5.2.5 Adsorption of Model Bio-oil Compounds on HBEA

The adsorption of anisole, m-cresol and guaiacol on HBEA was observed using a Nicolet 8700 FTIR spectrometer with an MCT/A detector. Each spectrum was recorded with 64 scans at a resolution of 4 cm^{-1}. For the adsorption of anisole, HBEA was pressed into a self-supported wafer and loaded into a vacuum FTIR transmission cell. The sample was activated at 400 °C for 1 h under high vacuum. Subsequently, a background spectrum was taken at 400 °C, 300 °C, 200 °C and 100 °C. At 100 °C, anisole was introduced into the vacuum cell and maintained at a pressure of 0.100 mbar for 15 min. The cell was evacuated for 30 min and a spectrum was taken. The sample was heated at 200 °C, 300 °C and 400 °C for 1 h and a spectrum was taken at each temperature. For the adsorption of m-cresol and guaiacol, HBEA was initially impregnated with the model compounds. About 250 mg of HBEA was mixed with 10 ml of chloroform solution that had 6 mg of m-cresol or guaiacol dissolved in it. The slurry was dried in a fume hood to allow chloroform to evaporate. Subsequently, the impregnated samples are pressed into a self-supported wafer and loaded into a vacuum transmission FTIR cell. The sample was evacuated under high vacuum ($<10^{-6}$ mbar), heated at 100 °C, 200 °C, 300 °C and 400 °C for 1 h, and a spectrum was collected at each temperature. A dried HBEA sample that was mixed with 10 ml of pure chloroform was used as a subtrahend for difference spectra under the same temperature.

5.2.6 *Operando* Transmission FTIR Spectroscopy

The catalyst was pressed into a circular self-supported wafer with a diameter of 2 cm. The wafer was loaded into a sample holder and it was assembled as part of the FTIR cell together with the cell body and heating block. The cell was built based on a design reported in literature as it has no heat and mass transfer limitation.[40] The *operando* FTIR cell was validated by comparing its kinetic data with the flow reactor (see Supporting Information). The assembled FTIR cell was placed into a Nicolet 8700 FTIR

spectrometer. Each spectrum was recorded with 32 scans at a frequency of one per minute for 8 h during reaction. Similar to the trickle bed reactor, the *operando* FTIR experiments were also performed at 400 °C, atmospheric hydrogen pressure (80 ml/min), and at a fixed W/F ratio of 0.0109 g_{cat} $(mmol_{feed}\ h^{-1})^{-1}$. The model compound was fed into the *operando* FTIR cell using an Agilent 1100 Series HPLC pump. All lines were heated to 300 °C to prevent condensation. The effluent line was connected to a Hiden HPR-20 QIC mass spectrometer to monitor the signal of the product stream over time, which is based on the mass of the known products from reactivity experiments.

5.2.7 Thermalgravimetric Analysis

Thermalgravimetric analysis **(**TGA) of each spent catalyst from the *operando* FTIR cell was completed using a Setsys Evolution TGA-DSC instrument from Setaram. Samples of ca. 20 mg were stabilized in zero air flowing at 50 mL/min at room temperature for 7 min before heating to 780 °C at 20 °C/min. This temperature was maintained for 20 min before the samples were cooled. Weight loss below 250°C was attributed to moisture and weight loss above 250°C was attributed to carbonaceous. Coke content (%) are reported on a moisture-free, coke-free catalyst basis.

5.3 Results

5.3.1 Catalyst Characterization

The results of nitrogen physisorption and hydrogen chemisorption are shown in Table 5.1. The surface area and pore volume of Pt/HBEA is slightly different compared to HBEA. H_2 chemisorption result indicated that the dispersion of Pt metal is 54%, while the average Pt particle size is 2.1 nm.

Table 5.1 Nitrogen physisorption and hydrogen chemisorption results.

Sample	N_2 Physorption		H_2 Chemisorption	
	Surface Area (m^2/g)	Pore volume (cm^3/g)	Dispersion (%)	Particle Size (nm)
HBEA	550	0.403	-	-
1.3 wt% Pt/HBEA	521	0.435	54	2.1

The XRD patterns of HBEA and Pt/HBEA contained characteristic peaks of HBEA at 7.7°, 21.6° and 22.6°, which corresponds to (1 0 1), (2 0 5) and (1 1 6) planes, respectively (Figure D.2).[41] In the case of Pt/HBEA, additional peaks were observed at 39.5° and 46.2°. These are assigned as the (1 1 1) and (2 0 0) planes of larger Pt particles (> 5nm).[18] Figure D.3 shows the ^{27}Al MAS NMR spectra of HBEA and Pt/HBEA. Both samples displayed peaks at 53 ppm and 0 ppm, which are assigned as tetrahedrally and octahedrally coordinated aluminum species, respectively.[42] Framework aluminum species are tetrahedrally coordinated while extra framework aluminum species are octahedrally coordinated.

The concentration of Lewis (LAS) and Brønsted acid sites (BAS) on Pt/HBEA was lower compared to HBEA (Figure 5.1). This is probably due to the presence of the Pt metal blocking some of the acid sites. All of the spent catalysts had lower concentrations of accessible acid sites. All of the spent Pt/HBEA catalysts had higher concentrations of Lewis acid sites compared to the corresponding spent HBEA samples.

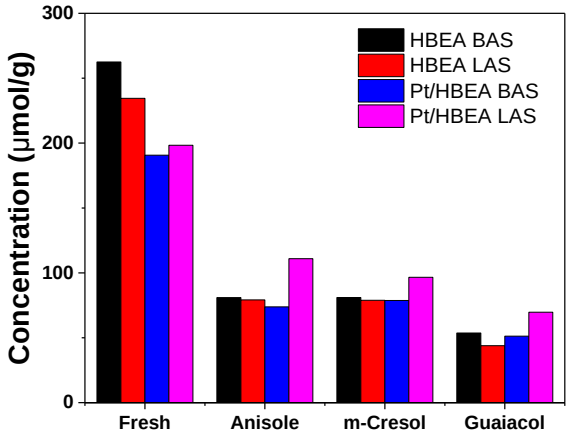

Figure 5.1 Concentration of Lewis (LAS) and Brønsted acid sites (BAS) of fresh and spent HBEA and Pt/HBEA catalysts. Reaction conditions: 400 °C, 80 ml/min H_2, W/F = 0.0109 g_{cat} $(mmol_{feed}\ h^{-1})^{-1}$.

5.3.2 Reactivity of Bio-Oil Model Compounds

Figure 5.2A shows the conversion of anisole over HBEA and Pt/HBEA. The conversion over HBEA started at 60% and decreased with increasing time on stream. For Pt/HBEA, there was a 100% conversion in the first 2 h, followed by slow deactivation. The products from HBEA were phenol, cresol, methylanisole and xylenol (Figure D.3A). In addition to these products, Pt/HBEA produced deoxygenated aromatics such as benzene, toluene and xylene (Figure D.3B and D.3C). In the case of m-cresol, Pt/HBEA initially showed a slightly higher conversion than HBEA (Figure 5.2B). With increasing time on stream, HBEA deactivated at a faster rate than Pt/HBEA. The products of m-cresol over HBEA were only p-cresol and o-cresol (Figure D.4A). However, in the presence of Pt metal, toluene and small amounts of methane and phenol were produced (Figure D.4B). Figure 5.2C shows the conversion of guaiacol over HBEA and Pt/HBEA. The conversion of guaiacol over HBEA was less than 5%. The addition of Pt metal increased the initial conversion increased to 60%, and it slowly decreased to 35% after 8

h. The products from HBEA were only isomers of methylcatechol (Figure D.5A). For Pt/HBEA, a wide variety of products was observed. Deoxygenated aromatics such as benzene and xylene were produced with methane (Figure D.5B). Among the oxygenated products, catechol was produced in a higher yield compared to phenol, cresol, xylenol, methylcatechol and high molecular weight products (Figure D.6C).

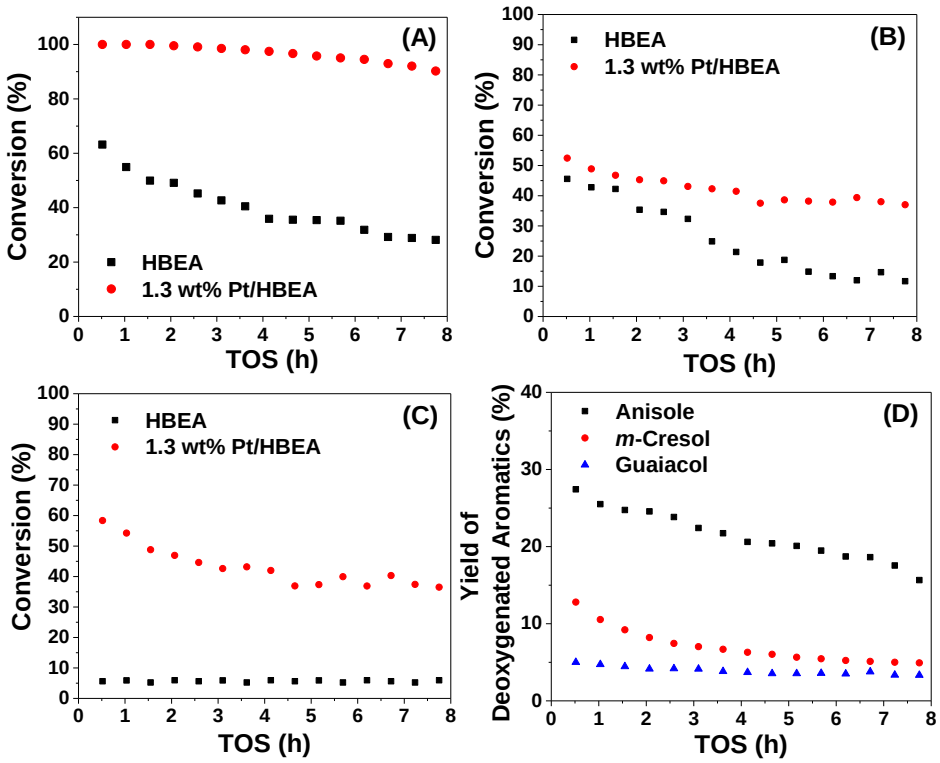

Figure 5.2 Conversion of (A) anisole, (B) m-cresol, (C) guaiacol over HBEA and 1.3 wt% Pt/HBEA, (D) yield of deoxygenated aromatics from anisole, m-cresol and guaiacol over 1.3 wt% Pt/HBEA. Reactions conditions: 400 °C, 80 ml/min H_2, W/F = 0.0109 g_{cat} $(mmol_{feed}\ h^{-1})^{-1}$.

Figure 5.2D compares the yield of deoxygenated aromatics from different bio-oil model compounds over Pt/HBEA under the same reaction conditions. As shown in Figure D.4, the deoxygenated aromatics from anisole consisted of benzene, toluene and

xylene. m-Cresol over Pt/HBEA only produced toluene as a deoxygenated aromatic (Figure D.5), while guaiacol over Pt/HBEA yielded benzene and xylene (Figure D.6). At the first data point after 0.5 h on stream, anisole displayed the highest yield of deoxygenated aromatics, followed by m-cresol and guaiacol. With increasing time on stream, the yield of deoxygenated aromatics from anisole and m-cresol decreased more rapidly compared to guaiacol.

5.3.3 FTIR Spectra of Anisole Adsorbed on HBEA

At room temperature, the FTIR spectrum of anisole on HBEA was similar to the spectrum of liquid anisole (Figure 5.3). The peaks at 1602 cm^{-1}, 1587 cm^{-1} and 1500 cm^{-1} are attributed to $\nu(C=C)_{ring}$ vibrations.[34, 43] The peaks at 1470 cm^{-1} and 1454 cm^{-1} are due to the $\delta_{asym}CH_3$ vibrations of the methoxy group, while the peak at 1443 cm^{-1} is assigned as the $\delta_{sym}CH_3$ vibration. As the temperature increased, the peaks at 1602 cm^{-1} and 1587 cm^{-1} merged into a band at 1592 cm^{-1}, while the peak at 1500 cm^{-1} red-shifted to 1495 cm^{-1}, indicating that the aromatic ring is interacting with Lewis acid sites to a certain extent.[34] The triplet peaks at 1470-1443 cm^{-1} merged into a band at 1458 cm^{-1}, which has been assigned as the $\delta_{asym}CH_3$ vibration of surface methyl groups attached to an oxygen atom.[34, 44] Its $\delta_{sym}CH_3$ vibration (1100 cm^{-1}) could not be observed due to the structural vibration of HBEA. By 400 °C, major changes were observed. Shoulders at 1525 cm^{-1} and 1508 cm^{-1} emerged, and they are due to the aromatic ring vibrations of para-disubstituted, and ortho- and meta-disubstituted benzenes, respectively.[43, 45] The peaks due to aromatic stretching vibrations at 1592 cm^{-1} and 1495 cm^{-1} shifted to 1596 cm^{-1} and 1491 cm^{-1}, respectively. This is probably due to the emergence of the new aromatic species. The emerging weak peak at 1383 cm^{-1} is attributed to the deformation vibration of CH_3 groups attached to aromatic rings.

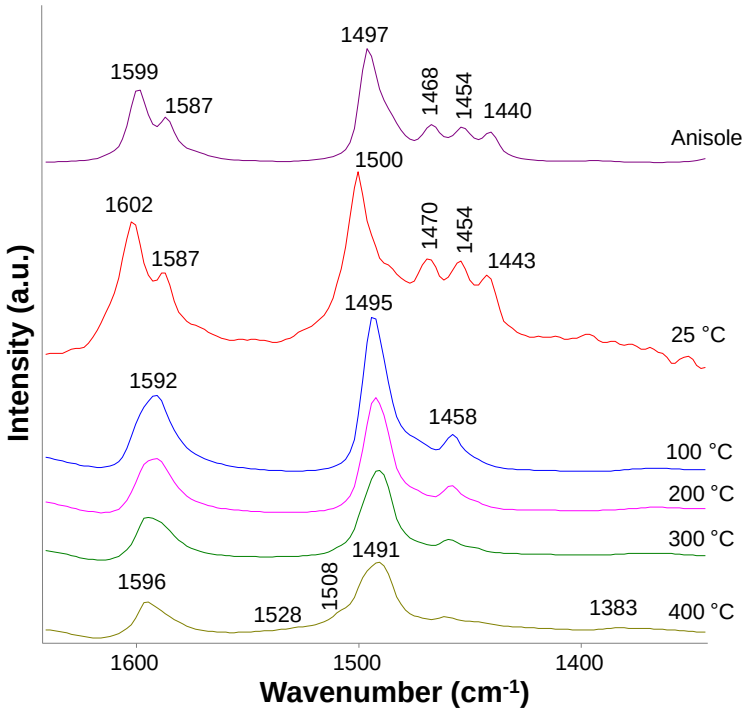

Figure 5.3 FTIR spectra of anisole adsorbed on HBEA at various temperatures.

5.3.4 FTIR Spectra of m-Cresol Adsorbed on HBEA

Figure 5.4 shows the FTIR spectra of m-cresol adsorbed on HBEA. At room temperature, a broad peak at 1635 cm^{-1} was observed, and this is due to physisorbed water. Additional peaks at 1489 cm^{-1} and 1452 cm^{-1} were also observed. As the temperature increased, the broad peak at 1635 cm^{-1} vanished, revealing three peaks at 1635 cm^{-1}, 1599 cm^{-1} and 1583 cm^{-1}. Furthermore, a broad peak at 1527 cm^{-1} was observed. The peaks at 1599 cm^{-1}, 1583 cm^{-1} and 1489 cm^{-1} are due to the $\nu(C=C)_{ring}$ vibrations of m-cresol.[43] The asymmetrical δCH_3 vibrations of the methyl group of pure m-cresol are observed at 1462 cm^{-1} and 1437 cm^{-1}. However, these two peaks became a broad peak at 1452 cm^{-1}, indicating that the methyl group has dissociated to form a surface CH_3.[34, 44] In addition, three more peaks were observed at 1389 cm^{-1}, 1352 cm^{-1} and 1327 cm^{-1}. The two former peaks are most likely related to the asymmetrical and symmetrical deformation vibration of a methyl group attached to an aromatic ring,

respectively.[43] These two peaks are not observed for pure m-cresol due to the broad peak at 1333 cm^{-1}, which is assigned as the phenolic δOH vibration.[46] When it is adsorbed on HBEA, this broad peak vanished. The rise of a peak at 1327 cm^{-1} with increasing temperatures could be attributed to ν(C-O) vibration. The two new peaks at 1635 cm^{-1} and 1527 cm^{-1} are most likely related to $\nu(C=C)_{ring}$ vibrations of new aromatic species that have been formed.

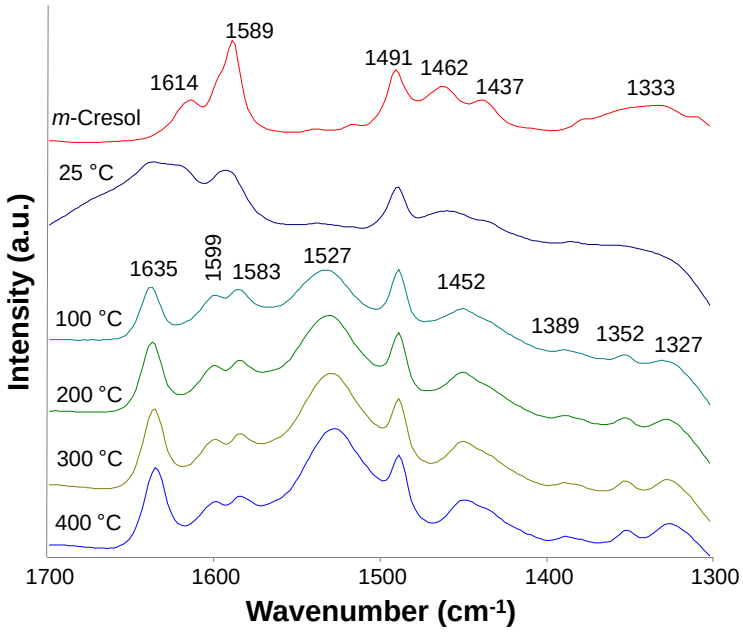

Figure 5.4 FTIR spectra of m-cresol adsorbed on HBEA at various temperatures.

5.3.5 FTIR Spectra of Guaiacol Adsorbed on HBEA

For the adsorption of guaiacol on HBEA at room temperature, a peak at 1632 cm^{-1} was observed and it is due to the presence of physisorbed water (Figure 5.5). The shoulder at 1610 cm^{-1} and the intense peak at 1497 cm^{-1} are assigned as the $\nu(C=C)_{ring}$ vibrations of the aromatic ring. The peaks around 1467 cm^{-1} are attributed to the δCH_3 vibrations of the methoxy group. Compared to pure guaiacol, the peak at 1360 cm^{-1} vanished when guaiacol is adsorbed on HBEA at room temperature. This indicates that

the hydrogen atom on the phenol has dissociated.[34] This peak has been assigned as the δOH vibration of the phenol group.[34] In addition, two peaks at 1327 cm^{-1} and 1292 cm^{-1} appeared, which are due to ν(C-O) vibration. As the temperature increased, the peak due to physisorbed water vanished, while the intensity for the rest of the peaks decreased slightly.

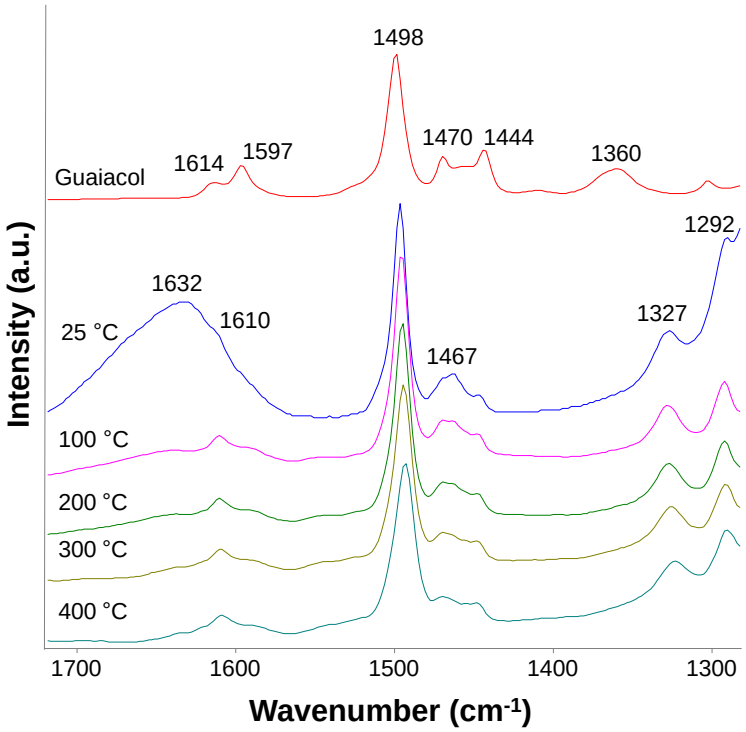

Figure 5.5 FTIR spectra of guaiacol adsorbed on HBEA at various temperatures.

5.3.6 *Operando* FTIR Spectra of Anisole over HBEA and Pt/HBEA

To understand and observe the evolution of surface species over time, an *operando* transmission FTIR gas flow cell was used under the same reaction conditions as the trickle bed reactor. The assignment for the relevant FTIR peaks are shown in Table 5.2. The *operando* FTIR cell was validated by comparing its kinetic result with the trickle bed reactor (Figure D.1). Figure 5.6A shows the FTIR spectra of anisole over HBEA in

10 min and multiple peaks were observed. The intense peak at 1595 cm^{-1} is assigned as the $\nu(C=C)_{ring}$ vibration of asymmetric aromatic compounds, while the small shoulder at 1560 cm^{-1} is due to the $\nu(C=C)_{ring}$ vibration of strongly adsorbed polynuclear aromatic species.[43, 45, 47] These polynuclear aromatic species are similar to compounds such as anthracenes and naphthalenes. The peak at 1530 cm^{-1} is attributed to *para*-disubstituted and 1,2,4-trisubstituted aromatics, while the shoulder at 1507 cm^{-1} is usually observed for *ortho*- and *meta*-disubstituted, and 1,2,3-trisubstituted aromatics.[43] The band at 1493 cm^{-1} is characteristic of aromatic rings. The peaks at 1455 cm^{-1} and 1379 cm^{-1} are attributed to the $\delta_{asym}CH_3$ vibration of a methyl group.[48] However, the peak at 1455 cm^{-1} can also be interpreted as the δCH_3 vibration of a CH_3 group attached to a surface oxygen.[34] Within 2 min on stream, vibrational modes due to various aromatic monomers were observed, along with the δCH_3 vibration of surface and aromatic methyl group. The formation of polynuclear aromatics (1560 cm^{-1}) was only observed after 4 min of time on stream, appearing as a shoulder. Subsequently, its intensity increased with increasing time on stream.

Table 5.2 FTIR peak assignments for hydrodeoxygenation of bio-oil model compounds.

Frequency (cm^{-1})	Assignment	Group	References
1600	$\nu(C=C)_{ring}$	Asymmetrical aromatics	43, 45
1593 - 1583	$\nu(C=C)_{ring}$	Aromatic six-membered rings	33, 43, 45
1500 - 1483	$\nu(C=C)_{ring}$		
1580 - 1570	$\nu(C=C)_{ring}$	Coke	49, 50, 51
1560 - 1540	$\nu(C=C)_{ring}$	Polynuclear aromatics	43, 47
1537 – 1518	$\nu(C=C)_{ring}$	*Para*-disubstituted aromatics 1,2,4-trisubstituted aromatics	43, 45
1507 – 1504	$\nu(C=C)_{ring}$	*Ortho*- and *meta*-disubstituted aromatics 1,2,3-trisubstituted aromatics	43, 45
1450	δCH_3	Surface methyl group	33, 34
1390 - 1370	$\delta_{asym}CH_3$	Aromatic methyl group	43, 45, 48
1350	$\delta_{sym}CH_3$		

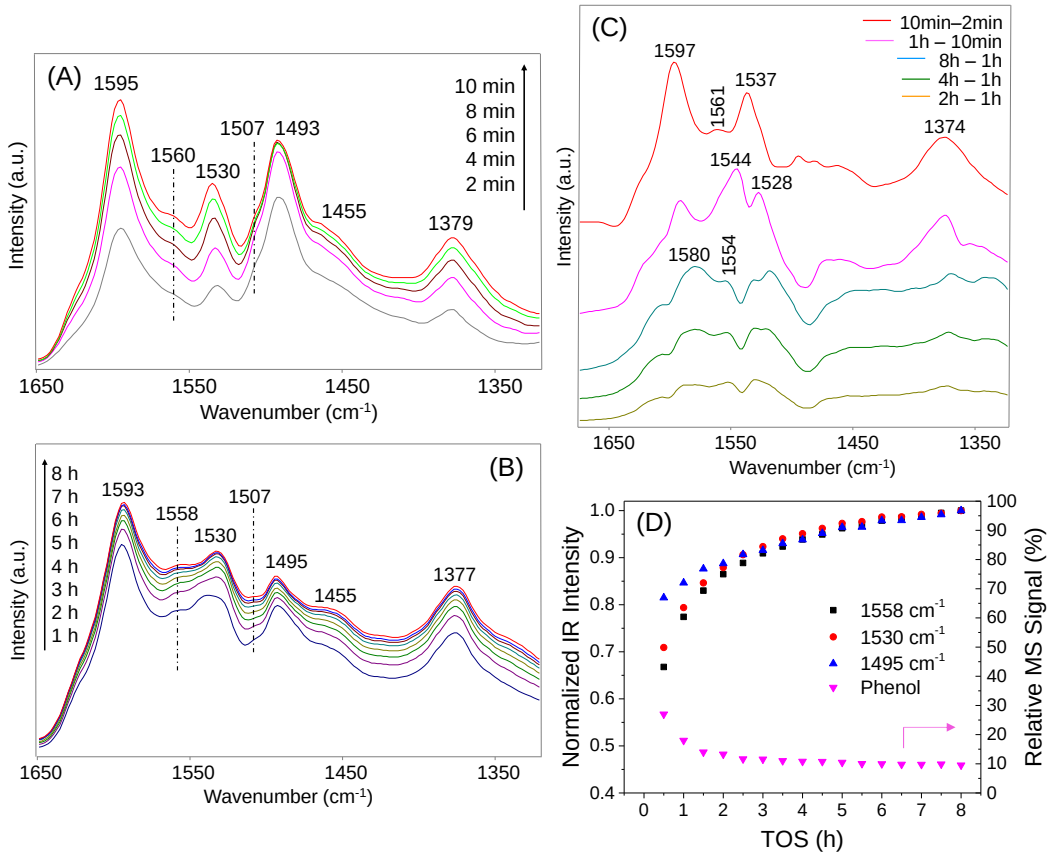

Figure 5.6 FTIR spectra of anisole over HBEA in (A) 10 min, (B) 8 h, (C) Difference FTIR spectra at various time scales, (D) Normalized IR intensity of peaks and relative MS signal of phenol,. Reactions conditions: 400 °C, 80 ml/min H_2, W/F = 0.0109 g_{cat} $(mmol_{feed}\ h^{-1})^{-1}$.

Over 8 h of time on stream, the intensity of all the peaks increased at a diminishing rate, indicating that the surface was approaching saturation (Figure 5.6B). The peaks at 1593 cm^{-1} and 1377 cm^{-1} became very intense, revealing that most of the aromatic monomers were asymmetrically substituted with methyl groups. To further elucidate the evolution of surface species over time, difference FTIR spectra at various time scales were shown for anisole over HBEA (Figure 5.6C). On a short time scale (10 min – 2 min), the growth of monoaromatics (1597 cm^{-1} and 1537 cm^{-1}) and methyl

groups (1374 cm^{-1}) was evident. A small amount of polynuclear aromatics (1561 cm^{-1}) was observed. Within 1 h, an intense peak at 1544 cm^{-1} appeared. It was reported that peaks between 1540-1550 cm^{-1} were not affected by N_2 flushing in the study of coke formation and have also been assigned as strongly adsorbed polynuclear aromatic species.[47] The frequency of substituted aromatics red-shifted to 1528 cm^{-1}, indicating that it had heavier or more substituents present.[43] At longer time scales (8 h to 2 h), the intensity of the peak at 1580 cm^{-1} increased, which is usually found for graphite and activated carbon, and is assigned as the $\nu(C=C)_{ring}$ of coke species.[49-51]

Figure 5.6D shows the normalized IR intensity of various peaks and the relative MS signal of phenol, the only product with reduced molecular mass. In the first 2 h of reaction, the relative MS signal of phenol decreased rapidly. The intensity of the polynuclear (1558 cm^{-1}) and substituted aromatics (1530 cm^{-1}) peaks followed an opposite trend, where it increased rapidly during the first 2 h, and continued to grow at the same rate compared to the aromatic six-membered rings (1495 cm^{-1}).

Figure 5.7A shows the FTIR spectra of anisole over Pt/HBEA over 8 h. Most of the same peaks as during the conversion of anisole over HBEA were observed (1593 cm^{-1}, 1525 cm^{-1}, 1507 cm^{-1}, 1492 cm^{-1}, 1452 cm^{-1} and 1375 cm^{-1}), and they have the same assignments as anisole over (Figure 5.6A). However, the peak due to polynuclear aromatics (1558 cm^{-1}) was not observed. The intensity of the peak due to asymmetrical aromatic species (1593 cm^{-1}) was comparable to the general six-membered aromatics (1492 cm^{-1}), as most of the deoxygenated products produced are symmetrical (benzene and toluene). For the difference FTIR spectra of anisole over Pt/HBEA at short time scale (10 min – 2 min), substituted monoaromatics (1596 cm-1, 1533 cm^{-1} and 1493 cm^{-1}) and methyl groups (1375 cm^{-1}) were also observed (Figure 5.7B). Between 10 min and 1 h time on stream, polynuclear aromatics (1546 cm^{-1}) were formed, but the peak was not as intense as compared to anisole over HBEA. The frequency of substituted aromatics also

red-shifted to 1527 cm^{-1}. At longer time scales, coke species (1580 cm^{-1}) began to grow with heavily substituted aromatics (1518 cm^{-1}).

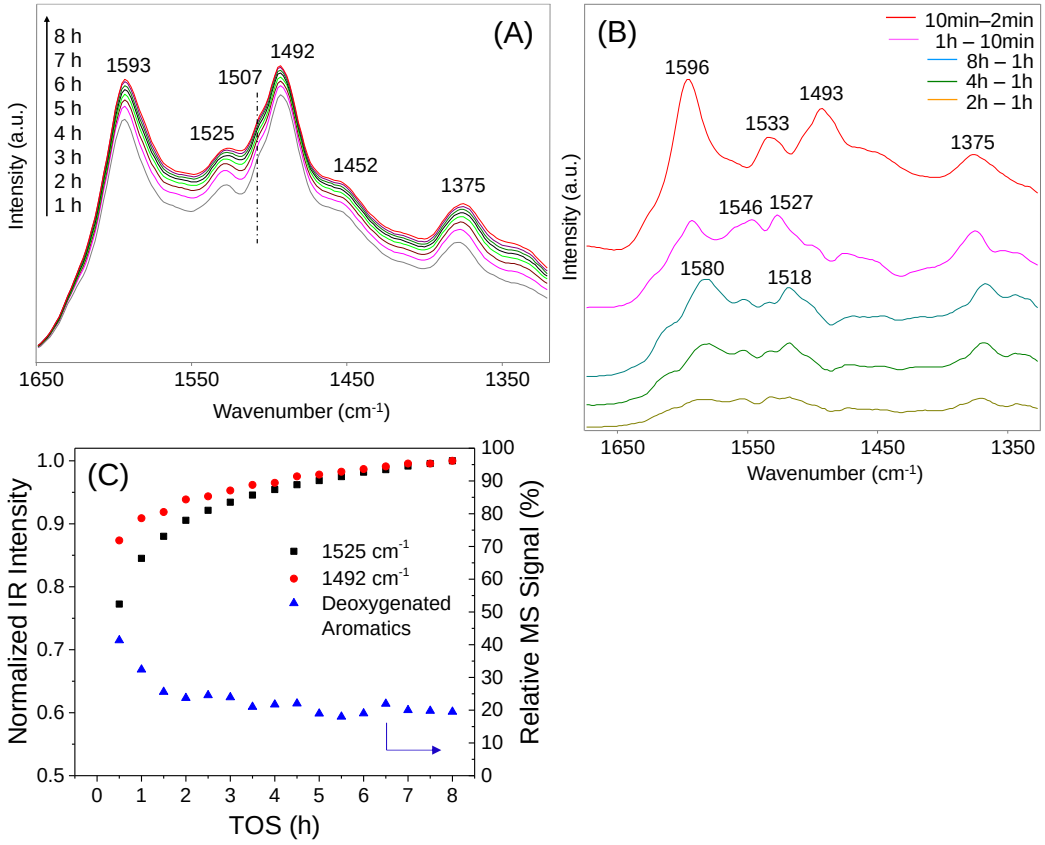

Figure 5.7 (A) FTIR spectra of anisole over 1.3 wt% Pt/HBEA in 8 h, (B) Difference FTIR spectra at various time scales, (C) Normalized IR intensity of peaks and relative MS signal of deoxygenated aromatics. Reactions conditions: 400 °C, 80 ml/min H_2, W/F = 0.0109 g_{cat} $(mmol_{feed}\ h^{-1})^{-1}$.

The relative MS signal of the deoxygenated aromatics (benzene, toluene and xylene) decreased rapidly in the first 2 h of reaction, while the normalized IR peak intensity of the substituted aromatic monomers (1525 cm^{-1}) increased rapidly relative to 1492 cm^{-1} (Figure 5.7B).

5.3.7 *Operando* FTIR Spectra of m-Cresol over HBEA and Pt/HBEA

The FTIR spectra of m-cresol over HBEA in the first 10 min of reaction showed the rise of several bands (Figure 5.8A). The peak at 1600 cm^{-1} is also assigned as asymmetric aromatic species, while the peaks at 1583 cm^{-1} and 1486 cm^{-1} are attributed to the $\nu(C=C)_{ring}$ vibrations of six-membered aromatic rings.[43, 45] After about 4 min of reaction, a shoulder at 1568 cm^{-1} appeared, and it is assigned to the presence of polynuclear aromatics.[47] Similarly, the growing shoulder at 1527 cm^{-1} is usually observed for *para*-disubstituted aromatics, while the peak at 1506 cm^{-1} is likely due to *ortho*- and *meta*-disubstituted aromatics. The δCH_3 vibration of the surface CH_3 group occurs at 1439 cm^{-1} and 1390 cm^{-1},[34, 44] while the asymmetric and symmetric δCH_3 vibration of methyl groups attached to an aromatic ring are observed at 1390 cm^{-1} and 1354 cm^{-1}, respectively. Initially, cresols are observed, indicating that isomerization is occurring over HBEA. However, after 4 min time on stream, the peak due to polynuclear aromatics (1568 cm^{-1}) appeared, while the peak due to asymmetric aromatics (1600 cm^{-1}) became increasingly intense.

Figure 5.8B shows the FTIR spectra of m-cresol over HBEA in 8 h. The intensity of all the peaks increased at a diminishing rate, indicating that the surface of the catalyst was approaching saturation. The peak at 1600 cm^{-1} was the most intense, as the surface was largely populated by asymmetric aromatic species. For the difference FTIR spectra of m-cresol over HBEA, an intense peak due to asymmetrical monoaromatics (1600 cm^{-1}) was observed on a short time scale (Figure 5.8C). Substituted monoaromatics (1591 cm^{-1}, 1506 cm^{-1} and 1485 cm^{-1}), methyl groups (1439 cm^{-1}, 1390 cm^{-1} and 1354 cm^{-1}), and polynuclear aromatics (1570 cm^{-1}) were also formed. At longer time scales, the polynuclear aromatic peak red-shifted to 1554 cm^{-1}, probably indicating that it had heavier or more substituents.[43] Furthermore, coke-like species were also observed (1580 cm^{-1}).

Since the products (o- and p-cresol) have the same mass to charge ratio as m-cresol, the MS signal between these compounds could not be differentiated. Hence, only the normalized IR peak intensity could be compared in Figure 5.8D. The polynuclear aromatics (1568 cm^{-1}) rapidly reached its maximum intensity, followed by substituted monoaromatics (1506 cm^{-1}) and the peak assigned to general $\nu(C=C)_{ring}$ vibration (1487 cm^{-1}).

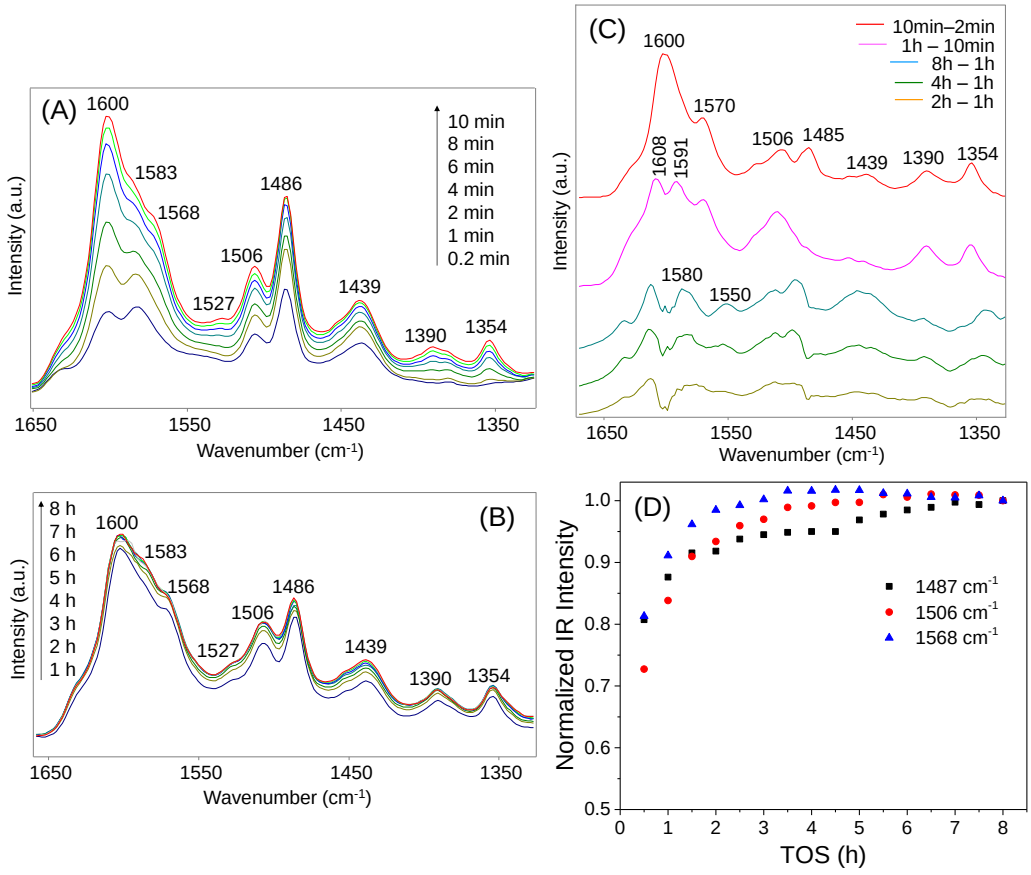

Figure 5.8 FTIR spectra of m-cresol over HBEA in (A) 10 min, (B) 8 h, (C) Difference FTIR spectra at various time scales, (D) Normalized IR intensity of peaks over time. Reactions conditions: 400 °C, 80 ml/min H_2, W/F = 0.0109 g_{cat} $(mmol_{feed}\ h^{-1})^{-1}$.

In the case of m-cresol over Pt/HBEA, the FTIR spectra shows the same peak at 1600 cm^{-1}, 1585 cm^{-1}, 1529 cm^{-1}, 1504 cm^{-1}, 1487 cm^{-1}, 1438 cm^{-1}, 1389 cm^{-1} and 1354 cm^{-1} (Figure 5.9A). These peaks have the same assignment as m-cresol over HBEA. However, the peak due to polynuclear aromatics (1568 cm^{-1}) was barely observed. Compared to m-cresol over HBEA, the intensity of the peak due to asymmetric aromatics at 1600 cm^{-1} is almost equivalent to 1487 cm^{-1} (general $\nu(C=C)_{ring}$ vibration). The overall intensity of the peaks also increased at a diminishing rate. The difference FTIR spectra of m-cresol over Pt/HBEA shows that substituted monomers (1603 cm^{-1}, 1527 cm^{-1}, 1506 cm^{-1}) and methyl groups (1435 cm^{-1}, 1390 cm^{-1} and 1354 cm^{-1}) were formed between 10 min and 2 min (Figure 5.9B). Compared to HBEA, the intensity of the peak due to polynuclear aromatics (1568 cm^{-1}) was lower. Coke-like species (1585 cm^{-1}) began to grow after 2 h, while the peaks due to monoaromatics (1493 cm^{-1}) remained to be very intense.

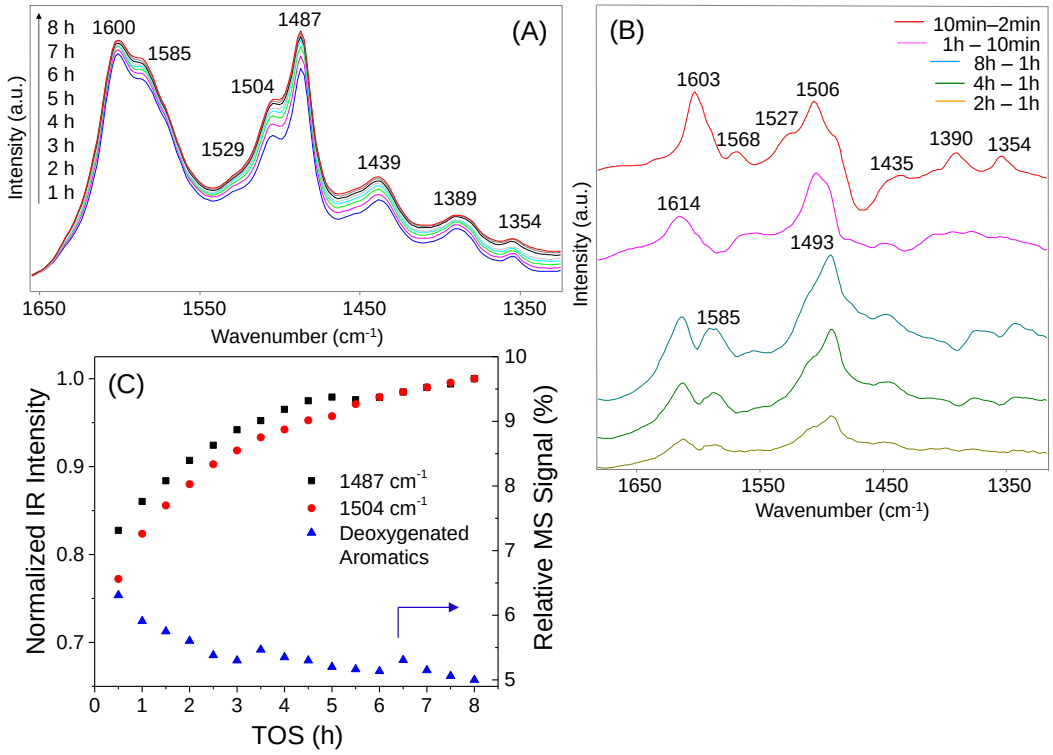

Figure 5.9 (A) FTIR spectra of m-cresol over 1.3 wt% Pt/HBEA in 8 h, (B) Difference FTIR spectra at various time scales, (C) Normalized IR intensity of peaks and relative MS signal of deoxygenated aromatics. Reactions conditions: 400 °C, 80 ml/min H_2, W/F = 0.0109 g_{cat} $(mmol_{feed}\ h^{-1})^{-1}$.

Figure 5.9C shows the normalized IR peak intensity of 1487 cm^{-1} (general $\nu(C=C)_{ring}$ vibration) and 1504 cm^{-1} (substituted monomers), and also the relative MS signal of deoxygenated aromatics (toluene) over time. Both peaks increased at the same rate. After 3 h of time on stream, the normalized intensity of the peak at 1487 cm^{-1} increased at a slower rate. The relative MS signal of toluene decreased rapidly in the first 3 h, followed by a slower decay.

5.3.8 *Operando* FTIR Spectra of Guaiacol over HBEA and Pt/HBEA

The FTIR spectra of surface species from guaiacol on HBEA over 8 h of time on stream showed four major peaks at 1583 cm^{-1}, 1500 cm^{-1}, 1450 cm^{-1} and 1374 cm^{-1} (Figure 5.10A). The peaks at 1583 cm^{-1} and 1500 cm^{-1} are assigned as $\nu(C=C)_{ring}$ vibrations, while the shoulder at 1450 cm^{-1} is attributed to δCH_3 vibrations of surface CH_3 group.[34, 44] The peak at 1374 cm^{-1} is related to δCH_3 vibrations of the methyl group attached to an aromatic ring. This indicates that there were two types of methyl groups present. The peaks for guaiacol over HBEA are extremely broad compared to anisole and m-cresol, suggesting that there could be contribution from other surface species, such as polynuclear aromatics (1560 cm^{-1}). This is shown in Figure 5.10C for the difference FTIR spectra of guaiacol over HBEA. At short time scales, both monoaromatic (1600 cm^{-1}) and coke (1570 cm^{-1}) peaks of similar intensity were observed. There is also a shoulder at 1540 cm^{-1}, which has been assigned as polynuclear aromatics.[47] With increasing time on stream, the peak at 1570 cm^{-1} became more intense, indicating that more coke-like species are formed on the surface.

Figure 5.10B shows the normalized IR peak intensity of the $\nu(C=C)_{ring}$ vibration (1583 cm^{-1}) and δCH_3 vibration (1374 cm^{-1}) of the methyl group. Both normalized IR peaks increased at the same rate, suggesting that the aromatic ring vibration is likely due to the presence of the transalkylated species.

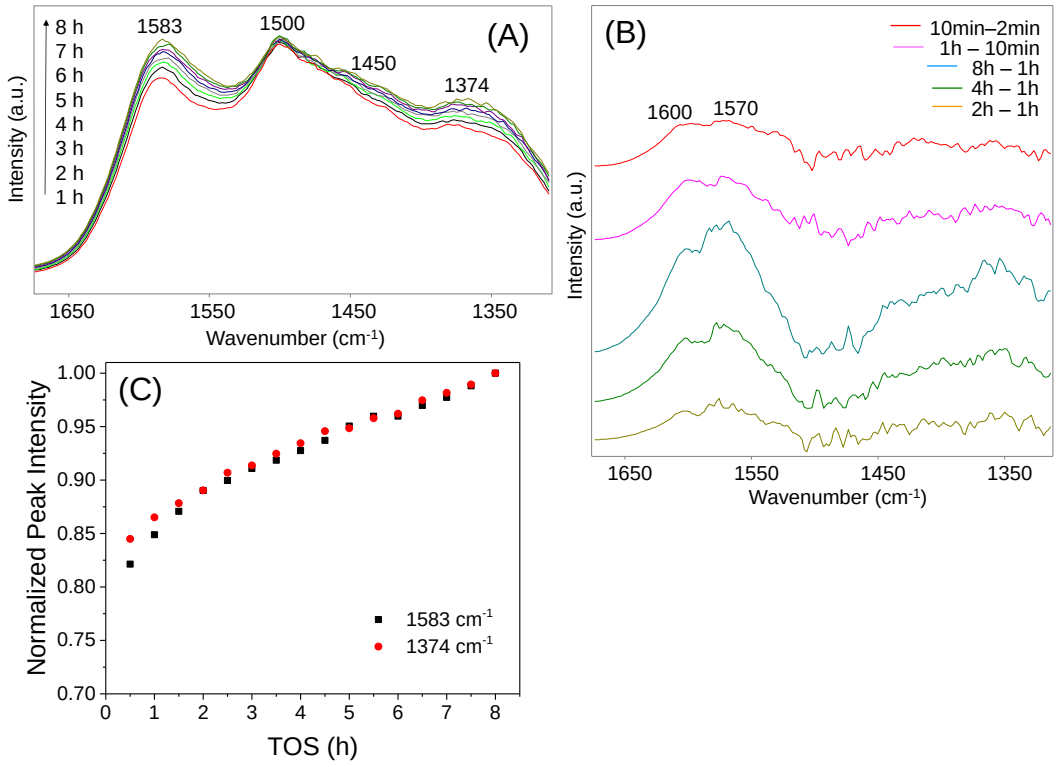

Figure 5.10. (A) FTIR spectra of guaiacol over HBEA in 8 h, (B) Normalized IR intensity of peaks over time, (C) Difference FTIR spectra at various time scales. Reactions conditions: 400 °C, 80 ml/min H_2, W/F = 0.0109 g_{cat} $(mmol_{feed}\ h^{-1})^{-1}$.

Figure 5.11A shows the FTIR spectra of guaiacol over Pt/HBEA in 8 h. Four broad peaks were also observed at 1589 cm^{-1}, 1502 cm^{-1}, 1452 cm^{-1} and 1380 cm^{-1}. These peaks have the same assignment as guaiacol over HBEA, indicating that transalkylated species were also present. For the difference spectra of guaiacol over Pt/HBEA, a shoulder at 1532 cm^{-1} (substituted monoaromatics) was observed in addition to asymmetrical aromatics (1606 cm^{-1}) and coke (1577 cm^{-1}) during short time scales (Figure 5.11B). At longer time scales, the intensity of the peak due to substituted monoaromatics decreased, while the intensity of the peak due to polynuclear aromatics increased.

Over 8 h of time on stream, only the intensity of the peaks at 1589 cm^{-1} and 1380 cm^{-1} increased. However, the increase in intensity was not significant (Figure 5.11C). The relative MS signal of deoxygenated aromatics (benzene and xylene) decreased with increasing time on stream.

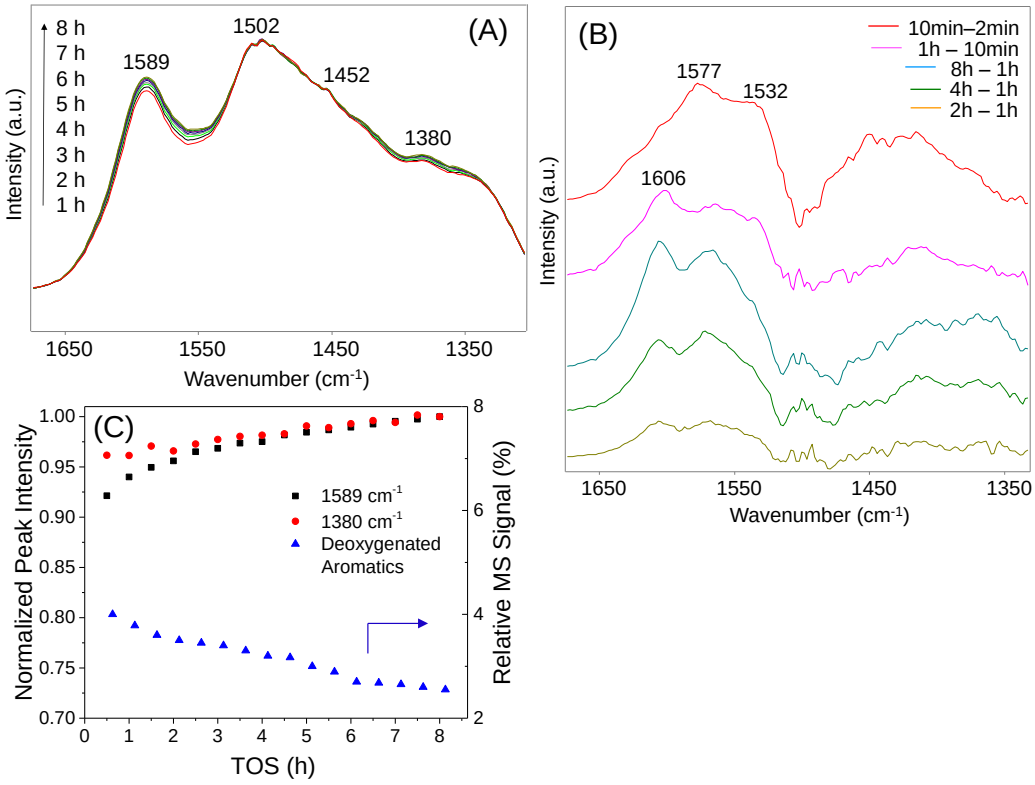

Figure 5.11. (A) FTIR spectra of guaiacol over 1.3 wt% Pt/HBEA in 8 h, (B) Normalized IR intensity of peaks and relative MS signal of deoxygenated aromatics, (C) Difference FTIR spectra at various time scales. Reactions conditions: 400 °C, 80 ml/min H_2, W/F = 0.0109 g_{cat} $(mmol_{feed}\ h^{-1})^{-1}$.

5.3.9 Thermalgravimetric Analysis

Table D.2 shows the coke content (%) of the spent HBEA and Pt/HBEA catalysts. Reactions with guaiacol produced the highest coke content, followed by m-cresol and

anisole, while all of the spent HBEA catalysts have more coke than spent Pt/HBEA. From the temperature-programmed oxidation (TPO) curves, the CO_2 evolution peak from spent HBEA occurred at a higher temperature compared to spent Pt/HBEA (Figure D.7). The peaks at 120 °C is related to the loss of water from the samples.

5.4. Discussion

5.4.1 Adsorption of Bio-Oil Model Compounds

There are limited reports on the adsorption of oxygenates that are typical for bio-oil model in literature. Popov et al. studied the adsorption of phenolic compounds on silica, alumina and sulfided CoMo catalysts.[34-36] On silica, it was reported that the aromatic compounds interact via hydrogen-bonding with silica hydroxyl groups. In the presence of Lewis acid sites on alumina, phenate species are formed. It was observed that the phenate species formed on alumina have limited interaction with the sulfide phase. The adsorption of m-cresol on sodium-exchanged zeolite was also reported.[46] Ion exchange between the acidic hydrogen of m-cresol and the sodium cation in zeolite was observed. However, none of these catalysts had Brønsted acid sites. Furthermore, sulfided CoMo catalysts are not attractive catalysts in HDO reactions as sulfur must be added into the feed to maintain its catalytic activity.[6-7] Since zeolites are commonly used in industry, it is crucial to understand the interaction of these phenolic compounds in the presence of Brønsted acid sites.

The adsorption of anisole on HBEA occurred through an interaction between the aromatic ring and catalyst surface above 100 °C while no interaction was observed at room temperature. This was indicated by the red-shift in the frequencies of the aromatic ring vibrations (Figure 5.3). In addition, the triplet bands of the methoxy was replaced by a single peak at 1458 cm^{-1}. It was suggested that the PhO-CH_3 bond was cleaved,

resulting in the formation of a surface methyl group.[34] This would also result in the formation of phenate species, which the oxygen atom is coordinated to a Lewis acid site. Unfortunately, the formation of the new ν(C-O) vibration could not be observed due to the strong structural vibrations of HBEA under 1300 cm^{-1}. The ν(C-O) vibrations of the phenate group on alumina were observed at 1295 cm^{-1} and 1248 cm^{-1}.[34] When the sample was heated to 400 °C, new aromatic species were formed as indicated by peaks at 1525 cm^{-1} and 1508 cm^{-1}. This indicates that reactions have occurred in the presence of Brønsted acid sites, as this was not observed for alumina.[34] The rise of the δCH_3 peak at 1383 cm^{-1} (aromatic methyl group) suggests that transalkylation occurred, where an aromatic hydrogen is substituted with a methyl group. This result agrees with the reactivity data of anisole over HBEA, where products such as cresols, xylenols and methylanisoles were produced (Figure D.4A), indicating that Brønsted acid sites are involved in the reaction.

Changes to its aromatic ring vibrations were observed when m-cresol is adsorbed on HBEA (Figure 5.4). Specifically, the red-shift and change in intensity of the peaks indicated that the aromatic ring of m-cresol interacted with the surface to a certain extent. The absence of the δOH vibration at 1333 cm^{-1} and the appearance of a ν(C-O) vibration at 1327 cm^{-1} suggest that a cresolate was formed,[52] which the hydrogen atom in the phenol group was dissociated and the oxygen atom is coordinated to a Lewis acid site. The ν(C-O) vibrational peak of the cresolate has a higher frequency compared to a phenolate, probably due to the presence of a methyl group that can stabilize the π bond.[23] The formation of two new peaks at 1635 cm^{-1} and 1527 cm^{-1} can be attributed to the isomerization of m-cresol to o- and p-cresol. p-Cresol has an intense $\nu(C=C)_{ring}$ vibration at 1514 cm^{-1}. In this case, it appears that its interaction with the surface caused a blue-shift in its aromatic vibrational frequency, indicating a higher electrodonation to the aromatic ring.[45, 53]

The adsorption of guaiacol on HBEA led to significant changes in the IR spectrum at room temperature compared to its liquid form (Figure 5.5). The disappearance of the δOH peak at 1360 cm^{-1} indicates that the hydrogen atom on the phenol group was dissociated. In addition, the appearance of two ν(C-O) peaks at 1327 cm^{-1} and 1292 cm^{-1} suggests that guaiacol has formed a bidentate surface species, or two different types of surface species. The continued existence and decreasing intensity of the methoxy vibrations around 1467 cm^{-1} indicates that some of the functional group remains intact. Thus, it is speculated that two surface species could be present. For the first species with the methoxy group present, the oxygen atom on the dissociated phenol group is coordinated to a Lewis acid site, while the oxygen atom of the methoxy group is engaged in a Lewis acid/base interaction, forming a methoxy phenate species. Similar interactions were observed for glycerol adsorbed on various metal oxides.[54-56] For the second species with the decomposed methoxy group, both of the oxygen atoms could be coordinated to one or more Lewis acid site, forming a doubly anchored phenate. This result is different compared to guaiacol adsorbed on alumina, which the methoxy group on guaiacol was decomposed to a surface methyl group by 100 °C.[34] Since Brønsted acid sites were not present, additional aromatic species are not formed. Interestingly, the PhO-Me bond dissociation energy in anisole was calculated to be around 58 kcal/mol, which is only 8 kcal/mol higher compared to guaiacol.[29] Nevertheless, the methoxy group in anisole decomposed easily. Hence, the difference in reactivity between anisole and guaiacol over HBEA can be largely attributed to steric effect, which is induced by the addition of an adjacent phenolic functional group in guaiacol.

5.4.2 Hydrodeoxygenation of Bio-oil Model Compounds

The hydrodeoxygenation of bio-oil model compounds has been studied over a wide variety of catalysts. These catalysts include sulfided NiMo and CoMo,[6-8] noble and base metals,[13-15, 18-23, 26] reducible metal oxides,[29-31] as well as carbides.[32] However, most

studies reported the HDO of only one model compound, such as anisole or guaiacol. Since bio-oil consists of different types of phenolics, it is useful to compare the HDO of various bio-oil model compounds under the same reaction condition. In this way, the effect of different functional groups and its position on the aromatic ring can be correlated to its reactivity.

Several HDO reaction mechanisms have been proposed for different types of catalysts. For the HDO of anisole over Mo_2C catalyst, it was found that the Ph-OMe bond was preferentially cleaved, producing benzene with high selectivity.[32] Based on reactivity results, the authors proposed that two separate active sites are required for the activation of hydrogen and anisole, and metallic sites are involved. However, in the case of reducible metal oxides such as MoO_3 and ceria-zirconia, it was proposed that a reverse Mars-van Krevelan reaction would occur.[29-31] Specifically, the oxygenated aromatic compounds would interact with surface oxygen vacancies and the Ph-O bond is also preferentially cleaved. Subsequently, the oxygen vacancy is regenerated by reduction with hydrogen. For sulfided NiMo and CoMo catalysts, a similar HDO mechanism was proposed with sulfur vacancies.[4-5]

In literature, most studies on HDO were performed over supported metals on metal oxides. On metals such as Pd, Ru, and Ni, the aromatic rings of reactants are preferentially hydrogenated. [12-15, 20, 26] This is followed by dehydration by an acidic support such as a zeolite, and the unsaturated carbon-carbon bond is hydrogenated again. Fe particles supported on poorly-acidic SiO_2 converted guaiacol to HDO products that retained their aromaticity.[57] Since guaiacol adsorbs on the silica support via its oxygen atoms rather than its aromatic ring, Olcese et al. proposed that the Ph-O bond is favorably attacked by spilt-over hydrogen species from the Fe metal particles. For the HDO of bio-oil model compounds over Pt supported catalysts, it was observed that the noble metal catalyzes demethylation first, followed by hydrodeoxygenation.[18, 24, 58-60]

In this study, phenol and catechol are formed from anisole and guaiacol, respectively, while methane is produced in both reactions (Figure D.3 and D.5). This result agrees with literature that the hydrogenolysis of the PhO-CH_3 bond is the preferential step.[18, 24, 60] The HBEA support can transfer the cleaved CH_3 to an aromatic ring, resulting in intra- or intermolecular rearrangement to form transalkylated or dealkylated products. In the presence of Pt metal, the dissociated methyl group is hydrogenated to form methane. During the reaction of m-cresol over HBEA, some methyl groups are transferred to a different position on the aromatic ring, resulting in isomerization products such as o- and p-cresol (Figure D.4A). Since the methoxy group is not present on m-cresol, it is not surprising that only a small yield of methane (< 0.5%) is produced from m-cresol over Pt/HBEA.

Following demethylation, four different pathways have been proposed for the hydrodeoxygenation of the phenolic oxygen atom. The first major pathway is direct hydrodeoxygenation to form aromatics and water. However, it has been shown that direct deoxygenation without activation of the aromatic ring is at least five orders of magnitude slower.[61] This is because the bond strength of Ph-OH is 83 kJ/mol stronger compared to an aliphatic C-OH bond.[4] The second proposed pathway is the hydrogenation of the aromatic ring, followed by dehydration to remove the oxygen atom, and hydrogenation again.[62] However, cycloalkanes or partially-hydrogenated products are not produced in this study. The third pathway proposed involves the partial hydrogenation of the aromatic ring.[18, 23, 62] This would enable the cleavage of the aliphatic C-O bond less energy intensive as the delocalization of the oxygen lone pair orbital is inhibited. Subsequently, dehydration of the oxygen atom would restore the aromaticity of the compound. Another alternative pathway involves the tautomerization of the phenol intermediate to 2,4-cyclohexadienone, followed by hydrogenation of the carbonyl group and dehydration.[63]

Comparing the yields of deoxygenated aromatic compounds provides insight on the degree of hydrodeoxygenation between different model compounds (Figure 5.2D).

Anisole has a 15% higher yield of deoxygenated aromatics compared to m-cresol even though both compounds have only one oxygen functional group. Since demethylation of the methoxy group in anisole is the first step toward hydrodeoxygenation (vide supra), the resulting intermediate to undergo deoxygenation would be phenol. It was suggested that the presence of a methyl group on an aromatic ring in m-cresol could strengthen the Ph-OH bond.[23] However, the bond dissociation energies of a Ph-OH bond between phenol (106.1 kcal/mol) and m-cresol (106.0 kcal/mol) were calculated to be very similar.[29] Thus, the significant difference in the degree of hydrodeoxygenation between anisole and m-cresol can be largely attributed to steric hindrance, where the additional methyl group in m-cresol could sterically hinder the accessibility of the active site, leading to lower HDO activity.

In the case of guaiacol, its yield of deoxygenated aromatics is lower compared to anisole and m-cresol. Similarly to anisole, the first step toward hydrodeoxygenation of guaiacol is the decomposition of the methoxy group, followed by deoxygenation of the two phenol groups in the presence of Pt metal.[61] The low yield of entirely deoxygenated aromatics from guaiacol is not surprising due to the presence of two oxygen functional groups. However, by comparing the deoxygenation of only one oxygen containing functional group, the yield of phenolics (phenol, cresols, and xylenols) from guaiacol is still lower compared to the yield of deoxygenated aromatics from anisole. Also, the yield of phenol from guaiacol is also lower compared to the yield of toluene from m-cresol. In addition, the bond dissociation energy of a Ph-OH bond is similar between guaiacol, phenol, and m-cresol.[29] This also supports the fact that steric hindrance plays an important role in the degree of hydrodeoxygenation, especially when an adjacent functional group is present on the aromatic ring.

5.4.3 Evolution of Surface Species from *Operando* FTIR Spectroscopy

Even though hydrodeoxygenation of various bio-oil model compounds have been studied and coking has been considered the most common route of deactivation, there is a lack of knowledge in the timescale on the evolution of surface species. To our knowledge, there have been no reports on *operando* IR spectroscopy performed for any HDO reactions. Understanding the evolution of surface species will allow refineries to anticipate the formation of polynuclear aromatics or hard coke and the associated deactivation of the catalysts, which requires harsh conditions (> 800 °C) to regenerate the catalysts.[64] In this way, the initial hydrogen-rich surface species can be easily stripped off, restoring the full activity of the catalysts. A milder regeneration protocol would prevent irreversible transformations, such as dealumination of zeolites during combustion of coke at high temperature, and thus, result in a longer lifetime of the catalyst.

During the conversion of anisole over HBEA and Pt/HBEA, substituted monoaromatics and rearrangement of methyl groups were initially observed (Figure 5.6 and 5.7). This is in agreement with the reactivity and adsorption results, which shows that anisole undergoes transalkylation or dealkylation to form various aromatics. In the case of HBEA, polynuclear aromatics were only observed after 4 min time on stream, indicating that these species are secondary products that only formed when the surface began to saturate. With increasing time on stream, the relative MS signal of phenol from HBEA and deoxygenated aromatics from Pt/HBEA decreased rapidly in the first 2 h, suggesting that the deactivation of the catalysts mainly took place during this period. The shift of the peaks at 1533 cm^{-1} and 1561 cm^{-1} to lower frequencies revealed that the mono- and polynuclear aromatics have heavier or more substituents in the first hour (Figure 5.6C and 5.7B). In addition, polynuclear aromatics were observed on Pt/HBEA, but its relative peak intensity was low compared to HBEA. After 1 h time on stream, carbonaceous species such as graphitic coke were observed, and became significant after 2 h time on stream. This is in line with the rapid increase in intensity of the mono and

polynuclear aromatic peak, followed by a slow growth (Figure 5.6C and 5.7B). This suggest that initially monoaromatics saturated the surface and condensed to form simple polynuclear aromatics. With increasing time on stream, these species began to have heavier and more substituents. After 1 h, more of these polynuclear aromatics continued to condense and form heavy polynuclear aromatics and coke, which blocked most of the active sites and deactivated the catalyst. This explains the rapid decrease in the relative MS signal of deoxygenated aromatics in the first 2 h of reaction (Figure 5.7C). Eventually, the surface is saturated with coke and heavy polynuclear aromatics. Figure 5.12 shows the timeline on the formation of surface species for anisole over Pt/HBEA.

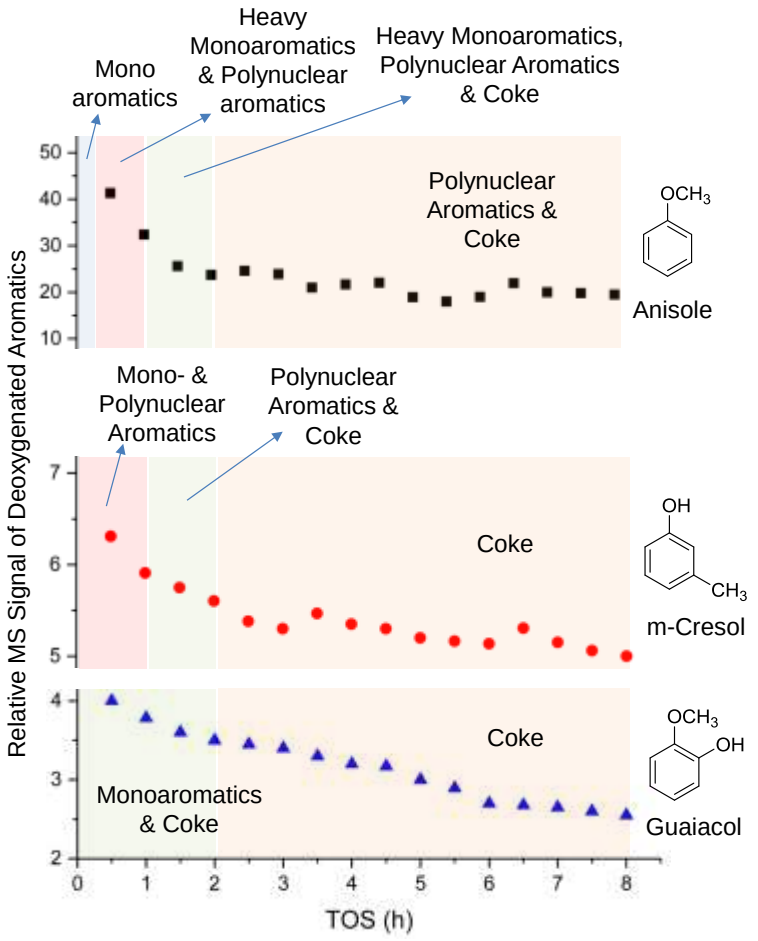

Figure 5.12 Timeline on the formation of surface species on Pt/HBEA.

During the conversion of m-cresol over HBEA, the formation of polynuclear aromatics was also observed after 4 min time on stream (Figure 5.8A), suggesting the condensation of monoaromatics. In the case of Pt/HBEA, the peak due to polynuclear aromatics was observed under short time scale (Figure 5.9B). Between 10 min and 1 h, the difference FTIR spectra shows that the intensity of the polynuclear aromatics peak increased on both HBEA and Pt/HBEA. Between 1 h and 2 h time on stream, coke-like species began to form on both HBEA and Pt/HBEA, while the intensity of polynuclear aromatics was reduced. This suggests that the polynuclear aromatics condensed to form coke which led to rapid deactivation as indicated by the decrease of the relative MS signal of deoxygenated aromatics. The rapid increase in the intensity of the 1568 cm^{-1} peak in the first 2 h followed by a slow increase provides further evidence of polynuclear aromatics condensation (Figure 5.8D). Interestingly, the red-shift in frequencies of mono and polynuclear aromatics was not observed for both catalysts. This indicates that the mass of the substituents were not largely affected over time, compared to anisole. One possible reason is the absence of the methoxy functional group. In the case of anisole, the rate of decomposition of the methoxy group decreased over time due to deactivation, resulting in heavier functional groups. For m-cresol, the substituents were always largely methyl groups. A timeline for the evolution of surface species for m-cresol over Pt/HBEA is shown in Figure 5.12.

For the conversion of guaiacol, the FTIR spectra between HBEA and Pt/HBEA are very similar (Figure 5.10 and 5.11), showing peaks due to monoaromatics, surface methyl group, and aromatic methyl group. The difference FTIR spectra showed that coke-like species were already formed on both catalysts on a short time scale. In addition, substituted aromatics (1532 cm^{-1}) were only observed on Pt/HBEA, which agrees with reactivity result. This is most likely attributed to the catalytic activity of the Pt metal, which accelerates the cleavage of the PhO-CH_3 bond.[18] With increasing time on stream, polynuclear aromatics continued to grow on both catalysts. The relative intensity of the

peak around 1580-1570 cm^{-1} for HBEA is higher compared to Pt/HBEA. Due to the low reactivity of guaiacol over HBEA, transalkylated aromatics were not observed. However, guaiacol is still able to condense to form polynuclear aromatics and coke, probably via hydrogen abstraction on the aromatic ring.[65]

The timeline for the evolution of surface species over Pt/HBEA indicates that the formation of polynuclear aromatics and coke is dependent on the bio-oil model compound (Figure 5.12). It is noted that the timeline may change under different reaction conditions, but it correlates the decrease in catalyst activity with the formation of polynuclear aromatics and coke. The formation of these species occurred latest in the HDO of anisole, followed by m-cresol. In the case of guaiacol, coke-like species was quickly observed. This is in line with the amount of carbon formed on the spent catalyst based on TGA/TPO analysis (Table D.2). With the reactant as anisole, the spent catalysts had the lowest amount of carbon, followed by m-cresol and guaiacol. One possible reason for the higher coke content from m-cresol is the large presence of the methyl functional group. Hydrogen abstraction is a key process in coke formation.[65] It was calculated that the presence of methyl groups can lower the activation energy in hydrogen abstraction, allowing the coke matrix to grow rapidly. In the case of guaiacol, it was observed that it forms a bidentate surface species easily on the Lewis acid sites of HBEA. However, the fact that coke was rapidly formed suggests that Brønsted acid sites can still catalyze aromatic condensation via protonation and hydrogen abstraction on the aromatic ring.[65-66] In the presence of Pt metal, the adjacent methoxy and phenolic functional groups could induce additional steric effect on the Pt surface, weakening the binding of the adsorbate and lower HDO activity.[67-68]

The TGA results indicate that the presence of Pt metal on HBEA reduces the amount of coke formation, which agrees with the *operando* FTIR results. In addition, the temperature of the CO_2 evolution peak from the spent HBEA catalysts is consistently higher compared to spent Pt/HBEA. This is probably due to the addition of Pt metal that

catalyzed the oxidation of coke. From the *operando* FTIR spectra, it was also observed that the presence of Pt can retard the formation of polynuclear aromatics and coke. It was reported that the diffusion barrier for the formation of carbon dimers is high on certain metallic surfaces.[69] Thus, coke formation could also be inhibited on the surface of Pt metal as it has a high dispersion (54%) on HBEA. The lower content of coke could also result from hydrogen spillover effect. Since hydrogen abstraction is involved in coke formation,[65] the atomic hydrogen species from Pt metal could migrate to the surface of the HBEA support and suppress the reaction by reversing the reaction.

Spillover of hydrogen species from metal particles to reducible support and graphitic carbon have been demonstrated.[70] However, the situation is different for nonreducible and defective supports such as zeolites. In this case, it is hypothesized that the slow deactivation rate by hydrogen spillover is related to Lewis acidity, where the hydrogen species can migrate to the Lewis acid sites of the HBEA support. Hydrogen spillover has been calculated to be energetically viable for aluminosilicates.[71] All of the spent Pt/HBEA catalysts were measured to have a higher concentration of Lewis acid sites compared to spent HBEA (Figure 5.1), supporting the hypothesis.

5.5. Conclusions

Anisole, m-cresol and guaiacol can adsorb on the Lewis acid sites of HBEA in different ways. For anisole, the methyl group is dissociated, and a phenate species is formed. The methyl group of m-cresol remains on the aromatic ring while a cresolate is formed. In the case of guaiacol, the methoxy group either decomposed or remained intact, forming a doubly anchored phenate or methoxy phenate species, respectively. It was found that their surface interactions and position of functional groups can affect the degree of hydrodeoxygenation, where steric hindrance plays an important factor. This resulted in anisole to have the highest degree of hydrodeoxygenation, followed by m-

cresol and guaiacol. From *operando* FTIR results, it was observed that the catalysts deactivated significantly in the first 2 h time on stream due to the formation of heavy monoaromatics and polynuclear aromatics, which methyl groups can accelerate its formation. Coke was rapidly formed in a higher quantity from guaiacol due its strong surface interaction, allowing Brønsted acid sites to catalyze aromatic condensation. The presence of lower carbon content on spent Pt/HBEA catalysts could be related to the high carbon diffusion barrier on Pt metal, or the suppression of hydrogen abstraction reaction in coke formation by hydrogen spilt-over species on Lewis acid sites. These results are of great importance in guiding conversion strategies, such as separating heavy bio-oil compounds to minimize deactivation, and using *operando* FTIR to detect coke formation.

5.6. References

1. Huber, G. W.; Iborra, S.; Corma, A. Synthesis of transportation fuels from biomass: Chemistry, catalysts, and engineering. *Chem. Rev.* **2006,** *106*, 4044-4098.

2. Bu, Q.; Lei, H. W.; Zacher, A. H.; Wang, L.; Ren, S. J.; Liang, J.; Wei, Y.; Liu, Y. P.; Tang, J. M.; Zhang, Q.; Ruan, R. A review of catalytic hydrodeoxygenation of lignin-derived phenols from biomass pyrolysis. *Bioresour. Technol.* **2012,** *124*, 470-477.

3. Czernik, S.; Bridgwater, A. V. Overview of applications of biomass fast pyrolysis oil. *Energy Fuels* **2004,** *18*, 590-598.

4. Furimsky, E. Catalytic hydrodeoxygenation. *Appl. Catal. A-Gen.* **2000,** *199*, 147-190.

5. Elliott, D. C. Historical developments in hydroprocessing bio-oils. *Energy Fuels* **2007,** *21*, 1792-1815.

6. Laurent, E.; Delmon, B. Influence of water in the deactivation of a sulfided NiMo gamma-Al_2O_3 catalyst during hydrodeoxygenation. *J. Catal.* **1994,** *146*, 281-291.

7. Laurent, E.; Delmon, B. Study of the hydrodeoxygenation of carbonyl, carboxylic and guaiacyl groups over sulfided como/gamma-Al_2O_3 and NiMo/gamma-Al_2O_3 catalysts .1. Catalytic reaction schemes. *Appl. Catal. A-Gen.* **1994,** *109*, 77-96.

8. Lin, Y. C.; Li, C. L.; Wan, H. P.; Lee, H. T.; Liu, C. F. Catalytic Hydrodeoxygenation of Guaiacol on Rh-Based and Sulfided CoMo and NiMo Catalysts. *Energy Fuels* **2011,** *25*, 890-896.

9. Fisk, C. A.; Morgan, T.; Ji, Y. Y.; Crocker, M.; Crofcheck, C.; Lewis, S. A. Bio-oil upgrading over platinum catalysts using in situ generated hydrogen. *Appl. Catal. A-Gen.* **2009,** *358*, 150-156.

10. Wildschut, J.; Mahfud, F. H.; Venderbosch, R. H.; Heeres, H. J. Hydrotreatment of Fast Pyrolysis Oil Using Heterogeneous Noble-Metal Catalysts. *Ind. Eng. Chem. Res.* **2009,** *48*, 10324-10334.

11. Wildschut, J.; Iqbal, M.; Mahfud, F. H.; Cabrera, I. M.; Venderbosch, R. H.; Heeres, H. J. Insights in the hydrotreatment of fast pyrolysis oil using a ruthenium on carbon catalyst. *Energy Environ. Sci.* **2010,** *3*, 962-970.

12. Zhao, C.; Kou, Y.; Lemonidou, A. A.; Li, X. B.; Lercher, J. A. Highly Selective Catalytic Conversion of Phenolic Bio-Oil to Alkanes. *Angew. Chem.-Int. Edit.* **2009,** *48*, 3987-3990.

13. Zhao, C.; Kou, Y.; Lemonidou, A. A.; Li, X. B.; Lercher, J. A. Hydrodeoxygenation of bio-derived phenols to hydrocarbons using RANEY (R) Ni and Nafion/SiO2 catalysts. *Chem. Commun.* **2010,** *46*, 412-414.

14. Zhao, C.; Lercher, J. A. Upgrading Pyrolysis Oil over Ni/HZSM-5 by Cascade Reactions. *Angew. Chem.-Int. Edit.* **2012,** *51*, 5935-5940.

15. Zhao, C.; Song, W. J.; Lercher, J. A. Aqueous Phase Hydroalkylation and Hydrodeoxygenation of Phenol by Dual Functional Catalysts Comprised of Pd/C and H/La-BEA. *ACS Catal.* **2012,** *2*, 2714-2723.

16. Zhao, C.; Lercher, J. A. Selective Hydrodeoxygenation of Lignin-Derived Phenolic Monomers and Dimers to Cycloalkanes on Pd/C and HZSM-5 Catalysts. *ChemCatChem* **2012,** *4*, 64-68.

17. Kubicka, D.; Kaluza, L. Deoxygenation of vegetable oils over sulfided Ni, Mo and NiMo catalysts. *Appl. Catal. A-Gen.* **2010,** *372*, 199-208.

18. Zhu, X. L.; Lobban, L. L.; Mallinson, R. G.; Resasco, D. E. Bifunctional transalkylation and hydrodeoxygenation of anisole over a Pt/HBeta catalyst. *J. Catal.* **2011,** *281*, 21-29.

19. Sitthisa, S.; Sooknoi, T.; Ma, Y. G.; Balbuena, P. B.; Resasco, D. E. Kinetics and mechanism of hydrogenation of furfural on Cu/SiO2 catalysts. *J. Catal.* **2011,** *277*, 1-13.

20. Sitthisa, S.; Resasco, D. E. Hydrodeoxygenation of Furfural Over Supported Metal Catalysts: A Comparative Study of Cu, Pd and Ni. *Catal. Lett.* **2011,** *141*, 784-791.

21. Ausavasukhi, A.; Huang, Y.; To, A. T.; Sooknoi, T.; Resasco, D. E. Hydrodeoxygenation of m-cresol over gallium-modified beta zeolite catalysts. *J. Catal.* **2012,** *290*, 90-100.

22. Nie, L.; Resasco, D. E. Kinetics and mechanism of m-cresol hydrodeoxygenation on a Pt/SiO2 catalyst. *J. Catal.* **2014,** *317*, 22-29.

23. Zhu, X. L.; Nie, L.; Lobban, L. L.; Mallinson, R. G.; Resasco, D. E. Efficient Conversion of m-Cresol to Aromatics on a Bifunctional Pt/HBeta Catalyst. *Energy Fuels* **2014,** *28*, 4104-4111.

24. González-Borja, M. Á.; Resasco, D. E. Anisole and Guaiacol Hydrodeoxygenation over Monolithic Pt–Sn Catalysts. *Energy Fuels* **2011,** *25*, 4155-4162.

25. Khromova, S. A.; Smirnov, A. A.; Bulavchenko, O. A.; Saraev, A. A.; Kaichev, V. V.; Reshetnikov, S. I.; Yakovlev, V. A. Anisole hydrodeoxygenation over Ni-Cu bimetallic catalysts: The effect of Ni/Cu ratio on selectivity. *Appl. Catal. A-Gen.* **2014,** *470*, 261-270.

26. Gutierrez, A.; Kaila, R. K.; Honkela, M. L.; Slioor, R.; Krause, A. O. I. Hydrodeoxygenation of guaiacol on noble metal catalysts. *Catal. Today* **2009,** *147*, 239-246.

27. Sun, J. M.; Karim, A. M.; Zhang, H.; Kovarik, L.; Li, X. H. S.; Hensley, A. J.; McEwen, J. S.; Wang, Y. Carbon-supported bimetallic Pd-Fe catalysts for vapor-phase hydrodeoxygenation of guaiacol. *J. Catal.* **2013,** *306*, 47-57.

28. Rensel, D. J.; Rouvimov, S.; Gin, M. E.; Hicks, J. C. Highly selective bimetallic FeMoP catalyst for C–O bond cleavage of aryl ethers. *J. Catal.* **2013,** *305*, 256-263.

29. Prasomsri, T.; Shetty, M.; Murugappan, K.; Roman-Leshkov, Y. Insights into the catalytic activity and surface modification of MoO3 during the hydrodeoxygenation of lignin-derived model compounds into aromatic hydrocarbons under low hydrogen pressures. *Energy Environ. Sci.* **2014,** *7*, 2660-2669.

30. Prasomsri, T.; Nimmanwudipong, T.; Roman-Leshkov, Y. Effective hydrodeoxygenation of biomass-derived oxygenates into unsaturated hydrocarbons by MoO3 using low H2 pressures. *Energy Environ. Sci.* **2013,** *6*, 1732-1738.

31. Schimming, S. M.; LaMont, O. D.; König, M.; Rogers, A. K.; D'Amico, A. D.; Yung, M. M.; Sievers, C. Hydrodeoxygenation of Guaiacol over Ceria–Zirconia Catalysts. *ChemSusChem* **2015,** *8*, 2073-2083.

32. Lee, W.-S.; Wang, Z.; Wu, R. J.; Bhan, A. Selective vapor-phase hydrodeoxygenation of anisole to benzene on molybdenum carbide catalysts. *J. Catal.* **2014,** *319*, 44-53.

33. Li, Y.; Zhang, C.; Liu, Y.; Hou, X.; Zhang, R.; Tang, X. Coke Deposition on Ni/HZSM-5 in Bio-oil Hydrodeoxygenation Processing. *Energy Fuels* **2015,** *29*, 1722-1728.

34. Popov, A.; Kondratieva, E.; Goupil, J. M.; Mariey, L.; Bazin, P.; Gilson, J. P.; Travert, A.; Mauge, F. Bio-oils Hydrodeoxygenation: Adsorption of Phenolic Molecules on Oxidic Catalyst Supports. *J. Phys. Chem. C* **2010,** *114*, 15661-15670.

35. Popov, A.; Kondratieva, E.; Gilson, J.-P.; Mariey, L.; Travert, A.; Maugé, F. IR study of the interaction of phenol with oxides and sulfided CoMo catalysts for bio-fuel hydrodeoxygenation. *Catal. Today* **2011,** *172*, 132-135.

36. Popov, A.; Kondratieva, E.; Mariey, L.; Goupil, J. M.; El Fallah, J.; Gilson, J. P.; Travert, A.; Mauge, F. Bio-oil hydrodeoxygenation: Adsorption of phenolic compounds on sulfided (Co)Mo catalysts. *J. Catal.* **2013,** *297*, 176-186.

37. Brunauer, S.; Emmett, P. H.; Teller, E. Adsorption of gases in multimolecular layers. *J. Am. Chem. Soc.* **1938,** *60*, 309-319.

38. Barrett, E. P.; Joyner, L. G.; Halenda, P. P. The determination of pore volume and area distributions in porous substances .1. Computations from nitrogen isotherms. *J. Am. Chem. Soc.* **1951,** *73*, 373-380.

39. Selli, E.; Forni, L. Comparison between the surface acidity of solid catalysts determined by TPD and FTIR analysis of pre-adsorbed pyridine. *Microporous Mesoporous Mat.* **1999,** *31*, 129-140.

40. Wang, J.; Kispersky, V. F.; Delgass, W. N.; Ribeiro, F. H. Determination of the Au active site and surface active species via operando transmission FTIR and isotopic transient experiments on 2.3 wt.% Au/TiO2 for the WGS reaction. *J. Catal.* **2012,** *289*, 171-178.

41. Prokešová, P.; Mintova, S.; Čejka, J.; Bein, T. Preparation of nanosized micro/mesoporous composites via simultaneous synthesis of Beta/MCM-48 phases. *Microporous Mesoporous Mat.* **2003,** *64*, 165-174.

42. Ravenelle, R. M.; Schussler, F.; D'Amico, A.; Danilina, N.; van Bokhoven, J. A.; Lercher, J. A.; Jones, C. W.; Sievers, C. Stability of Zeolites in Hot Liquid Water. *J. Phys. Chem. C* **2010,** *114*, 19582-19595.

43. Socrates, G., *Infrared and Raman Characteristic Group Frequencies*. Third ed.; John Wiley & Sons LTD: 2001;

44. Jones, A. J.; Iglesia, E. Kinetic, Spectroscopic, and Theoretical Assessment of Associative and Dissociative Methanol Dehydration Routes in Zeolites. *Angew. Chem.-Int. Edit.* **2014,** *53*, 12177-12181.

45. Colthup, N. B.; Daly, L. H.; Wiberley, S. E., *Introduction to Infrared and Raman Spectroscopy*. Third Edition ed.; Academic Press: 1990;

46. Murphy, B.; Davis, M.; Xu, B. The Effect of Adsorbed Molecule Gas-Phase Deprotonation Enthalpy on Ion Exchange in Sodium Exchanged Zeolites: An In Situ FTIR Investigation. *Top. Catal.* **2015,** *58*, 393-404.

47. Fernandez, C.; Stan, I.; Gilson, J.-P.; Thomas, K.; Vicente, A.; Bonilla, A.; Pérez-Ramírez, J. Hierarchical ZSM-5 Zeolites in Shape-Selective Xylene Isomerization: Role of Mesoporosity and Acid Site Speciation. *Chemistry – A European Journal* **2010,** *16*, 6224-6233.

48. Mathew, T.; Vijayaraj, M.; Pal, S.; Tope, B. B.; Hegde, S. G.; Rao, B. S.; Gopinath, C. S. A mechanistic approach to phenol methylation on Cu1-xCoxFe2O4: FTIR study. *J. Catal.* **2004,** *227*, 175-185.

49. Park, J. W.; Seo, G. IR study on methanol-to-olefin reaction over zeolites with different pore structures and acidities. *Appl. Catal., A* **2009,** *356*, 180-188.

50. Rozwadowski, M.; Lezanska, M.; Wloch, J.; Erdmann, K.; Golembiewski, R.; Kornatowski, J. Investigation of coke deposits on Al-MCM-41. *Chem. Mat.* **2001,** *13*, 1609-1616.

51. Palumbo, L.; Bonino, F.; Beato, P.; Bjorgen, M.; Zecchina, A.; Bordiga, S. Conversion of methanol to hydrocarbons: Spectroscopic characterization of Carbonaceous species formed over H-ZSM-5. *J. Phys. Chem. C* **2008,** *112*, 9710-9716.

52. Krishnakumar, V.; Kumar, M.; Prabavathi, N.; Mathammal, R. Molecular structure, spectroscopic studies (FTIR, FT-Raman and NMR) and HOMO–LUMO analysis of 6-chloro-o-cresol and 4-chloro-3-methyl phenol by density functional theoretical study. *Spectrochimica Acta Part A: Molecular and Biomolecular Spectroscopy* **2012,** *97*, 144-154.

53. Melián, E. P.; Díaz, O. G.; Araña, J.; Rodríguez, J. M. D.; Rendón, E. T.; Melián, J. A. H. Kinetics and adsorption comparative study on the photocatalytic degradation of o-, m- and p-cresol. *Catal. Today* **2007,** *129*, 256-262.

54. Foo, G. S.; Wei, D.; Sholl, D. S.; Sievers, C. Role of Lewis and Brønsted Acid Sites in the Dehydration of Glycerol over Niobia. *ACS Catal.* **2014**, 3180-3192.

55. Copeland, J. R.; Santillan, I. A.; Schimming, S. M.; Ewbank, J. L.; Sievers, C. Surface Interactions of Glycerol with Acidic and Basic Metal Oxides. *J. Phys. Chem. C* **2013,** *117*, 21413-21425.

56. Copeland, J. R.; Shi, X.-R.; Sholl, D. S.; Sievers, C. Surface Interactions of C2 and C3 Polyols with γ-Al2O3 and the Role of Coadsorbed Water. *Langmuir* **2012,** *29*, 581-593.

57. Olcese, R. N.; Bettahar, M.; Petitjean, D.; Malaman, B.; Giovanella, F.; Dufour, A. Gas-phase hydrodeoxygenation of guaiacol over Fe/SiO2 catalyst. *Appl. Catal. B-Environ.* **2012,** *115*, 63-73.

58. Nimmanwudipong, T.; Runnebaum, R. C.; Brodwater, K.; Heelan, J.; Block, D. E.; Gates, B. C. Design of a High-Pressure Flow-Reactor System for Catalytic Hydrodeoxygenation: Guaiacol Conversion Catalyzed by Platinum Supported on MgO. *Energy Fuels* **2014,** *28*, 1090-1096.

59. Nimmanwudipong, T.; Aydin, C.; Lu, J.; Runnebaum, R. C.; Brodwater, K. C.; Browning, N. D.; Block, D. E.; Gates, B. C. Selective Hydrodeoxygenation of Guaiacol Catalyzed by Platinum Supported on Magnesium Oxide. *Catal. Lett.* **2012,** *142*, 1190-1196.

60. Mu, W.; Ben, H.; Du, X.; Zhang, X.; Hu, F.; Liu, W.; Ragauskas, A. J.; Deng, Y. Noble metal catalyzed aqueous phase hydrogenation and hydrodeoxygenation of lignin-derived pyrolysis oil and related model compounds. *Bioresour. Technol.* **2014,** *173*, 6-10.

61. Lu, J.; Behtash, S.; Mamun, O.; Heyden, A. Theoretical Investigation of the Reaction Mechanism of the Guaiacol Hydrogenation over a Pt(111) Catalyst. *ACS Catal.* **2015,** *5*, 2423-2435.

62. Massoth, F. E.; Politzer, P.; Concha, M. C.; Murray, J. S.; Jakowski, J.; Simons, J. Catalytic Hydrodeoxygenation of Methyl-Substituted Phenols: Correlations of Kinetic Parameters with Molecular Properties. *The Journal of Physical Chemistry B* **2006,** *110*, 14283-14291.

63. de Souza, P. M.; Rabelo-Neto, R. C.; Borges, L. E. P.; Jacobs, G.; Davis, B. H.; Sooknoi, T.; Resasco, D. E.; Noronha, F. B. Role of Keto Intermediates in the Hydrodeoxygenation of Phenol over Pd on Oxophilic Supports. *ACS Catal.* **2015,** *5*, 1318-1329.

64. Bai, D.; Zhu, J. X.; Jin, Y.; Yu, Z. Simulation of FCC catalyst regeneration in a riser regenerator. *Chem. Eng. J.* **1998,** *71*, 97-109.

65. Hemelsoet, K.; Van Speybroeck, V.; Waroquier, M. A DFT-Based Investigation of Hydrogen Abstraction Reactions from Methylated Polycyclic Aromatic Hydrocarbons. *Chemphyschem* **2008,** *9*, 2349-2358.

66. Bartholomew, C. H. Mechanisms of catalyst deactivation. *Appl. Catal., A* **2001,** *212*, 17-60.

67. Song, W.; Liu, Y.; Barath, E.; Zhao, C.; Lercher, J. A. Synergistic effects of Ni and acid sites for hydrogenation and C-O bond cleavage of substituted phenols. *Green Chem.* **2015,** *17*, 1204-1218.

68. Dwiatmoko, A. A.; Lee, S.; Ham, H. C.; Choi, J.-W.; Suh, D. J.; Ha, J.-M. Effects of Carbohydrates on the Hydrodeoxygenation of Lignin-Derived Phenolic Compounds. *ACS Catal.* **2015,** *5*, 433-437.

69. Zuo, P.; Fu, Z.; Yang, Z. First-principles study on the mechanism of coking inhibition by the Ni(111) surface doped with IB-group metals at the anode of solid oxide fuel cells. *Journal of Power Sources* **2013,** *242*, 762-767.

70. Prins, R. Hydrogen Spillover. Facts and Fiction. *Chem. Rev.* **2012,** *112*, 2714-2738.

71. Im, J.; Shin, H.; Jang, H.; Kim, H.; Choi, M. Maximizing the catalytic function of hydrogen spillover in platinum-encapsulated aluminosilicates with controlled nanostructures. *Nat Commun* **2014,** *5*.

CHAPTER 6

Final Conclusions and Recommendation

The purpose of this dissertation is to illustrate the importance of surface interactions between biomass molecules and heterogeneous catalysts. The research field of biomass conversion continues to grow, and a wide variety of catalysts will be developed in the near future. As researchers continue to search for highly active and selective catalysts, it is also imperative to understand the surface interactions of these biomass reactants at a fundamental level. This would lead to the elucidation of elementary reaction steps, as well as the influence of different active sites, allowing effective conversion strategies to be formulated.

In Chapter 2, it was shown that glycerol is able to form a multidentate surface species on niobium oxide. Specifically, the primary alcohol group dissociates to form a bidentate alkoxy bond with two metal atoms, while the other primary alcohol group forms a Lewis acid/base interaction with one of the metal atoms. This form of coordinating results in polarization of the dissociated primary alcohol group. When Brønsted acid sites are also present the activated surface species is selectively dehydrated to form hydroxyacetone. On a different pathway, the secondary alcohol group undergoes dehydration by a Brønsted acid site to eventually form acrolein as the secondary carbenium ion intermediate formed is more stable compared to a primary carbenium ion intermediate formed during the elimination of the primary OH group. Furthermore, monoaromatics are formed from the condensation of multiple surface species. To obtain a high selectivity of acrolein, catalysts with only Brønsted acid sites can be used, such as heteropoly acids and sulfonic acid functionalized silica. In this study, it was shown that in order to minimize catalyst deactivation, it is important to have less than a monolayer of glycerol throughout the reaction. Alternatively, catalysts with a lower surface density of

Brønsted acid sites can be synthesized, or catalysts with large pore size can be utilized.[1] In this way, the monoaromatics will take a longer time to condense together to form graphitic coke, extending the lifespan of the catalysts. This study shows that a fundamental understanding of surface interactions is important.

In Chapters 3 and 4, it was shown that van der Waals interactions and defect sites are important in the hydrolysis of cellulose and cellobiose over carbon. In addition, weaker acid sites such as carboxylic acids, phenols and lactones can also participate in the reaction, and they are less active for the degradation of glucose. The mechanism for hydrolysis is likely due to the synergistic effect between defect sites and the in-plane functional groups. Initially, glucan chains are immobilized on the carbon surface due to the presence of van der Waals forces. A conformation change is induced when glucan chains are adsorbed on defect sites or edges of the carbon sheets. This enables the in-plane functional group to interact with the exposed glycosidic oxygen bond. Furthermore, these weaker acid sites are less accessible by glucose monomers, which limits degradation reactions. These findings are important and useful in formulating an effective process scheme for the hydrolysis of cellulose and oligosaccharides at an industrial level. It is proposed that the hydrolysis reaction can be carried out in a two-step process. In the first step, the cellulose feed can be hydrolyzed into short-chain glucans by strong solid acids or supercritical water. In the second step, the glucan chains can be selectively hydrolyzed into glucose monomers by using carbon catalysts functionalized with weaker acid sites. In this way, the yield of glucose can be maximized. However, mesoporous carbon catalysts with a large pore size are desirable compared to activated carbon as they can accommodate the long glucan chains. Currently, the lab-scale synthesis process of mesoporous carbon usually involves the use of strong acids or bases for the impregnation of sugars on mesoporous ordered silica (SBA-15), followed by carbonization at a high temperature and the removal of silica framework using hydrofluoric acid.[2] The roadblock

in this process would be the large scale production of these mesoporous carbon catalysts in a safe and sustainable manner.

In Chapter 5, the first *operando* transmission FTIR study was performed for hydrodeoxygenation (HDO) reaction to observe the evolution of surface species. In addition, it was shown that steric effect has a huge influence in the HDO of bio-oil compounds over Pt/HBEA. Anisole, m-cresol and guaiacol were chosen as model compounds due to differences in functional groups. Compared to anisole, the presence of the methyl group on m-cresol can sterically hinder the phenolic functional group from accessing the active site to undergo deoxygenation. For guaiacol, the adjacent methoxy and phenolic functional groups impose further steric hindrance. In addition, guaiacol can form strongly adsorbed bidentate surface species. Using *operando* FTIR spectroscopy, it was observed that the presence of methyl group and multiple oxygen functional groups can accelerate the formation of graphitic coke and deactivate the catalyst. These results provide important insight in the HDO of crude bio-oil at the industrial level, as it reveals the stages of deactivation and helps to formulate an effective reaction and regeneration process. Based on these findings, the HDO of crude bio-oil can be setup in a two-stage process. In the first stage, reducible metal oxides such as ceria-zirconia can be used as a catalyst.[3-4] It was reported that ceria-zirconia is effective in converting guaiacol to phenol, but has limited activity in converting phenol to benzene. Thus, this catalyst could be suitable for reducing the number of oxygen functional groups in the crude bio-oil compounds. Subsequently, Pt/HBEA can be used in the second stage of the process, where it can effectively deoxygenate the compounds with minimized steric hindrance at a lower deactivation rate. Since hydrogen spillover could retard the deactivation of catalyst, it is worthwhile to investigate this phenomenon at the fundamental level to exploit its advantage. Furthermore, zeolite Beta without Lewis acid sites could also be utilized, as phenolic molecules can bind strongly to these sites and potentially reduce the catalyst's reactivity. To elucidate the reaction mechanism of HDO over Pt/HBEA or any other

catalysts, deuterium could be used instead of hydrogen in the HDO of a simple bio-oil model compound (phenol). With the use of FTIR spectroscopy and mass spectrometry, the shift in vibrational frequencies and the increase in mass-to-charge ratio of the deoxygenated aromatics would indicate the number of substitutions by deuterium. This would reveal the elementary reaction step of hydrodeoxygenation, which has been largely debated in literature.

In conclusion, there is great potential in using heterogeneous catalysts for the conversion of biomass into targeted fuels and chemicals. I hope that this dissertation highlights the importance of understanding surface interactions and provides the foundation for future work in improving the efficiency of downstream processes.

6.1 References

1. Zhang, H.; Hu, Z.; Huang, L.; Zhang, H.; Song, K.; Wang, L.; Shi, Z.; Ma, J.; Zhuang, Y.; Shen, W.; Zhang, Y.; Xu, H.; Tang, Y. Dehydration of Glycerol to Acrolein over Hierarchical ZSM-5 Zeolites: Effects of Mesoporosity and Acidity. *ACS Catal.* **2015,** *5*, 2548-2558.

2. Chang, B. B.; Fu, J.; Tian, Y. L.; Dong, X. P. Multifunctionalized Ordered Mesoporous Carbon as an Efficient and Stable Solid Acid Catalyst for Biodiesel Preparation. *J. Phys. Chem. C* **2013,** *117*, 6252-6258.

3. Schimming, S. M.; Foo, G. S.; LaMont, O. D.; Rogers, A. K.; Yung, M. M.; D'Amico, A. D.; Sievers, C. Kinetics of hydrogen activation on ceria–zirconia. *J. Catal.* **2015,** *329*, 335-347.

4. Schimming, S. M.; LaMont, O. D.; König, M.; Rogers, A. K.; D'Amico, A. D.; Yung, M. M.; Sievers, C. Hydrodeoxygenation of Guaiacol over Ceria–Zirconia Catalysts. *ChemSusChem* **2015,** *8*, 2073-2083.

APPENDIX A

Supplementary Information for Chapter 2

A.1 Thermal gravimetric analysis and differential thermal analysis of niobic acid

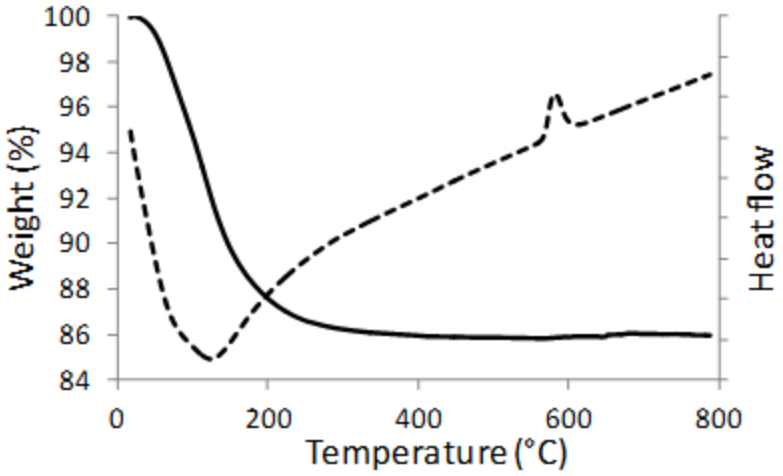

Figure A.1 TGA and DTA profiles of niobic acid during heating in air.

A.2 X-ray diffraction pattern of niobium oxide samples

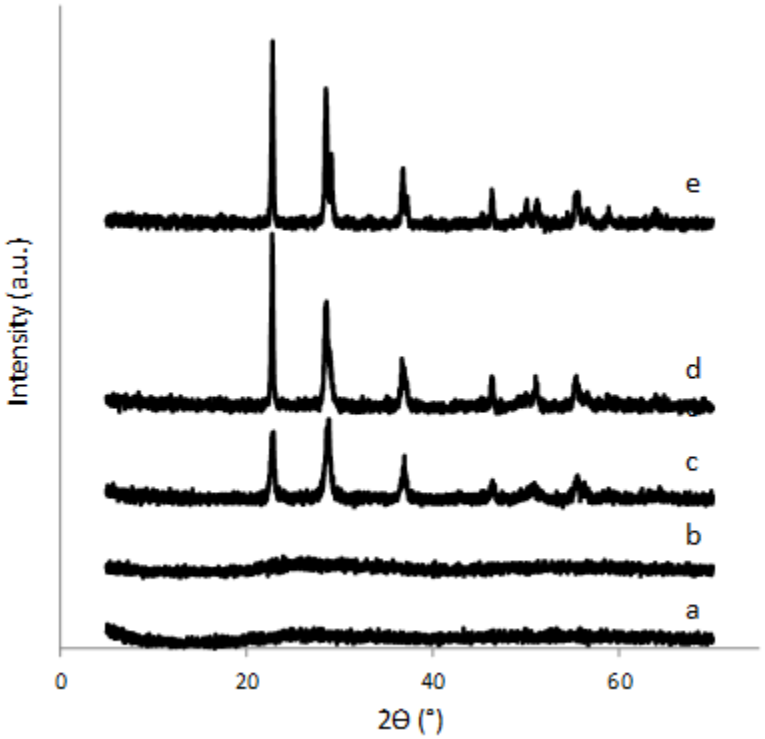

Figure A.2 XRD patterns of (a) NB350, (b) NB400, (C) NB500, (d) NB600, (d) NB700.

A.3 Pyridine adsorption followed by IR spectroscopy of NB500 and Na^+/NB500

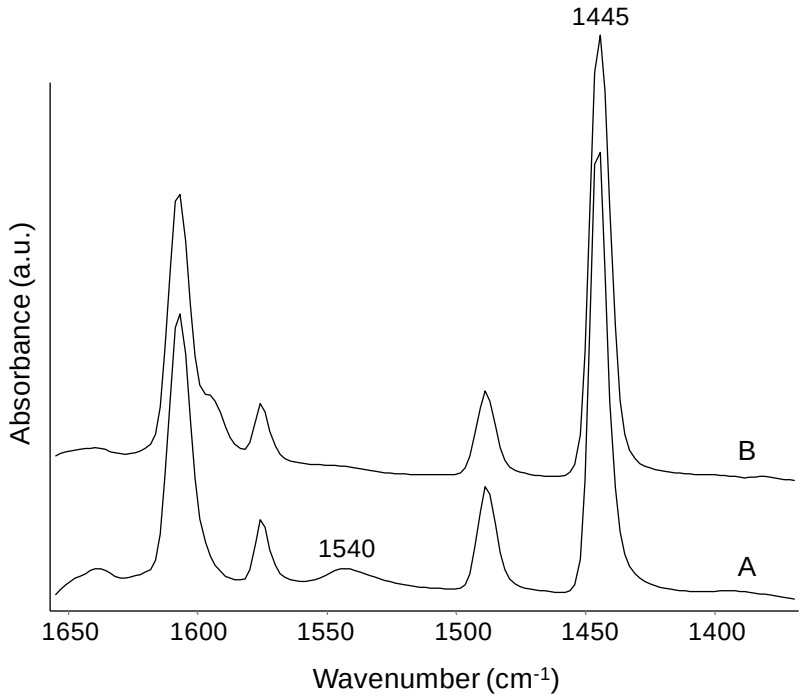

Figure A.3 FTIR spectra of pyridine adsorbed on (a) NB500, (b) Na^+/NB500.

A.4 DFT calculations on adsorbed surface species

For the adsorption of acrolein, the calculations examined the binding of the carbonyl group and the C=C double bond to the surface. Three stable structures were identified, and the most stable structure had acrolein bonded to two surface Nb atoms through both the carbonyl group and the C=C bond (Fig. A.4). When acrolein was bonded through only the carbonyl or only the C=C bond (Fig. A.4B and A.4A), there was no significant differences between the different rotational geometries of acrolein around the surface site. Vibrational frequencies were obtained for the most stable structure (Table A.3).

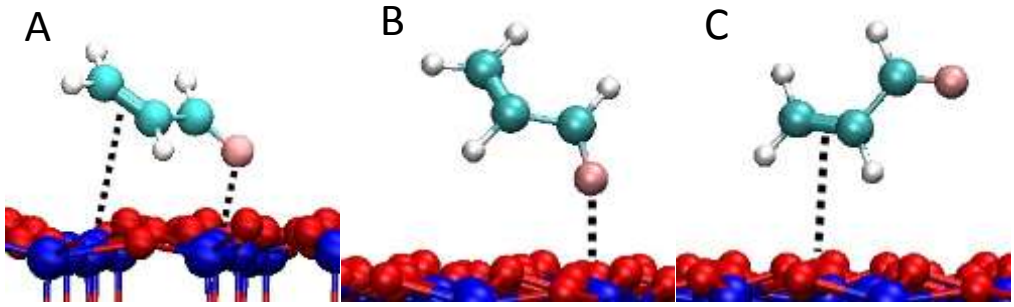

ΔE = 0.00 eV (ref) ΔE = 0.08 eV ΔE = 0.30 eV

Figure A.4 Adsorptions of acrolein on Nb terminated (100) surface of T-Nb_2O_5 (A) via C=O and C=C, (B) via C=O, (C) via C=C.

For the adsorption of 2-propene-1,2-diol, the calculation generated three stable adsorption geometries through relaxation of the isolated molecule in vacuum. In the most stable structure, the adsorbate binds to two surface Nb atoms through the primary hydroxyl group and the C=C bond (Fig. A.5A). The secondary hydroxyl group was found to tile away from the surface. The other two stable structures bind through either the primary or both hydroxyl groups (Fig. A.5B and A.5C). Both produced less favorable adsorption energies. Vibrational frequencies were obtained for the most stable structure (Table A.3). The adsorption of deprotonated 2-propene-1,2-diol was also calculated, and

adsorption was formed via the deprotonated primary hydroxyl group with a surface Nb (Fig. A.5D). This energy for this geometry was slightly lower than that of the first structure (Fig. A.5A). However, the energy difference of 0.04 eV was within the error margin. It also has to be noted that coverage effects would have to be considered to predict which of these structures is expected to form in an experiment. The vibrational frequencies for both structures (Table A.1) were too close to identify, which one is observed experimentally.

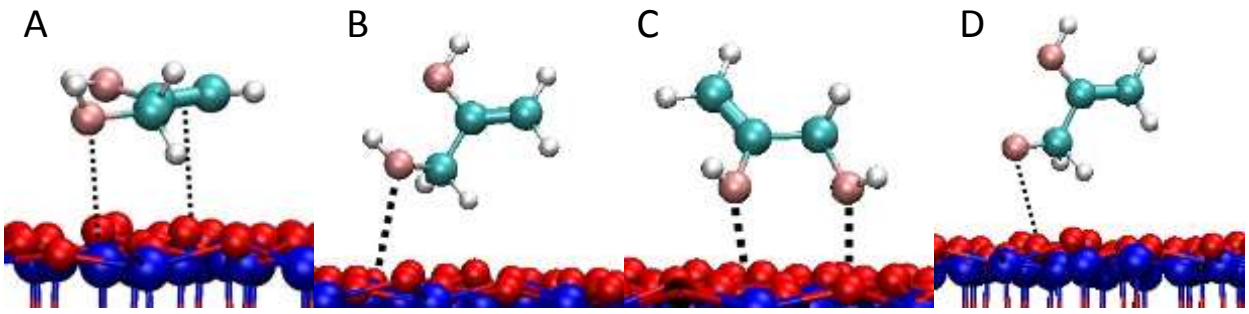

ΔE = 0.00 eV (ref) ΔE = 0.21 eV ΔE = 0.07 eV ΔE = -0.04 eV

Figure A.5 Adsorptions of 2-propene-1,2-diol (enol of hydroxyacetone) on Nb terminated (100) surface of T-Nb_2O_5 (A) via 1° OH and C=C, (B) via 1° OH, (C) via 1° and 2° OH, (D) via deprotonated 1° OH.

Table A.1 Calculated and experimental frequencies of 2-propene-1,2-diol adsorbed on NB500.

Calculated for Structure A / cm^{-1}	Calculated for Structure D / cm^{-1}	Experimental / cm^{-1}	Assignment
1578	1578	1575	νC=C
1378	1371	1378	δCH_2
1360	1354		δCH_2
1318	1310		δC-C
1303	1306		τC-C
1274	1267	1249	ωCH_2
1140	1139		νC-C
1061	1058	1050	νCO

Finally, for the adsorption of 1-propene-1,3-diol, the calculation examined the binding through the C=C bond and both of the hydroxyl groups (Fig. A.6). The adsorption through both of the hydroxyl groups created the most stable adsorbed species (Fig. A.6A). No stable structure was found, in which the 1-propene-1,3-diol was adsorbed through the C=C bond. This structure spontaneously relaxed to adsorption through the neighboring hydroxyl group (Fig. A.6B and A.6C). Vibrational frequencies for the most stable structure are given in Table S2.

All of the calculations assumed an isolated adsorbate on the surface, while the fourth geometry assumed a deprotonated alcohol group (Fig. A.6D). This structure was less stable than the most stable non-dissociatively adsorbed species (Fig. 1.6A). This study did not possess the computational capacity to fully explore the effect of neighboring adsorbates or water molecules, and these calculations were beyond the scope of this project.

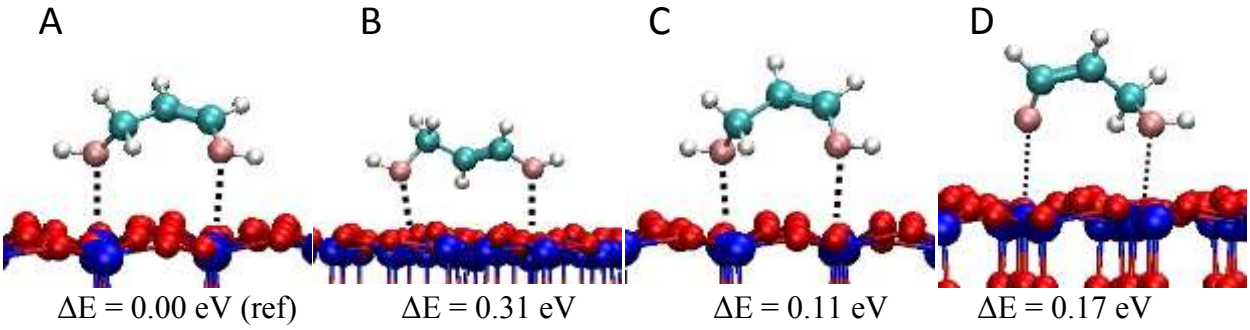

Figure A.6 Adsorption of 1-propene-1,3-diol on Nb terminated (100) surface of T-Nb_2O_5 (A) stable C-C-C backbone (B) C-C-C backbone oriented toward surface (C) C-C-C backbone shifted to one side (D) via deprotonated OH group.

Table A.2 Calculated frequencies of 1,3-propenediol adsorbed on Nb terminated (100) surface of T-Nb_2O_5.

Frequency/cm^{-1}	Assignment
1583	νC=C
1401	τCH_2
1369	νC=C-C
1292	νC-C-O
1227	ωCH
1199	νC=C-O
1138	δOH
1106	ωCH_2
1083	νC=C-C

A.5 FTIR spectra of acrolein and hydroxyacetone solution

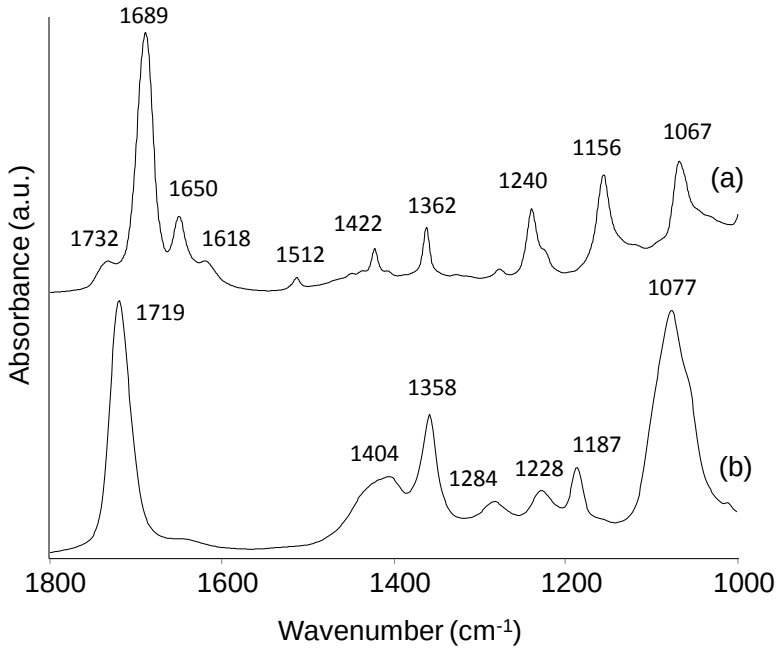

Figure A.7 FTIR spectra of (a) pure acrolein, (b) pure hydroxyacetone.

A.6 FTIR spectra of NB350 without glycerol

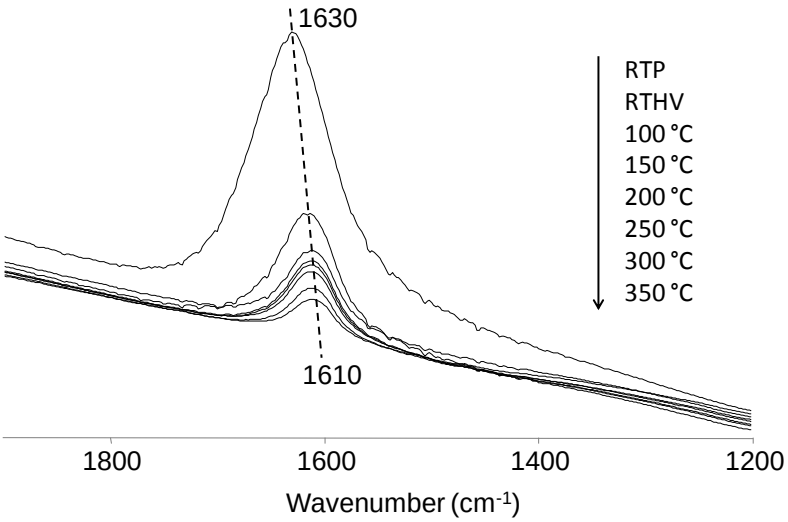

Figure A.8 FTIR spectra of 0 wt% glycerol on NB350.

A.7 FTIR spectra of 2 wt% glycerol on NB350 with 1 mbar water vapor

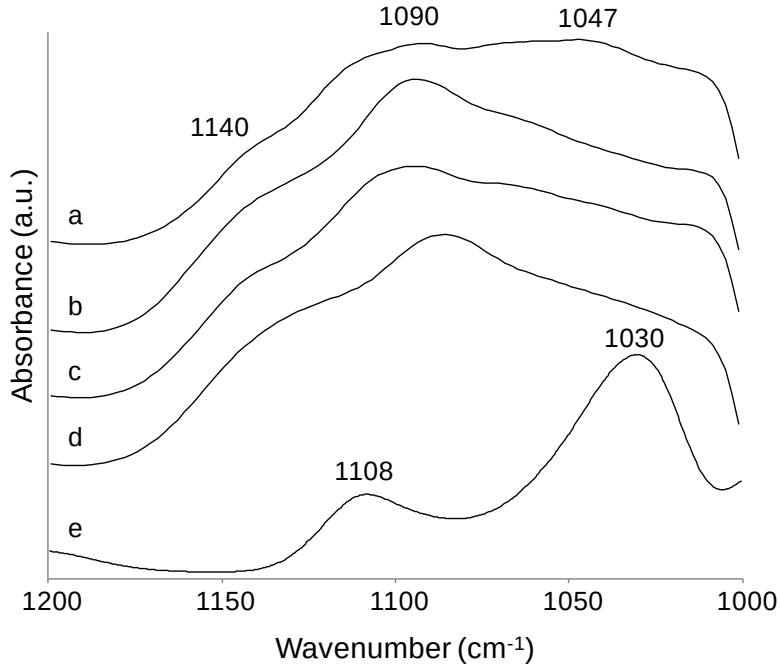

Figure A.9 FTIR spectra of 2 wt% glycerol on NB350 (a) RTP, (b) RTHV, (c) RT 1 mbar water vapor, (d) 350 °C 1 mbar water vapor, (e) pure glycerol.

Appendix B

Supplementary Information for Chapter 3

B.1 Raman spectra of carbon catalysts

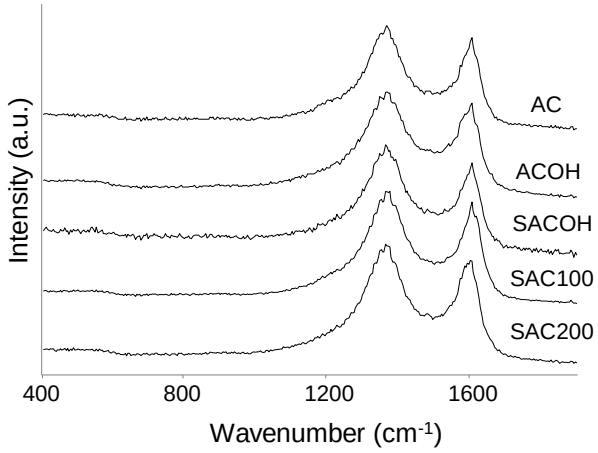

Figure B.1 Raman spectra of carbon samples.

B.2 XRD patterns of carbon samples

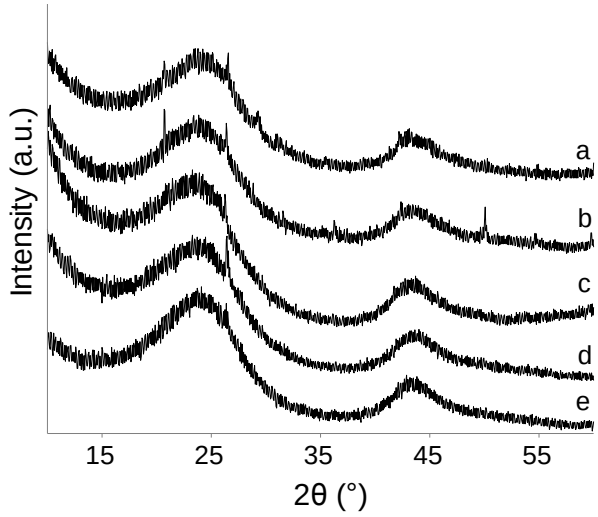

Figure B.2 XRD patterns of (a) AC, (b) ACOH, (c) SACOH, (d) SAC100, (e) SAC200.

B.3 ^{13}C DP MAS NMR spectra of carbon samples

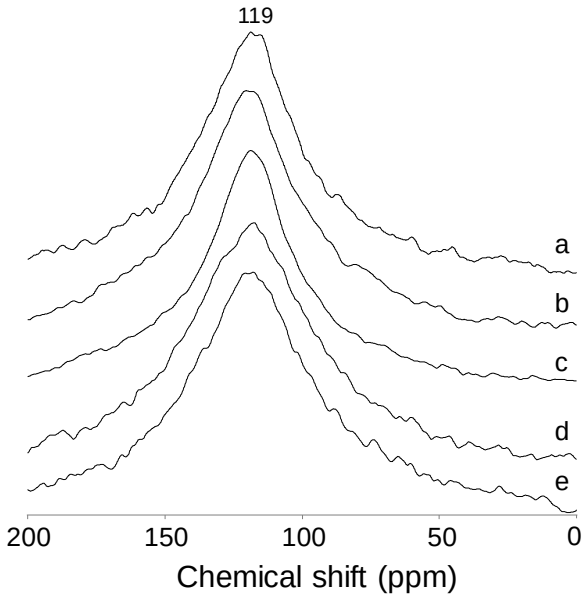

Figure B.3 ^{13}C DP MAS NMR spectra of carbon catalysts (a) AC, (b), ACOH, (c) SACOH, (d) SAC100, (e) SAC200.

B.4 Pore surface area of carbon samples

Table B.1 Pore surface area of carbon catalysts in different pore size range (m^2/g).

Catalyst	Between 0.49 to 1.1 nm[a]	Between 3.2 to 36 nm[b]
AC	290	147
ACOH	237	191
SACOH	265	199
SAC100	286	128
SAC200	285	134

[a]: Obtained by CO_2 physisorption
[b]: Obtained by N_2 physisorption

B.5 Concentration of sulfonic groups in carbon samples before and after hot liquid water treatment

Table B.2 Concentration of sulfonic groups before and after treatment at 150 °C in hot liquid water.

Catalyst	Before elution (μmol/g)	After elution (μmol/g)
ACOH	0	0
SACOH	150	31
SAC100	250	144
SAC200	287	153

B.6 XRD patterns of crystalline and ball-milled cellulose

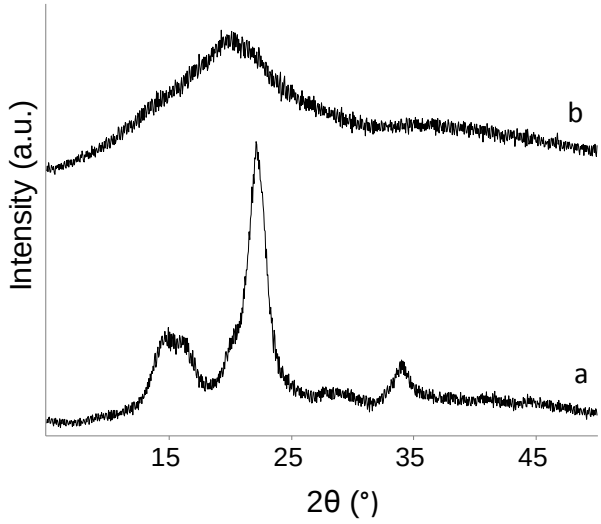

Figure B.4 XRD patterns of (a) cellulose, (b) cellulose ball-milled for 48 h.

B.7 GPC Characterization of Cellulose and Ball-Milled Cellulose

Table B.3 Weight-average (DP_w) and number-average (DP_n) degree of polymerization of cellulose and ball-milled cellulose.

Sample	DP_w	DP_n
Cellulose	346	51
Ball-milled Cellulose	296	48

B.8 Reactivity of H_2SO_4 and acetic acid in the hydrolysis of cellulose

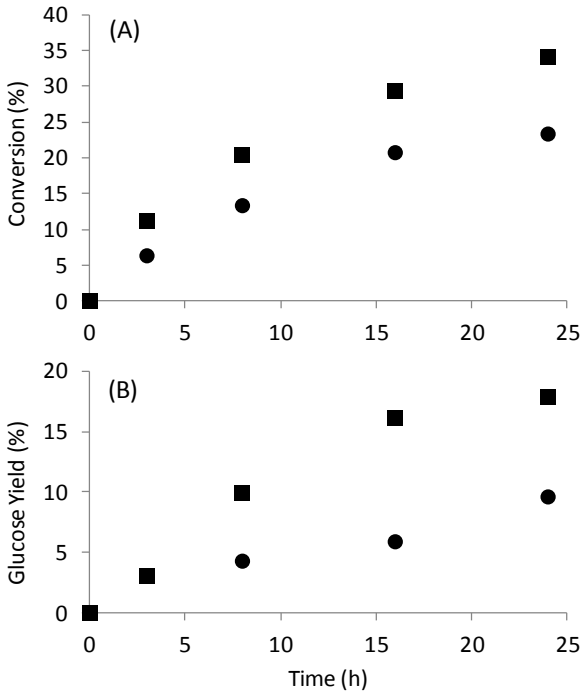

Figure B.5 (a) Conversion of cellulose and (b) glucose yield at various times using homogeneous catalysts: (■) 1.8 mM H_2SO_4, (●) 3.8 mM Acetic acid.

B.9 Langmuir adsorption isotherm

The Langmuir isotherm equation:

$$q = \frac{q_m K C_e}{1 + K C_e}$$

After rearranging:

$$\frac{C_e}{q} = \frac{1}{q_m} C_e + \frac{1}{q_m K}$$

where q = uptake (mg/g), Ce = equilibrium concentration (mol/L), q_m = maximum uptake (mg/g), K = adsorption coefficient (L/mol)

Calculating change in standard of free energy of adsorption (ΔΔG)

$$\Delta\Delta G = -RT\,ln(\frac{K_{cb}}{K_{glu}})$$

where R = gas constant (8.314 J/mol.K), T = room temperature (298 K), K_{cb} = adsorption coefficient of cellobiose (L/mol), K_{glu} = adsorption coefficient of glucose (L/mol)

Appendix C

Supplementary Information for Chapter 4

C.1 Mass Transfer Limitation Tests

To ensure that the reactions are not limited by internal mass transfer limitation, acidified carbon of different particle size was used. Figure S1 shows the steady state conversion of cellobiose with increasing time on stream. Since the conversion over catalysts with both particle sizes is similar, it is concluded that there is no internal mass transfer limitation.

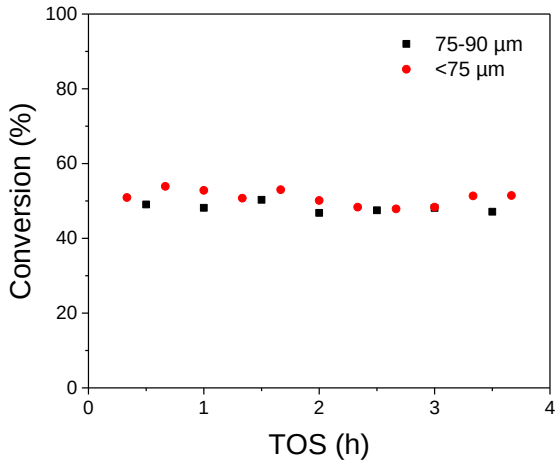

Figure C.1 Conversion of cellobiose (0.03M) using acidified carbon of different particle size. Reaction condition: 200 °C, 25 bar, 100 mg catalyst, 0.5 ml/min.

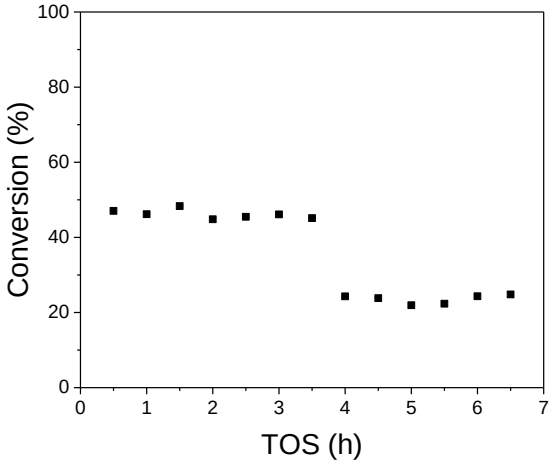

Figure C.2 Conversion of cellobiose (0.03 M) using acidified carbon. Reaction condition: 200 °C, 25 bar, 100 mg catalyst, 0.50 ml/min (0-3.5 h), 1.00 ml/min (3.5-7 h).

Subsequently, the flow rate of the cellobiose feed was doubled from 0.5 ml/min to 1.00 ml/min to ensure that the reaction was not limited by external mass transfer limitation. Figure S2 shows the conversion of cellobiose using acidified carbon with a particle size between 75 and 90 μm. To determine the reaction rate constant, the following first-order equation was used.

$$k' \frac{C_{A0} W}{F_{A0}} = \ln\left(\frac{1}{1 - x_A}\right)$$

where k' is the reaction rate constant ($L/g_{cat}.s$), C_{A0} is the initial concentration of the reactant (mol/L), W is the weight of the catalyst (g_{cat}), F_{A0} is the molar flow rate (mol/s), and X_A is the conversion. Table S1 shows the reaction rate constants obtained.

Table C.1 Value of reaction rate constant at different flow rates.

Flow Rate (ml/min)	**k' ($L/g_{cat}.s$) x 10^5**
0.50 ml/min	3.81
1.00 ml/min	3.72

Since the calculated reaction rate constants are similar, this implies that the rate of conversion is not limited under different flow conditions. Thus, there is no external mass transfer limitation under these reaction conditions.

C.2 Raman Spectra of Carbon Catalysts

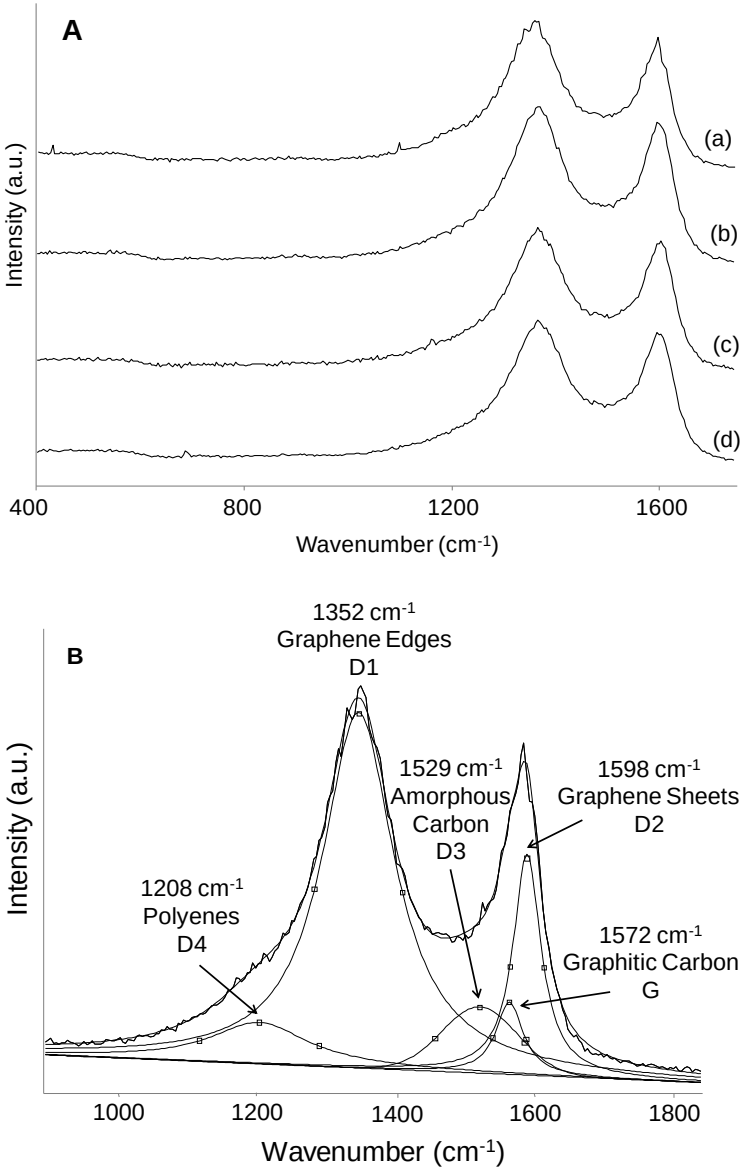

Figure C.3 (A) Raman spectra of (a) as-received carbon, (b) acidified carbon, (c) HWT acidified carbon, (d) reacidified carbon and (B) deconvoluted Raman spectrum of as-received carbon.

C.3 XRD Patterns of Carbon Catalysts

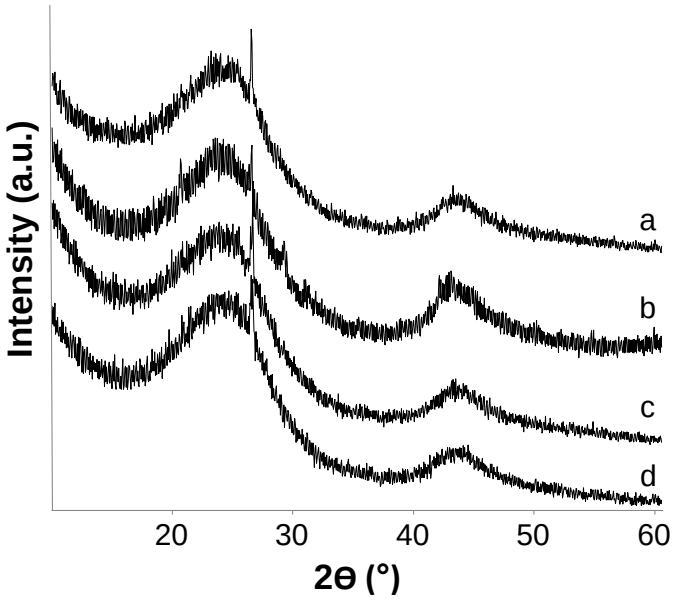

Figure C.4 XRD patterns of (a) as-received carbon, (b) acidified carbon, (c) HWT acidified carbon, (d) reacidified carbon.

C.4 ^{13}C DP MAS NMR Spectra of Carbon Catalysts

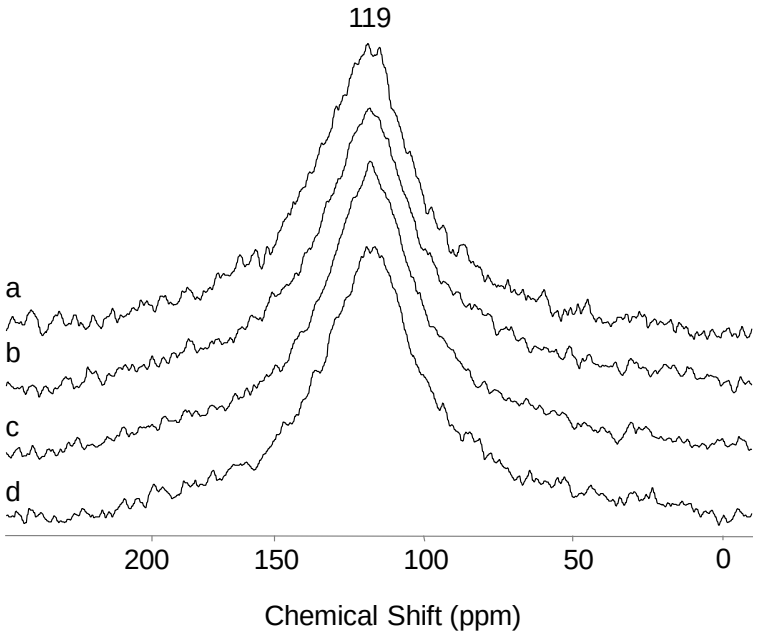

Figure C.5 ^{13}C DP MAS NMR spectra of (a) as-received carbon, (b) acidified carbon, (c) HWT acidified carbon, (d) reacidified carbon.

C.5 Pore Surface Area of Carbon Catalysts

Table C.2 Pore surface area of carbon catalysts in different pore size range.

Catalyst	Surface Area (m^2/g) Between 0.49 to 1.1 nm[a]	Surface Area (m^2/g) Between 3.2 to 36 nm[b]
As-received Carbon	290	163
Acidified Carbon	296	152
HWT Acidified Carbon	295	157
Reacidified Carbon	311	159

a: Determined by CO_2 physisorption
b: Determined by N_2 physisorption

C.6 Proton Induced X-ray Emission (PIXE) Analysis of Carbon Materials

Table C.3 Concentrations (wt%) of different elements in carbon catalysts.

Element	As-received Carbon	Acidified Carbon	HWT Acidified Carbon	Reacidified Carbon
Sodium	0.113	N/D	N/D	0.0175
Magnesium	0.487	0.0456	0.0358	0.0211
Aluminum	0.124	0.0186	0.0182	0.0147
Silicon	0.285	0.171	0.0787	0.128
Phosphorus	0.0550	N/D	N/D	N/D
Sulfur	0.160	0.358	0.321	0.225
Chlorine	0.0212	0.00494	0.00424	0.00347
Potassium	0.0632	N/D	N/D	N/D
Calcium	0.434	0.0545	0.0414	0.0337
Titanium	0.0077	0.00260	0.00191	0.0018
Chromium	N/D	0.00029	N/D	N/D
Manganese	0.0092	0.00059	0.00050	0.00038
Iron	0.161	0.0145	0.00984	0.00657
Nickel	N/D	0.00012	N/D	N/D
Copper	0.00065	0.00131	0.00107	0.00166
Zinc	0.00017	0.00014	N/D	0.00015
Selenium	N/D	0.00015	N/D	0.00011
Bromine	0.0011	0.00086	N/D	0.00033
Strontium	0.0040	0.00055	0.00047	0.00062
Lead	0.0050	N/D	N/D	N/D

N/D: Not determined due to detection limit

C.7 Concentrations of Weak Acid Sites on Carbon Materials Determined by Boehm Titration

Table C.4 Concentrations of different acid sites on carbon catalysts.

Catalyst	Phenol (μmol/g)	Lactone (μmol/g)	Carboxylic Acid (μmol/g)
As-received Carbon	29	63	37
Acidified Carbon	109	153	0
HWT Acidified Carbon	152	153	71
Reacidified Carbon	144	213	96

C.8 Reactivity of Carbon Catalysts in the Hydrolysis of Cellobiose

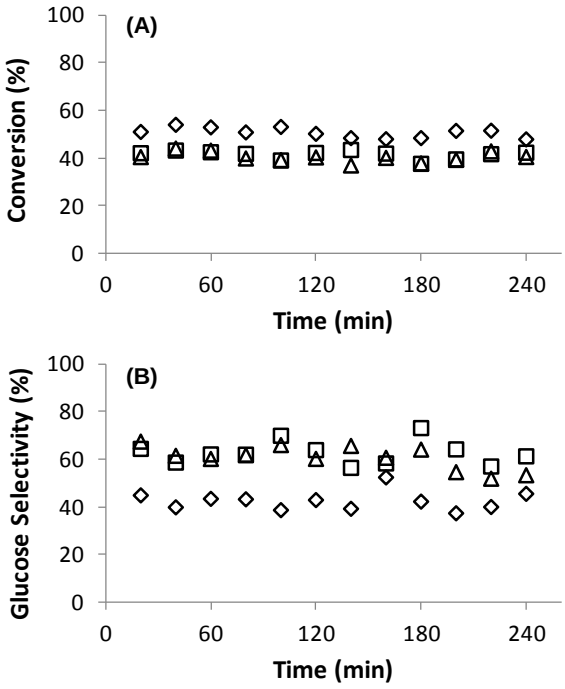

Figure C.6 (A) Conversion and (B) glucose selectivity of cellobiose hydrolysis using chemically treated carbon: (◊) acidified carbon, (□) HWT acidified carbon, and (Δ) reacidified carbon. Reaction condition: 200 °C, 25 bar, W/F = 0.111 g_{cat} (mmol h^{-1})$^{-1}$.

C.9 Selectivity of Fructose from Glucose over Carbon Catalysts

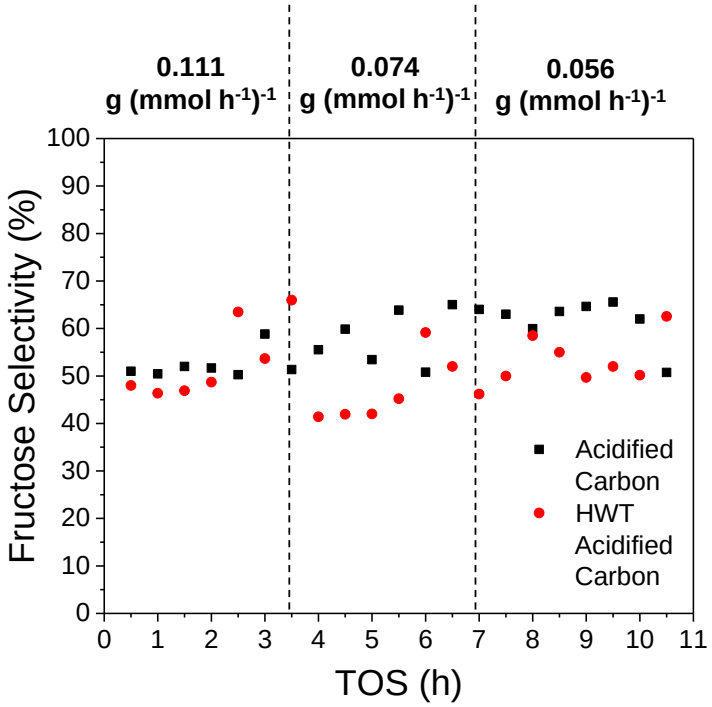

Figure C.7 Fructose selectivity from acidified carbon and HWT acidified carbon. Reaction condition: 200 °C, 25 bar.

C.10 Adsorption Isotherms of Glucose and Cellobiose on As-Received Carbon

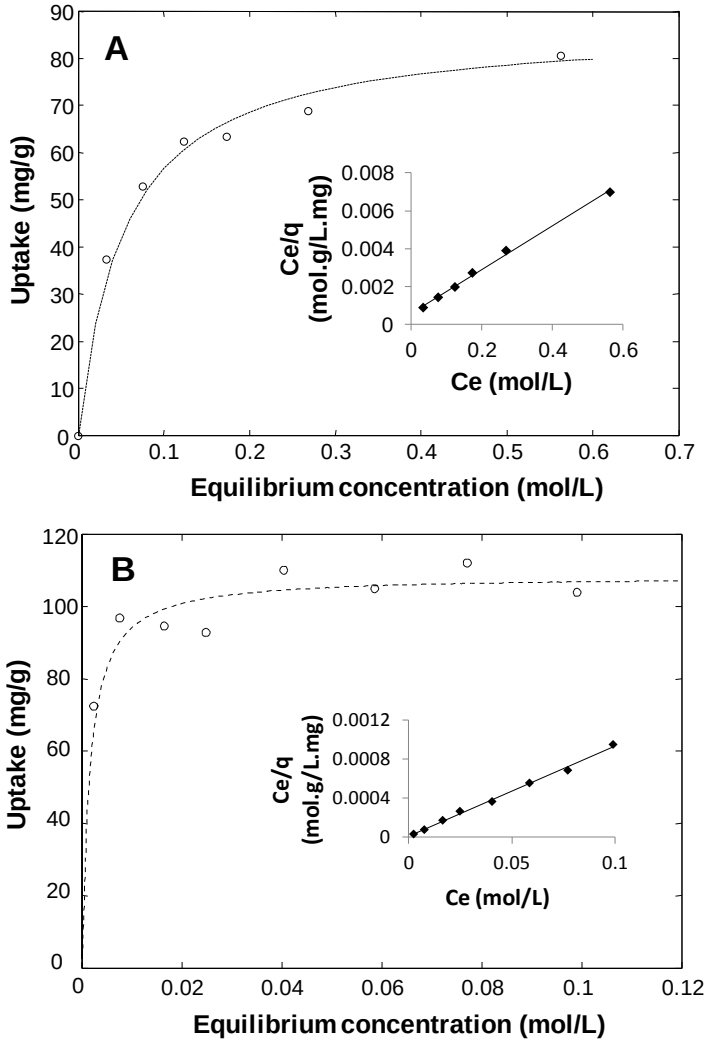

Figure C.8 Adsorption isotherms of (A) glucose, (B) cellobiose on AC. Insets: Linear regression plots of Langmuir isotherm parameters.

C.11 Validation of First Order Reaction

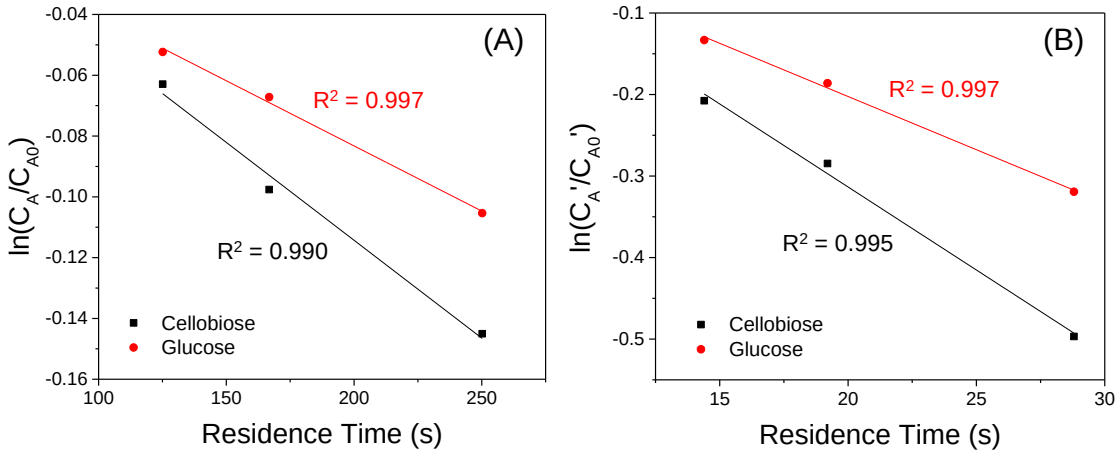

Figure C.9 Decay profile of cellobiose and glucose in an (A) empty reactor, and (B) acidified carbon catalyst bed. C_A and C_A' are the concentration of reactant before entering the reactor and catalyst bed, C_{A0} and C_{A0}' are the concentration of reactant exiting the reactor and catalyst bed.

Appendix D

Supplementary Information for Chapter 5

D.1 Weisz-Prater Criterion Tests for Internal Diffusion

To apply the Weisz-Prater criterion tests, the reaction rate of anisole over HBEA using different particle size was determined and shown in Table D.1.

Table D.1 Reaction rate of anisole over HBEA at TOS = 3 h for different particle size

	Particle Size (µm)	**Measured reaction rate (mol/g_{cat}.s) x 10^5**
R1	284	1.61
R2	83	1.62

Reaction condition: 400 °C, 80 ml/min H_2, W/F = 0.0109 g_{cat}/(mmol.h^{-1})

The following equations are used to determine whether the reactions are mass transfer limited.

Thiele modulus: $\phi_1 = R\sqrt{\frac{-r_{As}\rho_c}{D_e C_{As}}}$ (1)

Internal effectiveness factor: $\eta = \frac{3}{\phi_1^2}(\phi_1 coth\phi_1 - 1)$ (2)

Weisz-Prater parameter: $\eta\phi_1^2 = \frac{-r_A(obs)\rho_c R^2}{D_e C_{As}}$ (3)

Taking the ratio of the Thiele moduli for R1 and R2:

$\phi_1 = \left(\frac{R1}{R2}\right)\phi_2 = 3.422\phi_2$ (4)

Equation (5) was substituted into equation (6) and the ratio between R1 and R2 is taken so that the terms ρ_c, D_e and C_{AS} are canceled. Equation (7) was substituted into the final expression and it was solved using Matlab to obtain the following parameters:

For R2, $\eta = 0.9993$

For R1, $\eta = 0.9917$

The typical particle size used in the catalytic experiments is 83 μm, which suggest that the reactions are not controlled by internal diffusion.

D.2 *Operando* Transmission FTIR Cell Validation

To ensure that the kinetic data obtained from the *operando* FTIR cell is reliable, 1.3 wt% Pt/HBEA was used in the hydrodeoxygenation of anisole under the same reaction conditions as the flow reactor. Figure D.1 shows that the yield (flow reactor) and relative MS signal (*operando* FTIR cell) of the deoxygenated aromatics is comparable.

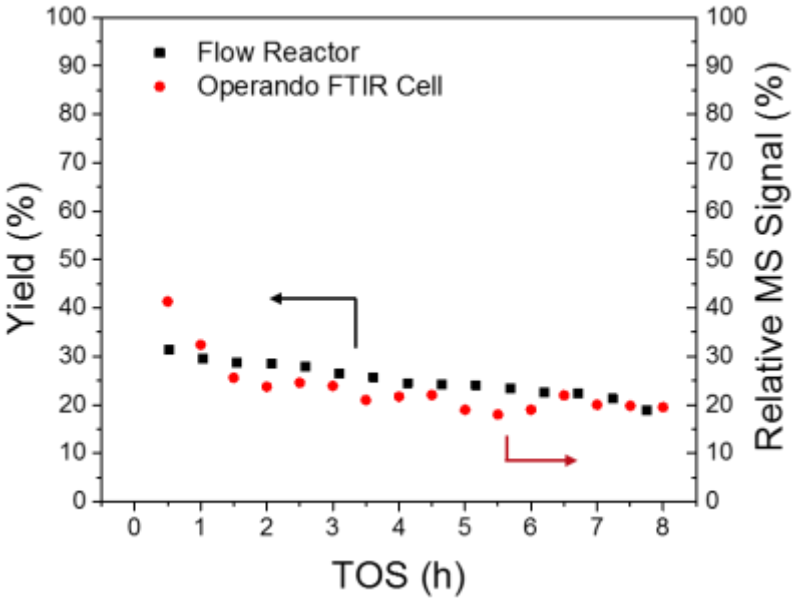

Figure D.1 Yield (flow reactor) and relative MS signal (*Operando* FTIR cell) of deoxygenated aromatics from anisole over 1.3 wt% Pt/HBEA. Reactions conditions: 400 °C, 80 ml/min H_2, W/F = 0.0109 g_{cat} $(mmol_{feed}\ h^{-1})^{-1}$.

D.3 X-ray Diffraction Pattern

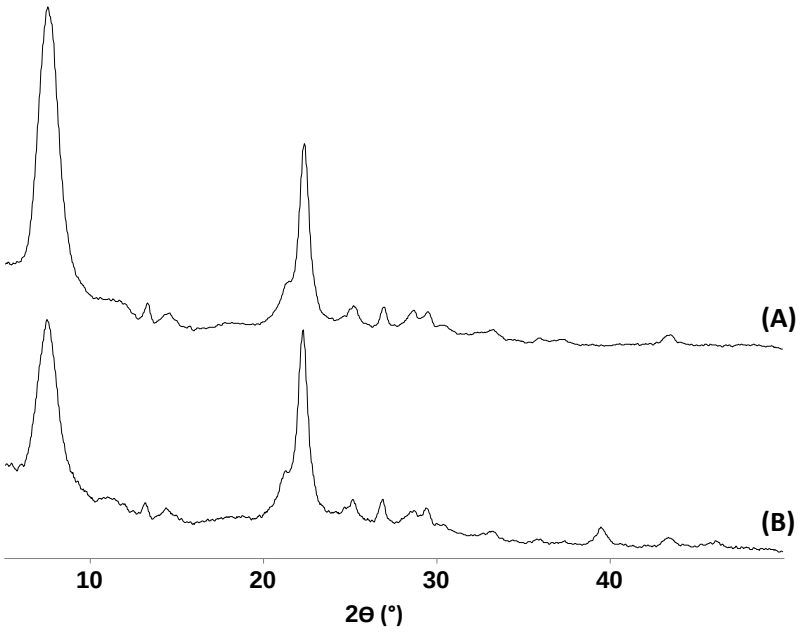

Figure D.2 XRD patterns of (A) HBEA and (B) 1.3 wt% Pt/HBEA.

D.4 ^{27}Al MAS NMR

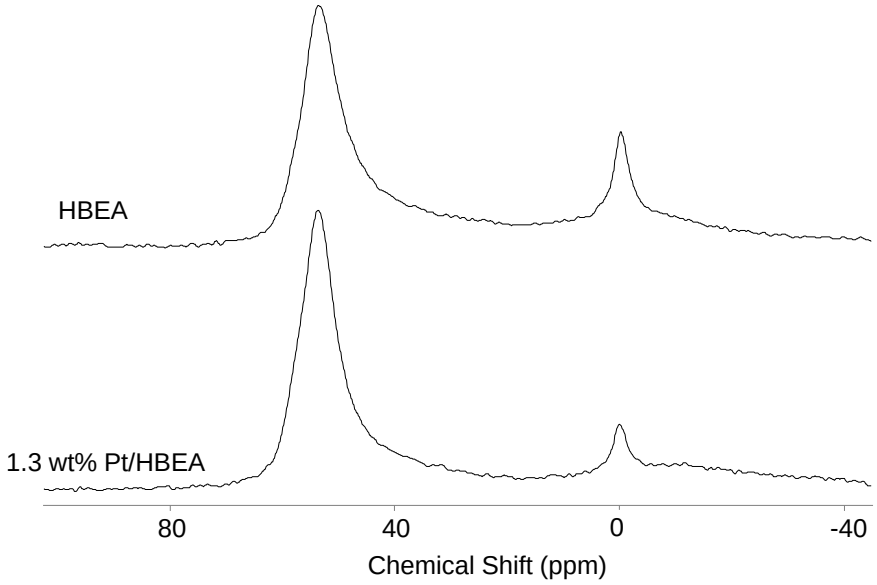

Figure D.3 ^{27}Al MAS NMR spectrum of HBEA and 1.3 wt% Pt/HBEA.

D.5 Products from Anisole over HBEA and Pt/HBEA

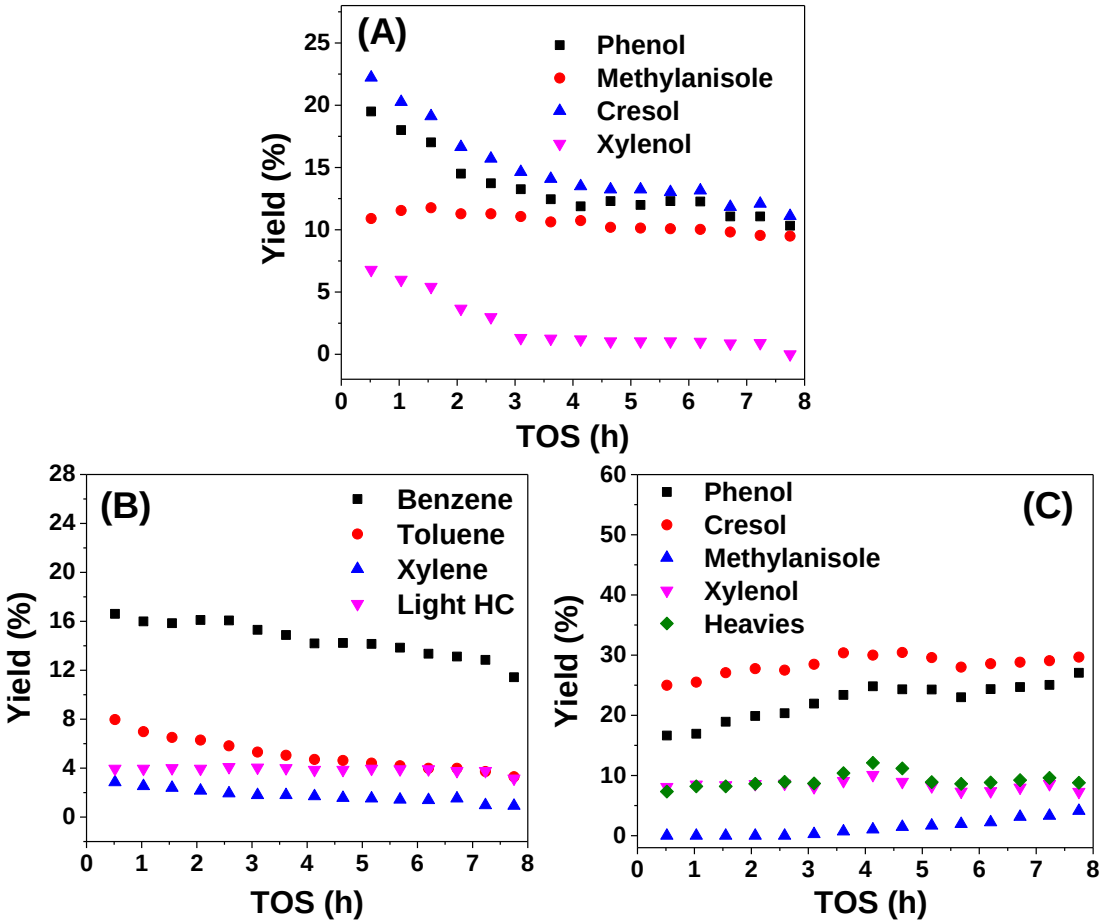

Figure D.4 (A) Yield of products from anisole over HBEA, (B) yield of deoxygenated products from anisole over 1.3 wt% Pt/HBEA, (C) yield of oxygenated products from anisole over 1.3 wt% Pt/HBEA. Reactions conditions: 400 °C, 80 ml/min H_2, W/F = 0.0109 g_{cat} $(mmol_{feed}\ h^{-1})^{-1}$.

D.6 Products from m-Cresol over HBEA and Pt/HBEA

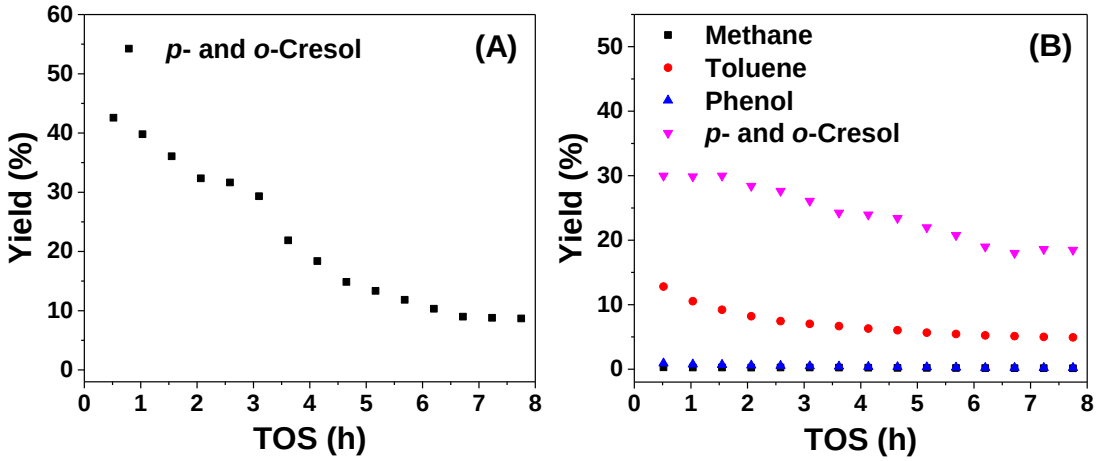

Figure D.5 (A) Yield of products from m-cresol over HBEA, (B) yield of products from m-cresol over 1.3 wt% Pt/HBEA. Reactions conditions: 400 °C, 80 ml/min H_2, W/F = 0.0109 g_{cat} $(mmol_{feed}\ h^{-1})^{-1}$.

D.7 Products from Guaiacol over HBEA and Pt/HBEA

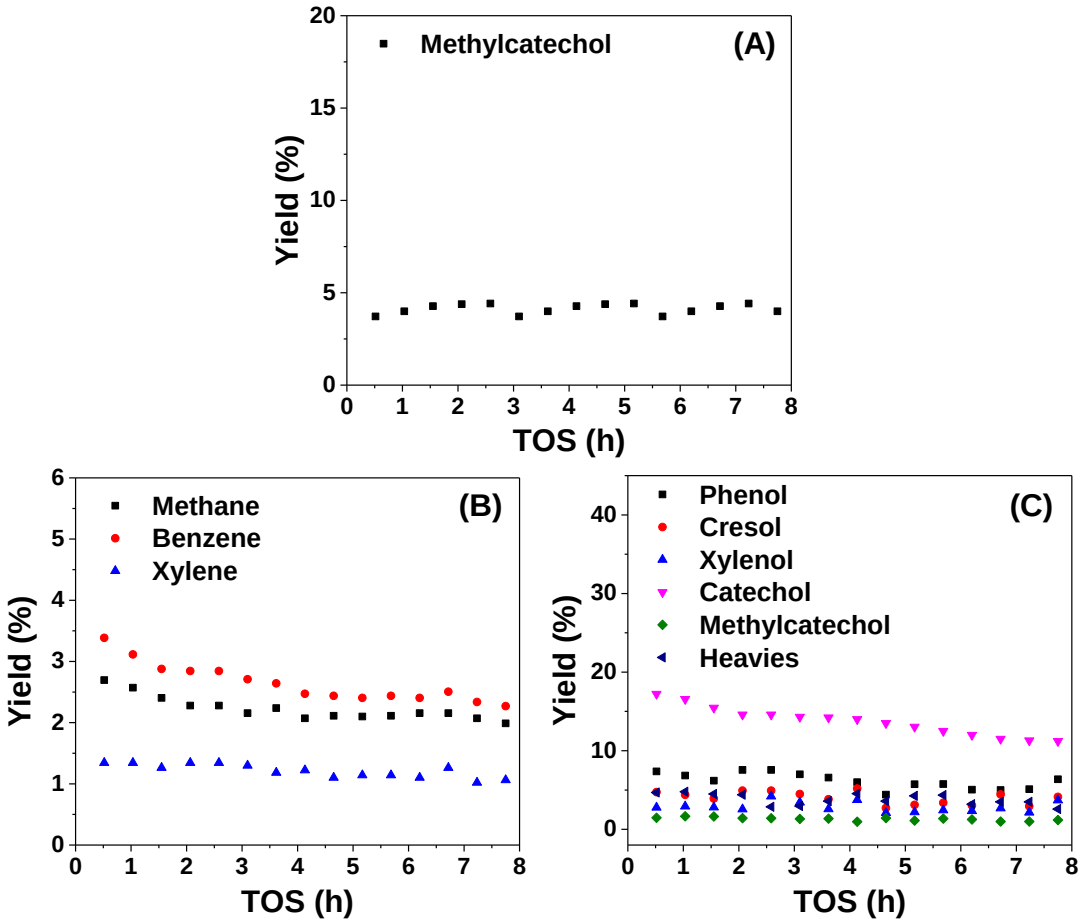

Figure D.6 (A) Yield of products from guaiacol over HBEA, (B) yield of deoxygenated products from guaiacol over 1.3 wt% Pt/HBEA, (C) yield of oxygenated products from guaiacol over 1.3 wt% Pt/HBEA. Reactions conditions: 400 °C, 80 ml/min H_2, W/F = 0.0109 g_{cat} $(mmol_{feed}\ h^{-1})^{-1}$.

D.8 Temperature Programmed Oxidation (TPO) of Spent Catalysts

Table D.2 Content of coke on spent catalysts.

	Coke formation (%)	
Reactant	**HBEA**	**Pt/HBEA**
Anisole	14.4	10.0
m-Cresol	15.2	13.7
Guaiacol	22.8	18.1

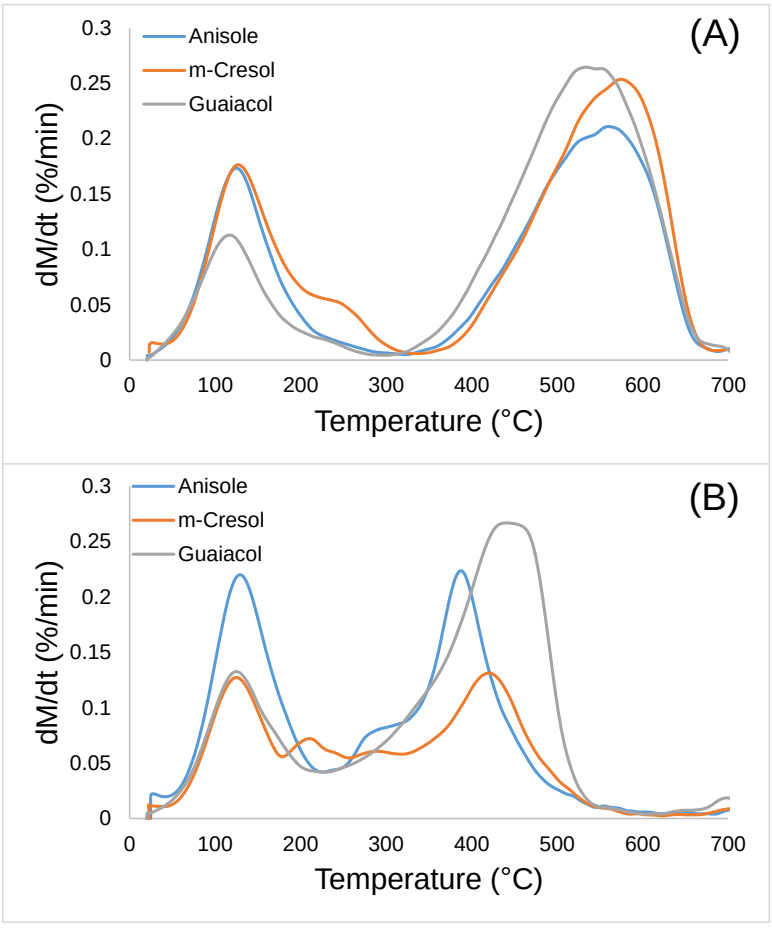

Figure D.7 Temperature programmed oxidation (TPO) of spent (A) HBEA, and (B) 1.3 wt% Pt/HBEA, after reaction with various model bio-oil compounds.